IMPROVING THE LIGHT YIELD AND TIMING RESOLUTION OF SCINTILLATOR-BASED DETECTORS FOR POSITRON EMISSION TOMOGRAPHY

DISSERTATION

zur Erlangung des akademischen Grades
doctor rerum naturalium
(Dr. rer. nat.)
im Fach Physik
eingereicht an der

Mathematisch-Naturwissenschaftlichen Fakultät
der Humboldt-Universität zu Berlin

von

Dipl.-Phys. Univ. Christof Thalhammer

Präsident der Humboldt-Universität zu Berlin
Prof. Dr. Jan-Hendrik Olbertz

Dekan der Mathematisch-Naturwissenschaftlichen Fakultät
Prof. Dr. Elmar Kulke

Gutachter:
1. Prof. Dr. Thoralf Niendorf
2. Prof. Dr. Oliver Benson
3. Prof. Dr. Uwe Pietrzyk

Tag der mündlichen Prüfung: 17. Juni 2015

Abstract

Positron emission tomography (PET) is a powerful medical imaging methodology to study metabolic and functional processes. It is based on the localization of molecular probes inside the subject through registration of gamma photons from positron-electron annihilation events. Hence, the detectors used for sensing these gamma photons are a key component of all PET systems. The light yield and coincident resolving time (CRT) of scintillator-based detectors are constrained by optical processes. These include light trapping in high refractive index media and incomplete light collection by the photosensor. To address these constraints, this work proposes the use of micro and nano optical devices with the ultimate goal to improve the signal to noise ratio and overall image quality of PET acquisitions. To meet this goal, detailed Monte Carlo simulation studies of a scintillator-based PET detector module are presented along with optical experiments.

A micro optical light concentrator (LC) with tapered geometry is proposed to improve the light collection of silicon photomultipliers on the Geiger-cell level. The influence of the concentrator geometry on its optical properties is studied in detail in simulations. The feasibility of fabricating LCs with variable taper angles and sub-micrometer accuracy is demonstrated. The angular transmission characteristics of these samples are validated with a goniometer setup. Monte Carlo simulation studies of a PET detector module equipped with LCs indicate a 15% increase in light yield and a 5% improvement in CRT. Light output measurements of individual scintillator crystals reveal a gain in light yield of 9% and improved timing by 4%. The sensitivity of the LC approach to fabrication-related inaccuracies is analyzed and next steps for the transfer of this technology to state of the art silicon photomultipliers are discussed.

Further, two-dimensional photonic crystals (PhCs) are proposed to reduce the light trapping in high-index scintillators. Realizing the challenge of combining the diffractive properties of PhCs with ray tracing algorithms based on geometric optics, this work presents a novel implementation that takes into account all wavelength-, angular-, and polarization-dependent PhC characteristics. Angle-resolved transmission measurements of samples fabricated with electron beam lithography are used to validate the new technique and to study the optical properties of PhCs. The combined approach is put to use to integrate an optimized PhC coating into the PET detector model. The simulation results underline the potential of PhCs to improve the light yield and timing of PET detectors, although not all configurations benefit to the same extent. For a detector setup considering polished scintillator crystals, 17% gain in light yield and a 5% improvement in CRT is predicted. For a setup consisting of etched scintillators with rougher surfaces, the calculations reveal more modest gains of 8% for the light yield and 3% for the CRT. A simulation study that combines LCs and PhCs indicates that the positive effects of both approaches culminate in substantial gains in light yield of 33% for the polished and 23% for the etched detector configuration. The corresponding improvements in CRT are computed to be 9% and 7% for the polished and etched configuration. Realizing the tradeoff between achieved gains through PhCs and required fabrication efforts, a novel manufacturing technique based on direct nano imprinting is presented. This approach combines reduced complexity and high accuracy. The feasibility of this approach is demonstrated and implications for future PET detector generations are discussed.

Zusammenfassung

Positronen-Emissions-Tomographie (PET) ist eine medizinische Bildgebungstechnik die es erlaubt biochemische und physiologische Prozesse zu untersuchen. Diese Methode basiert auf der Lokalisierung von Radiopharmaka im Körper des Patienten durch die Registrierung von Positron-Elektron Vernichtungsstrahlung. Daher stellt der Detektor zur Messung dieser Gamma Quanten einen der wichtigsten Komponenten eines jeden PET Systems dar. Die Lichtausbeute und Zeitauflösung Szintillator-basierter Detektoren wird von diversen optischen Mechanismen begrenzt. Dazu zählen die ineffiziente Lichtauskopplung aus Materialen mit hohem Brechungsindex sowie die begrenzte Sensitivität der Photodetektoren. Mit der Kenntnis dieser Einschränkungen präsentiert diese Arbeit Lösungsansätze auf der Basis mikro- und nano-optischer Technologien mit dem Ziel, ein besseres Signal-Rausch Verhältnis sowie bessere Bildqualität zur ermöglichen. Für diese Zwecke werden detaillierte Monte Carlo Simulationen in Verbindung mit optischen Experimenten verwendet.

Um die Sensitivität von Silizium Photoelektronenverfielfachern auf Geiger-Zellen Ebene zu verbessern wird ein mikro-optischer Lichtkonzentrator vorgeschlagen. Der Einfluss der Konzentratorgeometrie auf dessen optische Eigenschaften wird mit Hilfe von Simulationen untersucht. Weiterhin wird die Herstellung von Konzentratoren bei unterschiedlichen Reflektor-Winkeln mit Submikrometer-Genauigkeit demonstriert. Die winkelabhängigen Eigenschaften der Proben werden mit Hilfe eines Goniometeraufbaus untersucht. Monte Carlo Simulationen eines PET Detektormoduls ausgestattet mit einem Lichtkonzentrator sagen ein Gewinn an Lichtausbeute von 15% sowie eine verbesserte Zeitauflösung um 5% voraus. Messungen an einzelnen Szintillatorkristallen ergeben 9% mehr Lichtausbeute und 4% verbesserte Zeitauflösung. Die Arbeit untersucht die Abhängigkeit des Konzentrator-Ansatzes von herstellungsbedingten Ungenauigkeiten und diskutiert die notwendigen Schritte um diese Technologie in aktuelle Silizium Photoelektronenverfielfacher zu implementieren.

Weiterhin untersucht diese Arbeit zweidimensionale photonische Kristalle, die es ermöglichen mehr Licht aus Szintillatoren mit hohem Brechungsindex auszukoppeln. Da die Beugungseigenschaften photonischer Kristalle in der Regel nicht direkt in gewöhnliche *Ray Tracing* Algorithmen eingebunden werden können, wird eine neue Technik präsentiert. Diese berücksichtigt sämtliche wellenlängen-, winkel- und polarisations-abhängigen Charakteristika. Um diesen Ansatz zu validieren und die optischen Eigenschaften photonischer Kristalle zu untersuchen werden winkelabhängige Transmissionsmessungen an Proben durchgeführt, die mittels Elektronenstrahllithographie hergestellt wurden. Anschließend wurde die Simulationstechnik benutzt, um den Einfluss optimierter photonischer Kristalle auf die Eigenschaften eines PET Detektormoduls zu analysieren. Diese Studien zeigen, dass photonische Kristalle Ausbeute und Zeitauflösung eines PET Detektors verbessern können, wenn auch nicht alle untersuchten Konfiguration gleich von ihnen profitieren. Für eine Konfiguration bestehend aus polierten Szintillatoren werden ein Lichtausbeuten-Gewinn von 17% sowie eine Verbesserung der Zeitauflösung von 5% vorhergesagt. Bei geätzten Szintillatoren, die größere Oberflächenrauigkeit aufweisen, ergeben sich 8% Steigerung der Lichtausbeute und 3% verbesserte Zeitauflösung. Weitere Simulationsstudien eines kombinierten Ansatzes aus Lichtkonzentrator und photonischen Kristallen deuten darauf hin, dass sich die beiden Technologien nicht negativ beeinflussen. Stattdessen werden deutliche Gewinne der Lichtausbeute in Höhe von 33% für polierte und 23% für geätzte Szintillatoren ermöglicht. Die Verbesserungen in der Zeitauflösung machen etwa 9% und 7% aus. Angesichts des erheblichen Aufwandes bei der

Herstellung photonischer Kristalle präsentiert diese Arbeit eine neuartige Fertigungstechnologie basierend auf der *Direct Nano Imprinting* Methode. Diese verspricht einen vereinfachten Herstellungsprozess bei sehr hoher Genauigkeit. Die Machbarkeit dieser Methode wird demonstriert und Schlussfolgerungen für zukünftige Generationen von PET Detektoren werden diskutiert.

Contents

Abbreviations

AC attenuation correction

ADC analog-to-digital converter

Al aluminum

APD avalanche photodiode

BGO bismuth germanium oxide

CNT Fraunhofer Center for Nano Technologies

COR center of rotation

CPC compound parabolic concentrator

Cr chromium

CRT coincident resolving time

CT computed x-ray tomography

DLL dynamic link library

DRIE deep reactive ion etching

EBL electron beam lithography

EM electromagnetic

FDG fluorodesoxy glucose

FEP Fraunhofer Institute for Electron Beam- and Plasma Technology

FWHM full width at half maximum

G-APD avalanche photodiode in Geiger mode

HF hydrofluoric

ITO tin-doped indium oxide

KOH potassium hydroxide

LC light concentrator

LED leading edge discriminator

LOR line of response

LSO lutetium oxyorthosilicate

LUT look-up table

MC Monte Carlo

MRI magnetic resonance imaging

NaI(Tl) thallium-activated sodium iodide

NIL nano imprint lithography

PD photodiode

PDE photon detection efficiency

PDMS Polydimethylsiloxan

PET positron emission tomography

PhC photonic crystal

PMT photomultiplier tube

RI refractive index

RIE reactive ion etching

SCIL surface conformal imprint lithography

SEM scanning electron microscopy

Si silicon

$\mathbf{Si_3N_4}$ silicon nitride

$\mathbf{SiO_2}$ silicon dioxide

SiPM silicon photomultiplier

SNR signal-to-noise ratio

SOI silicon-on-insulator

TC tapered concentrator

TIR total internal reflection

TOF time-of-flight

UV ultraviolet

Chapter 1

Introduction

Positron emission tomography (PET) is a medical imaging technique for studying functional and metabolic processes in living subjects. Through the use of molecular probes consisting of compounds that are labeled with positron emitting radioisotopes, a broad range of biochemical mechanisms can be imaged and measured. Fueled by various improvements regarding radiopharmaceuticals, sensitivity, spatial resolution and fusion with anatomic imaging techniques, PET is among the fastest growing diagnostic methodologies [1]. Numerous studies showed the significant impact of PET on patient management and treatment planning [2–4]. Currently, PET is primarily used in three clinical fields. In oncology, PET applications include the diagnosis of cancer, staging and localization of malignant tissue for radiotherapy and surgery, detection of residuals or recurrence of the disease, and measuring the response to therapy [1, 5–7]. Recent progress in image quality and PET system availability has also driven new efforts in cardiac applications, such as myocardial viability examinations or diagnosis and assessment of coronary artery disease [8–10]. The third field is neurology, where PET is used for the early detection of Alzheimer's disease or differentiation between various forms of dementia [11, 12].

Technical advances in PET detector technology have played a crucial role for this positive development and continue to be of pivotal relevance. Among the most significant innovations was the introduction of the lutetium oxyorthosilicate scintillator, which provides an unprecedented combination of light output, sensitivity and timing properties [13]. This was a major driving force for the development of systems with increased spatial resolution [14] and motivated renewed interest in fast detectors for time-of-flight applications [15]. A more recent trend is the move towards semiconductor-based photosensors to replace the established photomultiplier tubes [16]. In this area, silicon photomultipliers (SiPMs) are a promising new technology which bears the potential to provide performance characteristics that match or even exceed the levels of state-of-the-art photomultiplier tubes [17, 18]. Additionally, SiPMs are insensitive to magnetic fields which makes them ideal candidates for hybrid systems combining PET and magnetic resonance imaging [19].

Despite these advances, the optical processes occurring in PET detectors still exhibit certain limitations. The transfer of photons from the scintillation location to the photosensor has a strong impact on several detector characteristics such as energy and timing resolution [20–22]. As these properties directly influence the signal-to-noise ratio, the optimization of the optical mechanisms promises further improvement of the detector performance. In current PET systems, a major limitation of the photon transfer stems from insufficient light extraction from scintillators [23]. Trapping of light leads to prolonged photon trajectories which cause increased absorption losses. Also, the efficient extraction of photons at their first incidence on the scintillator exit face is expected to improve the timing resolution, which is not exclusively defined by the total amount of registered photons but also depends on their propagation time distribution [24]. In current detectors, light trapping is caused by total internal reflection occurring at the interface of the high refractive index scintillator and the low index optical glue, which is used to couple the scintillator to the photosensor [25]. A promising means to increase the light extraction from high-index media are slabs of two-dimensional photonic crystals (PhCs) [26]. These consist of layers that exhibit a biperiodic modulation of the refractive index with geometric dimensions in the range of the wavelength of the incident light [27]. Photons impinging on these gratings are scattered into various diffraction orders which can lead to the extraction of light beyond the total internal reflection threshold. First studies demonstrated the applicability of PhCs to individual crystals of inorganic scintillators and showed improved light output and timing resolution [24, 28].

For novel detector designs implementing SiPMs, the incomplete light collection by these photosensors represents another considerable constraint. These devices consist of a multitude of individual microcells which are separated by insensitive areas leading to a geometric fill factor in the range from 30% to 80% [29]. Consequently, only a certain fraction of photons impinging on the SiPM is registered whereas the remaining photons are either absorbed or reflected by the inactive sensor zones. Although reflected light might return to an active microcell later on, the increased detection of light at an early phase of the signal is expected to be of particular importance for the timing resolution [30]. The SiPM light collection could be increased through the use of a light concentrator (LC) that prevents photons from impinging on the insensitive areas and redirects them towards the active cells [31].

Realizing these challenges, this work proposes the use of PhCs to enhance the light extraction from scintillators and the application of LCs to SiPMs to increase the photon collection with the ultimate goal to improve the light yield and timing resolution of PET detector systems. The impact of these approaches are studied using optical Monte Carlo simulations which have proven to be a powerful tool to study the propagation of scintillation photons in PET detectors [21, 22, 32–34]. Equipping an interface with PhCs does not only change the transmission characteristics, but also manipulates the photon trajectories through scattering into various diffraction orders. These effects are usually not taken into account by conventional simulation tools based on geometric optics. Previous approaches to implement PhCs into these algorithms consisted in analytical models [25] or look-up tables that contained lists of angle-dependent transmission coefficients [23]. However, these techniques neglected the scattering properties of PhCs. To overcome this shortcoming, this work presents a novel method of implementing the full diffractive nature of PhCs into an established ray tracing software. To study the optical properties of PhCs and LCs in detail and to validate the combined simulation approach, angle-resolved transmission measurements are conducted using samples produced with various semiconductor fabrication technologies. The verified simulation methods are then put to use to evaluate the impact of optimized PhC and LC configurations on the light yield and timing resolution of a state-of-the-art PET detector module. The influence of fabrication-related imperfections and wavelength-dependent effects are considered. Potential adverse effects caused by the combination of LCs and PhCs are discussed. The benefit of LCs for the light collection is demonstrated in scintillator-based experiments. Finally, first results of a novel fabrication technology based on direct nano imprinting are presented, which constitutes a promising alternative for the realization of PhCs on scintillator surfaces in a way that is compatible with future implementations in commercial detector systems.

Chapter 2

Detector Systems for Positron Emission Tomography

This chapter introduces the physical principles of PET, gives an overview over the different components of clinical PET systems, and summarizes important characteristics describing the detector performance. These sections are based to a large extent on Refs. [1, 35–37].

2.1 Basics of Positron Emission Tomography

2.1.1 Fundamental Principles

A PET system consists of three main components: an annular gantry of detectors, a moveable patient bed to position the subject inside the gantry, and computer stations for the collection of the raw data, image reconstruction, and processing. For every PET examination, a radiopharmaceutical is administered to the subject via inhalation or injection into the bloodstream. This tracer consists of a biologically active molecule that is labeled with a positron emitting radionuclide. The actual PET scan begins after a certain delay time, which is necessary to allow the transport and uptake of the radiopharmaceutical by the organ of interest. The radionuclide emits a positron, which travels only a short path inside the subject due to strong elastic and inelastic scattering with the atoms of the adjacent tissue. Eventually, the positron annihilates with an electron which leads to the emission of 2 gamma photons each having an energy of 511 keV. Because the kinetic energy of the positron and electron are usually very low at the moment of annihilation, the conservation of momentum leads to antiparallel trajectories of the 511 keV photons. These are registered by the detectors inside the gantry surrounding the subject. If two photons are detected within a certain timing window (typically a few nanoseconds), a coincidence event is recorded along the line of response (LOR) connecting the two sensors. The event is transformed into polar coordinates within the gantry and saved as a sinogram, representing the number of recorded events per LOR. By collecting a large number of sinograms, the location of the annihilation event can be determined. Using additional datasets for detector normalization and attenuation correc-

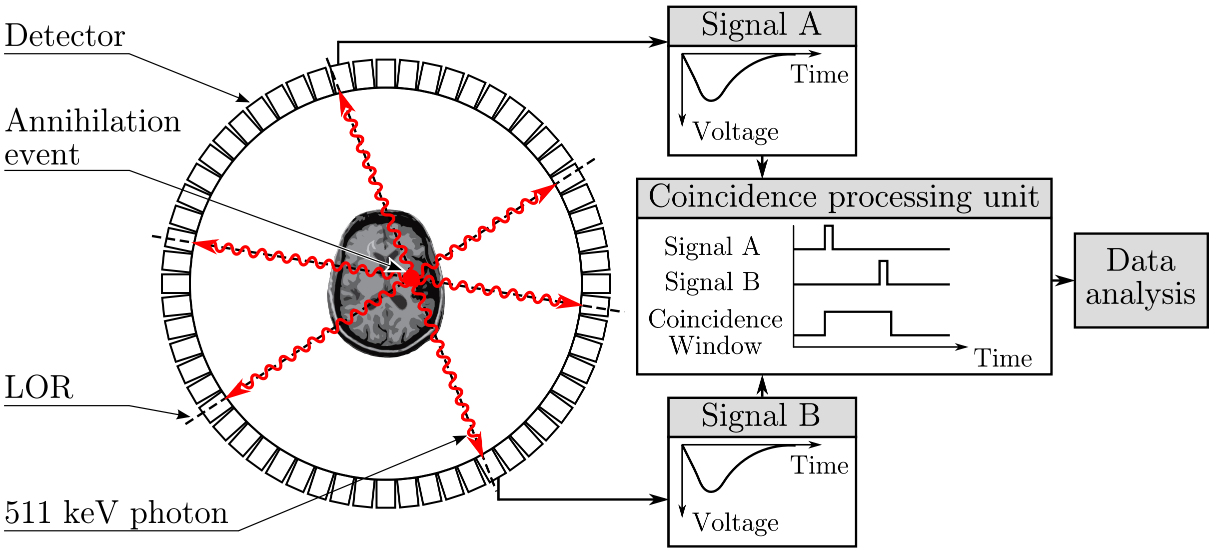

Figure 2.1: Principle of a PET acquisition: antiparallel 511 keV photons are registered by a pair of detectors. If the two signals occur within a certain time window, a coincident event is recorded along the corresponding LOR. The figure is based on Ref. [1] using an artistic modification of a brain image taken from Ref. [38].

tion, the image can be reconstructed to yield a spatial distribution of the concentration of the radiopharmaceutical inside the subject.

In current clinical practice, ^{18}F fluorodesoxy glucose (FDG) is the most commonly used radiopharmaceutical. It is an analogue of glucose which allows studying the metabolism of cells, a mechanism that is of special interest for oncology and neurology. FDG-PET offers a substantial advantage in localizing potentially malignant tissue compared to a purely anatomical imaging procedure, since often metabolic changes precede morphological changes associated with disease [35, 39–41].

2.1.2 PET Detector Components

An essential part of any PET system is the detector array, which is used to register the gamma photons emitted by the annihilation event. There are different types of detectors for sensing high energy radiation, such as proportional gas chambers and semiconductor detectors. Today, scintillation detectors are most commonly used for PET, since they offer the best combination of sensitivity and accuracy [1].

A scintillation detector consists of two main components, a scintillating medium which converts incident gamma radiation into photons within the visible or ultraviolet spectrum (scintillation photons), and a photosensor which registers the scintillation photons and converts them into an electrical signal. Further components used in PET detectors include reflective wrappings or coatings for the optical isolation of adjacent scintillator crystals, collimators made of tungsten to reduce the detection of scattered gamma photons, and optical glue which couples the scintillator crystal and the photosensor (see Fig. 2.2).

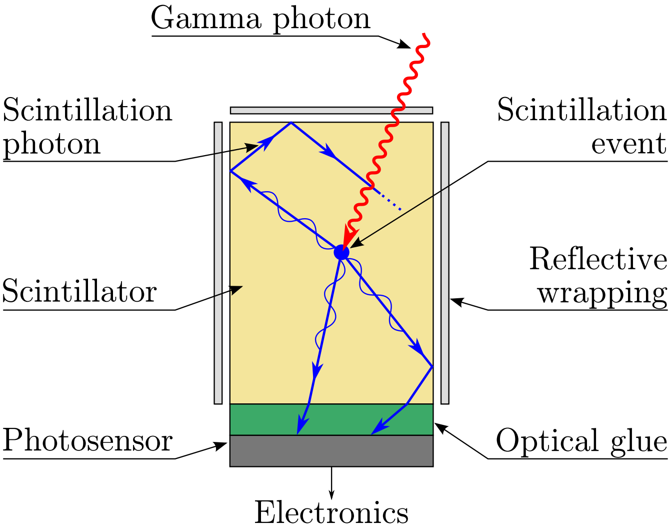

Figure 2.2: Schematic of a scintillation detector for gamma radiation. The colors used for the individual components are consistent with the other figures in this work.

2.1.3 Combining PET with Other Imaging Modalities

The contrast and resolution of PET acquisitions make it difficult to identify anatomical structures reliably. This leads to a limited accuracy of localizing the regions of increased metabolic activity and represents a major challenge in interpreting data obtained from PET scans. The limited spatial resolution can be improved significantly by using additional data from imaging methodologies that provide detailed anatomical information such as computed x-ray tomography (CT) or magnetic resonance imaging (MRI).

Furthermore, supplemental data from CT or MRI can be used for the attenuation correction (AC) of PET acquisitions, in order to replace the conventional approach of transmission scanning with rod- or point sources with the ultimate goal to decrease patient dose and reduce examination times [42]. AC is a necessary requirement for the quantitative analysis of PET data, since it adjusts the signals detected by the PET system to compensate for the attenuation of 511 keV photons on their way from the annihilation location to the detector.

In CT-based AC, a linear scaling algorithm transforms the attenuation data acquired from a CT scan for an energy interval of e.g. 40 to 140 keV into an attenuation map at 511 keV [43, 44]. Since the anatomic information provided by MRI correlates to the density of hydrogen nuclei and tissue-specific relaxation constants [45], MRI-AC techniques are more complicated and base on segmentation approaches or use general atlas datasets which are transformed to match a given subject [46].

The co-registration of datasets from PET and CT/MRI that have been acquired on different scanners requires the use of computer algorithms for image fusion. Although this approach works for relatively fixed organs, its efficiency is strongly reduced for other regions of the body because of variations in patient positioning and internal movement of organs. The co-registration can be significantly improved by using combined PET/CT or PET/MRI scanners that allow sequential image acquisitions with two modalities without removing the patient from the bed [42, 47, 48]. The first prototype of a PET/CT hybrid system was presented in 2000 [42] and the technology has been accepted rapidly in the field of oncology because it provides more information and increased accuracy compared to separate acquisitions on conventional scanners [49].

Combining PET and MRI systems is technically more challenging. For decades, photomultiplier tubes (PMTs) have been the preferred photosensors in PET detectors because of their high gain and fast response (see Sec. 2.4.1.1 for details). Since they are based on the movement of electrons in an electric field, these sensors are highly sensitive to the static magnetic fields of MRI systems. Recent progress in semiconductor-based photosensors that are insensitive to magnetic fields have facilitated prototype PET/MRI hybrid systems for animal [50] and human brain imaging [38]. These developments led to the introduction of first commercial whole body systems in 2011 [51]. The new technology of SiPMs, which combine insensitivity to static magnetic fields with excellent timing resolution, are expected to play an important role in future PET systems [17, 18, 52, 53]. Therefore, this work focuses on detector configurations that use SiPMs as photosensors.

2.2 PET Detector Characteristics

PET systems exist in various configurations depending on the specific imaging application. They differ in multiple aspects such as the scintillation material, the detector design, the system size, and its geometry. Hence, there is a variety of parameters that can be used to characterize the performance of PET detectors including spatial resolution, count rate, scatter fraction or sensitivity [1].

In this section, the two important detector characteristics energy resolution and timing resolution are introduced, which have a substantial influence on the signal-to-noise ratio (SNR) of a PET acquisition. Both characteristics are strongly correlated to the light yield of the detector N_{Det}, which is the number of scintillation photons that are registered by the photosensor.

2.2.1 Interaction of Electromagnetic Radiation with Matter

To understand the detection process and characteristics of PET systems, it is important to discuss the different mechanisms of interaction between electromagnetic (EM) radiation and matter. After the emission of the 511 keV annihilation photons, they must first traverse the subject before they can be detected by the sensor. Hence, various interactions can occur with the tissue of the subject, the scintillating medium, and any other material within the scanner, e.g. collimators or patient bed. Regarding 511 keV gamma photons, the two main mechanisms for these interactions are Compton scattering and the photoelectric effect. Other effects like Rayleigh scattering, pair production or photonuclear reactions are neglected in this discussion, since they do not play a significant role for the energies of interest in PET.

2.2.1.1 Compton Scattering

The inelastic scattering of photons with loosely bound electrons is called Compton scattering. This process leads to a deviation of the incident gamma photon and the transfer of energy to the recoil electron (see Fig. 2.3a). A small fraction of this energy is required for the atomic binding energy, the rest is converted into kinetic energy of the electron. Using the laws of conservation of energy and momentum, the energies of the scattered photon and the recoil electron as well as the recoil angle can be calculated. The energy E'_γ of the photon after Compton interaction can be derived from the scattering angle α through

$$E'_\gamma = \frac{E_\gamma}{1 + \frac{E_\gamma}{m_{\mathrm{El}}c^2}\left(1 - \cos(\alpha)\right)} \, , \tag{2.1}$$

where E_γ is the initial energy of the gamma photon, m_{El} is the rest mass of an electron, and c is the speed of light.

Compton scattering is the dominant effect for the interaction of photons with tissue for energies in the range from 100 keV to approximately 2 MeV [1]. The energy losses due to this effect must be considered when analyzing the spectrum of events registered by the PET detector (see Sec. 2.2.2).

2.2.1.2 Photoelectric Effect

In the photoelectric effect, the entire energy of the incident photon is transferred to an orbital electron of the absorbing medium as illustrated in Fig. 2.3b. The ejected electron is called photoelectron and has a kinetic energy of $E_{\mathrm{Kin}} = E_\gamma - E_{\mathrm{B}}$, where E_γ is the energy of the incident photon and E_{B} denotes the binding energy of the orbital electron. Usually, the photoelectric effect occurs for electrons of an inner shell and the resulting vacancy is often filled by an electron from an outer shell with the emission of a characteristic x-ray. Instead, the energy can also be released through the ejection of a second electron called Auger electron. The probability for the photoelectric absorption of photons in a medium strongly depends on the atomic number Z of the material. For the interaction of 511 keV photons with typical scintillator materials, the photoelectric effect has a similar importance as Compton scattering. However, photoelectric absorption in tissue plays a dominant role for photon energies less than approximately 100 keV. Although this energy is significantly lower than the 511 keV of PET annihilation photons, it is of importance for the application of AC in combined PET/CT systems.

2.2.2 PET Events and Signal-to-Noise Ratio

A PET detector registers three types of coincidence events: true, scattered, and random events. In the case of a true coincidence, the annihilation photons undergo no significant interaction prior to their detection. These are the signals which provide the correct LOR and yield the actual image information.

In contrast to this, in a scattered coincidence one or both photons are Compton scattered within the imaging field of view, e.g. within the subject. Since such events lead to the

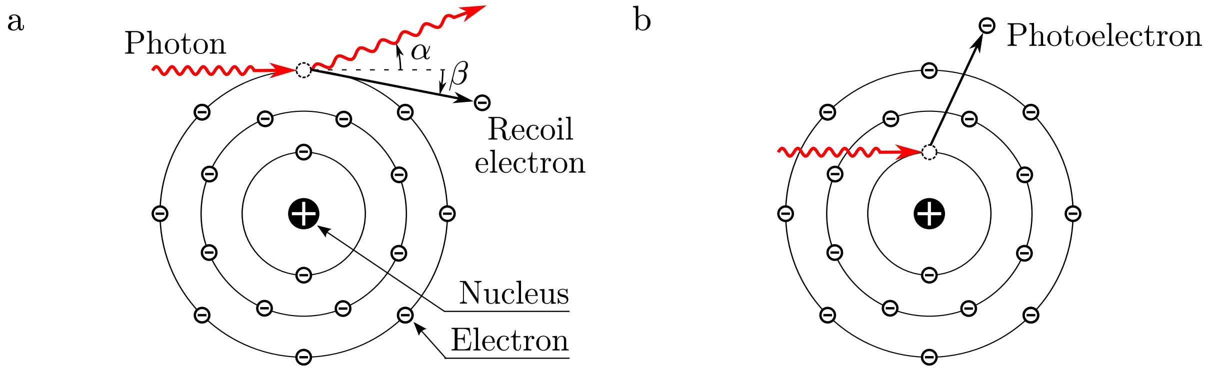

Figure 2.3: (a) Illustration of Compton scattering. The emission angle β and the kinetic energy of the recoil electron can be derived from the scattering angle α. (b) Illustration of photoelectric effect. Adapted from Ref. [1].

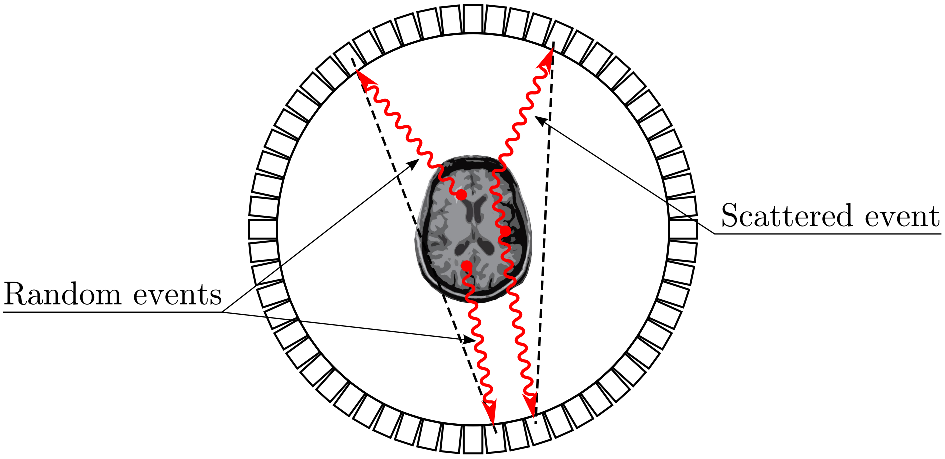

Figure 2.4: Illustration of scattered and random events in PET, which lead to wrong assignments of the LOR (dashed lines). Adapted from Ref. [1].

incorrect assignment of the LOR (see Fig. 2.4), they lead to a decrease in image contrast. Random events are signals that are detected within the coincidence timing window, although they stem from unrelated annihilation events. These signals add to the image background and deteriorate its SNR.

The count rates C of these different kinds of coincidence events influence the SNR of a PET acquisition. In a simple model that bases on a cylinder of diameter D with a uniform distribution of radioactivity and that uses analytical back-projection for the reconstruction of the PET image, the SNR can be estimated through

$$\mathrm{SNR} = A\,\frac{1}{\sqrt{N_{\mathrm{El}}}} \cdot \sqrt{\frac{C_T^2}{C_T + C_S + C_R}}\,. \tag{2.2}$$

Here, C_T is the number of true coincidence events registered by the detector, C_S is the number of scattered events, C_R is the number of random events, and A is a constant representing the influence from the radioactive source and the detector geometry. The parameter $N_{\mathrm{El}} = D/d$ corresponds to the number of volume elements of size d that contain activity along the assigned LOR. [15, 54, 55]

2.2.3 Energy Resolution

The output signal of a PET detector is proportional to the power absorbed in the scintillator, which allows measuring the energy of the incident gamma photon. The energy resolution δE of a PET detector array quantifies the accuracy of this measurement.

In a typical PET acquisition, the detector registers a broad spectrum of energies as depicted in Fig. 2.5. The variations in the event energies are caused by the incomplete energy deposition inside the scintillator through the Compton effect and by inelastic scattering of gamma photons prior to their detection. At the lower border of the spectrum, the backscattering peak (see Fig. 2.5) corresponds to the absorption of annihilation photons which have been backscattered prior to their absorption, i.e. scattering under an angle α of 180° which leads to a maximum of energy transfer to the recoil electron (see Eq. 2.1). The upper border of this region is called Compton edge and stems from the energy deposited in the scintillator through backscattering.

The most important information of the spectrum lies in the photopeak which is localized at the upper end of the detected energies. It stems from the photoelectric absorption of annihilation photons which have lost only small fractions or no energy through Compton scattering. The energy resolution of a detector can be measured using the photopeak with

$$\delta E = \frac{\Delta E}{E} \ , \tag{2.3}$$

where ΔE is the full width at half maximum (FWHM) of a Gaussian fit to the photopeak and E is the abscissa of the peak, i.e. 511 keV for PET. A narrow peak indicates good energy resolution and hence smaller values of δE stand for a better accuracy in measuring the energy. A good energy resolution is beneficial for the SNR of the acquisition, because it helps to reduce the count rate C_S of scattered events (see Eq. 2.2) through the application of a narrow energy gate. This gate, which is set in the spectrum around the photopeak, is used to reject events that have undergone Compton scattering with large scattering angles.

The energy resolution of a system is influenced by the statistical variations of the scintillation process, the light transport from the scintillation location to the photosensor, and the photosensor response. According to Refs. [56, 57], these influences can be determined through the study of the average total charge $\overline{Q}$ of the anode pulse of a PMT, which is optically coupled to a scintillator crystal:

$$\overline{Q} = \overline{N_{\mathrm{Scint}}}\, \overline{p}\, \overline{M} \ . \tag{2.4}$$

Here, $\overline{N_{\mathrm{Scint}}}$ is the average number of scintillation photons generated by the absorption of the annihilation photon, $\overline{p}$ is the average transfer efficiency corresponding to the probability of a scintillation photon reaching the photocathode of the PMT, and $\overline{M}$ is the average electron multiplication factor of the PMT. Using the fractional variance defined as $v(x) = var(x)/\overline{x}^2$, where $var(x)$ and $\overline{x}$ are the variance and mean value of x, δE is correlated to Q through

$$\delta E = 2.355 \sqrt{v(Q)} \ . \tag{2.5}$$

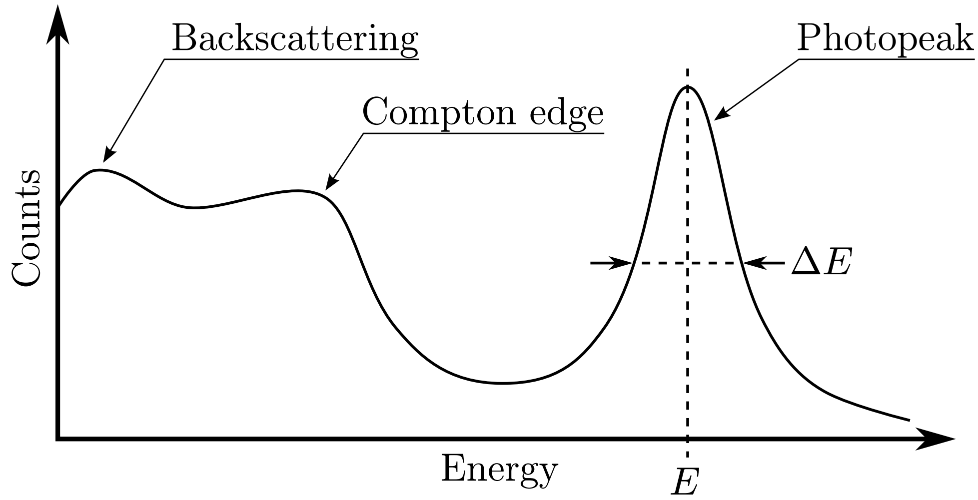

Figure 2.5: Drawing of an energy spectrum of a typical PET measurement. The FWHM of the photopeak and its position yield the energy resolution of the system. Further prominent features are the backscattering peak and the Compton edge.

Note that the factor of 2.355 stems from the correlation between FWHM and standard deviation for normal distributions. According to Ref. [56], $v(Q)$ can be written as

$$v(Q) \approx \left(v(N_{\text{Scint}}) - \frac{1}{\overline{N_{\text{Scint}}}} \right) + v(p) + \frac{1 + v(M)}{\overline{N_{\text{Scint}}}\,\overline{p}} \ . \tag{2.6}$$

Based on Eqs. 2.5 and 2.6, the individual contributions from the scintillation process, the transfer efficiency, and the PMT can be expressed through

$$\delta E^2 = \delta E_{\text{Intr}}^2 + \delta E_p^2 + \delta E_M^2 = 5.55\, v(Q) \ . \tag{2.7}$$

Here, δE_{Intr} is the intrinsic energy resolution of the scintillator (see Sec. 2.3.2), which corresponds to 2.355 times the square root of the bracketed term in Eq. 2.6. The transfer resolution $\delta E_p = 2.355 \cdot v(p)^{1/2}$ depends on various aspects such as the optical properties of the scintillator or the quantum efficiency of the PMT's photocathode. The photomultiplier resolution δE_M corresponds to the last term in Eq. 2.6,

$$\delta E_M = 2.355 \sqrt{\frac{1 + v(M)}{\overline{N_{\text{Scint}}}\,\overline{p}}} \ . \tag{2.8}$$

This correlation indicates that an increase in $\overline{N_{\text{Scint}}}\ \overline{p}$, i.e. the mean number of photons reaching the photosensor, reduces δE_M which in turn reduces δE. Consequently, an increase in the light yield of the detector leads to an improvement of the energy resolution.

2.2.4 Timing Resolution

The timing resolution of a PET system indicates the accuracy of measuring the arrival times of detected annihilation photons. Since PET is based on the measurement of coincidence events, the timing resolution has a direct influence on the width of the coincidence window (see Fig. 2.1). Detectors which have a good timing resolution allow using short coincidence windows. This reduces the count rate C_R of random events and increases the SNR of the system according to Eq. 2.2.

Further improvement of the SNR can be achieved by using time-of-flight (TOF) reconstruction. According to Eq. 2.2, SNR is inversely proportional to the square root of the number of volume elements N_{El} along the LOR that are used for the back-projection. The TOF method can reduce N_{El} by tagging each detected event with the difference in the arrival times Δt of the two gamma photons. Using the speed of light c, the position of the annihilation event along the LOR can be calculated through

$$x = \frac{1}{2} c \cdot \Delta t \; , \tag{2.9}$$

where x is the distance from the center of the LOR (see Fig. 2.6). The uncertainty δt in this measurement is called the coincident resolving time (CRT). Consequently, the accuracy δx of measuring the position x is given through

$$\delta x = \frac{1}{2} c \cdot \delta t \; . \tag{2.10}$$

Through the determination of x, TOF reconstructions utilize only $N_{\mathrm{TOF}} = \delta x / d$ elements for back-projection instead of N_{El}. According to Ref. [55], the SNR of a TOF acquisition compared to the $\mathrm{SNR}_{\mathrm{Conv}}$ of the conventional approach can be expressed as

$$\mathrm{SNR}_{\mathrm{TOF}} = \sqrt{\frac{D}{\delta x}} \cdot \mathrm{SNR}_{\mathrm{Conv}} = \sqrt{\frac{2D}{c \cdot \delta t}} \cdot \mathrm{SNR}_{\mathrm{Conv}} \; . \tag{2.11}$$

Thus, a better timing resolution, i.e. a lower timing inaccuracy δt, translates into an increase in SNR using the TOF method. Equation 2.11 also indicates that the CRT required for a certain improvement in SNR depends on the size D of the subject. For instance, considering whole-body imaging ($D \approx 40$ cm), a CRT of 500 ps yields an estimated SNR gain by a factor of 2.3. Although the expression in Eq. 2.11 is based on analytical reconstruction, it also serves as an estimate for the gain in SNR for other reconstruction methods [55].

The CRT of a PET system is limited by statistical fluctuations in the detection process, which is governed by Poisson statistics [58]. Hence, the probability of the photosensor detecting N scintillation photons within the time interval 0 to t is given through

$$P(t)_N = f(t)^N \, \frac{\exp(-f(t))}{N!} \; . \tag{2.12}$$

Here, $f(t)$ is the expected amount of detected photons between 0 and t with $f(\infty) = N_{\mathrm{Det}}$ being the total light yield [59]. $f(t)$ is strongly influenced by the intrinsic scintillator timing

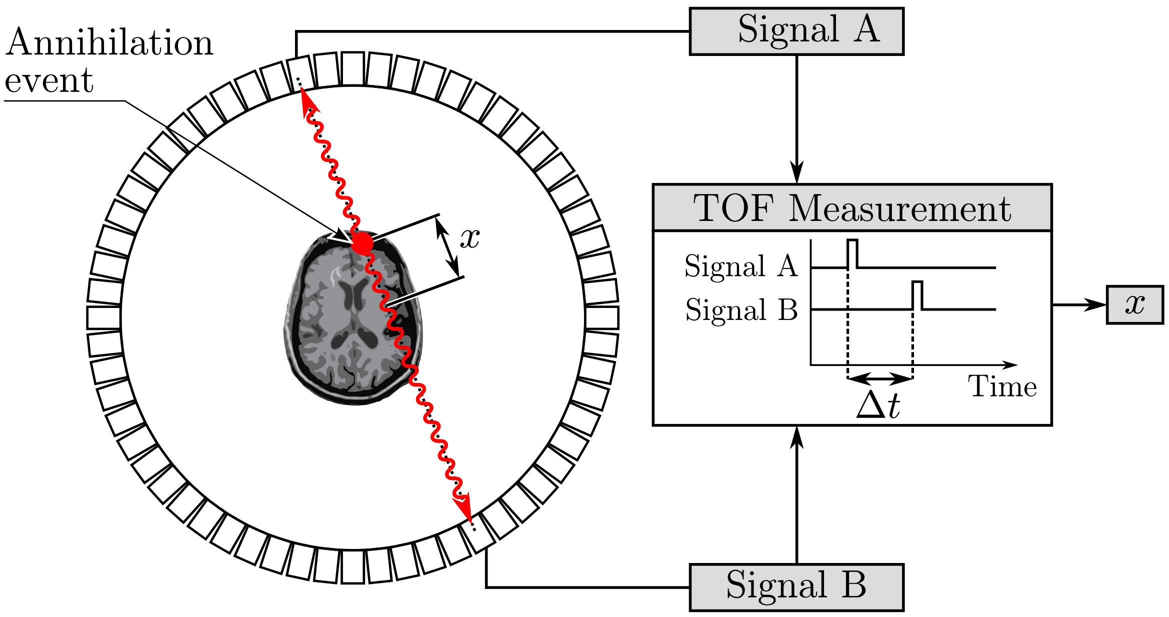

Figure 2.6: Illustration of TOF reconstruction: the position of the annihilation event x relative to the center of the LOR is derived from the difference in the arrival times Δt. Adapted from Ref. [1].

characteristics τ_{Rise} and τ_{Decay} (see Sec. 2.3.2). Thus, the CRT of a detector can be estimated through [60]

$$\delta t \propto \sqrt{\frac{\tau_{\text{Rise}}\,\tau_{\text{Decay}}}{N_{\text{Det}}}}\,. \tag{2.13}$$

This indicates that an increase in the light yield of the detector leads to an improvement of the CRT. However, a detailed analysis shows that the CRT is not exclusively defined by the light yield and the scintillator characteristics τ_{Rise} and τ_{Decay}. Another important factor is the light transfer from the scintillation location to the photosensor which results in a certain distribution of photon propagation times that influence the timing. The reason for this is that the actual timing information of the gamma event is determined using the rising slope of the photosensor output signal. For this aspect, the light transfer plays a significant role [60–62]. Hence, the improvement of the timing resolution requires not only an increase in the total light yield, but also a favorable temporal distribution of the detected photons.

There are several other aspects that have an impact on the timing resolution. Among these are the intrinsic timing resolution of the photosensor, the read-out electronics, and the signal processing technique. Reference [63] gives a comprehensive survey over the numerous factors influencing the CRT and presents a simple model that estimates δt using the sum of squares of all individual contributions.

A more precise calculation of the CRT can be achieved using Monte Carlo (MC) simulations. Various approaches have been presented [64–67] which consider multiple aspects such as the optical photon transfer, device-specific photosensor characteristics, and influences from electronic signal processing.

2.3 Scintillators

This section introduces and characterizes scintillators, which are a key component of any PET detector together with the photosensor. Scintillators are materials which convert high energy photons or the kinetic energy of particles into light, mostly in the visible or ultraviolet spectrum. Different types of scintillating media exist, e.g. organic-based liquids, plastics, gases, and inorganic crystals. Since inorganic crystals offer favorable properties in terms of their high density and intrinsic light yield, they are the most widely used type of scintillators for PET systems [1, 68].

2.3.1 Scintillation Process

The conversion of the incident radiation into scintillation photons is the result of a luminescence process, which is either fluorescence, phosphorescence or delayed fluorescence. Fluorescence is the prompt emission of visible light after the excitation of the scintillator by incident radiation and hence is the most desirable process for radiation detection. Phosphorescence and delayed fluorescence involve long delay times between excitation and light emission and represent unfavorable contributions to the luminescence process.

The fluorescence process in inorganic scintillators consists of several complex mechanisms, such as relaxation of initial electron excitation, thermalization, charge carrier trapping, etc. [69, 70]. In the following, the process is described in a simplified version. The EM field of the periodically arranged atoms or molecules in a crystal lattice leads to the formation of energy bands which define all allowed electron states. Between these bands exists an intermediate range of energies called band gap, in which electrons can never be found in the pure crystal. These band gaps typically have a width E_{Gap} of a few electron volts (see Fig. 2.7). The last band filled with electrons is called the valence band, the first unfilled band is called conduction band. [71]

EM radiation that propagates through a scintillator can transfer energy to electrons which can lead to their excitation to the conduction band leaving a hole in the valence band. This electron-hole pair can recombine under the emission of a photon, which has an energy corresponding to the band gap. However, this is an inefficient process which competes with the radiationless recombination through interactions with phonons. Thus, small amounts of impurities are added to the crystal to increase the probability of scintillation photon emission. These impurities are called activators and create sites in the crystal lattice that have energy states within the band gap of the pure crystal. The energies of the so-called luminescence centers define the emission spectrum of the scintillator. After the generation of the electron-hole pair, both charge carriers quickly migrate inside the crystal to activator sites where they can recombine through the emission of a scintillation photon delayed only by the lifetime of the activator states. Hence, the time characteristics of a scintillator are mainly determined by the decay time of the activator states. [69]

Alternatively, electrons can occupy activator states for which the de-excitation to the ground state is forbidden. Additional energy is required to raise the electron to a state of higher energy from which it can recombine. One possible form for this is thermal energy which leads

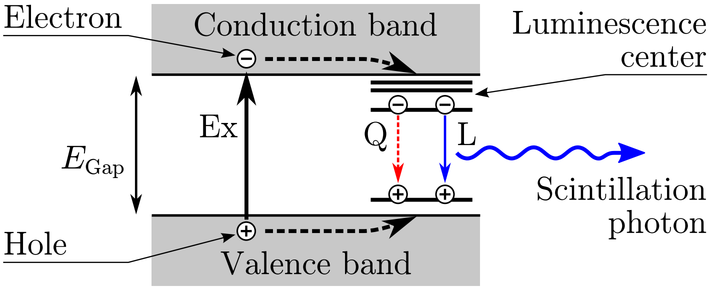

Figure 2.7: Illustration of the scintillation process in inorganic crystals. The absorption of energy from incident EM radiation can lead to the excitation of an electron into the conduction band (Ex) yielding an electron-hole-pair. Electrons and holes quickly migrate to luminescence centers. From these states, recombination can occur through luminescence (L) emitting a scintillation photon or through radiationless quenching (Q). Adapted from Ref. [72].

to the slow process of phosphorescence and a resulting afterglow of the scintillator. Another mechanism which produces no light emission is called quenching, during which electrons are captured at activator sites and recombine through radiationless transitions to the ground state.

Because the luminescence occurs only through the activator sites, the scintillator crystal can be highly transparent for the emitted photons. This is an important aspect, since a self absorption of the scintillator bulk would severely limit the light yield of the detector. [1, 37, 68]

2.3.2 Scintillator Characteristics

There are several properties of scintillators that are critical for their applicability in medical imaging. This section provides an overview over these different physical characteristics and their implications for the design of a PET detector.

2.3.2.1 Stopping Power

The stopping power indicates the average amount of 511 keV photons that interact with the scintillator and depends on the intrinsic attenuation coefficient and the scintillator geometry. The attenuation can be described by the Lambert-Beer law

$$I(x) = I(0)\exp(-\mu_{\mathrm{Att}}\, x) \ , \tag{2.14}$$

where $I(0)$ is the intensity of the photon beam incident on the scintillator, x is the thickness of the scintillator and $I(x)$ is the intensity of the beam that propagated through the scintillator without interaction. The linear attenuation coefficient μ_{Att} describes the probability that an interaction with the medium occurs. It can be calculated by summing the individual attenuation coefficients for the different forms of interaction:

$$\mu_{\mathrm{Att}} = \mu_{\mathrm{Compton}} + \mu_{\mathrm{Photo}} + \mu_{\mathrm{Other}} \ . \tag{2.15}$$

Here, μ_{Compton} and μ_{Photo} are the attenuation coefficients of the material for Compton scattering and the photoelectric effect and μ_{Other} represents the attenuation coefficients of other mechanisms such Rayleigh scattering or pair production. The attenuation coefficient μ_{Att} is a material property of the scintillating medium and depends on its density and effective atomic number [73]. The stopping power has a direct influence on the sensitivity of the PET system and puts constraints to the scintillator dimensions. Besides the total attenuation coefficient μ_{Att}, it is also preferable to have a material having as high a ratio $\mu_{\text{Photo}}/\mu_{\text{Compton}}$ as possible to obtain good energy resolution. [1, 37]

2.3.2.2 Scintillator Timing Characteristics

The signal decay time τ_{Decay} characterizes the timing properties of the scintillation light emission. It depends mainly on the lifetime of the activator states. The decay time is one of the key factors determining the CRT of a PET detector through its influence on $f(t)$, which is the expected amount of photons detected in the interval from 0 to t (see Eq. 2.12). $f(t)$ can be expressed through

$$f(t) = a \int_0^t g(t)\,\mathrm{d}t \,, \tag{2.16}$$

where a is a constant which is proportional to the total amount of photoelectrons ($f(\infty)$) and $g(t)$ is a model that describes the temporal distribution of the scintillation light emission. Conventionally, $g(t)$ was described using a mono-exponential correlation using only τ_{Decay}. However, recent progress in fast scintillators and improved electronics led to the modeling of $g(t)$ using both rise and decay times [59, 74]:

$$g(t) \propto \exp(-\frac{t}{\tau_{\text{Decay}}}) \left(1 - \exp(-\frac{t}{\tau_{\text{Rise}}})\right) \,. \tag{2.17}$$

Based on this model, Fig. 2.8 depicts an exemplary temporal distribution of scintillation light emission. As indicated in Eq. 2.13, τ_{Rise} and τ_{Decay} have a direct impact on the timing resolution of the detector.

2.3.2.3 Brightness

The brightness of a scintillating material is defined as the number of scintillation photons generated per absorbed energy (photons/keV). In conjunction with the light transfer efficiency and the sensitivity of the photosensor, the brightness is a crucial factor determining the light yield of the detector and hence of significant importance for the energy and timing resolution.

2.3.2.4 Intrinsic Energy Resolution

The energy resolution of a PET detector is influenced by several factors. One of these aspects is the intrinsic energy resolution of the scintillator δE_{Intr}. This parameter is mainly connected to two effects. The first is that all scintillators have a certain non-proportionality in their response to the incident radiation. This stems from the statistical processes involved

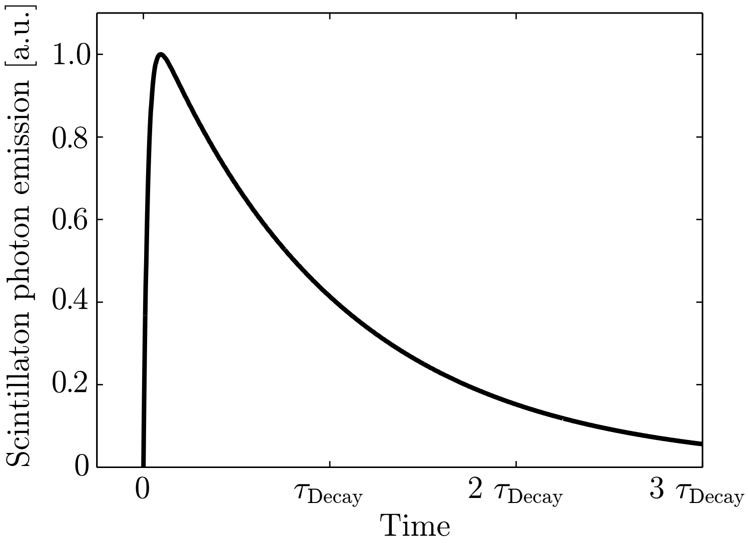

Figure 2.8: Temporal distribution of scintillation light emission according to Eq. 2.17 for a ratio $\tau_{\text{Rise}}/\tau_{\text{Decay}}$ of 1/40.

in creation of secondary electrons through Compton scattering and the photoelectric effect. The second contribution to δE_{Intr} is due to inhomogeneities in the crystals, which cause local variations of the scintillation light output. A possible source for such inhomogeneities is a varying concentration of the luminescence centers in the scintillator.

2.3.2.5 Emission Wavelength

The spectrum of the scintillation photons depends on the energy levels of the luminescence centers. To achieve high detection efficiency, it is crucial that the photosensor coupled to the scintillator is highly sensitive to the wavelengths of the generated photons.

2.3.2.6 Optical Properties

Besides the response of scintillators to the incident 511 keV photons, their optical properties regarding the propagation of the scintillation photons also have a strong impact on the detector performance. Scintillator crystals can be highly transparent for wavelengths of their own emission spectrum. Nevertheless, scattering and absorption of scintillation photons inside the crystal occur which reduces the light yield and hence negatively influences δE and δt. Besides these bulk effects, scintillation photons can also be scattered by the crystal surfaces which potentially influences the amount of photons extracted from the scintillator. Finally, the refractive index of the scintillator crystal also plays an important role, because it can constrain the light transfer from the scintillator through the optical grease to the photosensor. A detailed discussion of the optical mechanisms in the detection process is given in Sec. 2.5.1.

2.3.3 PET Scintillators

There are numerous scintillator materials that can be utilized for PET. Most of these materials have certain drawbacks. These include low stopping power and poor timing characteristics in the case of thallium-activated sodium iodide (NaI(Tl)) or a lack of brightness in the case bismuth germanium oxide (BGO) [75]. Although barium fluoride (BaF_2) and cesium fluoride (CsF) provide excellent timing characteristics which led to their use in early TOF PET systems, they also suffer from insufficient brightness and stopping power [76–79]. In 1992, the new scintillator lutetium oxyorthosilicate (LSO) was presented [13] which appears to exhibit almost ideal characteristics:

- The brightness of LSO is comparable to NaI(Tl)
- The stopping power is almost as high as for BGO
- The decay constant is short compared to NaI(Tl) and BGO

A comparison of the physical properties of various scintillators is given in Table 2.1. Although LSO has a high light output, its intrinsic energy resolution is inferior to NaI(Tl). One reason for this behavior is the non-proportional response to incident radiation [57]. Another disadvantage is that the ^{176}Lu content of LSO leads to a low level of natural radioactivity. This has no significant impact on PET though, since the radiation has a very low emission rate [1, 75].

Because of its favorable characteristics, LSO has attracted a lot of attention by various research groups [80–83] and is expected to play an important role in future PET systems [84, 85]. The first commercial implementation was in 1998 in a high resolution PET scanner tailored for brain imaging [86]. Today, LSO scintillators are implemented in a broad range of clinical systems including conventional PET scanners [87], PET/CT hybrids [88, 89], and the first clinical whole-body PET/MRI system [51]. The brightness of LSO in conjunction with its short decay time permits overcoming the limitations of BaF_2 and CsF and facilitates PET systems with improved timing performance. This can be used to improve the SNR, especially regarding TOF applications [15, 90]. For all these reasons, this work focuses on PET detector configurations based on LSO scintillators.

Table 2.1: Physical properties of selected inorganic scintillators for PET. Note that lower values of δE indicate a better energy resolution. λ_{Peak} is the wavelength at the peak of the scintillator emission spectrum and the index of refraction is given for λ_{Peak}. Data taken from Ref. [1].

Property	NaI(Tl)	BGO	BaF_2	LSO
μ_{Att}^{-1} at 511 keV [mm]	29.3	11.6	22.0	12.3
τ_{Decay} [ns]	230	300	0.6	40
Brightness [photons/keV]	38	6	2	29
δE_{Intr} [%]	5.8	3.1	4.3	9.1
λ_{Peak} [nm]	410	480	220	420
Index of refraction	1.85	2.15	1.56	1.82

2.4 Photosensors

This section describes different types of photosensors, which are the second key component of any PET detector besides the scintillator. After the introduction of the established technologies, the emerging trend of SiPMs is presented. The latter technology paves the way for PET/MRI hybrid systems with TOF capability [18, 19].

2.4.1 Established Photosensors

2.4.1.1 Photomultiplier Tubes

Photomultiplier tubes are the most common type of photosensor in commercial PET systems. As illustrated in Fig. 2.9, they convert incident photons into electrons using a photocathode. These electrons are multiplied through acceleration in an electric field and generation of secondary electrons through multiple dynode stages. The initial photoelectron is typically amplified by a factor of 10^6 or more. [68]

PMTs are the oldest and most reliable type of photosensor for the detection of scintillation light. Through their high amplification factors they provide a high signal-to-noise ratio for low levels of incident light. Also, they offer a fast response that allows their use in TOF systems [91]. On the other hand, they are rather bulky, expensive, and their sensitivity is limited by the quantum efficiency of the photocathode, which is usually around 25% [37]. Further drawbacks include limited long term stability caused by degradation of the photocathode and dynode material, reduced entrance window transparency, and permeation of helium through glass which leads to increased dark current and ultimately causes breakdown and the end of PMT service life. PMT's principle of operation makes them highly sensitive to magnetic fields which deteriorates the anode sensitivity and gain [92]. To utilize conventional PMTs for a hybrid PET/MRI system, it is necessary to place them in regions of the magnetic fringe field with magnetic flux densities below 10 mT and use optical fibers to connect scintillators and photosensors [93]. This approach degrades the detector performance and dictates a complex and impractical system design. Consequently, alternative photosensors based on semiconductors are preferred for PET/MRI hybrids, since they are highly insensitive to magnetic fields as demonstrated in various studies using magnetic flux densities up to 9.4 T [50, 94]

2.4.1.2 Avalanche Photodiodes

Avalanche photodiodes (APDs) are an alternative to PMTs that offer several advantages. Through the use of standard production processes of the semiconductor industry, these photosensors can be fabricated in a rather cost-efficient way. Also, the sensors are small compared to conventional PMTs and mechanically robust, which facilitates compact scanner designs. In combination with proper housing, their principle of operation results in no significant long term degradation. Another major advantage compared to PMTs is their insensitivity to high magnetic fields.

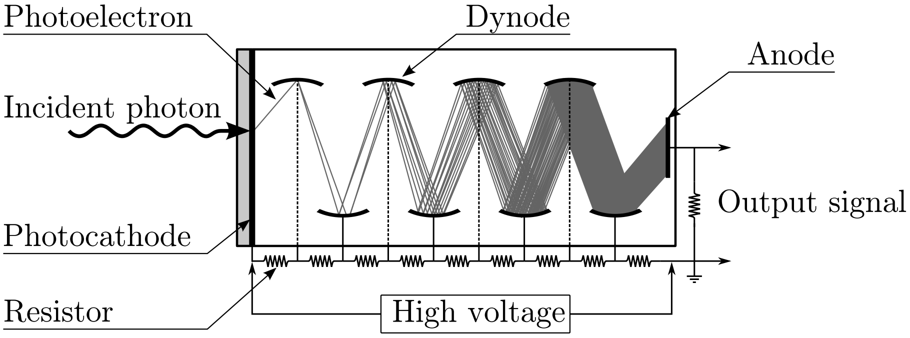

Figure 2.9: Schematic of a photomultiplier tube illustrating the amplification process through 8 dynode stages. The figure is based on Ref. [68].

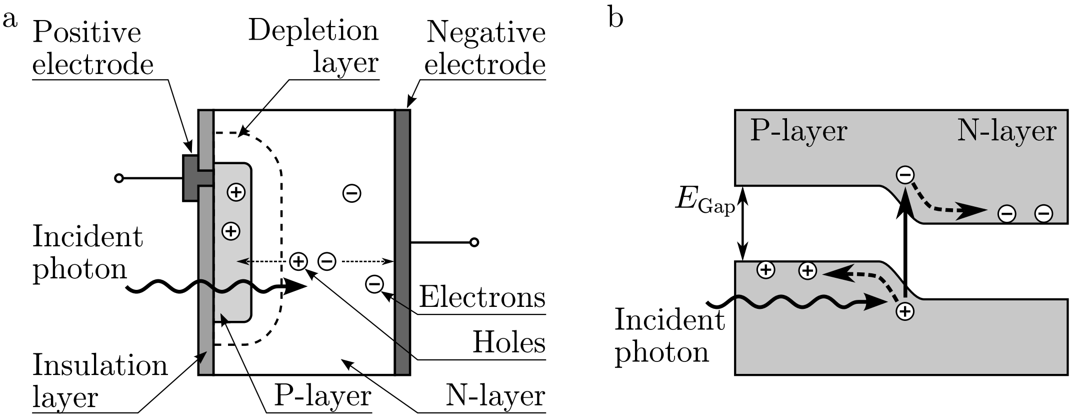

Figure 2.10: (a) Schematic of a silicon PD illustrating the generation of current flow through the separation of holes and electrons. (b) Energy band diagram of the P-N-junction of a silicon photodiode having a band gap E_{Gap}. The deformation of the bands illustrates the mechanism that causes the accumulation of holes and electrons in the P- and N-layer, respectively. Adapted from Ref. [96].

This type of photosensors is based on the detection principle of silicon photodiodes (PDs), which is illustrated in Fig. 2.10. These devices consist of a P-N-junction formed within a silicon substrate with different doping regions. If the energy of an incident photon is larger than the band gap, electron-hole-pairs can be generated. These lead to current flow between positive and negative electrodes proportional to the amount of absorbed photons. APDs are modified PDs in which a reverse bias voltage (approximately 100-200 V) leads to a multiplication of the electron-hole pairs through impact ionization. Typical gains are in the range of 10^2 to 10^3. The fact that this is relatively low compared to conventional PMTs is partly compensated by a higher quantum efficiency so that APDs provide sufficient SNR for the application in PET. On the downside APDs are prone to temperature variations and changes in the bias voltage. Also, their timing resolution is not suitable for TOF PET. [1, 37, 95]

2.4.2 Silicon Photomultipliers

2.4.2.1 Principles

A novel solid state photosensor that offers the advantages of semiconductor-based sensors and bears the potential to facilitate TOF PET are silicon photomultipliers. SiPMs consist of an array of APDs, connected in parallel and operated in Geiger mode. In this mode of operation, the reverse bias applied to the APDs is higher than their breakdown voltage which leads to an amplification of the initial electron-hole pair by factors of up to 10^6. However, the output pulse of an APD in Geiger mode (G-APD) is independent of the number of initial electron-hole pairs. Hence, the signal stemming from an individual photon incident on the G-APD is indistinguishable from signals that are caused by multiple incident photons. Therefore, SiPMs consist of a large number of small pixels (microcells), each of which contain one G-APD working as single photon counter (see Figs. 2.11 and 2.12a). Since the output of all microcells is gathered in one electrode, the SiPM signal is the sum of all fired pixels. Knowing the output pulse of an individual cell allows calculating the number of fired cells from the overall signal. [17, 97]

Each pixel of an SiPM has a quenching resistor connected in series as shown in the schematic in Fig. 2.12b. This provides a negative feedback which decelerates and eventually stops the avalanche process. After that, the microcell is recharged to prepare it for the detection of the next photon. The recharging process is characterized through the recovery time, which depends on the quenching resistor and the capacitance of the microcell. [17, 53]

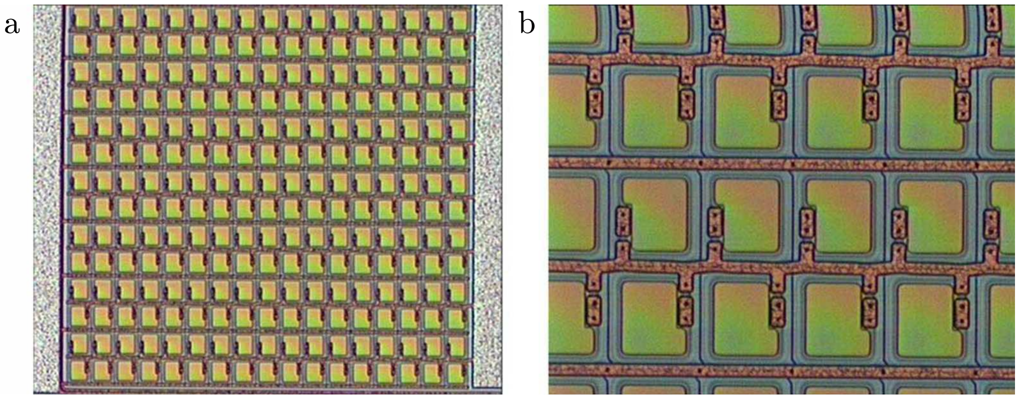

Figure 2.11: (a) Microscope image of an SiPM with a size of (1 × 1) mm^2 consisting of 289 microcells. (b) Magnified view of the SiPM from (a) showing the individual microcells with the electrodes and quenching resistors. The pixels have a photosensitive area of (40 × 40) μm^2 and a pitch of 58 μm. Images are taken from Ref. [98].

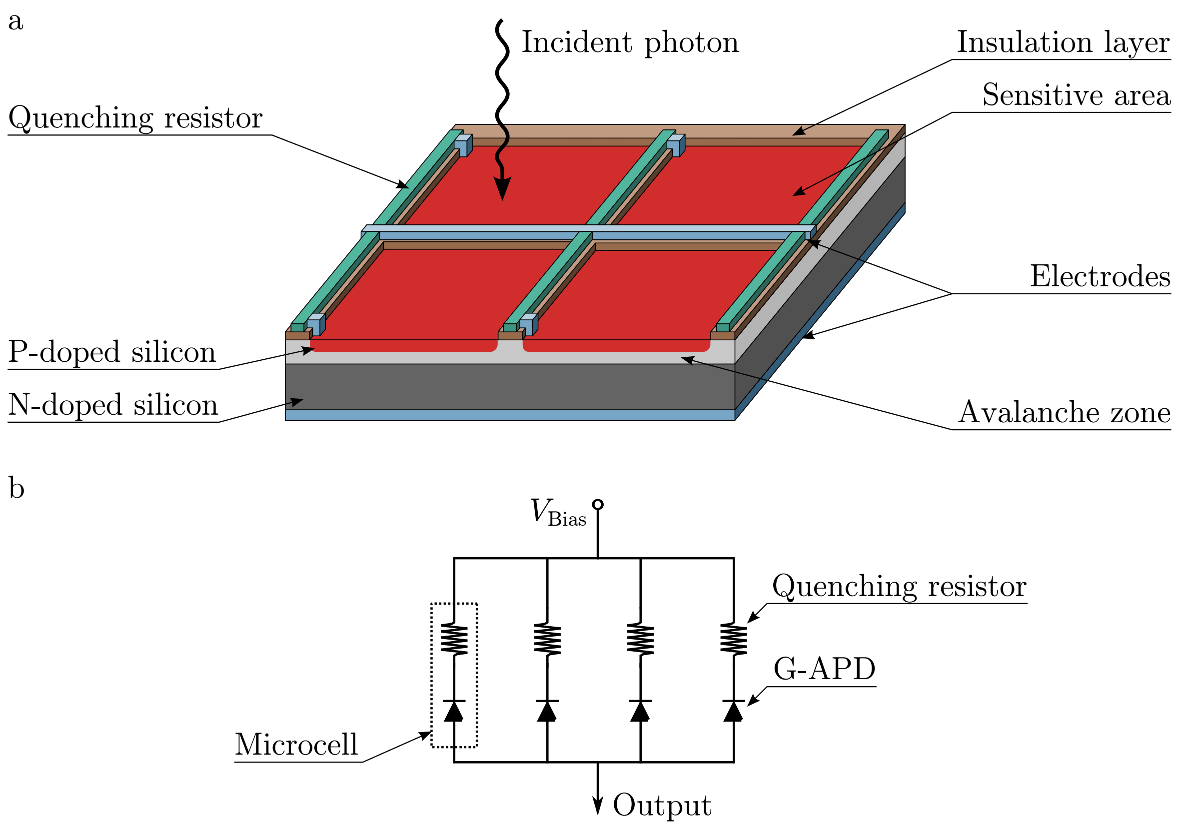

Figure 2.12: (a) Schematic of an SiPM (P-on-N structure) showing 2×2 microcells. The sensitive areas are usually equipped with an anti-reflective coating (not shown). (b) Electric scheme of an SiPM and its biasing circuit. The voltage V_{Bias} normally lies below 100 V. Adapted from Refs. [17, 53]

2.4.2.2 Sensitivity and Dynamic Range

Because of the need for quenching resistors and electrodes, only a certain fraction of the SiPM surface area is sensitive to incident photons. This fraction is called the geometric fill factor f_{Geo}, defined as

$$f_{\text{Geo}} = \frac{\text{sensitive pixel area}}{\text{total pixel area}} \,. \tag{2.18}$$

The overall photon detection efficiency (PDE) of an SiPM is defined as

$$\text{PDE} = q \cdot f_{\text{Geo}} \cdot P_{\text{Av}} \,, \tag{2.19}$$

where q is the quantum efficiency for the electron-hole pair production and P_{Av} is the avalanche probability. Quantum efficiency is an intrinsic property of the silicon of SiPMs and strongly depends on the wavelength of the incident light. Values up to 90% can be reached within the visible spectrum. P_{Av} mainly depends on the voltage applied to the sensor and can be increased by using larger bias values. This, however, also increases the detrimental effects of dark counts, optical cross talk, and afterpulsing. Since G-APDs produce the same output for single and multiple incident photons, the SiPM signal is only proportional to the flux of incident photons if the following relation is valid:

$$N_{\mathrm{Inc}} \cdot \mathrm{PDE} < N_{\mathrm{Cells}} \,. \tag{2.20}$$

N_{Inc} is the number of photons incident on the sensor and N_{Cells} is the number of microcells. Therefore, the dynamic range of the SiPM depends on the parameters PDE and N_{Cells}. For an SiPM with a given size, a large value of N_{Cells} results in small microcells. Thus, the quenching resistors occupy a larger fraction of the sensor area reducing the geometric fill factor f_{Geo}, which in turn decreases the PDE. Consequently, there is a trade-off between the dynamic range and the sensitivity of an SiPM. For applications that require a large dynamic range such as PET, SiPMs with small microcells are favorable. Devices with large microcells are best suited for applications demanding a high sensitivity. [99]

SiPMs that have been proposed for the application in PET have a microcell size between $(25\times25)\ \mu\mathrm{m}^2$ and $(100\times100)\ \mu\mathrm{m}^2$, geometric fill factors in the range from 30% to 80%, and PDE values from 20% to 45% [18, 19].

2.4.2.3 Dark Counts

Thermal excitation in the bulk of the SiPM can lead to the generation of electron-hole pairs without incident photons. This noise is amplified through the avalanche mechanism and produces an output pulse which is identical to the signal of an absorbed photon. The dark count rate is typically in the MHz per mm^2 regime. Possible means to reduce thermal noise are cooling the SiPM or the usage of a lower bias voltage. Also, minimizing impurities and crystal defects in the fabrication of the device can reduce dark counts. [99]

2.4.2.4 Optical Crosstalk

Another source of noise is the optical crosstalk between adjacent microcells. The charge carriers generated by the avalanche in the G-APD cell can recombine and produce photons. These photons can propagate through the semiconductor, reach a neighboring microcell and trigger an avalanche. Possibilities to suppress optical crosstalk are larger microcell pitches or trenches filled with opaque materials between the pixels. Both measures, however, have negative impact on the PDE by reducing f_{Geo}. [53, 98, 100]

2.4.2.5 Afterpulsing

Charge carriers can be trapped inside the silicon and released again after a certain delay time. This delay can be very short, which leads to a prolongation of the recovery time of the microcell. Alternatively, the delay is rather long (microsecond range) and the carrier is released after the cell has been recharged. This can trigger an avalanche without the incidence of a photon resulting in noise. [99]

2.4.2.6 Timing Characteristics

The temporal characteristic of the output pulse of an G-APD cell is defined by a steeply rising slope at the beginning, caused by the fast Geiger discharge process (typically a few hundred ps) and a decay, which is given by the recovery time of the microcell. The recovery time depends on the quenching resistor and the capacitance of the SiPM. Since the capacitance of an SiPM increases with its area, larger sensors usually have longer recovery times. Typical recovery times range between 30 and 200 ns. [53]

The timing resolution of a detector critically depends on the statistical variation of the response time to an incident photon. This jitter is influenced by fluctuations in the avalanche process, e.g. lateral diffusion of the charge carriers, and by statistical variations in the detection due to the temporal slope of the output pulse. Conventionally, the timing resolution of an SiPM is given as FWHM of the temporal distribution of detected photons. This is illustrated in Fig. 2.13, where the different contributions from the SiPM, the used laser, and the electronics lead to an overall FWHM of 123 ps. The individual contribution of commercial SiPMs ranges between 40 and 100 ps, which makes them excellent candidates for the use in TOF applications. [53, 99]

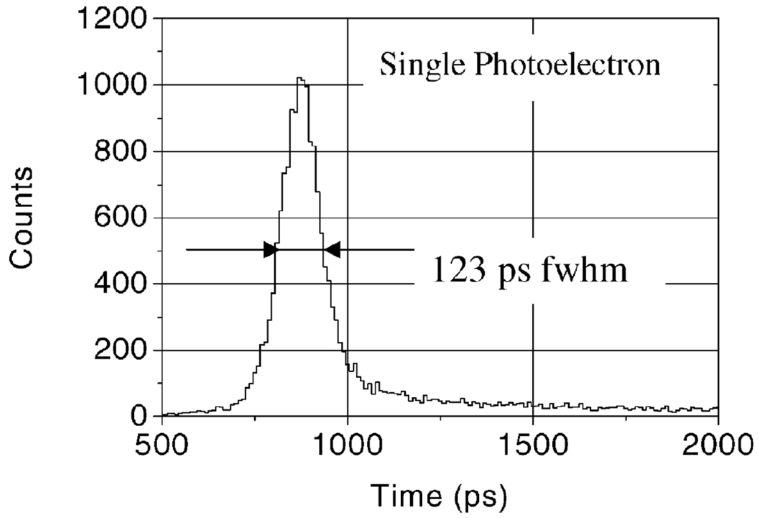

Figure 2.13: Distribution of single photoelectron detection times showing the jitter of an SiPM defining the timing resolution of the device. The given FWHM of 123 ps includes contributions from the measurement setup (laser and read out electronics) resulting in an intrinsic resolution of the SiPM of approximately 100 ps. Values and figure are taken from Ref. [101].

2.5 Impact of Optical Processes on Detector Performance

The intrinsic scintillator properties and the photosensor characteristics are key determinants for the light yield and timing performance of a PET detector. An equally important factor is the light transfer from the scintillation location to the photosensor. In the following section, the optical processes involved in this transfer are introduced. Next, the mechanisms which reduce the efficiency of the scintillation light transfer and hence limit the detector performance are discussed. This discussion considers only detector configurations that use SiPM sensors.

2.5.1 Optical Processes of Scintillation Light Transfer

2.5.1.1 Bulk Processes

As the energy of scintillation photons is significantly lower than the energy of the gamma photons from PET events (e.g. $E(\lambda = 420 \text{ nm}) \approx 3$ eV vs. $511 \cdot 10^3$ eV), the interaction mechanisms of Compton scattering or photoelectric absorption are not dominant for the propagation of light through scintillators. Instead, various elastic and inelastic scattering mechanisms occur in inorganic scintillator crystals. Among these are Brillouin and Raman scattering by the crystal lattice and Rayleigh scattering from implanted activator species or impurities induced by the fabrication process [102].

In general, the absorption in scintillators is rather low. The reason for this behavior is that the energy of scintillations photons is smaller than E_{Gap}, since the emission occurs through the luminescence centers within the band gap. Due to a certain overlap between the absorption and emission spectra in scintillators [83], photons can be absorbed by the crystal bulk. This can cause the emission of luminescence photons leading to an effect similar to inelastic light scattering. Recent studies have shown that this can be the dominant mechanism for scattering [103]. Further bulk absorption is caused by inelastic interactions with impurities.

The transmission of an EM wave through a certain medium is usually described through the exponential relationship from Eq. 2.14 using the attenuation coefficient μ_{Att}. In the following, μ_{Att} is replaced through the attenuation length $l_{\text{Att}} = \mu_{\text{Att}}^{-1}$ for frequencies in the visible spectrum. The impact of bulk scattering and absorption on l_{Att} is calculated through [32]

$$\frac{1}{l_{\text{Att}}} = \frac{1}{l_{\text{Scatt}}} + \frac{1}{l_{\text{Abs}}} \, , \tag{2.21}$$

where l_{Scatt} and l_{Abs} are the characteristic lengths of bulk scattering and absorption, respectively.

2.5.1.2 Interface Processes

During the propagation from the scintillation location to the photosensor, photons interact many times with various material interfaces, e.g. the surfaces of the scintillator crystals, the interfaces between scintillator, optical glue, and photosensor or the reflective wrapping surrounding the detector.

There are three main factors that influence the interaction of EM waves with the interface of two materials:

- polarization of the EM wave
- refractive index (RI) of the two media
- topography or roughness of the interface

Polarization EM waves are transversal, which means that the electric and magnetic field vectors $\vec{E}$ and $\vec{H}$ are oscillating in directions perpendicular to the propagation described by the wave vector $\vec{k}$. The directions of $\vec{E}$ and $\vec{H}$ are indicated through the polarization of the EM wave, which can be linear, elliptic or circular. In the case of an EM wave impinging on a material interface, the polarization can be expressed in the base of the two orthogonal states of S- and P-polarization using the plane of incidence. This plane is defined through the normal vector of the interface $\vec{n}$ and the wave vector $\vec{k}$. In this system, the S- and P-state represent the linear polarizations of $\vec{E}$ being perpendicular and parallel to the plane of incidence, respectively (see Fig. 2.14). As elliptic or circular polarizations can be represented through two linear polarizations having a certain phase shift, any state of polarization $\vec{q}$ can be expressed through a linear combination

$$\vec{q} = A\,\vec{s} + B\,\vec{p}\,, \tag{2.22}$$

where $\vec{s}$, $\vec{p}$ are unit vectors along the S- and P-states, and A, B are complex coefficients.

Refractive Index The RI is a complex-valued and frequency-dependent material property,

$$n(\nu) = n'(\nu) + \mathrm{i}\,n''(\nu)\;, \tag{2.23}$$

that describes how a medium affects the speed of propagating light and the refraction at material interfaces. The imaginary component n'' is only non-zero in absorbing materials and correlates to the absorption length l_{abs} from Eq. 2.21 via

$$l_{\mathrm{Abs}}(\nu) = \frac{c}{4\pi\nu n''(\nu)}\;, \tag{2.24}$$

with ν being the frequency of the EM wave and c being the speed of light in vacuum. In this work, n always represents a complex-valued RI. However, if the imaginary component is negligibly small, it is omitted and only the real part is given. Optically anisotropic materials have a RI that depends on the polarization state and propagation direction of the EM wave, which is called birefringence [104].

Reflection and Transmission at Plain Interfaces The reflection and transmission coefficients R and T for a plain interface between two media having RIs n_1 and n_2 are given

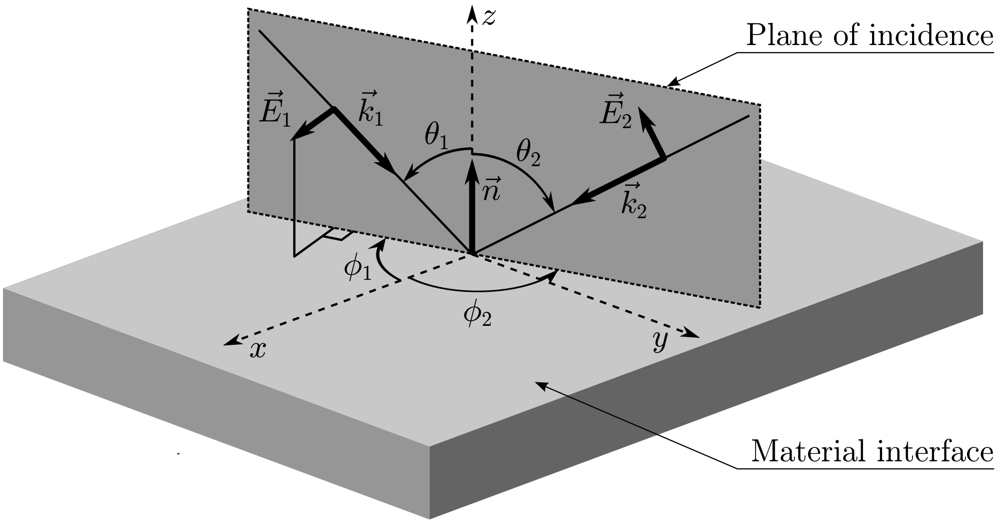

Figure 2.14: Illustration of the polarization of an EM wave impinging on a material interface. Waves 1 and 2, having wave vectors $\vec{k}_1$ and $\vec{k}_2$, are incident with angles (θ_1,ϕ_1) and (θ_2,ϕ_2) with respect to the local coordinate system (x,y,z). Wave 1 is S-polarized and the electric field vector $\vec{E}_1$ is perpendicular to the plane of incidence. Wave 2 is P-polarized and $\vec{E}_2$ lies within the plane of incidence. For clarity, the magnetic field vectors $\vec{H}_1$ and $\vec{H}_2$ are not shown.

by the Fresnel equations [104]:

$$R_\mathrm{S} = \left| \frac{n_1 \cos(\theta) - n_2 \cos(\theta_\mathrm{r})}{n_1 \cos(\theta) + n_2 \cos(\theta_\mathrm{r})} \right|^2 , \tag{2.25}$$

$$R_\mathrm{P} = \left| \frac{n_1 \cos(\theta_\mathrm{r}) - n_2 \cos(\theta)}{n_1 \cos(\theta_\mathrm{r}) + n_2 \cos(\theta)} \right|^2 , \tag{2.26}$$

$$T_\mathrm{S} = \left| \frac{n_2 \cos(\theta_\mathrm{r})}{n_1 \cos(\theta)} \right| \left| \frac{2 n_1 \cos(\theta)}{n_1 \cos(\theta) + n_2 \cos(\theta_\mathrm{r})} \right|^2 , \tag{2.27}$$

$$T_\mathrm{P} = \left| \frac{n_2 \cos(\theta_\mathrm{r})}{n_1 \cos(\theta)} \right| \left| \frac{2 n_1 \cos(\theta)}{n_1 \cos(\theta_\mathrm{r}) + n_2 \cos(\theta)} \right|^2 . \tag{2.28}$$

Here, the subscripts S and P denote the two states of S- and P-polarization, θ is the incident angle with respect to the interface normal (see Fig. 2.14), and θ_r is the refracted angle given by Snell's law

$$n_1 \sin(\theta) = n_2 \sin(\theta_\mathrm{r}) . \tag{2.29}$$

In the case of the transition from a high-index medium to a low-index medium ($n_1 > n_2$), total internal reflection (TIR) occurs for all incident angles larger than the threshold

$$\theta_\mathrm{TIR} = \arcsin\left(\frac{n_2}{n_1}\right) . \tag{2.30}$$

Reflection and Transmission at Rough Interfaces The application of Eqs. 2.25-2.28 for calculating the transmission and reflection behavior of a material interface is limited to highly smooth surfaces. Without extensive polishing procedures, the surfaces of inorganic scintillator crystals exhibit a certain roughness stemming from the fabrication process. This can have a substantial impact on the scattering, reflection, and transmission behavior of the interfaces which in turn influences the light yield and timing of a PET detector [105, 106].

The interaction of light with rough surfaces depends on the dimensions of the surface structures, the wavelength of the EM wave, and the incident angle. There are various analytical approaches to model the scattering from rough surfaces, for example Lambert's law for isotropically diffusive interfaces or approximate techniques based on Maxwell's equations such as the Beckmann-Kirchhoff theory [107] for non-diffusive rough surfaces. Furthermore, computational models exist to rigorously calculate the scattering from different surface topographies [108] and dedicated setups have been presented that measure the reflectance and scattering of specially prepared scintillator samples as a function of the incident angle [106].

2.5.2 Limiting Factors of Detector Performance

2.5.2.1 Photon Transfer inside Scintillators

In the first step of the scintillation light transfer, the photons must propagate from their emission location towards the scintillator exit face, i.e. the area of the crystal which is coupled to the photosensor via optical glue. In current commercial whole-body PET systems based on LSO crystals, the scintillators have dimensions of approximately (4×4×20) mm^3. With a linear attenuation coefficient of $\mu_{\mathrm{Att}} = 0.081\ \mathrm{mm}^{-}1$ (see Table 2.1) and assuming normal incidence of the annihilation photons, approximately 50% of the gamma photons are absorbed within the first 6 mm of the LSO which implies that these scintillation photons must propagate at least 14 mm through the crystal. Additionally, the scintillation light is emitted isotropically, which leads to further prolongation of the trajectories. Consequently, scintillation photons interact multiple times with the crystal surfaces as illustrated in Fig. 2.15a. The bulk and surface scattering can lead to yet another prolongation of the photon paths. Longer trajectories obviously increase the amount of light being absorbed by the scintillator bulk and ultimately limit the detector light yield.

The negative consequences for the timing resolution are twofold: i) the bulk absorption reduces the light yield of the detector N_{Det}; ii) the prolonged photon paths lead to an unfavorable propagation time distribution which has a negative influence on the CRT.

Further absorption of light can occur when photons leave the scintillator and interact with the reflective materials that may surround the crystal. Although commercial wrappings such as Teflon have a very high reflectance, they always exhibit a certain amount of absorption and transmission [34, 106].

2.5.2.2 Light Extraction from Scintillators

In the second step of the scintillation light transfer, photons that impinge on the scintillator exit face must be extracted into the optical glue coupling scintillator and photosensor. Scintillators currently used in commercial PET scanners have high RIs (see Table 2.1) versus typical optical glues. In the case of an LSO crystal with $n_{\mathrm{LSO}} = 1.82$ coupled to a glue with $n_{\mathrm{Glue}} = 1.47$ [22, 25], the TIR threshold is $\theta_{\mathrm{TIR}} = 53.9°$(see Fig. 2.15b). Hence, photons impinging on the exit face with shallow angles beyond θ_{TIR} are trapped inside the scintillator which leads to prolonged optical path lengths and increased bulk absorption. This trapping causes a substantial limitation of the light yield. Although photons can be extracted at later recurrences on the exit face, their long trajectories are detrimental for the CRT of the detector.

2.5.2.3 Light Collection by Photosensors

In the last step of the scintillation light transfer, the photons are extracted from the scintillator crystal, propagate through the optical glue and impinge on the photosensor. One factor limiting the light collection by photosensors is reflection at the interface glue/sensor. This effect is usually minimized using anti-reflective coatings. However, all photosensors have a certain amount of insensitive area.

In SiPM arrays, there are two sources for inactive sensor areas. The first is the gap between neighboring SiPM chips mounted on the carrier board. In a recent module with dimensions similar to current PET detectors, the multiple channels with a size of (3.77×3.77) mm^2 are assembled on a carrier board separated by a gap of approximately 200 μm, which leads to a fraction of 10% of inactive area [29]. The second and more important source is the intrinsic geometric fill factor of SiPMs, which depends on the design of the device and the requirements regarding sensitivity and dynamic range.

Incomplete light collection caused by inactive areas decreases the amount of extracted photons registered by the photosensors. Depending on the surface of the inactive area, incident light is either absorbed or reflected. In the latter case, there is a certain probability that photons return to the photosensor and are registered at a later recurrence. However, bulk absorption and scattering as well as light trapping limits this probability and the additional propagation time of photons being detected at later recurrences has a negative impact on the CRT of the detector.

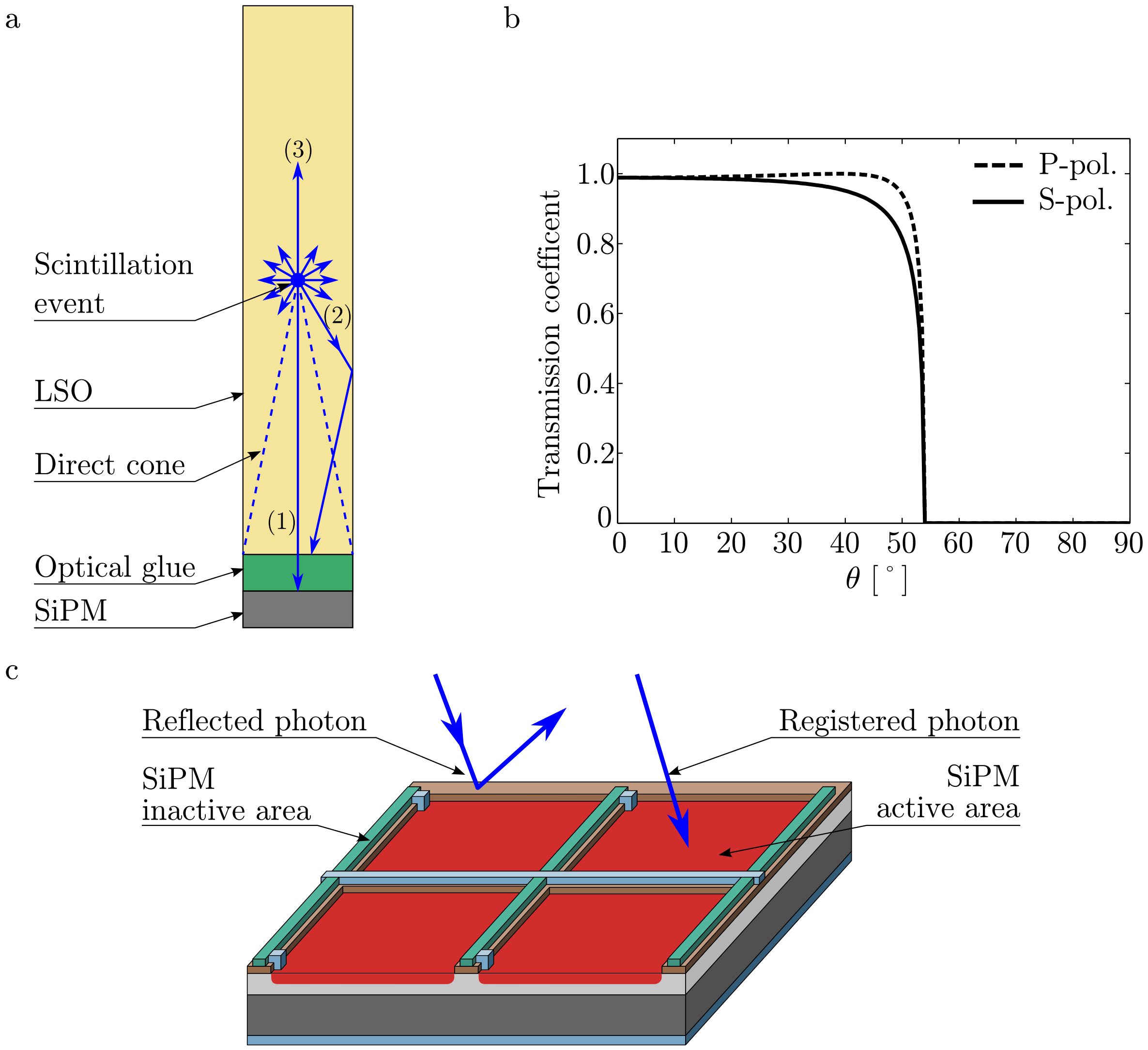

Figure 2.15: Summary of the limiting factors of detector performance caused by the photon propagation. (a) Drawing of isotropic emission of scintillation photons in an LSO crystal. Only photons like (1) emitted within a certain solid angle (direct cone) can impinge on the exit face without surface interactions (neglecting bulk scattering). Most photons like (2) interact at least once with the lateral scintillator walls, half of them like (3) have initial propagation directions that point away from the exit face. (b) Transmission coefficient calculated with Fresnel equations for the transition of light from LSO ($n_{\text{LSO}} = 1.82$) into optical glue ($n_{\text{Glue}} = 1.47$) showing the TIR cutoff at $\theta = 53.9°$. (c) Incomplete light collection of an SiPM caused by reflection or absorption of photons through inactive sensor areas.

Chapter 3

Approaches for Improving Light Yield and Timing Resolution

This chapter introduces different approaches used to mitigate the limitations of PET detector performance caused by optical effects. Besides giving an overview of the various technical possibilities, the chapter provides a detailed introduction into the basic principles of light concentrators and photonic crystal, which are the two concepts proposed by this work.

3.1 Concentrator for Improved Light Collection

Various studies have suggested the use of optical devices to funnel light onto the photosensor chips [109, 110]. These works concentrated on the sensor as a whole, neglecting the intrinsically limited f_{Geo}, which represents a main limitation of the sensor light collection. Although devices with increased fill factors of up to 75% have been presented recently [111], the working principle of SiPMs and the requirements of PET regarding the timing and dynamic range put constraints on the maximum f_{Geo}. A fill factor of approximately 61% currently represents a common value for SiPMs suitable for PET applications [18, 19].

Few concepts have been proposed to improve the light collection on the microcell level yet. These include refractive elements such as arrays of microlenses mounted on the SiPM surface [31]. Instead of refractive elements, this work proposes reflective LCs with special focus on the improved detection of photons at an early phase of the scintillation pulse for improved timing performance.

3.1.1 Principles of Light Concentrators

Light concentrators are optical devices that transfer the irradiance incident on an aperture A_{In} onto a smaller receiver plane $A_{\mathrm{Rec}} < A_{\mathrm{In}}$. There are various forms of LCs which either belong to the class of imaging or non-imaging optics. Imaging devices such as lenses or parabolic concentrators produce an image of the light source which maintains the relative dimensions of the original object. Non-imaging devices collect the light from the source without forming an image [112]. A further classification distinguishes between reflective, refractive or mixed types. LCs are mainly used in solar energy applications, e.g. in solar thermal installations [113]. Also, LCs are combined with small high-efficiency photovoltaic cells with the goal to reduce the quantity of expensive photovoltaic semiconductor material [114]. LCs can be characterized through a concentration factor C defined as

$$C = \frac{A_{\mathrm{In}}}{A_{\mathrm{Rec}}} \,. \tag{3.1}$$

An upper limit C_{Max} exists for all LCs, which can be derived using the second law of thermodynamics [112, 115]. This limit is correlated to the maximum acceptance angle θ_{Acc} of a concentrator through

$$C_{\mathrm{Max}} \leq \frac{1}{\sin^2 \theta_{\mathrm{Acc}}} \,. \tag{3.2}$$

Light incident on the LC aperture with an angle $\theta > \theta_{\mathrm{Acc}}$ is rejected and does not reach the receiver plane.

3.1.2 Compound Parabolic Concentrator

An established type of LC is the compound parabolic concentrator (CPC), which belongs to the class of non-imaging devices [116]. It consists of parabolic reflectors where the curvature and height of the reflectors define the maximum acceptance angle θ_{Acc} of the device (see Fig. 3.1). In the two-dimensional case, CPCs are called ideal concentrators as they reach the theoretical concentration limit which results in a rectangular acceptance characteristic as shown in Fig. 3.2 [115]. Three-dimensional configurations do not exhibit ideal behavior and the acceptance characteristic show a continuous transition around θ_{Acc} [112].

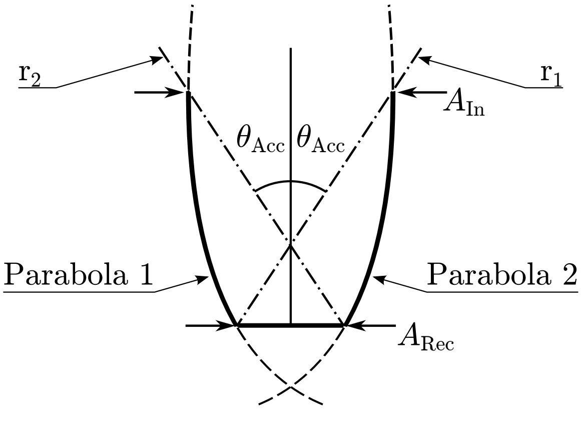

Figure 3.1: Drawing of a CPC consisting of two parabolic reflectors. The straight lines r_1 and r_2 connecting the edges of the receiver plane A_{Rec} and the aperture A_{In} are parallel to the axes of the parabolas and indicate the maximum acceptance angle θ_{Acc}. Adapted from Ref. [115].

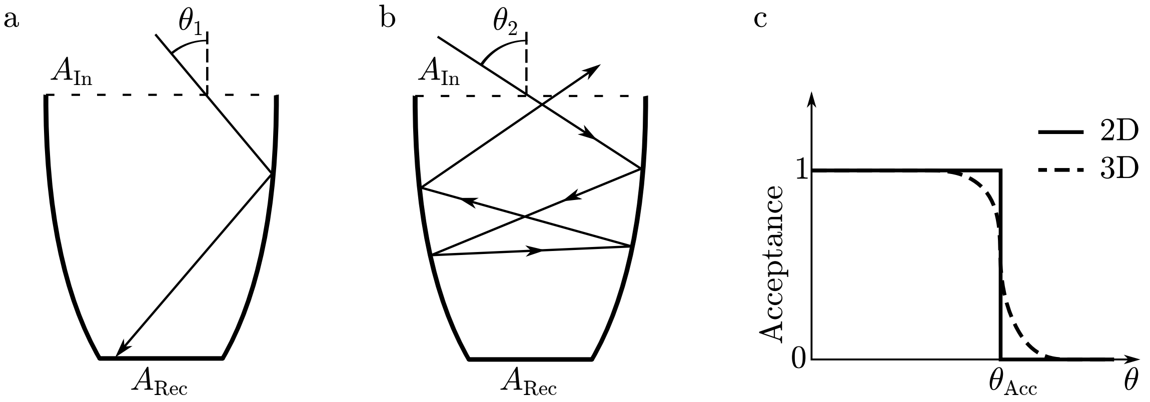

Figure 3.2: Drawing of the trajectory of a photon incident on a CPC with an incident angle $\theta_1 < \theta_{\mathrm{Acc}}$ which is redirected towards A_{Rec} (a) and of a photon incident with $\theta_2 > \theta_{\mathrm{Acc}}$ which is rejected and exits the CPC through the aperture A_{In} (b). (c) In two dimensions, CPCs exhibit so-called ideal behavior and accept all incident photons with $\theta < \theta_{\mathrm{Acc}}$ while rejecting all other photons. Three-dimensional CPCs show a similar behavior but have a continuous transition region around θ_{Acc}.

3.1.3 Tapered Concentrator

An alternative type of concentrator similar to the CPC is the tapered concentrator (TC), which consists of linear reflectors instead of parabolic ones (also called pyramidal concentrator or V-trough [115], see Fig. 3.3). A TC is characterized by three parameters:

- the input aperture A_{In}
- the receiver plane A_{Rec}
- the taper angle ζ_{C}

The height H_{C} of the concentrator is given through

$$H_{\mathrm{C}} = \frac{A_{\mathrm{In}} - A_{\mathrm{Rec}}}{2\,\tan \zeta_{\mathrm{C}}} \ . \tag{3.3}$$

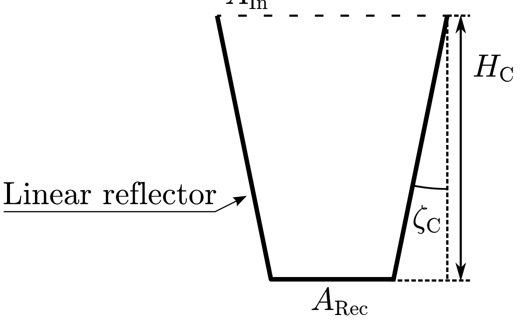

Figure 3.3: Schematic of a tapered concentrator.

In contrast to CPCs, TCs exhibit a transition region of decreasing angular acceptance in the two-dimensional case. This region lies between two angles ϑ_1 and ϑ_2, which can be derived by studying the geometry in Fig. 3.4. In this approach, reflections from the tapered concentrator walls are replaced through mirror images of the concentrator arranged on a reference circle [115]. This geometry yields the correlations

$$\vartheta_1 = \arcsin\left(\frac{A_{\mathrm{Rec}}}{A_{\mathrm{In}}}\right) - \zeta_{\mathrm{C}} \ , \tag{3.4}$$

$$\vartheta_2 = \arcsin\left(\frac{A_{\mathrm{Rec}}}{A_{\mathrm{In}}}\right) + \zeta_{\mathrm{C}} \ . \tag{3.5}$$

The two angles ϑ_1 and ϑ_2 indicate that for TCs, the acceptance of photons does not only depend on the incident angle but also on the incidence location of photons on the aperture A_{In}, which is illustrated in Fig. 3.5. This is not the case for two-dimensional CPCs, which can be seen from the strictly rectangular acceptance curve in Fig. 3.2c. The maximum acceptance angle of a TC can be defined as the center between ϑ_1 and ϑ_2:

$$\theta_{\mathrm{Acc}} = \arcsin\left(\frac{A_{\mathrm{Rec}}}{A_{\mathrm{In}}}\right) \ . \tag{3.6}$$

Eq. 3.6 suggests that θ_{Acc} does not depend on the taper angle ζ_{C} but is solely defined by the concentration factor $C = A_{\mathrm{Rec}}/A_{\mathrm{In}}$. However, the transition region has a width of $2\zeta_{\mathrm{C}}$ provided by Eqs. 3.4 and 3.5. Hence, TCs with a small taper angle (i.e. a large height) have a narrow transition region around θ_{Acc}. In three dimensions, the angular acceptance curve is similar to the two-dimensional case but exhibits a more continuous slope as shown in Fig. 3.5c. A comparison of TCs with CPCs for a fixed concentration factor C indicates that TCs require a higher average number of reflector interactions [115]. This limits their performance when using lossy reflector materials, especially regarding configurations with small taper angles.

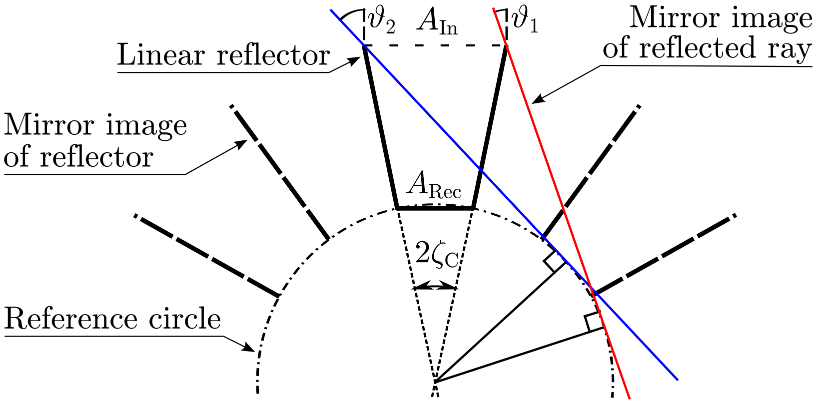

Figure 3.4: Construction of the characteristic angles ϑ_1 and ϑ_2 of a TC using mirror images arranged on a reference circle. Adapted from Ref. [115].

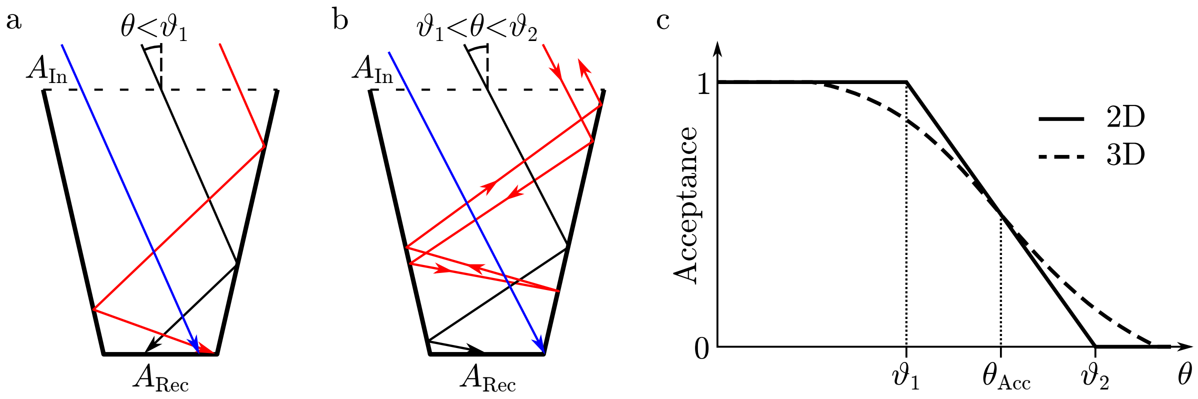

Figure 3.5: Possible ray trajectories in a TC. (a) All rays incident with $\theta < \vartheta_1$ are accepted by the concentrator. (b) For rays incident with $\vartheta_1 < \theta < \vartheta_2$, the acceptance depends on the incidence location. c) Angular acceptance characteristic of a TC illustrating the transition region between ϑ_1 and ϑ_2 and the smoothed slope in the three-dimensional case.

3.1.4 Application of Light Concentrator on SiPM Surface

The angular acceptance curves of CPCs and TCs indicate that all photons incident with low angles can be collected in the ideal case without absorption losses. Since the first photons that are extracted from the scintillator and impinge on the SiPM tend to have rather direct trajectories and low incident angles, both concentrator designs represent promising strategies to enhance the detection of early photons and to improve the timing.

Assuming a simplified SiPM geometry of quadratic microcells with $f_{\text{Geo}} = 61.5\%$ and a 50 μm pitch yields an active area of (39.2×39.2) μm^2 per microcell. An LC mounted on top of such an SiPM must be adjusted precisely to these dimensions yielding a structure with features in the micrometer range. These requirements can potentially be met by microfabrication technologies used in the semiconductor industry. In this field, various physical and chemical etching techniques as well as additive processes such as chemical vapor deposition allow the fabrication of miniaturized devices with exact control of their mechanical, electrical, and optical properties [117]. Although these technologies offer a high degree of flexibility and accuracy regarding the fabricated geometries, realizing a micrometer-scaled CPC with exactly tailored parabolic features is highly challenging. Consequently, this work proposes an SiPM equipped with a surface-mounted TC to improve the light collection. In the remainder of this work, the term light concentrator always refers to a tapered concentrator.

Commercial SiPMs are usually encapsulated, e.g. using a resin potting, to provide optical transparency combined with mechanical protection of the device. To achieve improved light collection through an LC, it must be assembled directly on top of the SiPM within the encapsulation as illustrated in Fig. 3.6a. An important limitation of this approach is shown in Fig. 3.6b. LCs cannot collect all incident light and even reject certain photons, which would be registered in a configuration without a concentrator. These opposing effects must be balanced in the correct way to gain more photons with incident angles $\theta < \theta_{\text{Acc}}$ than are rejected in the region of $\theta > \theta_{\text{Acc}}$. This can be achieved by optimizing the concentrator geometry for the given angular distribution of incident photons.

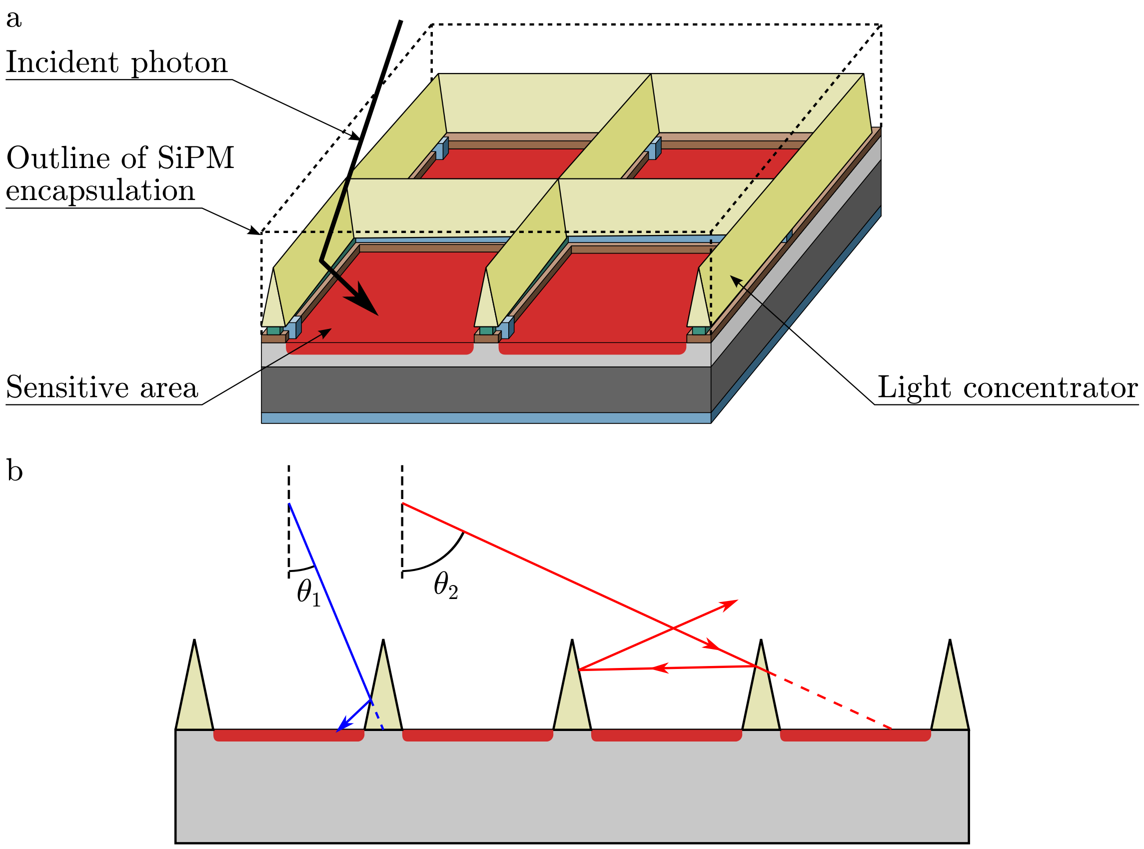

Figure 3.6: a) Drawing of LC assembled on SiPM surface covering the inactive area with the goal to redirect photons onto the sensitive microcells (see Fig. 2.12 for a detailed description of the SiPM). b) Illustration of light collection through an LC mounted on an SiPM. All photons incident with an angle $\theta_1 < \vartheta_1$ impinge on the active area of the SiPM. Photons incident with $\theta_2 > \vartheta_1$ can be rejected by the LC. The dashed lines indicate the photon trajectory in a configuration without concentrator.

3.2 Photonic Crystals for Improved Light Extraction

3.2.1 Overview of Approaches for Increased Light Extraction

Besides the sensor light collection, the trapping of photons inside the scintillator crystal due to TIR is another constraint that limits the detector performance. Extracting light from materials with a high RI into materials with a low RI is a well-known problem, not only for scintillator-based detectors but also in other fields, such as light emitting diodes fabricated with high-index semiconductors. Hence, there are various strategies addressing this issue. This section gives a short overview over these approaches.

3.2.1.1 Refractive Index Matching

The light extraction from scintillators is limited by TIR that occurs at the interface between the scintillator material and the optical glue. Consequently, using optical glue with the appropriate RI, i.e. $n_{\text{Glue}} \geq n_{\text{Scintillator}}$, would be the most effective way to prevent light trapping. However, conventional optical glues have RIs of approximately 1.5 or smaller [21, 22, 32, 118], whereas scintillators used in current PET systems have RIs of 1.8 or larger (see Table 2.1). Currently, no optical coupling agent is available that combines $n_{\text{Glue}} > 1.5$ and sufficiently low absorption over the scintillator emission spectrum.

In fact, matching the RI of the optical glue to the scintillator only leads to increased light extraction if the remaining materials are index-matched as well. For example, SiPMs are encapsulated with resin potting or glass with an RI < 1.6. Hence, having an optical glue with $n_{\text{Glue}} = n_{\text{Scintillator}}$ while maintaining an SiPM epoxy with $n_{\text{Epoxy}} = 1.59$ would merely shift the TIR to the interface glue/epoxy.

3.2.1.2 Conventional Anti-Reflective Coatings

Another option to prevent light trapping might be to use conventional dielectric anti-reflective coatings, which are routinely used for optical components. In this category, gradient-index films which provide a continuous transition of the RI between the two materials are amongst the most efficient approaches, since they exhibit excellent anti-reflective characteristics for a broad spectrum of incident angles and wavelengths [119].

However, all conventional anti-reflective coatings only serve to reduce Fresnel reflection and have no impact on TIR. This can be derived from a stack of N dielectric layers. Repeated application of Snell's law indicates that the TIR cutoff is given through

$$\theta_{\text{TIR}} = \arcsin\left(\frac{n_{\text{Min}}}{n_1}\right) \ , \tag{3.7}$$

where n_1 is the RI of the first medium and n_{Min} is the lowest RI of all subsequent layers. For monotonously decreasing RIs, n_{Min} corresponds to the RI n_N of the last layer and hence θ_{TIR} only depends on the first and last medium. Thus, conventional anti-reflective coatings are no effective approach to mitigate TIR-related light trapping in high-index scintillator crystals.

3.2.1.3 Structured Material Interfaces

A successful way to manipulate the light trapping due to TIR is structuring the material interface. Depending on the type of structure (ordered or random) and on the characteristic dimensions in relation to the wavelength, different mechanisms can be distinguished.

If the features of the structured interface are significantly smaller than the wavelength, they cannot be resolved by the EM wave and appear as a uniform medium having an effective RI. This effect can be used to tailor gradient-index coatings [120] but has no impact on TIR.

If the features are significantly larger than the wavelength, the interaction is governed by the laws of geometric optics. Actually, such refractive structures do not prevent TIR. However,

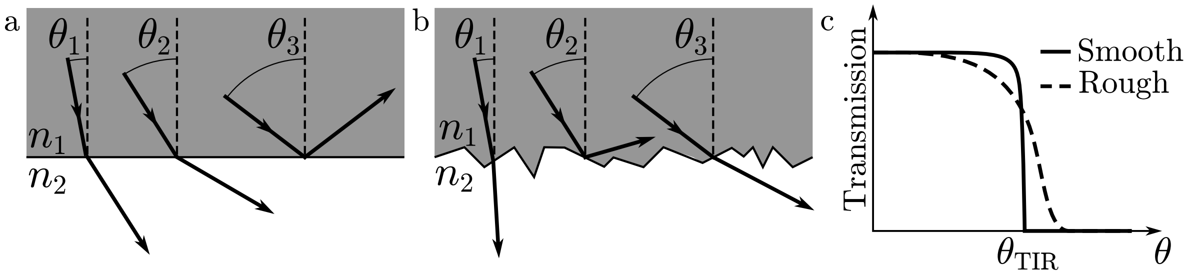

Figure 3.7: Illustration of the different transmission behaviors of a smooth material interface (a) and a rough interface consisting of refractive facets (b). The facets facilitate the extraction of photons with incident angles $\theta_3 > \theta_{\mathrm{TIR}}$ but also lead to the reflection of some photons with $\theta_2 < \theta_{\mathrm{TIR}}$. This yields a transmission characteristic lacking the abrupt cutoff at θ_{TIR} as illustrated in (c).

replacing a plain material interface through a topography of refractive facets can change the transmission behavior as different oblique surfaces are available for the incident light as illustrated in Fig. 3.7. Scintillator crystals are usually grown in large cylinders and then cut into pixels. Without polishing procedures, this results in intrinsically rough surfaces consisting of a statistical distribution of refractive facets. Consequently, scintillator surfaces naturally exhibit a transmission behavior that is rather distinct from ideally plain interfaces [106]. Instead of randomly rough interfaces, refracting micro-structures can be fabricated with a specific geometry. The advantage of this approach is that it allows tailoring the transmission characteristic of a surface for a given angular distribution of incident photons. First studies used microlens arrays to increase the extraction from light emitting diodes [121]. Recently, implementations of this strategy have been presented for scintillators using micro pyramids [122] and wedge-shaped cavities [72]. The disadvantage of this approach is that it requires micromachining the surface of the scintillator materials. This approach involves intricate processes such as mechanical sawing or laser ablation. Due to this drawback, these subtractive approaches are not in the focus of this work.

Alternatively, surface features that have dimensions comparable to the wavelength can be used to scatter light and avoid TIR. Again, statistically distributed scattering centers can be employed for this approach [123, 124] and first implementations on scintillators have been presented [125]. In order to have more control over the scattering properties of a material interface, periodic features with specific geometry parameters can be fabricated including implementations using dielectric microspheres [126] or metallic nanostructures [127]. Photonic crystals are another technology based on periodic scattering structures. During the last years, they have been employed in various light emitting diodes (see Ref. [128] for a detailed review) and recently have been proposed for scintillator applications [21, 24, 28, 129]. Since these additive technologies can be realized through deposition of thin layers on the scintillator surfaces instead of subtractive methods that require micromachining of the scintillator itself, this work proposes PhC-enhanced scintillator surfaces to increase the light extraction. The following sections will give a detailed introduction into the principles of PhCs.

3.2.2 Theory of Photonic Crystals

PhCs are materials that have a periodically modulated RI with characteristic dimensions similar to the wavelength of the incident light. Depending on the number of dimensions that exhibit the periodicity, they can be separated into one-, two-, and three-dimensional PhCs (see Fig. 3.8). PhCs manipulate the propagation of light in a similar manner as solid state crystals influence the motion of electrons. The following sections give a short summary of the comprehensive introduction into the theory of PhCs presented in Ref. [27].

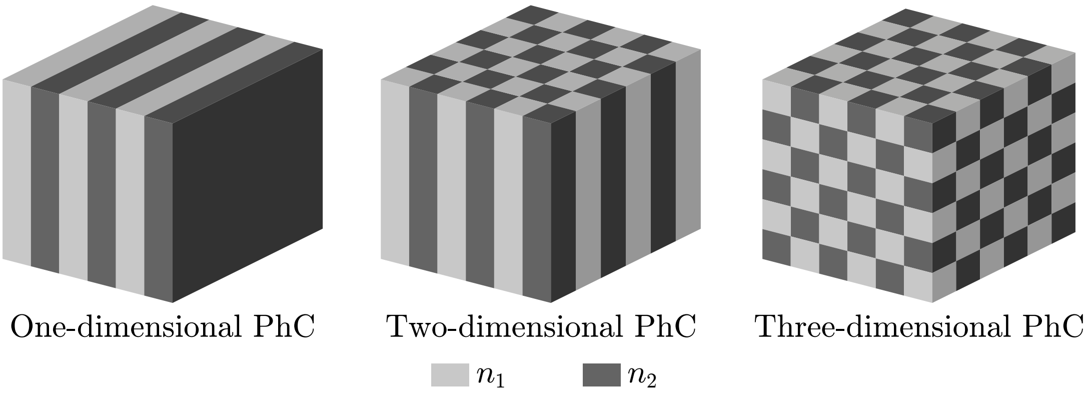

Figure 3.8: Illustration of one-, two-, and three-dimensional PhCs consisting of two materials having RIs n_1 and n_2. Adapted from Ref. [130].

3.2.2.1 A Brief Summary of the Bloch Theorem in Conventional Crystals

A conventional crystal consists of atoms or molecules arranged in a periodic structure, i.e. the crystal lattice. Since the de Broglie wavelength of a free electron is comparable to typical lattice constants in crystals, the propagation of electrons must be described using the laws of quantum mechanics. Neglecting electron-electron interactions, the stationary Schrödinger equation is given through

$$\hat{H}\psi = \left(-\frac{\hbar^2}{2m_{\mathrm{El}}} \vec{\nabla}^2 + V(\vec{r}) \right) \psi = \epsilon\psi \ , \tag{3.8}$$

where $\hat{H}$ is the Hamiltonian corresponding to the bracketed term in Eq. 3.8, $\hbar$ is the Planck constant divided by 2π, m_{El} is the electron mass, $V(\vec{r})$ is the periodic electric potential of the crystal lattice depending on the position $\vec{r}$, ϵ is the energy eigenvalue of the electron, and ψ is the quantum-mechanical wave function of the electron. According to the Bloch theorem, a general solution for Eq. 3.8 is given through

$$\psi(\vec{r}) = \exp(\mathrm{i}\vec{k}\vec{r}) \cdot u_{\vec{k}}(\vec{r}) \ . \tag{3.9}$$

Here, $\vec{k}$ is the wave vector of the electron and $u_{\vec{k}}(\vec{r})$ is a function that exhibits the same periodicity as the potential $V(\vec{r})$. Based on this theory, the electron energy $\epsilon(\vec{k})$ can be calculated as a function of the wave vector yielding the so-called band diagrams. The solution in Eq. 3.9 describes electron waves that can propagate through a crystal almost like waves in

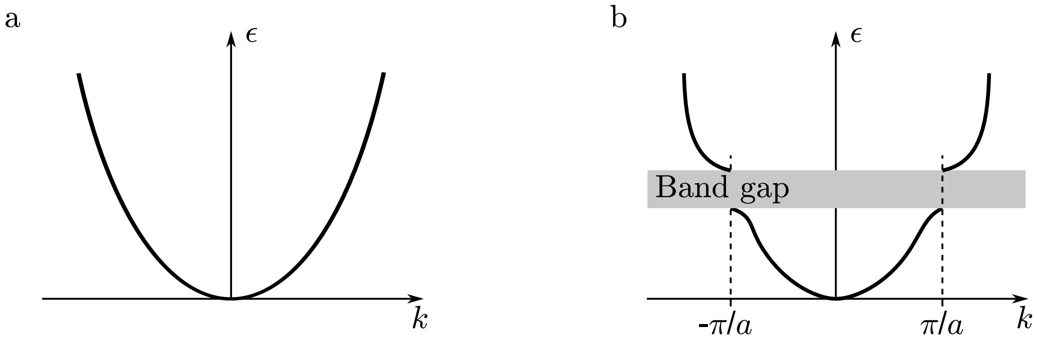

Figure 3.9: a) Energy as a function of the wave vector for a free electron. b) Energy versus wave vector for an electron propagating through a one-dimensional crystal with lattice constant a. Bragg scattering leads to the formation of a band gap.

free space despite of the lattice. However, Bragg-scattering leads to the formation of band gaps which are energy intervals that cannot be occupied by electrons (see Fig. 3.9). The concept of band structures in conjunction with the Fermi energy can be used to distinguish between conducting, semi-conducting and isolating materials.

3.2.2.2 Maxwell Equations

After the short recapitulation of the Bloch theorem and band structures in conventional crystals, this section uses the Maxwell equations to obtain equations that facilitate the calculation of the EM fields in a PhC. These serve as a base for the subsequent sections where Bloch states in PhCs are derived with the ultimate goal to discuss the optical properties of PhCs.

The macroscopic Maxwell equations are [131]:

$$\vec{\nabla} \cdot \vec{B}(\vec{r},t) = 0 \ , \tag{3.10}$$

$$\vec{\nabla} \cdot \vec{D}(\vec{r},t) = \rho(\vec{r},t) \ , \tag{3.11}$$

$$\vec{\nabla} \times \vec{E}(\vec{r},t) = -\frac{\partial \vec{B}(\vec{r},t)}{\partial t} \ , \tag{3.12}$$

$$\vec{\nabla} \times \vec{H}(\vec{r},t) = \vec{J}(\vec{r},t) + \frac{\partial \vec{D}(\vec{r},t)}{\partial t} \ . \tag{3.13}$$

The constituents of Eqs. 3.10-3.13 and other parameters that are relevant for this discussion are listed in Table 3.1. In this work, only PhCs are considered that consist of dielectric materials with no sources of EM radiation, i.e. ρ and $\vec{J}$ are set to 0. Also, the field strengths are assumed to be small and the materials to be isotropic and lossless, which leads to a correlation between the electric and displacement field through

$$\vec{D}(\vec{r},t) = \varepsilon_0 \, \varepsilon(\vec{r}) \vec{E}(\vec{r},t) \ . \tag{3.14}$$

Similarly, the magnetic components can be correlated through

$$\vec{B}(\vec{r},t) = \mu_0 \vec{H}(\vec{r},t) \ , \tag{3.15}$$

Table 3.1: List of relevant EM quantities for the discussion of PhCs.

Symbol	Description
$\vec{E}$	Electric field
$\vec{H}$	Magnetic field
$\vec{D}$	Electric displacement field
$\vec{B}$	Magnetic induction field
ρ	Free charge density
$\vec{J}$	Current density
ε_0	Permittivity constant of free space
ε	Relative permittivity of a material
μ_0	Permeability constant of free space
μ	Relative permeability of a material

where $\mu(\vec{r})$ was set to 1 as is the case for most dielectric materials. Another consequence of this simplification is that the RI n only depends on ε,

$$n(\vec{r}) = \sqrt{\varepsilon(\vec{r})}\ . \tag{3.16}$$

Consequently, Eqs. 3.10-3.13 can be rewritten in terms of $\vec{E}$ and $\vec{H}$:

$$\vec{\nabla} \cdot \vec{H}(\vec{r}, t) = 0\ , \tag{3.17}$$

$$\vec{\nabla} \cdot [\varepsilon(\vec{r})\vec{E}(\vec{r}, t)] = 0\ , \tag{3.18}$$

$$\vec{\nabla} \times \vec{E}(\vec{r}, t) = -\mu_0 \frac{\partial \vec{H}(\vec{r}, t)}{\partial t}\ , \tag{3.19}$$

$$\vec{\nabla} \times \vec{H}(\vec{r}, t) = \varepsilon_0\, \varepsilon(\vec{r}) \frac{\partial \vec{E}(\vec{r}, t)}{\partial t}\ . \tag{3.20}$$

Since Eqs. 3.17-3.20 are linear, the spatial and temporal dependencies can be separated and the solutions for $\vec{E}$ and $\vec{H}$ can be written as harmonic waves of the frequency ω,

$$\vec{E}(\vec{r}, t) = \vec{E}(\vec{r})\ \exp(-\mathrm{i}\omega t)\ , \tag{3.21}$$

$$\vec{H}(\vec{r}, t) = \vec{H}(\vec{r})\ \exp(-\mathrm{i}\omega t)\ . \tag{3.22}$$

Combining these with Eqs. 3.19-3.20 allows to derive an equation for $\vec{H}$,

$$\vec{\nabla} \times \left(\frac{1}{\varepsilon(\vec{r})} \vec{\nabla} \times \vec{H}(\vec{r}) \right) = \left(\frac{\omega}{c} \right)^2 \vec{H}(\vec{r})\ , \tag{3.23}$$

which uses the vacuum speed of light $c = 1/\sqrt{\varepsilon_0\, \mu_0}$. Hence, the spatial distribution of $\vec{H}$ can be derived as a function of the frequency ω, given that the spatial distribution of the relative permittivity $\varepsilon(\vec{r})$ is known. Through Eq. 3.20, this also allows calculating $\vec{E}$.

3.2.2.3 Photonic Crystal Lattice

As introduced earlier, PhCs consist of a periodically modulated RI. Using Eq. 3.16, this characteristic can be expressed as an invariance of the permittivity ε under certain translation operations:

$$\varepsilon(\vec{r}) = \varepsilon(\vec{r} + \vec{R}) \; . \tag{3.24}$$

In analogy to the Bravais lattice of conventional crystals, this translation $\vec{R}$ is a linear combination of the primitive lattice vectors $(\vec{a}_1, \vec{a}_2, \vec{a}_3)$ of the PhC:

$$\vec{R} = C_1\vec{a}_1 + C_2\vec{a}_2 + C_3\vec{a}_3 \; , \tag{3.25}$$

with C_1, C_2, and C_3 being integer coefficients. The counterpart of this system in the $\vec{k}$-space is called the reciprocal lattice, which is defined through a set of primitive reciprocal lattice vectors $(\vec{b}_1, \vec{b}_2, \vec{b}_3)$. Hence, all wave vectors that yield plane waves with the periodicity of the PhC lattice are given trough the reciprocal lattice vector $\vec{G}$,

$$\vec{G} = C_1'\vec{b}_1 + C_2'\vec{b}_2 + C_3'\vec{b}_3 \; , \tag{3.26}$$

where C_1', C_2', and C_3' are integer coefficients. The different lattice vectors are correlated trough

$$\vec{a}_i \cdot \vec{b}_j = 2\pi\delta_{ij} \; , \tag{3.27}$$

where δ_{ij} is the Kronecker delta. [71]

3.2.2.4 Bloch States for Photonic Crystals

In analogy to the operator-based Schrödinger equation (see Eq. 3.8), the problem of solving Eq. 3.23 to find the spatial distribution of the EM field in a PhC can be tackled using operators. Through the definition of the operator $\hat{O}$, that acts on a vector $\vec{v}$ as

$$\hat{O}\,\vec{v} = \vec{\nabla} \times \left(\frac{1}{\varepsilon(\vec{r})} \vec{\nabla} \times \vec{v} \right) \; , \tag{3.28}$$

the calculation of $\vec{H}$ through Eq. 3.23 becomes an eigenvalue problem:

$$\hat{O}\vec{H}(\vec{r}) = \left(\frac{\omega}{c} \right)^2 \vec{H}(\vec{r}) \; . \tag{3.29}$$

Thus, $(\omega/c)^2$ are the eigenvalues of $\hat{O}$ and the eigenvectors $\vec{H}$ identify various propagation modes of EM radiation through the PhC. Since $\hat{O}$ is a linear operator, a linear combination of two different solutions $\vec{H}_1$ and $\vec{H}_2$ is an eigenvector of $\hat{O}$, too. Furthermore, it can be shown that $\hat{O}$ is a Hermitian operator [130]. Hence, all eigenvalues of $\hat{O}$ are real numbers and two eigenfunctions $\vec{H}_1$, $\vec{H}_2$ are orthogonal if they have different frequencies, $\omega_1 \neq \omega_2$. If two eigenvectors have identical eigenvalues, they are called degenerate, which for example is the case for solutions that result from certain symmetry operations.

The impact of the periodicity of PhCs on the solutions for $\vec{H}$ can be studied with the help of the translation operator $\hat{T}$. This operator is defined through its effect on a function $\vec{v}(\vec{r})$ as

$$\hat{T}_{\vec{d}}\,\vec{v}(\vec{r}) = \vec{v}(\vec{r} + \vec{d}) \; . \tag{3.30}$$

Since the operators $\hat{T}$ and $\hat{O}$ commute [130], the eigenfunctions of $\hat{T}$ can be used to find a solution for $\hat{O}$. Hence, the Bloch theorem can be applied to the eigenvalue problem in Eq. 3.29 in the same way as for conventional crystals [71, 130], yielding solutions in the form of

$$\vec{H}_{\vec{k}}(\vec{r}) \propto \exp(\mathrm{i}\vec{k}\vec{r}) \cdot u_{\vec{k}}(\vec{r}) \ . \tag{3.31}$$

Here, $u_{\vec{k}}(\vec{r})$ is a function exhibiting the same periodicity as the PhC lattice,

$$u_{\vec{k}}(\vec{r}) = u_{\vec{k}}(\vec{r} + \vec{R}) \ . \tag{3.32}$$

The solution in Eq. 3.31 is the equivalent of Eq. 3.9 for the solutions of the Schrödinger equation for electrons. An important characteristic of Bloch states is that two eigenstates that differ only through the addition of a reciprocal lattice vector $\vec{G}$, i.e. $\vec{H}_{\vec{k}}$ and $\vec{H}_{\vec{k}+\vec{G}}$, are identical and have the same eigenvalue. Consequently, the complete information about all Bloch states in a PhC is contained within the first Brillouin zone, which is the primitive cell of the reciprocal lattice.

3.2.2.5 Photonic Crystal Band Structure and Optical Properties

In the previous section, the solutions for Eq. 3.23 consisting of Bloch functions $\vec{H}_{\vec{k}}(\vec{r})$ were derived. Since the eigenvalue problem of the Hermitian operator $\hat{O}$ in Eq. 3.29 can be constrained to the first Brillouin zone, the result will be a discrete spectrum of eigenvalues. For each $\vec{k}$-value, this will lead to an infinite set of modes with increasing frequency ω, labeled through the index j. Since $\vec{k}$ is a continuous variable, the results $\omega_j(\vec{k})$ are continuous functions which are called photonic bands. A band structure such as depicted in Fig. 3.10a can be used to derive the optical properties of PhCs.

Similarly to conventional crystals, PhC band structures can exhibit band gaps which represent frequency regions in which photons cannot not propagate through the PhC. These band gaps form since different photonic modes have distinct EM field distribution patterns. Depending on whether the electric field of a mode is concentrated more in regions of the PhC with high or low RI, the frequency of the mode is lowered or increased which leads to the formation of band gaps. Hence, the width of the band gap strongly depends on the RI-contrast between the PhC constituents and large contrasts are required for wide band gaps. [130]

The PhC band structure and the occurence of band gaps are the key characteristics of PhCs and pave the way for various applications such as omni-directional mirrors [132], waveguiding [133], beam splitting [27], polarizing [134], so-called superlenses [135] and superprisms [136], negative refraction [137, 138], and others.

3.2.3 Light Extraction through Photonic Crystals

The characteristic band structures of PhCs lead to notable optical properties. It has been shown by S. Fan et. al. [26], that these features can be used to increase the light extraction from high-index materials. For this, usually PhC slabs are used, which are two-dimensional (2D) PhCs that have only finite extension in the third dimension. The band structure of these

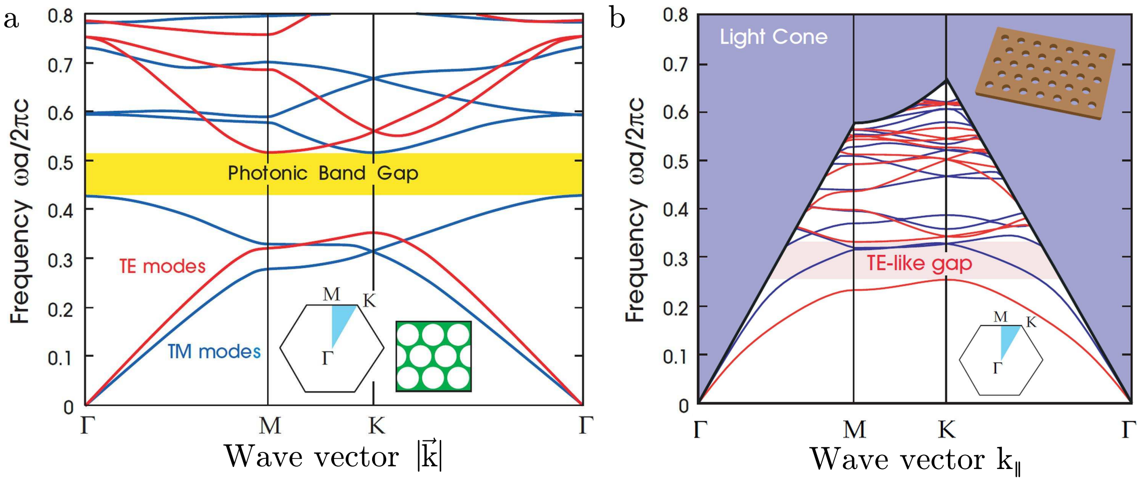

Figure 3.10: a) Photonic band structure calculated for a 2D PhC consisting of hexagonally arranged air columns ($\varepsilon = 1$) in a dielectric substrate ($\varepsilon = 13$). The TE (transverse electric) and TM (transverse magnetic) modes are equivalent to S- and P-polarization, respectively. The horizontal axis shows $|\vec{k}|$ along the outline of the so-called irreducible Brillouin zone depicted as blue triangle in the inset. b) Equivalent of (a) for a PhC slab. The horizontal axis shows the wave vector component within the slab plane. The broken symmetry along the third dimension leads to a continuum of radiative modes that are not guided within the slab (shaded area). The border of this continuum is called the light cone. Images taken from Ref. [130].

slabs differ from those of conventional PhCs (see Fig. 3.10b), as there must be distinguished between guided modes that are trapped inside the PhC and the continuum of radiative modes that leave the slab. The increase of light extraction through PhC slabs is based on various effects, such as tailored band structures [26, 139] or diffraction of guided modes into the ambient medium [140–142]. Through fabricating such a PhC slab on the exit face on a scintillator crystal (see Fig. 3.11), this effect can be transferred to PET detectors in order to avoid light trapping.

3.2.3.1 Light Diffraction through Photonic Crystals

An intuitive way to understand the effect of a PhC slab at a material interface is treating it as a biperiodic dielectric diffraction grating. The concept of PhC-enhanced light extraction studied in this work (see Fig. 3.11) considers grating structures with dimensions in the range of the wavelength ($\lambda \approx 420$ nm) on mm^2-sized scintillator surfaces and layer thicknesses (e.g. of the optical glue) of 100 micrometers or more. Hence, the involved diffraction effects can be treated within the Fraunhofer regime. In Fig. 3.12, the interaction of light with a material boundary is illustrated for a plain interface versus an interface equipped with a diffraction grating. In the case of light impinging with $\theta > \theta_{\mathrm{TIR}}$ on the interface without diffraction grating, all photons are reflected due to TIR. However, in the presence of a diffraction grating, there exist certain diffraction orders which facilitate the extraction of light even for the case $\theta > \theta_{\mathrm{TIR}}$. A disadvantage of the grating is, that there are also various diffraction orders in the reflection direction, which can lead to increased reflection for $\theta < \theta_{\mathrm{TIR}}$ compared to the

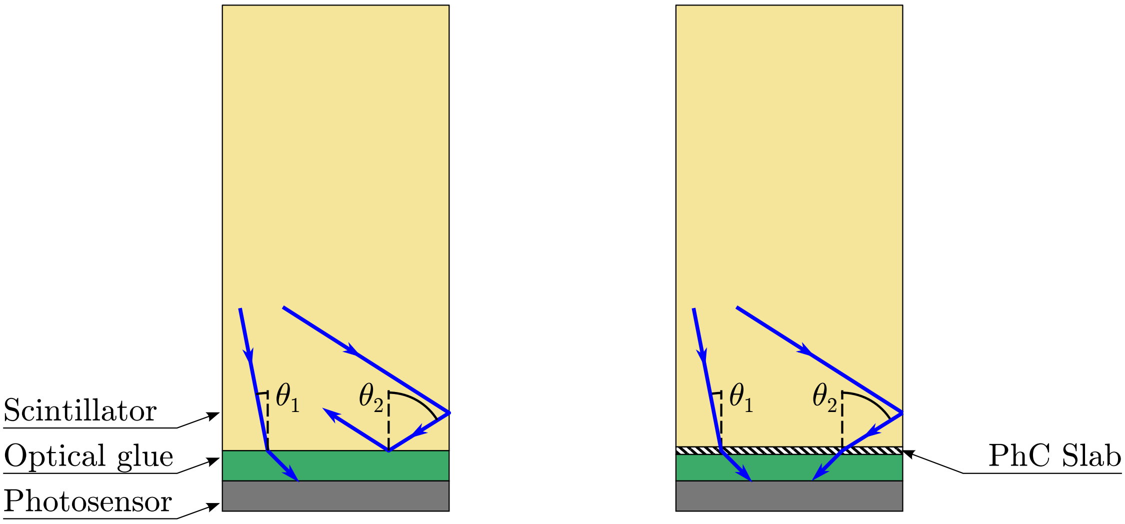

Figure 3.11: Illustration of the concept to improve the light extraction from scintillators using PhC slabs. In a conventional detector with polished scintillator surfaces (left), only photons with $\theta_1 < \theta_{\mathrm{TIR}}$ can be extracted whereas photons with $\theta_2 > \theta_{\mathrm{TIR}}$ are trapped. Inserting a PhC slab at the interface scintillator/glue (right) bears the potential to increase the light extraction.

plain interface. For a 1D grating, the angle θ_m of the m-th transmitted diffraction order is given through the grating equation

$$a\left(n_2 \sin\theta_m - n_1 \sin\theta\right) = m\lambda_0 \ , \tag{3.33}$$

where a is the grating pitch, n_1 and n_2 are the RIs of the first and second medium, respectively, and λ_0 is the vacuum wavelength. The geometry used to derive the grating equation is shown in Fig. 3.13. The diffraction patterns of 2D gratings can be obtained through a superposition of two 1D gratings. Eq. 3.33 also facilitates the distinction between two kinds of diffraction orders. Diffraction orders with an index m that yield $|\sin\theta_m| < 1$ are propagating orders representing EM waves that are reflected or transmitted by the grating. Diffraction orders that lead to $|\sin\theta_m| \geq 1$ are evanescent orders. These have a complex $\vec{k}$-component perpendicular to the grating which indicates that the intensity of the corresponding EM waves decays exponentially with the distance from the grating and cannot be detected at distances larger than a few wavelengths [143].

For a given configuration of n_1, n_2 and a fixed incident angle, the position and total number of all non-evanescent diffraction orders depend only on the grating pitch a and not on any other property of the grating. Nevertheless, for the efficient light extraction through a PhC grating, it is important that as many scintillation photons as possible are diffracted into an extracted order, i.e. a propagating diffraction order pointing towards the ambient medium. The amount of light that is diffracted into a certain order is given by its diffraction efficiency, which depends on the details of the grating geometry and the RIs of the grating materials. Through adjusting these parameters, the diffraction efficiencies can be manipulated which influences the overall transmission characteristic of the PhC. This can be used to tailor a PhC that yields increased light extraction for a given angular distribution of incident photons. The

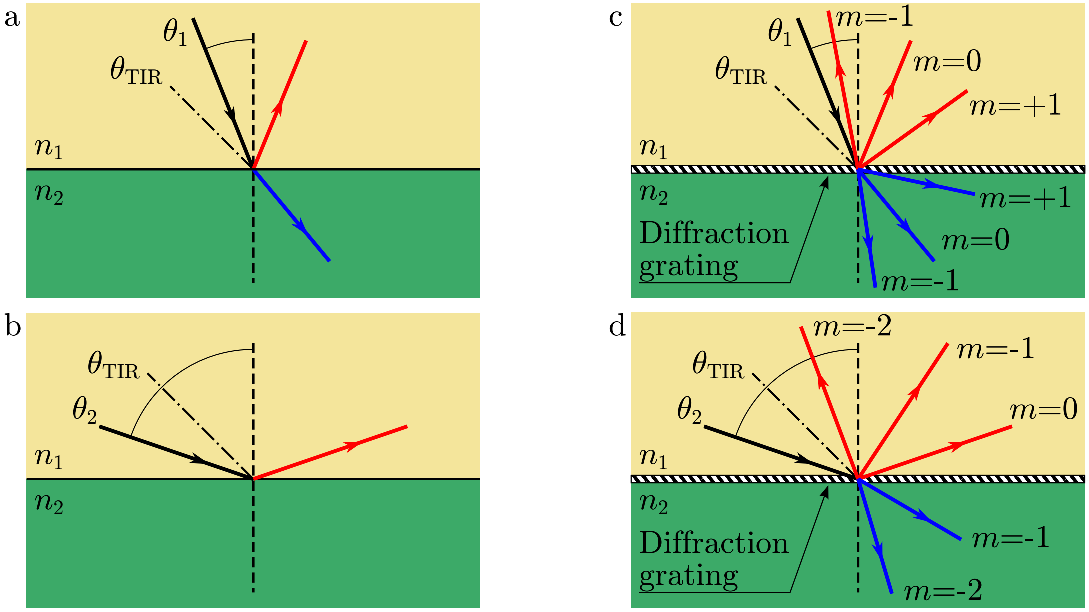

Figure 3.12: Illustration of light extraction through a diffraction grating. Without grating at the interface and for $\theta_1 < \theta_{\text{TIR}}$ (a), incident waves can be refracted (blue) and reflected (red), whereas for $\theta_2 > \theta_{\text{TIR}}$ only reflection is allowed. In the presence of a diffraction grating (c,d), there exist various diffraction orders in both directions. In the case of $\theta_2 > \theta_{\text{TIR}}$, these orders can lead to the extraction of light despite TIR (d).

calculation of diffraction efficiencies is usually done with numerical methods, as analytical solutions can only be found for very simple cases [143]. There is a variety of numerical methods, all of which are based on the Maxwell equations and solve for the distribution of the scattered EM field in certain spatial directions, i.e. diffraction orders. An overview of these methods is given in Ref. [143].

Once the diffraction efficiencies for a given grating are known, the obtained information is two-fold: i) the overall reflection and transmission coefficient of the PhC grating can be calculated through summing over all efficiencies; ii) the new wave vector $\vec{k}'$ of the photon after the diffraction process is given by the angles of the order into which the photon is diffracted. Another important aspect is the spectral behavior of PhC gratings. The grating equation indicates that the positions and efficiencies of the diffraction directly depend on the wavelength of the incident light. Since scintillator crystals have emission spectra with a width of a few hundreds of nanometers, this wavelength-dependent aspect cannot be neglected and must be taken into account when studying the effects of PhCs.

3.2.4 Correlation between Photonic Bands and Diffraction

The diffracting effect of PhC gratings can be interpreted through the coupling of EM waves to certain PhC modes. For this, consider a plane EM wave of vacuum wave length λ_0 propagating inside of a substrate medium (n_1) with wave vector $\vec{k}_1$ towards the interface with the ambient medium ($n_2 < n_1$) as depicted in Fig. 3.14. Inside of the substrate, $\vec{k}_1$ has the length $|\vec{k}_1| = n_1 k_0$ with k_0 being the vacuum wave vector length $k_0 = 2\pi/\lambda_0$. The absolute

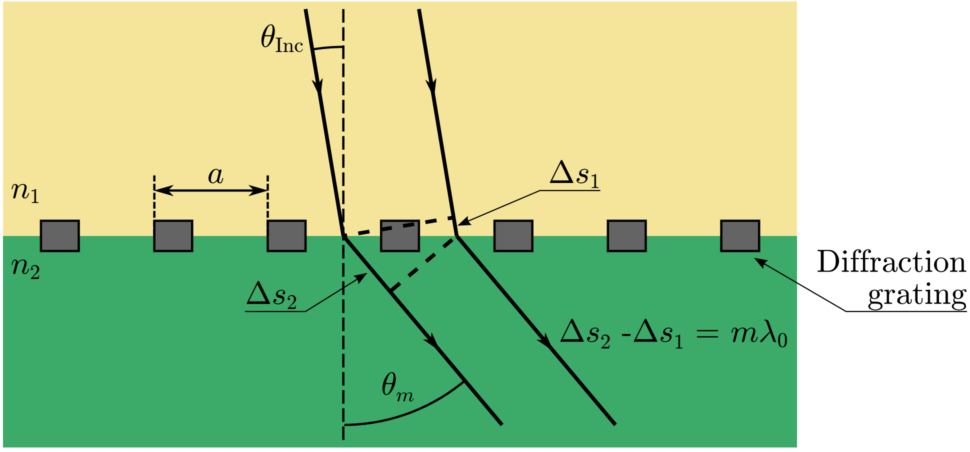

Figure 3.13: Diffraction of light from a 1D grating at the interface between medium 1 (n_1) and medium 2 ($n_2 < n_1$). Diffraction orders occur at angles θ_m, for which the path difference $\Delta s_2 - \Delta s_1$ is an integer multiple of the wavelength λ_0. This leads to the correlation from Eq. 3.33.

value of the in-plane component $\vec{k}_{xy}$ (see Fig. 3.14) is given through $|\vec{k}_{xy}| = n_1 k_0 \sin\theta_1$. At a plain interface, this component is conserved [104],

$$n_1 k_0 \sin\theta_1 = n_2 k_0 \sin\theta_2 \ , \tag{3.34}$$

which is equivalent to Snell's law. Hence, only waves that fulfill

$$\left|\vec{k}_{xy}\right| < \frac{n_2}{n_1} k_0 \tag{3.35}$$

can be extracted into the ambient medium which results in the effect of TIR. In the presence of a PhC grating at the material interface, an incident EM wave couples to a Bloch mode of the PhC. Due to the periodicity of the grating, all PhC modes identified through the in-plane wave vector $\vec{k}_m = \vec{k}_{xy} + m\vec{G}$ are degenerate, where m indicates the index of the mode and $\vec{G}$ is a reciprocal lattice vector. Hence, EM waves that would normally be trapped inside the substrate medium can couple to a degenerate Bloch mode that has a wave vector $\vec{k}_m$ fulfilling the extraction condition from Eq. 3.35 and radiate into the ambient medium. This coupling of modes through addition of a reciprocal lattice vector can be illustrated through the Ewald construction[1] depicted in Fig. 3.15.

---

[1] Note that the Ewald construction in this context differs from the known construction for x-ray diffraction, as the conservation of energy can be fulfilled through the third component of $\vec{k}$.

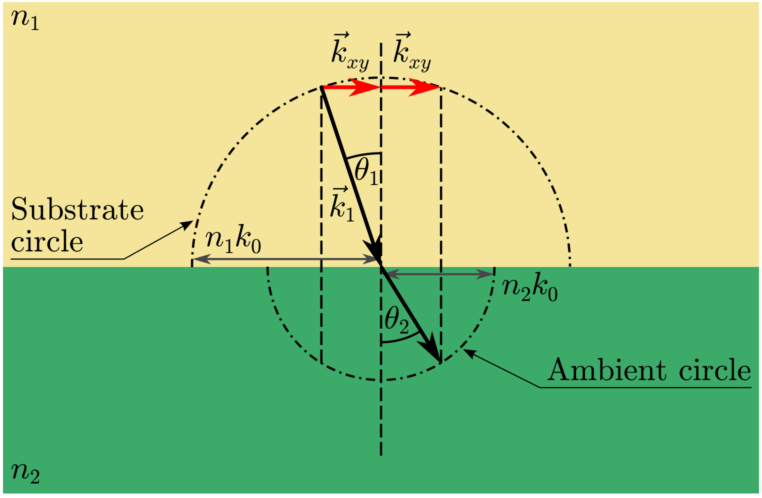

Figure 3.14: Illustration of the refraction at a material interface using $\vec{k}$-vectors. The radius of the substrate circle is $|\vec{k}_1| = n_1 k_0$, the ambient circle has a radius of $n_2 k_0$. The conservation of $|\vec{k}_{xy}|$ yields Snell's law and the effect of TIR. Adapted from [144].

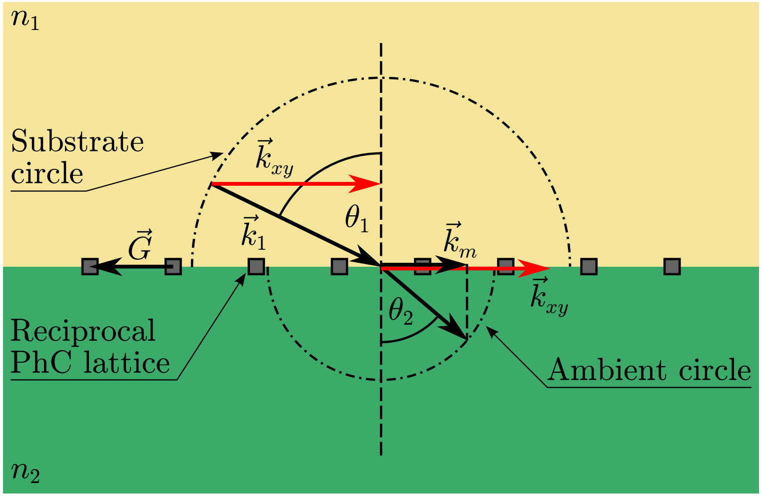

Figure 3.15: Illustration of the light extraction through PhCs through coupling of Bloch modes. The EM wave is incident from the substrate medium (n_1) on the material interface to the ambient medium ($n_2 < n_1$) with an angle $\theta_1 > \theta_{\mathrm{TIR}}$. Since $|\vec{k}_{xy}|$ does not fulfill the extraction condition from Eq. 3.35, the wave would normally be trapped inside the substrate. In the presence of the PhC grating, the wave can couple to another PhC mode identified through $\vec{k}_m = \vec{k}_{xy} + \vec{G}$. If this mode lies within the ambient circle, the EM wave can be extracted into the ambient medium.

Chapter 4

Materials and Methods

This chapter introduces the simulation techniques utilized to study the impact of LCs and PhCs on the light yield and timing resolution of a state-of-the-art PET detector configuration. Furthermore, the methods used to fabricate LC and PhC samples are described and the optical setup serving for the validation of their optical characteristics is presented. Finally, the experiments involving LSO scintillators are described, which allowed measuring the impact of LCs on the light output and timing.

4.1 Simulations

4.1.1 Optical Monte Carlo Simulations

The MC simulations of the scintillation photon propagation inside a PET detector were carried out with the ray tracing software Zemax (Radiant Zemax, Redmond, WA, USA). The software applies the laws of geometric optics to trace light rays through various dielectric materials. To adapt the ray tracing tool to the requirements of simulating a scintillator-based detector configuration, some additional mechanisms were implemented in this work. These extensions are described in the following.

4.1.1.1 Absorption

The absorption of photons must be distinguished between bulk effects and the absorption through surface coatings or thin layers. The bulk absorption through lossy dielectrics can be expressed through the imaginary part n'' of the complex RI or through the absorption length l_{Abs}. In Zemax, all traced rays start with a certain initial intensity, which decreases continuously if the ray propagates through a lossy medium. In this work, the trajectories of individual photons were calculated, which were considered to have the binary intensity values of 0 or 1. Hence, bulk absorption was modeled using a binary method based on l_{Abs}. In this approach, the length l of the photon path in a certain medium was used in conjunction with

l_{Abs} to calculate the absorption probability P_{Abs} through

$$P_{\mathrm{Abs}} = 1 - \exp\left(-\frac{l}{l_{\mathrm{Abs}}}\right) . \tag{4.1}$$

A random number was utilized to decide whether the photon is absorbed within the medium and terminated or whether the tracing continues.

As this absorption mechanism is not a built-in function of Zemax, it was implemented through a dynamic link library (DLL) interface of the software that allows the application of user-defined interaction mechanisms. The source code of the binary absorption model, which was written in the programming language C, was provided by Dr. D. Henseler (Siemens Healthcare, Forchheim, Germany) and has been validated in experiments [22].

Scintillation photons can also be absorbed by thin surface layers, for example by imperfect reflective wrappings. Zemax does not provide a setting that allows a binary absorption-decision for thin layers and coatings. Therefore, two different approaches have been used to achieve this mechanism. To model imperfect reflective wrappings, a custom written DLL was implemented, that makes a MC decision based on a random number and the user-input data for reflection, transmission and absorption coefficients. These coefficients were assumed to be independent of the incident angle, which is a common simplification [34]. In specific cases, the application of this DLL was not feasible due to limitations of the Zemax geometry interface. For this purpose, a second approach which was based on a simple reflective coating on the surface of a bulk-absorbing material was used. The coating was defined through a look-up table (LUT) listing the reflection and transmission coefficients as a function of the incident angle and polarization. In this list, the coating absorption was set to 0 to maintain the binary character of the interaction.

4.1.1.2 Rough Surfaces

Although Zemax provides different scattering models for surfaces, e.g. Gaussian- or Lambertian scattering, these have no influence on the transmission behavior of the interface. This is a poor approximation of the behavior of rough surfaces, as these can have transmission properties that differ substantially from plain interfaces. To overcome this limitation, a custom implementation of a microfacet surface model as described in Ref. [145] was written in the programming language C and implemented into Zemax as a DLL.

In this approach, the material interface is considered to consist of microscopic refractive facets that are tilted by an angle α with respect to the normal of the macroscopic interface (see Fig. 4.1). The roughness of the surface is described through σ_α, which is the variance of the Gaussian distribution of tilt angles α. For each photon incident on the interface, random numbers are used to generate a microfacet according to the σ_α-distribution. Then, the reflection and transmission coefficients are calculated with the Fresnel Eqs. 2.25-2.28. Based on these coefficients and another random number, a MC decision between reflection and transmission is made and the new wave vector of the scattered photon is calculated using Snell's law. Finally, this data is returned to the ray tracing algorithm. The transmission coefficients for different σ_α values calculated with this model are depicted in Fig. 4.2.

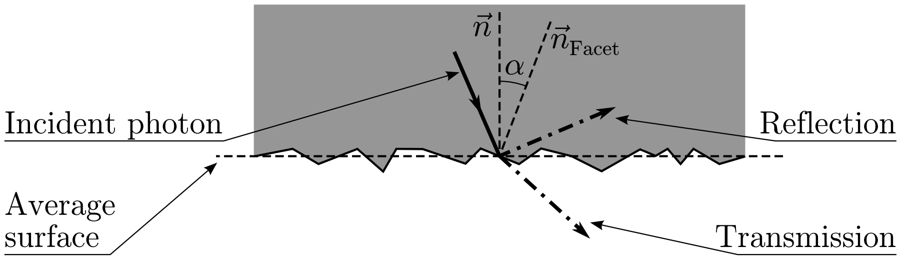

Figure 4.1: Microfacet model of a rough material interface. The facet normals $\vec{n}_{\text{Facet}}$ are tilted by an angle α with respect to the average surface normal $\vec{n}$. The reflection and transmission coefficients are calculated based on the statistically distributed microfacet.

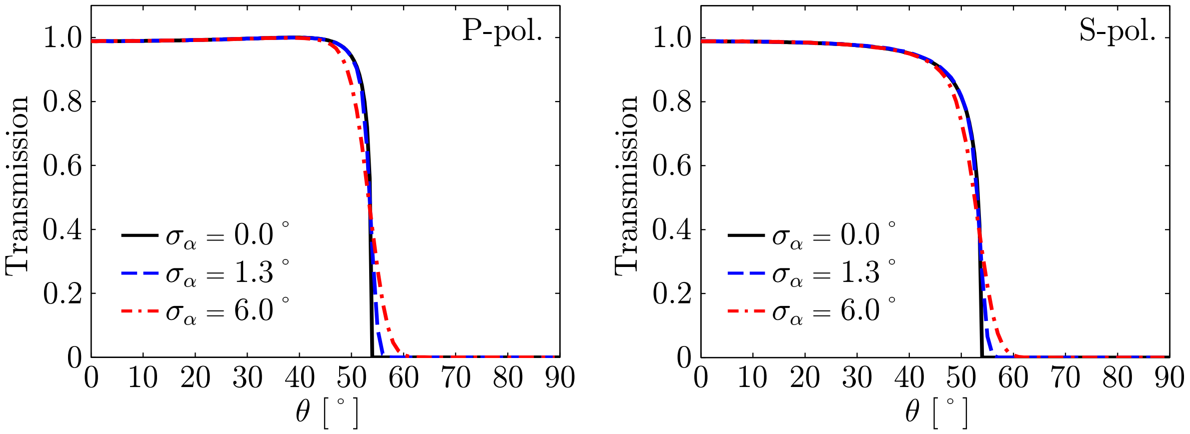

Figure 4.2: Transmission coefficient of an interface between $n_1 = 1.82$ and $n_2 = 1.47$ derived from the microfacet normal for three different roughness values σ_α. A value of $\sigma_\alpha = 0.0°$ corresponds to a plain surface with the transmission calculated through Fresnel equations. The depicted roughness values lead to a modest smoothing of the transition around the TIR cut off.

There are more complex strategies to simulate the scattering behavior of rough surfaces, e.g. the unified model which provides a weighted combination of Lambertian, purely specular and microfacet surface interactions [145]. Another work combined these models with LUTs from surface measurements [34]. However, it was shown in Ref. [22] that also simplified scattering models can suffice to model the photon propagation in PET detectors reliably.

4.1.1.3 Diffracting Interfaces

Zemax offers only limited support of diffractive objects. To study the impact of PhC slabs on the light propagation in a PET detector, another custom extension on DLL-basis was required. As this involved the simulation of the PhC behavior in a dedicated environment, this implementation is detailed in Sections 4.1.2 and 4.1.3.

4.1.1.4 Scintillation Locations

The interaction of 511 keV gamma photons with the scintillator material was calculated prior to the optical simulations using Geant4 [146] (Data was provided by Dr. J. Breuer, Siemens Healthcare, Forchheim, Germany). This algorithm computes the deposition of energy inside the scintillators through photoelectric absorption and Compton scattering. For this work, 511 keV gamma photons from a monoenergetic source were simulated, which were distributed uniformly over the entrance faces of the scintillator crystals and entered the pixels perpendicularly. The results of these calculations were used to create a list which provides the information about the locations and amounts of energy deposition. At these positions, point sources were placed in the ray tracing algorithm which isotropically emitted randomly polarized photons.

4.1.1.5 Post-Processing

The results from the optical MC simulations were post-processed using Matlab (The Mathworks, Natick, MA, USA) to gain insight into the angular distributions within the scintillator crystal and the propagation times of detected photons. Both parameters were mandatory prerequisites for the studies of PhCs and LCs. Post-processing was also used to generate photon look-up tables, which are required for the timing simulations (see Sec. 4.1.5).

4.1.2 Photonic Crystal Simulations

The diffraction of light through PhCs cannot be calculated by the ray tracing used for the optical MC simulations. To evaluate the impact of PhCs on the light propagation, a Maxwell-solver is required that calculates the diffraction by the PhC. For this purpose this work uses GD-Calc software (KJ Innovation, Santa Clara, CA, USA) which is based on the rigorous coupled wave analysis [147]. The following sections are mainly based on Ref. [148].

4.1.2.1 Representation of Photonic Crystals in GD-Calc

In GD-Calc, a PhC slab is represented through a layer (called stratum) positioned between the superstrate from which light is incident (with RI n_{Sup}) and the substrate (n_{Sub}) as depicted in Fig. 4.3a. Within the PhC stratum, the grating geometry is modeled through cuboids, all of which have a constant RI. If the PhC contains round features, these have to be approximated in a staircase manner as depicted in Fig. 4.3b,c. A more complex geometry in which the PhC structures also vary with the z-position, such as conical-shaped cavities, requires the use of several layers. However, this work only considers PhC structures that do not depend on the z-position like cylinders. GD-Calc is only applicable to structures that are periodic within the x-y-plane and every grating is defined through a set of parameters as illustrated in Fig. 4.3 including

- primitive lattice vectors ($\vec{a}_1$, $\vec{a}_2$)
- lattice pitch $a = |\vec{a}_1| = |\vec{a}_2|$

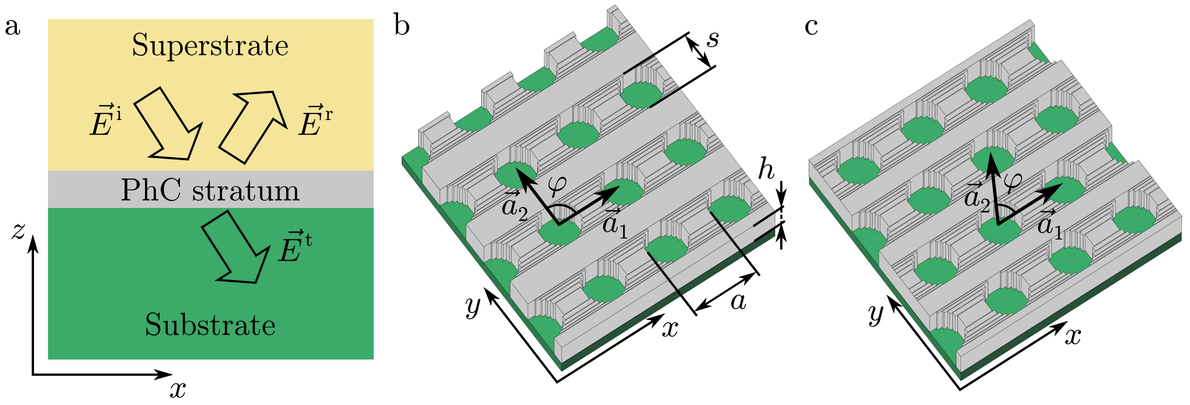

Figure 4.3: a) Drawing of the simulated domain in GD-Calc. The arrows illustrate the directions of the EM plain waves corresponding to the electric fields $\vec{E}$. The superscripts denote **i**ncident, **r**eflected, and **t**ransmitted waves. Perspective view of the cuboid representation of an orthogonal (b) and a hexagonal (c) PhC grating within GD-Calc. Note that in (b) and (c), the number of cuboids approximating the rounded edges has been reduced and the filling material of the cavities as well as the superstrate are not shown for illustration purposes.

- cavity size s
- grating height h
- grating bulk RI n_{Bulk}
- cavity RI n_{Cav}

The grating symmetry is defined by the angle φ between $\vec{a}_1$ and $\vec{a}_2$. A value of $\varphi = 90°$ yields an orthogonal grating and $\varphi = 60°$ corresponds to a hexagonal grating.

4.1.2.2 Expansion of Electromagnetic Field and Permittivity

The electric field in a configuration as depicted in Fig. 4.3 can be expressed through a sum of the incident field $\vec{E}^{\mathrm{i}}$ in the superstrate, the reflected field $\vec{E}^{\mathrm{r}}$ in the superstrate, and the transmitted field $\vec{E}^{\mathrm{t}}$ in the substrate,

$$\vec{E} = \vec{E}^{\mathrm{i}} + \vec{E}^{\mathrm{r}} + \vec{E}^{\mathrm{t}} \ . \tag{4.2}$$

In the following, the superscripts "i", "r", and "t" always connote quantities corresponding to incidence, reflection, and transmission, respectively. The incident field is given through a plane wave

$$\vec{E}^{\mathrm{i}}(\vec{r}) = \vec{E}^{\mathrm{i}}_0 \exp(\mathrm{i}\, \vec{k}^{\mathrm{i}} \cdot \vec{r}) \ , \tag{4.3}$$

with $\vec{E}^{\mathrm{i}}_0$ being a constant vector and $\vec{k}^{\mathrm{i}}$ being the wave vector of the incident field. As shown in Sec. 3.2.2, the x-y-component of the total electric field is a periodic function in the presence of a PhC slab. Hence, $\vec{E}$ can be represented through a Fourier expansion in x and y,

$$\vec{E}(\vec{r}) = \sum_{m_1,m_2} \mathcal{F}_{2D}\vec{E}(\vec{r}, m_1, m_2) \exp\left(\mathrm{i}\, \vec{k}_{xy}(m_1, m_2) \cdot \vec{r}_{xy}\right) \ , \tag{4.4}$$

where the 2D Fourier harmonics (m_1, m_2) correspond to the 2D diffraction orders of the PhC grating, $\vec{k}_{xy}$ and $\vec{r}_{xy}$ are the x-y-plane projections of $\vec{k}$ and $\vec{r}$, and $\mathcal{F}_{2D}\vec{E}(\vec{r}, m_1, m_2)$ is the 2D Fourier coefficient given through

$$\mathcal{F}_{2D}\vec{E}(\vec{r}, m_1, m_2) = \vec{E}_0(m_1, m_2)\ \exp\left(\mathrm{i}\,\vec{k}(m_1, m_2)\cdot\vec{r}\right)\ . \tag{4.5}$$

Generally, the diffraction orders m_1 and m_2 in the series of Eq. 4.4 range from $-\infty$ to ∞. For numerical computations, they must be limited to a finite number. In analogy to $\vec{E}$, the total magnetic field $\vec{H}$ can be expressed through

$$\vec{H}(\vec{r}) = \sum_{m_1, m_2} \mathcal{F}_{2D}\vec{H}(\vec{r}, m_1, m_2)\ \exp\left(\mathrm{i}\,\vec{k}_{xy}(m_1, m_2)\cdot\vec{r}_{xy}\right)\ . \tag{4.6}$$

Since the PhC structure in GD-Calc is modeled through a stack of layers that consist of cuboids (in our case a single layer), the permittivity within a stratum does not depend on z,

$$\varepsilon(\vec{r}) = \varepsilon(\vec{r}_{xy})\,. \tag{4.7}$$

As for the electric and magnetic fields, the periodicity of the PhC allows representing the permittivity within the grating through a Fourier series,

$$\varepsilon(\vec{r}_{xy}) = \sum_{l_1, l_2} \mathcal{F}_{2D}\varepsilon(l_1, l_2)\exp\left(\mathrm{i}\,(l_1\vec{b}_1 + l_2\vec{b}_2)\cdot\vec{r}_{xy}\right)\ , \tag{4.8}$$

using the Fourier order indices l_1 and l_2 as well as the primitive reciprocal lattice vectors $\vec{b}_1$ and $\vec{b}_2$. The in-plane wave vectors of the diffraction orders are correlated to the projection of the incident wave vector $\vec{k}^{\mathrm{i}}_{xy}$ through

$$\vec{k}_{xy}(m_1, m_2) = \vec{k}^{\mathrm{i}}_{xy} + m_1\vec{b}_1 + m_2\vec{b}_2\ , \tag{4.9}$$

Based on Eq. 4.9, the third component $k_z(m_1, m_2)$ can be derived through the correlations between the wave vector lengths,

$$|\vec{k}^{\mathrm{i}}| = |\vec{k}^{\mathrm{r}}|\ , \tag{4.10}$$

$$|\vec{k}^{\mathrm{i}}| = \frac{n_{\mathrm{Sup}}}{n_{\mathrm{Sub}}}|\vec{k}^{\mathrm{t}}|\ , \tag{4.11}$$

where the first equation applies to reflected orders and the second applies to transmitted orders.

4.1.2.3 Calculation of Scattering Matrices

The propagation of the EM wave in the presence of the PhC slab is calculated by GD-Calc using scattering matrices (S-matrices), that represent a linear mapping function correlating the amplitudes and phases of an EM wave incident on one side of a stratum and outgoing from the opposite side. If the grating consists of more than one stratum, the individual S-matrices are stacked to obtain the total S-matrix.

The S-matrix of a stratum is derived from the macroscopic Maxwell Eqs. 3.10-3.13 using the series representations for $\vec{E}$, $\vec{H}$, and ε given in Eqs. 4.4, 4.6 and 4.8. The number of diffraction orders retained in the Fourier expansions (N_{Orders}) have a significant impact on the accuracy and computation time of the algorithm. On the one hand, the stair-case approximation of the geometry caused by the block-wise partitioning requires sufficiently large values for N_{Orders} to avoid spikes of the EM fields at the block corners. On the other hand, the calculation time scales approximately with N^3_{Orders}. Thus, an initial convergence test was performed to evaluate a value for N_{Orders} that balances accuracy and computation time.

4.1.2.4 Correlation between Incident and Diffracted Fields

Consider the incidence of a plane EM wave with arbitrary polarization vector $\vec{q}$ on the PhC slab. As introduced in Sec. 2.5.1, any polarization can be represented in the base $(\vec{s}, \vec{p})$ of the linear S- and P-polarization states with complex-valued coefficients A and B,

$$\vec{q} = A\,\vec{s} + B\,\vec{p}\,. \tag{4.12}$$

The electric field of the incident wave is then given through

$$\vec{E}^{\mathrm{i}}_{A,B}(\vec{r}) = E^{\mathrm{i}}_0\,(A\,\vec{s} + B\,\vec{p})\,\exp\left(\mathrm{i}\,\vec{k}^{\mathrm{i}}\cdot\vec{r}\right)\ , \tag{4.13}$$

wherein E^{i}_0 is a constant. For each diffraction order (m_1, m_2) retained in the Fourier series, the GD-Calc algorithm yields two S-matrices, one for reflection ($\boldsymbol{R}(m_1, m_2)$) and one for transmission ($\boldsymbol{T}(m_1, m_2)$). These are 2×2 matrices with complex-valued entries,

$$\boldsymbol{R}(m_1, m_2) = \begin{pmatrix} R_{\mathrm{SS}}(m_1, m_2) & R_{\mathrm{SP}}(m_1, m_2) \\ R_{\mathrm{PS}}(m_1, m_2) & R_{\mathrm{PP}}(m_1, m_2) \end{pmatrix}\ , \tag{4.14}$$

$$\boldsymbol{T}(m_1, m_2) = \begin{pmatrix} T_{\mathrm{SS}}(m_1, m_2) & T_{\mathrm{SP}}(m_1, m_2) \\ T_{\mathrm{PS}}(m_1, m_2) & T_{\mathrm{PP}}(m_1, m_2) \end{pmatrix}\ . \tag{4.15}$$

$\boldsymbol{R}$ and $\boldsymbol{T}$ correlate the incident and diffracted electric fields through linear transformations,

$$\begin{pmatrix} \vec{E}^{\mathrm{r}}_{\mathrm{S}}(\vec{r}_1, m_1, m_2) \\ \vec{E}^{\mathrm{r}}_{\mathrm{P}}(\vec{r}_1, m_1, m_2) \end{pmatrix} = \boldsymbol{R}(m_1, m_2)\cdot \begin{pmatrix} \vec{E}^{\mathrm{i}}_{\mathrm{S}}(\vec{r}_1) \\ \vec{E}^{\mathrm{i}}_{\mathrm{P}}(\vec{r}_1) \end{pmatrix}\ , \tag{4.16}$$

$$\begin{pmatrix} \vec{E}^{\mathrm{t}}_{\mathrm{S}}(\vec{r}_2, m_1, m_2) \\ \vec{E}^{\mathrm{t}}_{\mathrm{P}}(\vec{r}_2, m_1, m_2) \end{pmatrix} = \boldsymbol{T}(m_1, m_2)\cdot \begin{pmatrix} \vec{E}^{\mathrm{i}}_{\mathrm{S}}(\vec{r}_1) \\ \vec{E}^{\mathrm{i}}_{\mathrm{P}}(\vec{r}_1) \end{pmatrix}\ . \tag{4.17}$$

Here, the subscripts S and P connote the projections of the electric field onto the $\vec{s}$ and $\vec{p}$ polarization states. For the transformations through $\boldsymbol{R}$ and $\boldsymbol{T}$, the electric fields are evaluated at points $\vec{r}_1 = (x_1, y_1, z_1)$ and $\vec{r}_2 = (x_2, y_2, z_2)$, which have identical in-plane coordinates,

$$x_1 = x_2\ , \tag{4.18}$$

$$y_1 = y_2\ . \tag{4.19}$$

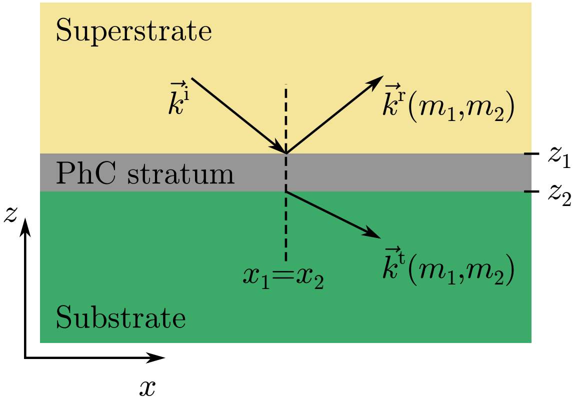

Figure 4.4: Illustration of wave vectors of incident, reflected, and transmitted field for a GD-Calc calculation showing the coordinates used for the transformations in Eqs. 4.16 and 4.17.

The vertical coordinates z_1 and z_2 indicate the superstrate- and substrate-oriented boundaries of the PhC slab (see Fig. 4.4), respectively.

The power of the incident and diffracted EM waves are proportional to the square of the electric field amplitude. Hence, Eqs. 4.16 and 4.17 can be used to calculate the fraction of incident power that has been diffracted into a certain order (m_1, m_2), i.e. the diffraction efficiency $D(m_1, m_2)$. For the polarization state $\vec{q}$ defined through (A, B), the efficiencies of the reflected and transmitted orders are given through

$$D^{\mathrm{r}}_{A,B}(m_1, m_2) = -\frac{|A\,R_{\mathrm{SS}} + B\,R_{\mathrm{SP}}|^2 + |A\,R_{\mathrm{PS}} + B\,R_{\mathrm{PP}}|^2}{|A|^2 + |B|^2} \cdot \frac{\mathrm{Re}\,(k^{\mathrm{r}}_z)}{\mathrm{Re}\,(k^{\mathrm{i}}_z)} \, , \tag{4.20}$$

$$D^{\mathrm{t}}_{A,B}(m_1, m_2) = -\frac{|A\,T_{\mathrm{SS}} + B\,T_{\mathrm{SP}}|^2 + |A\,T_{\mathrm{PS}} + B\,T_{\mathrm{PP}}|^2}{|A|^2 + |B|^2} \cdot \frac{\mathrm{Re}\,(k^{\mathrm{t}}_z)}{\mathrm{Re}\,(k^{\mathrm{i}}_z)} \, , \tag{4.21}$$

wherein Re denotes the real part of a complex number and k_z are the z-components of the wave vectors which can be derived through Eqs. 4.10 and 4.11. Note that all matrix elements of $\boldsymbol{R}$ and $\boldsymbol{T}$ as well as k^{r}_z and k^{t}_z implicitly depend on the diffraction order (m_1, m_2), which has been omitted for brevity. These correlations indicate that only propagating orders have non-zero diffraction efficiences, since evanescent orders have purely imaginary k^{r}_z or k^{t}_z components. The overall reflection and transmission coefficients R and T of a PhC can be calculated by summing over all diffraction efficiencies,

$$R_{A,B} = \sum_{m_1,m_2} D^{\mathrm{r}}_{A,B}(m_1, m_2) \, , \tag{4.22}$$

$$T_{A,B} = \sum_{m_1,m_2} D^{\mathrm{t}}_{A,B}(m_1, m_2) \, . \tag{4.23}$$

4.1.3 Implementation of Photonic Crystal Simulations

For the implementation into the optical ray tracing algorithm, PhCs were translated into LUTs that contained bins of incident angles θ and ϕ (see Fig. 4.5). The elevation angle θ of light incident on the PhC slab was varied from 0° to 180°. Values $\theta > 90°$ correspond to light coming from the substrate side instead of the superstrate side. Due to the symmetry of the PhC in the x-y-plane, the azimuth angle ϕ ranged from 0° to 45° for orthogonal and from 0° to 30° for hexagonal PhC gratings. For each (θ, ϕ)-bin, the wave vector of the incident electric field was defined as

$$\vec{k}^{\mathrm{i}} = \frac{2\pi}{\lambda_0 \, n_{\mathrm{Sup}}} \begin{pmatrix} \sin\theta \ \cos\phi \\ \sin\theta \ \sin\phi \\ \cos\theta \end{pmatrix} , \tag{4.24}$$

with λ_0 being the vacuum wavelength of the EM wave. With this incident field, a GD-Calc simulation was invoked and the resulting $\boldsymbol{R}$ and $\boldsymbol{T}$ matrices in conjunction with the corresponding wave vectors of all non-evanescent orders were written into the LUT. To limit the LUT's file size, the propagating orders were sorted by their efficiency and only the first 25 were stored. The diffractive properties of PhCs depend on the wavelength of the incident photon. To facilitate a direct incorporation of this dependency, one LUT was calculated for each wavelength of the spectrum of interest.

The LUTs were incorporated into a custom DLL written in the programming language C. The PhC coating was implemented into the optical MC simulations through assigning the DLL to a material interface in Zemax. For each photon hitting this interface, the optical ray tracing tool passes the incident angles (θ, ϕ), polarization $\vec{q}$, and wavelength λ of the photon to the DLL. The DLL first determines the LUT corresponding to λ, selects the proper (θ, ϕ)-bin of LUT(λ), and utilizes the corresponding scattering matrix entries in conjunction with the polarization $\vec{q}$ of the incident photon to calculate the diffraction efficiencies according to Eqs. 4.20 and 4.21. Interpreting these diffraction efficiencies as MC probabilities, a

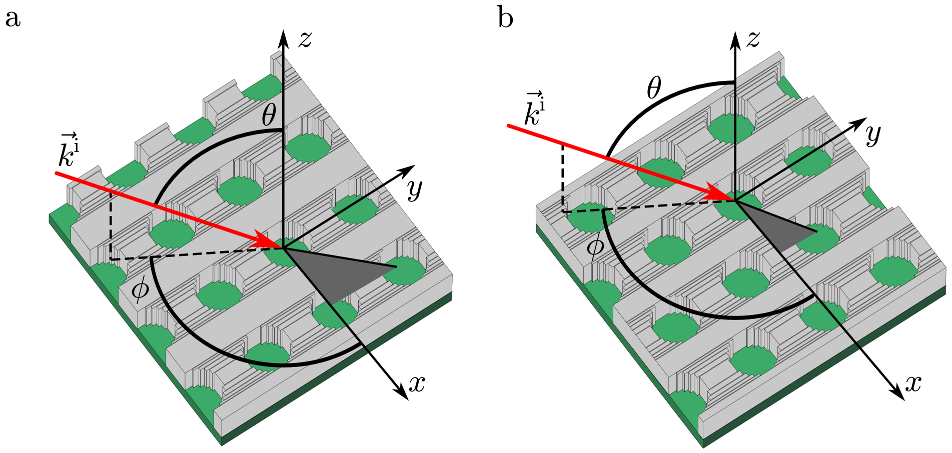

Figure 4.5: Definition of the incident angles (θ, ϕ) for a PhC with orthogonal (a) and hexagonal (b) symmetry. The gray triangular areas indicate the ϕ-range for the two types of gratings.

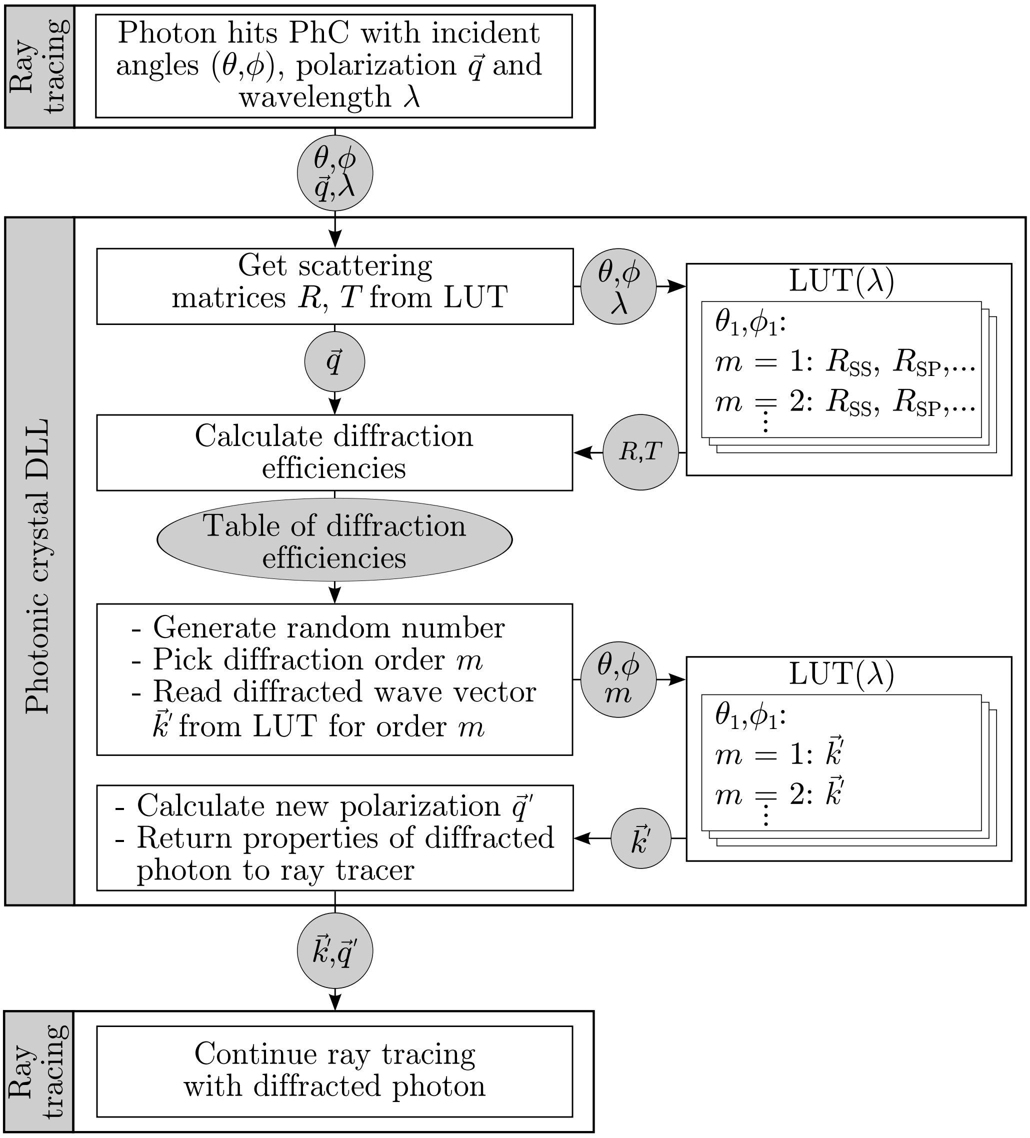

Figure 4.6: Illustration of the custom-written DLL for the implementation of PhCs into the optical MC simulations. Note that the diffraction order indices (m_1, m_2) are combined to the index m in this schematic.

random number is used to decide between reflection and transmission and to select a certain order. The wave vector $\vec{k}'$ contained in the LUT for the selected order implies a new base of polarization states $(\vec{s}', \vec{p}')$. This is utilized in conjunction with Eq. 4.16 or 4.17 to obtain the polarization $\vec{q}'$ of the diffracted wave. Finally, the photon is returned to the optical MC simulation with the diffracted wave vector $\vec{k}'$ and the new polarization state $\vec{q}'$. A summary of the DLL workflow is shown in Fig. 4.6.

4.1.4 Photonic Crystal Parameter Sweeps

The PhC parameters a, s, h, n_{Bulk}, n_{Cav} and the grating type (orthogonal or hexagonal) influence the transmission characteristic of the grating. To gain a general understanding of the significance of the individual PhC properties, initial parameter sweeps were conducted. These studies also served to obtain a set of PhC configurations for the fabrication of first samples with the goal to validate the simulations in optical experiments (see Sections. 4.2 and 4.3).

All PhC configurations were qualified through their extraction efficiency χ_{PhC}, which was calculated as the fraction of extracted photons over the number of incident photons:

$$\chi_{\text{PhC}}(i) = \frac{\int_0^{\pi/2} T_{\text{PhC}}(\theta)\, D(i,\theta)\, \mathrm{d}\theta}{\int_0^{\pi/2} D(i,\theta)\, \mathrm{d}\theta} \,. \tag{4.25}$$

Here, $T_{\text{PhC}}(\theta)$ is the transmission coefficient of the PhC at an incident elevation angle θ averaged over all azimuth angles ϕ calculated with GD-Calc. The angular distribution $D(i,\theta)$ derived from the optical simulations in Zemax indicates the number of photons incident with θ summed over all ϕ at the i-th incidence on the LSO exit face.

To find a PhC configuration that provides the most efficient light extraction from the scintillator crystals of a certain detector configuration, the transmission characteristic $T_{\text{PhC}}(\theta)$ as a function of the different PhC properties was analyzed through parameter sweeps. Afterwards, this data could be combined with the any angular distribution $D(i,\theta)$ to determine optimal PhC settings. This approach was chosen instead of an optimization algorithm, since it facilitated the flexible determination of favorable PhC parameters for different angular distributions without the need for new calculations.

4.1.5 Coincident Resolving Time Simulations

The data obtained from the optical simulations was utilized to predict the CRT of the detector. For this, another MC simulation introduced by Breuer et al. [67] was used. This method models the SiPMs and the amplifier electronics to calculate the resulting electrical signals, taking into account several SiPM properties provided by the vendor [29]. Among these are an afterpulsing probability of 40%, a cross talk probability of 27%, a dark count rate of $100{\cdot}10^3$ counts per second, and a single photon timing resolution of 230 ps. Next, a time stamp for the scintillation event is derived through analyzing the calculated electrical signal with computational models of an amplifier and a leading edge discriminator (LED). This procedure is repeated for $100{\cdot}10^3$ simulated gamma events and the resulting distribution of time stamps is fitted with a Gaussian function. The timing resolution is then defined as the FWHM of this fit. For $100{\cdot}10^3$ simulated gamma events, the statistical inaccuracy of the timing resolution was 0.5 ps. Finally, the LED threshold is optimized to yield the minimum possible timing resolution which is then multiplied by $\sqrt{2}$ to obtain the CRT which takes into account the detection of two gamma photons in coincidence by two identical detectors. The described simulation tool was provided by Dr. J. Breuer, Siemens Healthcare, Forchheim, Germany. Details about this method and an experimental validation are given in Ref. [67].

4.1.6 Reference PET Detector Setup

4.1.6.1 General Detector Parameters

The impact of LCs and PhCs on the light yield and timing resolution was examined for the PET detector setup depicted in Fig. 4.7. This configuration is similar to the detector implemented in the current generation of whole-body PET-MR hybrid systems (Biograph mMR, Siemens Healthcare, Erlangen, Germany) regarding several aspects, such as the scintillator material, size, and arrangement [51, 149]. This current commercial detector configuration is based on APDs as photosensors which were replaced by SiPMs in the presented model. The detector consisted of an array of 8×8 LSO crystals with a size of (4×4×20) mm^3 and an RI of $n_{\mathrm{LSO}} = 1.82$ [150]. The bulk scattering and absorption lengths were set to $l_{\mathrm{Scatt}} = 250$ mm and $l_{\mathrm{Abs}} = 600$ mm [22]. For the Geant4 simulations, the linear attenuation coefficient for 511 keV gamma photons was set to $\mu_{\mathrm{Att}} = 0.081\ \mathrm{mm}^{-1}$ [1].

The individual crystals were separated by 50 μm air gaps. Five sides of the scintillator array were surrounded by a specular reflector material having a reflection/transmission/absorption coefficient of 96%/3%/1% [22]. At the remaining side, the exit faces of the scintillator crystals were coupled to the photosensors via a 100 μm thick layer of optical glue ($n_{\mathrm{Glue}} = 1.47$ [22]). The photosensors were encapsulated with an epoxy window having a thickness of 350 μm and an RI of $n_{\mathrm{Epoxy}} = 1.59$ (Hamamatsu Photonics, Hamamatsu, Japan, private communication, September 28, 2013). The bottom of the detector configuration was an array of 8×8 SiPMs made of a Silicon substrate ($n_{\mathrm{Si}} = 5.09$ [151]). Each SiPM had a size of (3.9×3.9) mm^2 and was centered underneath an LSO crystal. They had a fill factor of $f_{\mathrm{Geo}} = 64\%$, which is similar to current state-of-the art SiPMs in prototype PET systems [19]. The microcell structure of the SiPM was modeled as quadratic active cells with a size of (40×40) $\mu\mathrm{m}^2$ and a cell pitch in both directions of 50 μm (see Fig. 4.8). The sensor was modeled with a wavelength-dependent PDE based on data provided by the vendor [29] (see Sec. 4.1.6.3).

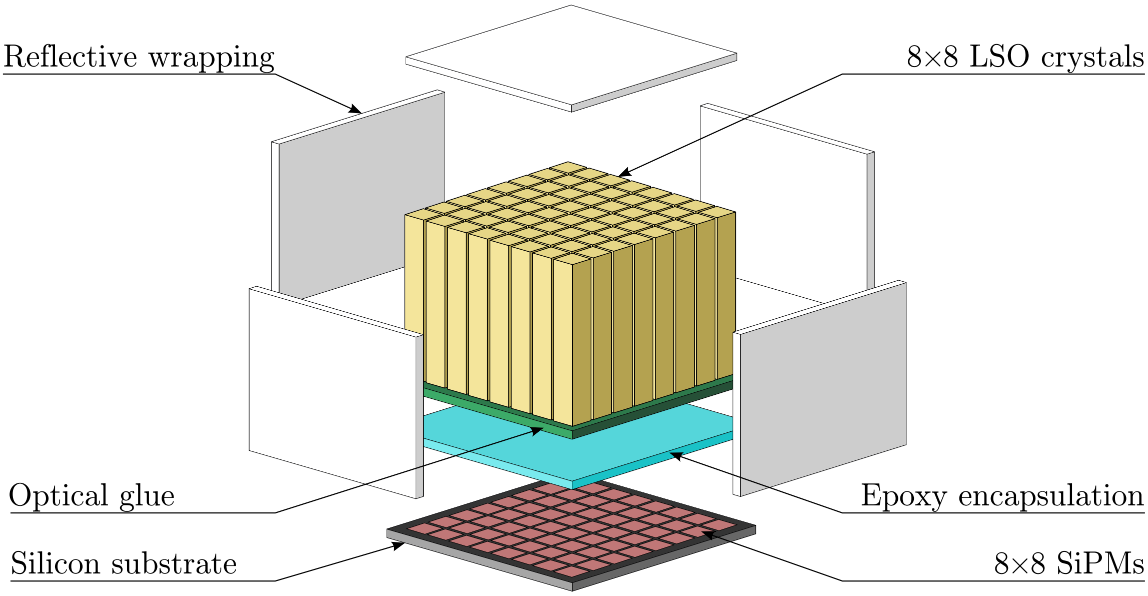

Figure 4.7: Detector setup used for the optical MC simulations.

Due to the lack of detailed information about the optical properties of the SiPM surface, two assumptions were made:

1. The dielectric antireflective coating of the SiPM active areas was made of a layer having an RI of $n_{\mathrm{ARC}} = 2.86$ and a thickness of 37 nm. These parameters were derived as the optimal single layer coating for $\lambda = 420$ nm using the formulas given in Ref. [104].

2. Based on the microscope image of a state-of-the art SiPM (MPPC-S11064-050P, Hamamatsu Photonics) shown in Fig. 4.8, the inactive area separating the active cells of the SiPM was modeled as 50% absorbing and 50% reflective using a Lambertian scattering distribution.

The MC simulations of this PET detector configuration used data from 4000 gamma events computed with Geant4. For each event, 1000 scintillation photons were generated in Zemax, leading to a total number of $4{\cdot}10^6$ traced photons. The statistical inaccuracy was estimated as the standard deviation of the results from 10 repeated simulation runs. Regarding the relative light yield Γ, i.e. the fraction of all simulated photons registered by the SiPM, an inaccuracy below 0.1% was obtained.

A configuration as described above is called a block detector, which is a common design for commercial PET systems [1]. There are various forms of detector layouts which differ in aspects such as the size of the array or the material which is used to fill the empty space between the crystals. In this case, a configuration was used in which the scintillators are separated only by air gaps. Since the angle of TIR for the transition from LSO to air is 33.3°, these gaps lead to a notable optical insulation between the pixels and light incident on the lateral scintillator walls with a shallow angle is funneled towards the exit face. Nevertheless, the absence of reflective material inside the array causes sharing of light between the crystals. This cross talk must be taken into account when deriving the originating scintillator pixel of the detected photons. Usually, an algorithm based on Anger logic is used for this purpose, which performs a centroid positioning through relating the intensities of the individual photosensors to the total amount of detected photons [1].

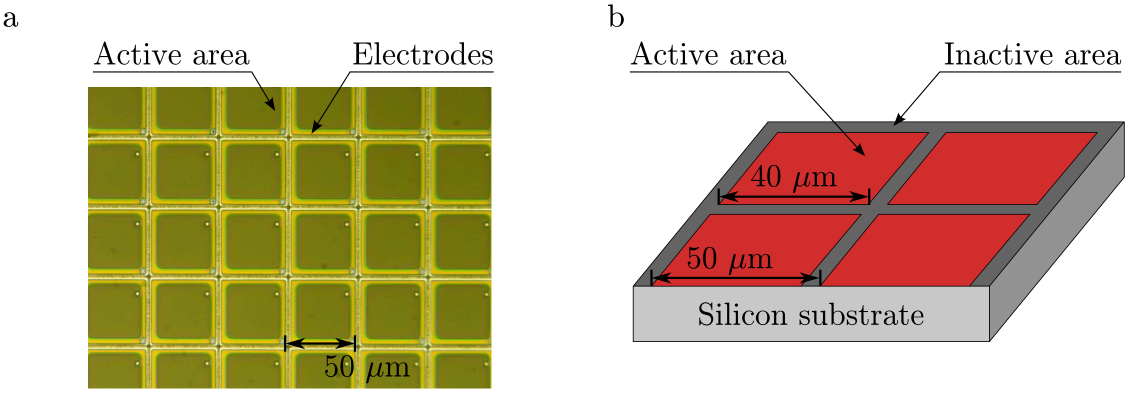

Figure 4.8: a) Microscope image of the SiPM serving as model for the optical simulations. b) Drawing of the simplified SiPM model used in the simulations consisting of quadratic active cells coated with an antireflective layer (not shown) on an absorbing silicon substrate.

4.1.6.2 Surface Roughness: Polished vs. Etched Configuration

To study the impact of the scintillator surface roughness on the effects caused by LCs and PhCs, two variations of the described detector configuration were examined:

1. **Polished**: This configuration represents scintillators with surfaces that were mechanically polished to achieve a very low surface roughness. The resulting crystals have highly smooth surfaces and appear like polished glass. The microfacet angle distribution is characterized through $\sigma_\alpha = 1.3°$.
2. **Etched**: This configuration models scintillators with surfaces that were chemically etched to reduce the roughness that results from the fabrication process. Etching results in rougher surfaces compared to mechanical polishing and is a procedure that is routinely used in the production of commercial PET systems as it is significantly less expensive and time consuming compared to mechanical treatments [152]. To an observer, these crystals appear translucent with an opacity that is notably more pronounced than in polished crystals. In this case, the roughness is characterized through $\sigma_\alpha = 6.0°$.

In both cases, the values for σ_α were taken from Ref. [34]. In the following, quantities related to the polished or etched configuration are identified through the subscripts "Pol" and "Etch", respectively.

4.1.6.3 Simulated Wavelengths

All optical MC simulations of PET detector modules were performed using the wavelength distribution of the LSO emission spectrum from Ref. [150]. This distribution was sampled from 380 nm to 600 nm in 20 nm intervals yielding 12 discrete wavelength values with weighted intensities (see Fig. 4.9a) for the isotropic light sources in the ray tracing tool. Since the RI of LSO exhibits only minor dispersion over the LSO emission spectrum [153], it was set to the constant value of $n_{\mathrm{LSO}} = 1.82$. Also, the scattering and absorption coefficients as well as the optical properties of the remaining detector components such as reflective wrapping, optical glue or epoxy window were assumed to be independent of the wavelength. This simplification has no significant impact on the simulations results of the optical simulations as demonstrated in Ref. [22]. For the LCs, coatings with measured spectral reflectivity were used for the computations. The wavelength-dependent functionality of the PhC implementation was already described in Sec. 4.1.3.

The PDE of SiPMs strongly depends on the wavelength of the incident light. In this work, the characteristics of the above mentioned commercial SiPM were used. Since the definition of the PDE contains the geometric fill factor f_{Geo} (see Eq. 2.19) and the optical model of the SiPMs consists of discrete active and inactive areas leading to $f_{\mathrm{Geo}} = 64\%$, the PDE values taken from Ref. [29] were corrected by a factor of 1/0.64 leading to the spectral sensitivity shown in Fig. 4.9b. For each photon being absorbed by the active SiPM areas, its wavelength was used in conjunction with the corresponding sensitivity to make a MC decision whether the photosensor registers or ignores the photon.

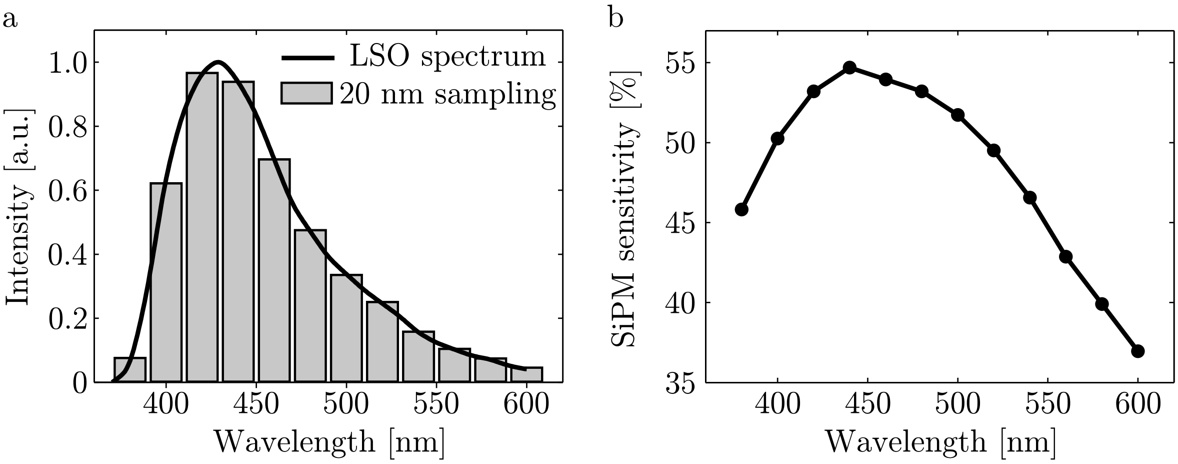

Figure 4.9: a) Normalized emission spectrum of the LSO crystal used for the optical calculations. The spectrum was derived through interpolating the data shown in Ref. [150] and sampled in 20 nm intervals. b) Spectral sensitivity of SiPMs used for the reference PET detector module based on Ref. [29].

4.2 Sample Fabrication

4.2.1 Light Concentrator

This section summarizes the workflow and processes involved in the preparation of the LC samples. Detailed descriptions of the applied micromechanical fabrication techniques can be found in Refs. [117, 154].

4.2.1.1 Fabrication Workflow

The process flow of the concentrator sample fabrication is illustrated in Fig. 4.10. The light concentrators were micromachined into silicon-on-insulator (SOI) substrates having a diameter of 150 mm. These wafers consisted of three layers: the handle layer made of silicon (Si), an insulation layer of silicon dioxide (SiO_2), and the Si device layer.

First, the substrates were prepared for the etching processes that produced the concentrator geometry. For this, the wafers were coated with a 100 nm layer of silicon nitride (Si_3N_4) on all sides using low pressure chemical vapor deposition (see step b in Fig. 4.10). Then, a 1.4 μm thick layer of photoresist was spin coated onto the device layer side (c) and structured with the concentrator geometry using ultraviolet (UV) lithography and subsequent wet development (d). This pattern was transferred into the Si_3N_4-layer through reactive ion etching (e). After removing the photoresist on the device layer (f), the Si_3N_4-film on the handle layer side was structured with large quadratic openings underneath the concentrator geometry using the same processes as before with a different lithography mask (g-i). Finally, the photoresist was removed in an O_2-plasma oven (j).

The total area of the concentrator was (10×10) mm^2 at the center of a (20×20) mm^2 chip that provided mechanical stability and safe handling of the device. The parameters A_{In} and

A_{Rec} of the concentrator samples were chosen to match the SiPM microcell geometry used in the simulated PET detector configuration. Thus, A_{In} was (50×50) μm^2 and A_{Rec} was (40×40) μm^2. The fabrication of concentrator samples with various heights H_{C} was tested with two different strategies, which are detailed in Sec. 4.2.1.3

After machining the concentrator geometry into the device layer (see step k in Fig. 4.10), the concentrator fields were opened by etching large cavities into the handle layer (l). For this purpose potassium hydroxide (KOH) etching was used (see Sec. 4.2.1.3 for details). To prevent the device layer from being etched, the substrates were inserted into a dedicated handler that only exposed one side of the wafer. After this opening step, the wafer was put into a aqueous solution of hydrofluoric (HF) acid (10% concentration). This process removed both the SiO_2 layer covering the concentrator and the Si_3N_4-films still remaining on the substrate surfaces from previous steps (m).

The available UV lithography in this work had a limited resolution allowing the fabrication of features with a minimum size of approximately 3 μm. Hence, an iterative process was utilized to reduce the width of the concentrator ridges (see steps m, n). The first step of this procedure was thermal oxidation of the Si bulk leading to the formation of approximately 1 μm SiO_2. In this process, one part of the resulting SiO_2 lies below the former Si surface, the rest extends beyond the original surface (see Fig. 4.11). The second step was wet chemical removal of the SiO_2 through HF etching. Since this process does not only reduce the ridge,

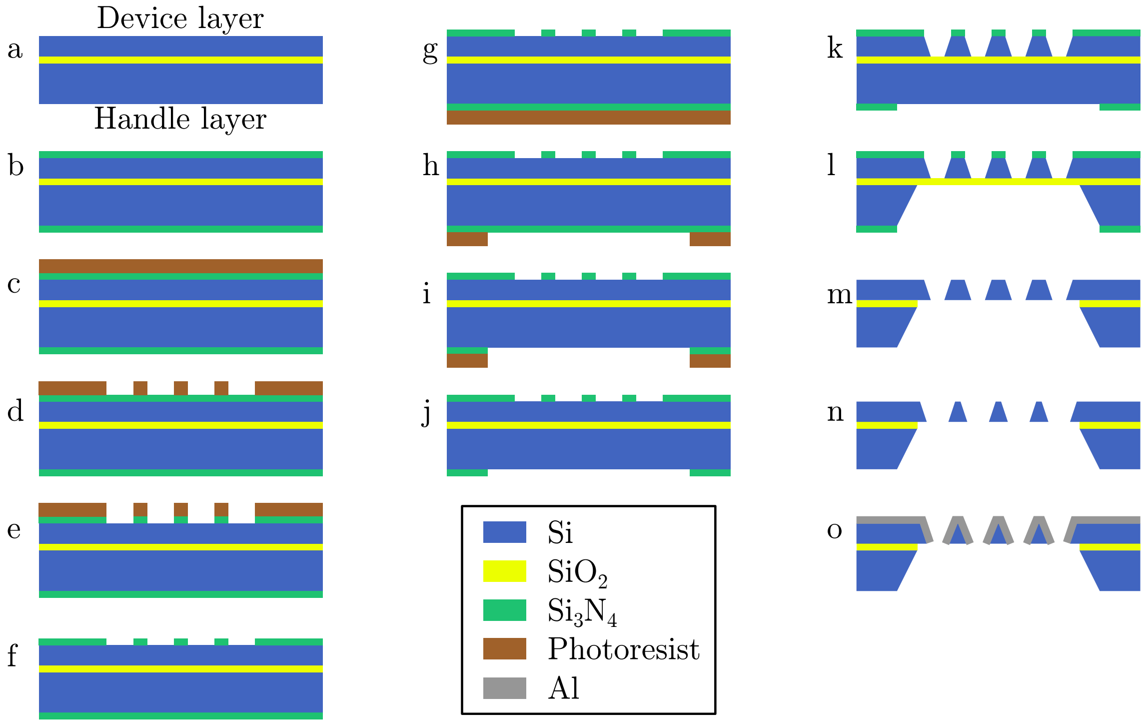

Figure 4.10: Process flow of the LC sample fabrication. The individual steps are explained in the text. Note that the geometric dimensions are strongly modified for illustrative purposes. For example, the actual LC samples had 200 cavities on the device layer side (10 mm length divided by 50 μm pitch) whereas here only 4 cavities are drawn.

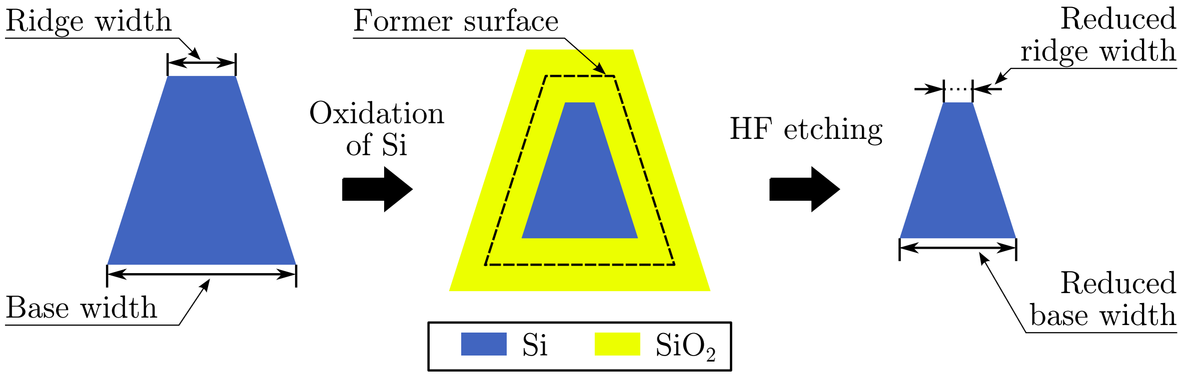

Figure 4.11: Illustration of the process used to reduce the concentrator ridge width. Note that this drawing ignores the rounding of corners which occurs due to the diffusion profile of the oxidation process.

but also the base width of the concentrator geometry, this two stage procedure was repeated several times until either the specified ridge or base width was achieved.

4.2.1.2 Reflective Coating and Dicing

There are both metallic and dielectric coatings that provide high reflectivity over a range of wavelengths such as the emission spectrum of LSO scintillators. The reflective properties of metallic coatings usually depend less on the polarization or angle of the incident light compared to dielectric films, but metals also involve more losses [104]. In this work, aluminum (Al) was used as reflective coating, as it provides high reflectivity over the all wavelengths of the LSO spectrum. A 100 nm thick layer was deposited on the LC samples using DC magnetron sputtering. To validate the reflective properties of the coating and to obtain proper values for the optical simulations, the complex-valued RI of the deposited Al layer was measured using an ellipsometry setup [155] (external service provided by M. Kaiser, Hochschule München, Germany). Finally, the wafers were cut into individual sample chips using a laser dicing system.

4.2.1.3 Etching of Concentrator Cavities

As explained above, two different strategies were tested to micromachine the LC geometry into the device layer of the SOI substrates: KOH etching and deep reactive ion etching (DRIE). This section provides a brief summary of these techniques.

KOH Etching Wet chemical etching of Si in an aqueous KOH solution is based on a chemical reaction between the hydroxide content and the Si of the substrate according to

$$\mathrm{Si} + 2\mathrm{H_2O} + 2\mathrm{OH^-} \rightarrow [\mathrm{SiO_2}(OH)_2]^{2-} + 2\mathrm{H_2}\,. \tag{4.26}$$

The etch rate of this process strongly depends on the plane of the Si crystal exposed to the KOH solution which leads to anisotropy of the etching [156]. The different planes of a crystal

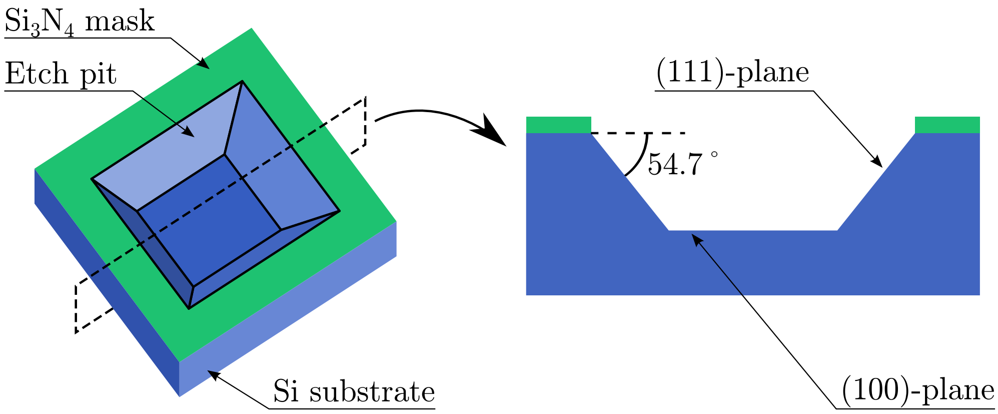

Figure 4.12: Perspective and cross section view of KOH etching in a Si crystal using a Si_3N_4 mask resulting in etch pits with sidewalls defined by the {111} crystal planes.

are identified trough Miller indices [71]. Si crystallizes in a diamond cubic lattice structure. If the (100)-plane of a Si crystal is exposed to a KOH solution, the etched cavities exhibit oblique sidewalls as illustrated in Fig. 4.12. These are defined by the {111}-planes, because the corresponding directions have the lowest etch rate. This allows the fabrication of cavities with highly smooth sidewalls and 90° corners. However, the resulting concentrator taper angle ζ_C cannot be varied, as it is defined as 90° - 54.7° = 35.3° by the crystal lattice.

Deep Reactive Ion Etching The technique of DRIE combines physical etching through the bombardment of the substrate with ions (anisotropic process) with plasma etching through a chemical reaction between a gas mixture and the substrate surface (isotropic process). By adjusting the concentrations of the individual gas components and the electrode bias voltage which determines the kinetic energy of the bombarding ions, cavities with tapered sidewalls can be fabricated [117]. In contrast to the KOH technique, this process allows to modify the angle of the cavity walls to a certain degree.

4.2.1.4 Encapsulation of Concentrator Samples

The LC samples resulting from the workflow depicted in Fig. 4.10 were suitable for the optical experiments serving for the validation of the transmission characteristics (see Sec. 4.3). However, they needed to be further processed in order to prepare them for LSO-based measurements of the light yield and timing. In this experiment, the samples are positioned between a PMT and a scintillator crystal and grease is used to provide optical coupling between the components (see Sec. 4.4). Therefore, the fragile LC structures must be mechanically stabilized and the cavities in the samples must be filled with a material having an RI similar to the used grease. This was achieved with the processes summarized in Fig. 4.13 using a highly-transparent epoxy (Epo-Tek 305, $n_{\mathrm{EpoTek}} = 1.48$ at $\lambda = 589$ nm, Epoxy Technology, Billerica, MA, USA) in conjunction with glass chips made of Borofloat ($n_{\mathrm{BF}} = 1.48$ at $\lambda = 420$ nm [157]) having a thickness of 700 μm. First, a thin layer of the epoxy was dispensed on a (20×20) mm^2 glass chip. Next, the completely processed LC sample was placed "face-down" on the chip. Through carefully moving the LC laterally, a thin homogeneous epoxy layer was achieved and large fractions of enclosed air bubbles could be removed. Further removal of enclosed air could be achieved through placing the glass/epoxy/LC stack in a vacuum desiccator. Afterwards, a second glass chip of size (10×10) mm^2 was inserted in to the large cavity at the backside of the LC sample. Through the epoxy that had penetrated the concentrator grid from the bottom, this second glass chip sealed the LC. The final step of the encapsulation process was curing the epoxy in an oven at 80° C for 60 minutes.

In the scintillator-based experiment, the light output and timing was also measured for another type of sample representing the reference of a plain SiPM. To this end, the encapsulation process explained above was repeated for LC samples from which the concentrator grid was mechanically removed leaving only a Si frame with (10×10) mm^2 opening (see Fig. 4.13f). For these samples, the second glass chip had a metal grid made of chromium (Cr) that mimicked the microcell structure of a plain SiPM (see Sec. 4.4 for details). For this, a glass substrate was coated with a 90 nm thick layer of Cr (DC magnetron sputtering) which was structured with quadratic openings of (40×40) μm^2 and a 50 μm pitch in order to match the fill factor f_{Geo} of the SiPM considered for the simulation studies. Cr was chosen as coating material as this provided partially absorbing and partially reflective properties similar to the assumptions about the SiPM inactive areas. The structuring of the Cr layer was done using UV lithography and wet-chemical processing with a commercial Cr etching solution (Chrome Etch 18, Micro Resist Technology, Berlin, Germany). Finally, the processed wafer was cut into (10×10) mm^2 chips using a dicing saw.

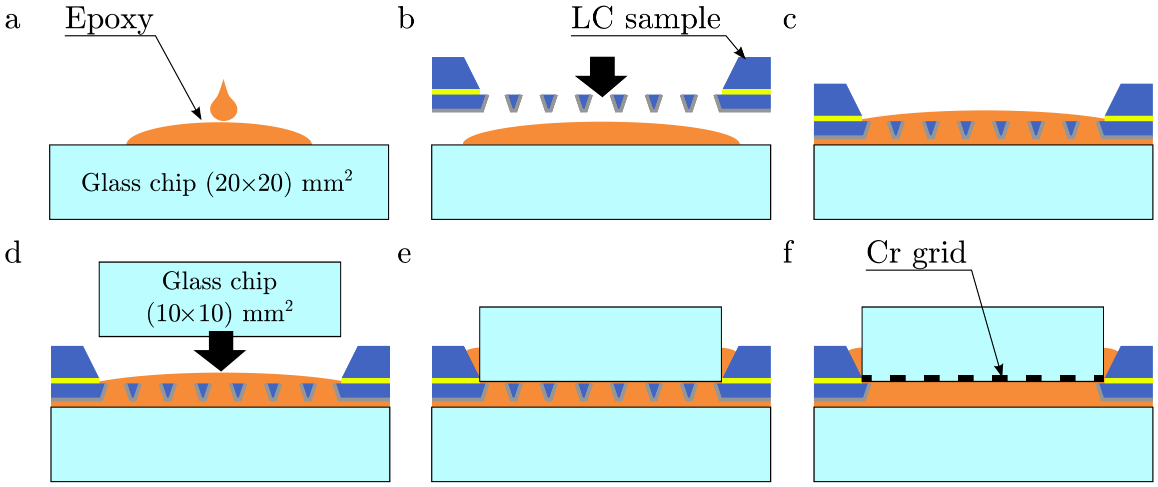

Figure 4.13: Process flow of the LC sample encapsulation for the scintillator-based experiments. After dispensing of the epoxy (a), the LC sample is placed on top of the glass chip (b,c). Finally, the second glass chip is inserted on top (d) and the epoxy is thermally cured (e). The second type of sample serving as a reference used an LC sample with removed concentrator and a glass chip with a Cr grid on its surface (f).

4.2.2 Photonic Crystals

This section presents the two methods that were used for the fabrication of PhC samples. The first approach was electron beam lithography (EBL), which offers high degrees of accuracy and flexibility regarding the grating parameters and allows writing several structures with different geometries on a single substrate. Therefore, this technique was chosen for the fabrication of a first sample series, which served to evaluate the optical properties of PhCs and allowed the validation of the optical simulation framework.

The disadvantages of EBL are its complexity and large costs, which significantly constrain its applicability for future implementations of PhC-coated scintillators in commercial PET systems. The second fabrication approach using direct nano imprinting bears the potential to overcome these limitations. In this method, a mold that contains the inverse of the required PhC structures is utilized to replicate the PhC patterns in a rather simple and cost-efficient way. With this novel approach, a second set of samples with fixed grating parameters was fabricated to evaluate the feasibility of direct nano imprinting and characterize the resulting PhCs.

4.2.2.1 Fabrication using Electron Beam Lithography

The first series of PhC samples was fabricated through structuring a layer of electron beam resist. A 450 nm thick layer of resist ($n_{\mathrm{Resist}} = 1.59$ at a wavelength $\lambda = 405$ nm, Fraunhofer Center for Nano Technologies (CNT), Dresden, Germany, private communication, March 11 2013) was spin coated onto a 700 μm thick Borofloat glass substrate having a diameter of 150 mm. To achieve the nm-resolution of the PhC structures, EBL [117] was used with a square shaped beam and subsequent wet development of the resist (spin coating and lithography was provided by Fraunhofer CNT). The application of EBL facilitated writing several samples with different grating parameters (pitch and cavity size) on one substrate. The patterned area was (8×8) mm^2 per sample. The application of EBL requires a conducting substrate to avoid charging effects. For this purpose, magnetron sputtering was used to deposit a 100 nm thick layer of tin-doped indium oxide (ITO) on the glass substrates prior to spin coating of the resist (external service provided by Fraunhofer Institute for Electron Beam- and Plasma Technology (FEP), Dresden, Germany). ITO was chosen for this purpose as it combines conductivity and optical transparency ($n_{\mathrm{ITO}} = 2.06 + \mathrm{i}\cdot0.01$ at $\lambda = 405$ nm, FEP, private communication, March 11 2013). Finally, the wafers were cut into individual chips of (10×16) mm^2 with a mechanical dicing saw. The actual PhC parameters of the resulting samples, i.e. cavity size s and pitch a, were measured using scanning electron microscopy (SEM). This analysis was conducted after the optical experiments, since the SEM investigations required the deposition of a thin metallic layer (a few nm of platinum), which significantly changed the optical properties of the sample.

4.2.2.2 Direct Nano Imprinting of Photonic Crystals

The second series of PhC samples were manufactured through direct nano imprinting which is closely related to nano imprint lithography (NIL). This lithography technique represents

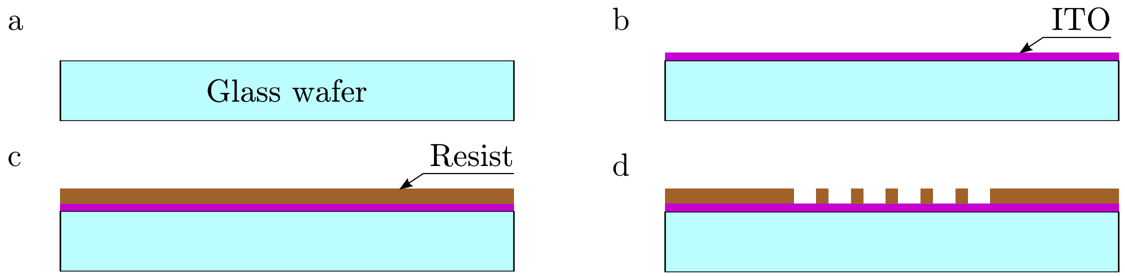

Figure 4.14: Process flow of the PhC sample fabrication. Glass substrates (a) were coated with a 100 nm layer of ITO (b) and a 450 nm layer of resist (c). Then, EBL with subsequent wet development was used to write the PhC structures into the resist (d). (Note that the geometric dimensions are strongly modified for illustrative purposes)

a promising alternative to EBL for structuring a resist with nanometer-scale resolution, high throughput, and relatively low costs. NIL consists of two main steps: first, a mold is fabricated with conventional lithographic processes such as EBL; secondly, the mold is pressed into a resist layer producing a thickness contrast which can then be used for the subsequent pattern transfer into the substrate. The advantage of NIL is, that the costly and time consuming conventional lithography steps must be conducted only once. Afterwards, the fabricated mold can be used several times which leads to reduced costs and high throughput [158]. This lithography technique has already been used to manufacture nano structures that enhanced the photon extraction from light-emitting diodes [159, 160] and improved the performance of solar cells [161]. The first implementation on scintillator surfaces has been presented recently by Lecoq et al. [24]. In their study, NIL was used instead of EBL to structure the resist for the subsequent pattern transfer into a PhC layer of Si_3N_4 through RIE.

To further simplify the fabrication process, this work proposes direct nano imprinting of the PhC geometry into a polymer that is deposited onto the scintillator surface and serves as PhC bulk material as illustrated in Fig. 4.15. This method is even more cost-effective as the approach presented in Ref. [24] since it requires no RIE step. To achieve uniform imprinting on the scintillator faces despite their surface roughness and minor vertical misalignment between the adjacent pixels (see Fig. 4.16), surface conformal imprint lithography (SCIL) can be used which utilizes a mold that consists of a nano structured PDMS film attached to a 200 μm thin glass substrate. This flexible mold in conjunction with a tailored pressure-based imprinting mechanism provides a means to achieve high resolution NIL over large areas as demonstrated in Ref. [162] for a 150 mm diameter Si wafer.

The PDMS mold used in the SCIL process was formed from a Si master as illustrated in Fig. 4.17. First, a 150 mm diameter Si substrate was structured with the PhC geometry using laser interference lithography, in which the photoresist is illuminated with the superposition of two coherent UV laser beams [163]. This technique was chosen as it allowed the exposure of the entire wafer area in one step. In contrast to this, structuring the wafer with a sequential method such as EBL would have required significantly more time. The pattern was transferred into the Si substrate using RIE (etching and lithography were external services provided by Amo Gmbh, Aachen, Germany).

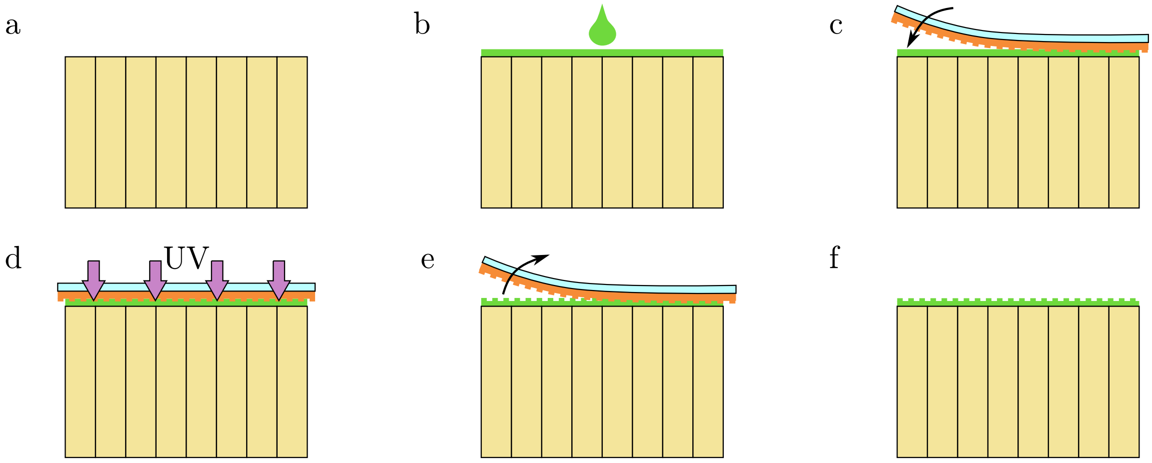

Figure 4.15: Proposed process flow of direct PhC imprinting on scintillator crystals. An array of 8×8 LSO pixels as considered in the reference detector (a) is coated with a layer of the high-index A54 polymer (b). Next, a mold consisting of PDMS on a flexible glass substrate is used to imprint the PhC structures into the polymer (c). After UV-curing of the polymer (d), the mold is released (e) resulting in the LSO array equipped with a PhC coating (f). Note that the PhC structures are drawn with strong magnification for illustrative purposes.

Casting of the PDMS mold from the Si master and imprinting of the PhC structures were conducted in collaboration with Dr. R. Ji and colleagues in the laboratories of Suess Microtec, Garching, Germany. For this, the liquid PDMS was dispensed on the Si master, the 200 μm glass substrate was placed on top, and the PDMS was thermally cured. Finally, the cured PDMS was fastened to the glass with adhesive tape and detached from the Si wafer. Next, a layer of approximately 200 nm of the polymer A54 (Brewer Science, Rolla, MO, USA) was spin coated on a 150 mm glass substrate (Borofloat). This polymer was chosen, as it offers a rather high RI (see Sec. 5.3.5.1 for measurements) and is curable with UV radiation. Its application for direct imprinting of micro and nano structures has already been demonstrated in several studies for light emitting diodes [124, 164, 165]. After spin coating, the PhC structures were imprinted into the A54 polymer film using a mask aligner equipped with a SCIL toolkit (Süss Microtec). The UV curing was performed with a duration of 15 min at 1000 W. Consequently, the PDMS mold was released from the wafer surface, the substrate was unloaded from the SCIL system, and the polymer was further annealed on a hotplate for 30 min at a temperature of 250°. Finally, the wafer was cut into sample chips of (16×10) mm^2 with a mechanical dicing saw.

Direct imprinting of PhCs on the surface of LSO crystals instead of glass wafers was not feasible in this work, since the used SCIL equipment was not compatible with the geometry of available scintillator crystals.

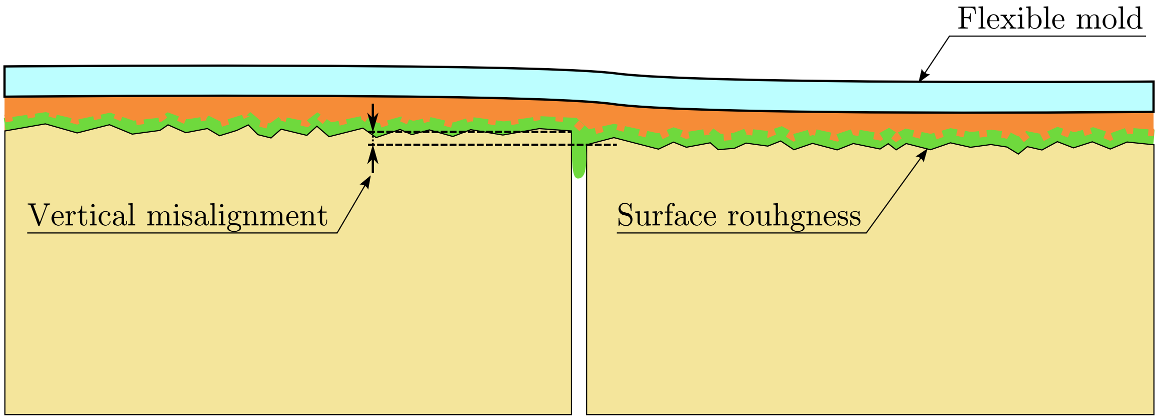

Figure 4.16: In SCIL, the flexible mold allows the imprinting on slightly rough surfaces and the compensation of vertically misaligned LSO pixels to a certain degree. Note that the PhC structures are drawn with strong magnification for illustrative purposes.

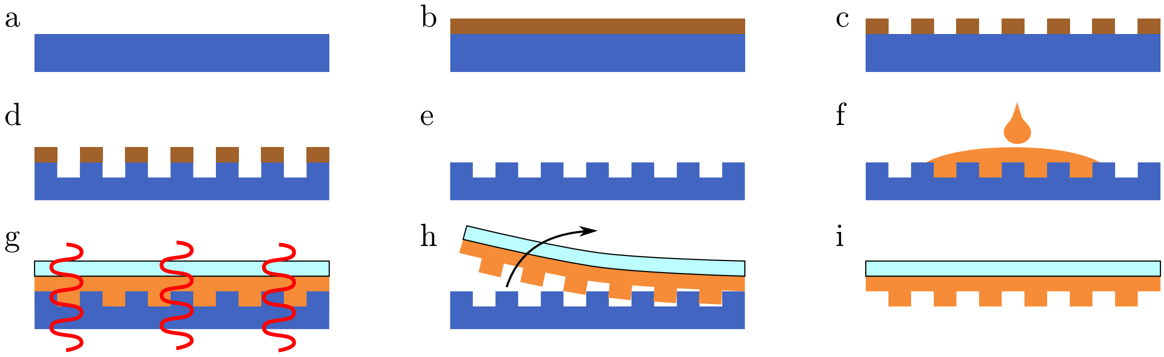

Figure 4.17: Fabrication of the PDMS mold for SCIL. A 150 mm Si wafer (a) was coated with a photoresist (b) which was structured using laser interference lithography (c). Next, the pattern was transferred into the Si using RIE (d) and the resist was removed yielding the Si master for the PDMS mold reproduction (e). For this, liquid PDMS was dispensed (f) and cured thermally with the 200 μm glass substrate placed on top (g). Afterwards, the final PDMS mold was detached from the Si master (h,i).

4.3 Validation of Transmission Characteristics

4.3.1 Goniometer Setup

The angular transmission characteristics of LC and PhC samples were measured with the experimental setup shown in Fig. 4.18, which was realized in collaboration with Dr. T. Führer, Prof. Dr. T. Walther and colleagues at the Technical University Darmstadt, Germany. Through a replication of this experiment within the optical simulation framework, these measurements facilitated a validation and refinement of the computational models used for the LCs and PhCs.

The setup consisted of a goniometer with a laser diode module mounted on a motorized arm. This allowed the variation of the incident angles $(\theta_\mathrm{L}, \phi_\mathrm{L})$ of the laser on a sample positioned in the goniometer center. The laser had a wavelength of 405 nm, which is similar to the peak of the LSO emission spectrum at 420 nm. The polarization q of the beam was switched between S- and P-polarization using a half-wave plate. The laser module was equipped with lenses and an aperture to provide a collimated beam with a Gaussian profile. Using a charge-coupled device camera, the beam profile was recorded yielding the spatial distribution shown in Fig. 4.19a with a FWHM of 160 ± 2 μm.

A bare Si-PD having a sensitive area of (10×10) mm^2 was mounted in a tailored holder. The position of the PD was shifted in all three dimensions from the the goniometer center of rotation (COR) as shown in Fig 4.20. The distances were derived from the geometric requirements of the PhC samples taking into account the lateral translation of the laser beam for $\theta_\mathrm{L} > 0°$. The PD current was converted into voltage by a transimpedance amplifier and read out by a computer equipped with an analog-to-digital converter (ADC). A custom

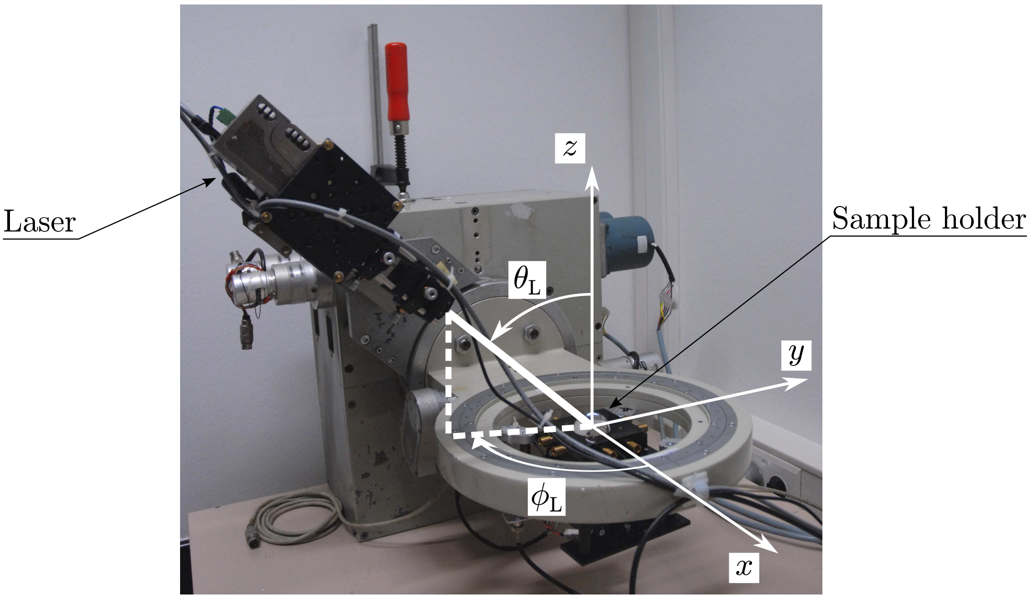

Figure 4.18: Photograph of the goniometer setup at the Technical University Darmstadt used for the angle-resolved transmission measurements. The solid white line illustrates a laser beam impinging on a sample with incident angles $(\theta_\mathrm{L}, \phi_\mathrm{L})$.

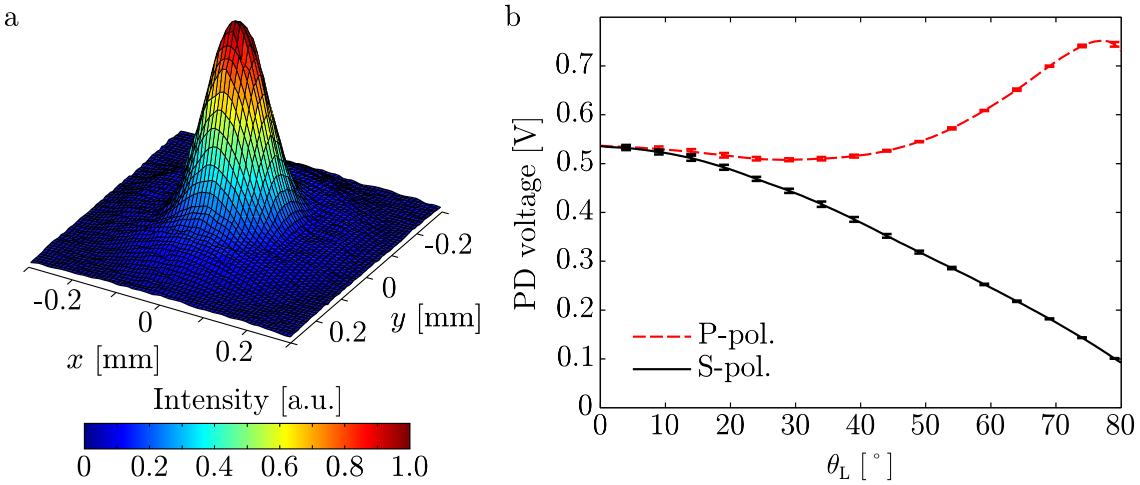

Figure 4.19: a) Normalized beam profile of the laser used in the goniometer setup recorded with a charge-coupled device camera. b) Angular sensitivity of the PD for the two states of S- and P-polarization. The error bars indicate the standard deviation of the datasets acquired at different ϕ_L-values.

program (written in LabView, Texas Instruments, TX, USA) recorded the ADC output and controlled the goniometer motors allowing automatized measurements. For each incident angle (θ_L,ϕ_L) and polarization state q, the PD voltage $U_{Meas}(\theta_L,\phi_L,q)$ was measured 50 times at a laser output power of 5 mW, which led to a standard deviation of the registered voltage below 0.1%. The PD angular sensitivity was measured for θ_L ranging from 0° to 80° in 1°-steps and ϕ_L ranging from 0° to 90° in 10°-steps. The results were averaged over ϕ_L and yielded the characteristic shown in Fig. 4.19b. The measurements and the programming of the read-out program were realized in collaboration with Dr. T. Führer, Prof. Dr. T. Walther, and colleagues.

4.3.2 Light Concentrator Measurements

The LC samples were placed on top of the PD holder yielding a vertical distance of 500 μm between PD surface and LC bottom. For each sample, self-calibrated measurements were conducted through performing the experiment in two different configurations, once in the concentrator configuration C_{Conc} and once in the plain configuration C_{Plain} (see Fig. 4.21). For C_{Conc}, the LC samples were positioned over the PD with the receiver side A_{Rec} facing the PD, which mimicked an SiPM equipped with a perfectly aligned LC. As illustrated in Fig. 4.21a, rays that impinged on the LC structure with $\theta_{L,1} < \theta_{Acc}$ were redirected towards the PD whereas rays having an angle $\theta_{L,2} > \theta_{Acc}$ were rejected by the LC and could not reach the PD. For C_{Plain}, the samples were placed in a reverse manner with the input side A_{In} facing the PD. Seen from above, this setup resembled a plain SiPM having a finite geometric fill factor without LC. Light that impinged on the base of the LC structures was reflected and could not impinge on the PD as illustrated in Fig. 4.21b. Light that entered the LC cells at shallow angles θ_L was redirected by the oblique surfaces which changed the incident angle on the PD. Hence, a PD equipped with the LC sample in the plain configuration had a different angular sensitivity compared to a real SiPM, especially for large θ_L-values.

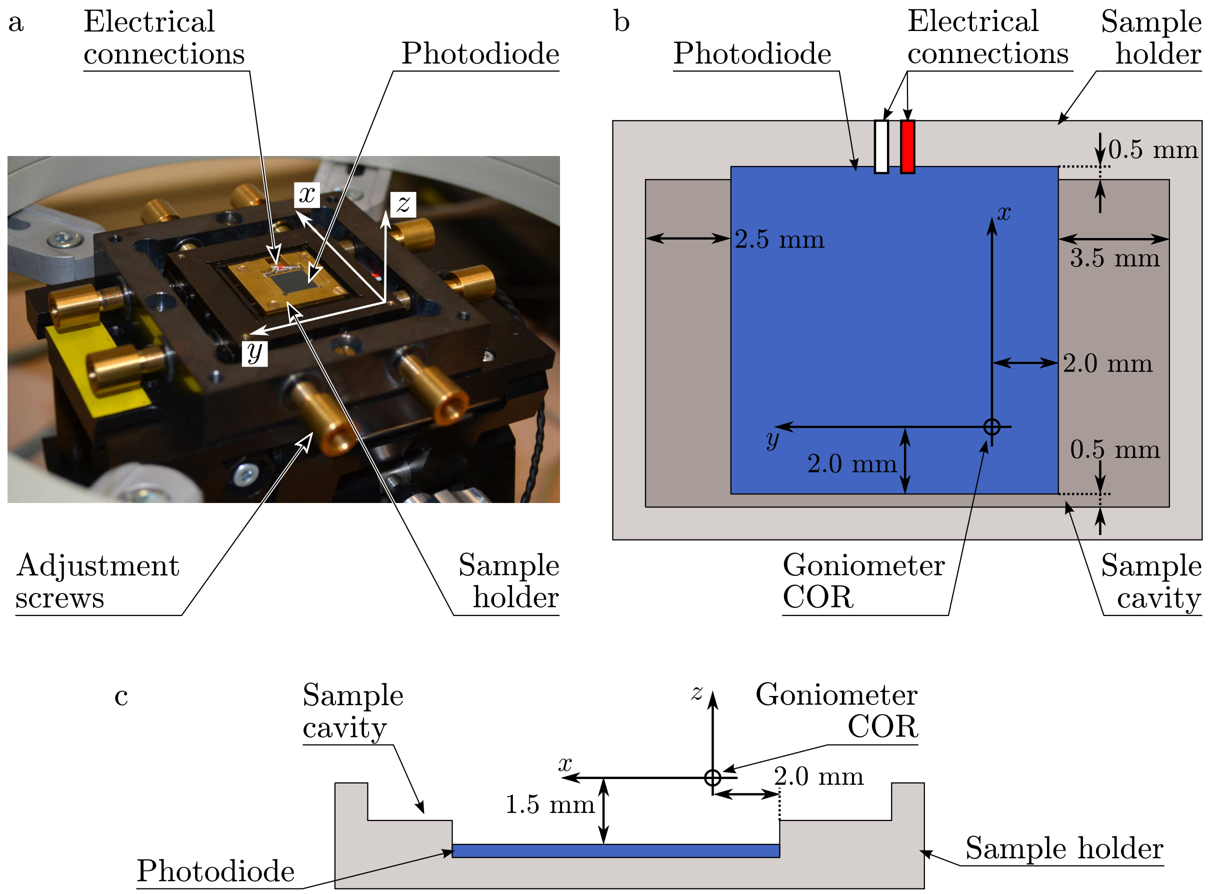

Figure 4.20: a) Photograph of the sample holder with integrated PD. The indicated screws allow adjusting the lateral position of the holder. Schematic drawing of the sample holder and PD seen from above (b) and in cross-section view (c) showing the position of the setup relative to the goniometer COR. A cavity was machined into the holder to allow reproducible positioning of the PhC samples. (Dimensions in z-direction in (c) are not to scale for illustration purposes)

This measurement procedure involved only one photosensor and one sample positioned in two different configurations. This reduced confounding influences from device-specific sensitivity variations of different photosensors and geometric discrepancies between distinct LC samples. The optical characterization of each LC sample involved four measuring sequences that consisted of acquiring data for the two configurations C_{Conc} and C_{Plain}, each for the S- and P-polarization states of the incident light. During these sequences, the incident angle θ_{L} was varied from 0° to 80° in 1°-steps, ϕ_{L} ranged from 0° to 90° in 1°-steps.

The coherent light emitted by the laser diode in conjunction with the highly uniform and reflective concentrator geometry led to interferometric oscillations of the measured PD signal similar to the transmission of an etalon. However, an LC integrated into a PET detector only interacts with incoherent scintillation photons. Therefore, the oscillations in the PD signal $U_{\mathrm{Meas}}(\theta_{\mathrm{L}}, \phi_{\mathrm{L}}, q)$ were removed in the post-processing using a moving average filter. For this, each data point $U_{\mathrm{Meas}}(\theta_{\mathrm{L}})$ at fixed values of ϕ_{L} and q was recalculated to obtain a filtered

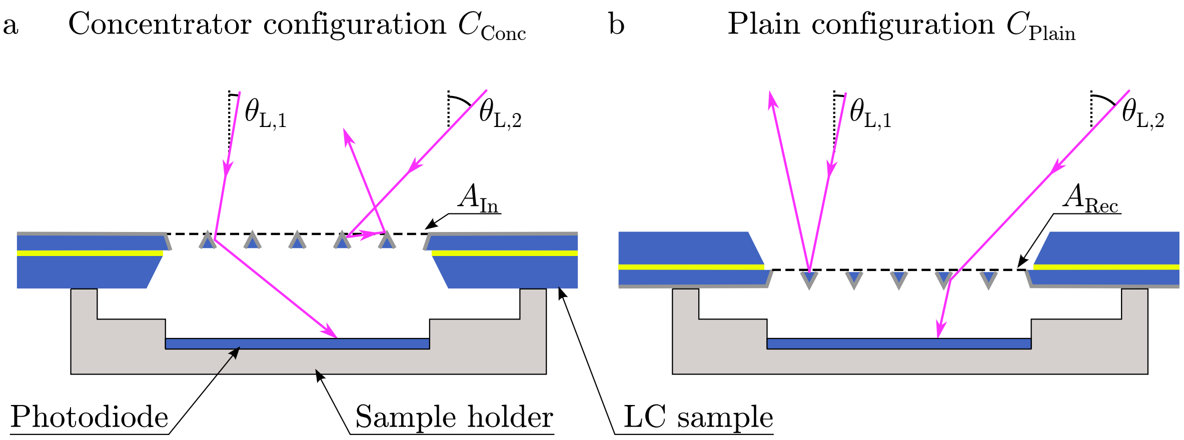

Figure 4.21: Illustration of the experimental setup for LC transmission measurements in concentrator configuration (a) with the LC side A_{In} facing the light source and in plain configuration (b) with A_{Rec} facing the light source. The violet lines depict exemplary ray trajectories. (Dimensions are not to scale for illustration purposes)

signal $U_{\mathrm{Filtered}}(\theta_{\mathrm{L}})$ through

$$U_{\mathrm{Filtered}}(\theta_{\mathrm{L}}) = \frac{1}{2N+1} \sum_{i=-N}^{N} U_{\mathrm{Meas}}(\theta_{\mathrm{L}} + i \cdot \Delta\theta_{\mathrm{L}}) \ , \tag{4.27}$$

wherein N is the half-width of the averaging window and $\Delta\theta_{\mathrm{L}}$ is the θ_{L}-increment of 1°. In this work, this filter was applied with $N = 2$ and iterated 3 times. The error $\delta U_{\mathrm{Filtered}}(\theta_{\mathrm{L}})$ of the obtained signal was estimated through

$$\delta U_{\mathrm{Filtered}}(\theta_{\mathrm{L}}) = \sqrt{\frac{1}{2N+1} \sum_{i=-N}^{N} \Big(U_{\mathrm{Meas}}(\theta_{\mathrm{L}} + i \cdot \Delta\theta_{\mathrm{L}}) - U_{\mathrm{Filtered}}(\theta_{\mathrm{L}} + i \cdot \Delta\theta_{\mathrm{L}})\Big)^2} \ . \tag{4.28}$$

4.3.3 Photonic Crystal Measurements

The PhC samples were placed in the cavity machined into the PD holder, which provided a defined lateral position (see Figs. 4.22 and 4.20) and a vertical distance of 200 μm between PD and sample. The sample orientation was chosen so that the PhC coating was facing the sensor. The sample was illuminated under different incident angles through a glass hemisphere (diameter 40 mm, $n_{\mathrm{HS}} = 1.82$ at $\lambda = 405$ nm) placed on top. A 600 μm thick film of Polydimethylsiloxan (PDMS) was used as optical coupling agent between sample and hemisphere (see Sec. 4.3.4 for optical properties). The hemisphere was placed inside the goniometer so that the center of its planar surface coincided with the goniometer COR. The lateral position of sample and PD were chosen off-center to account for the lateral displacement of the laser beam for $\theta_{\mathrm{L}} > 0°$ as illustrated in Fig. 4.22.

The accuracy of the goniometer setup $\delta\theta_{\mathrm{L}}$ regarding the elevation angle θ_{L} was determined using a calibration experiment. For this, the transmission characteristic of a glass chip (Borofloat) without PhC coating was measured. Based on this measurement, $\delta\theta_{\mathrm{L}}$ was determined by comparing the TIR-related cutoff in the measured PD signal with the theoretical value

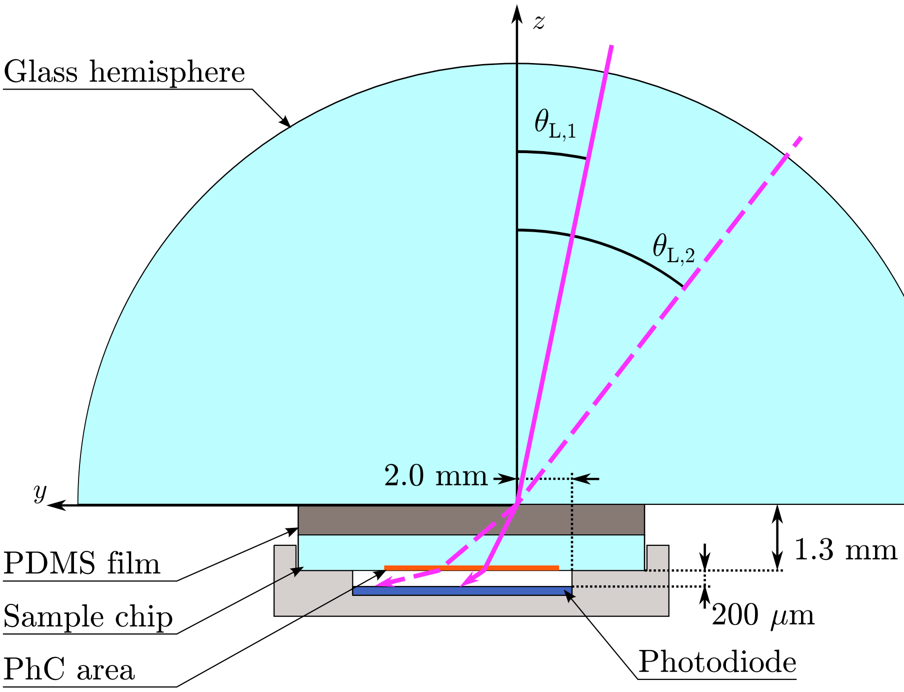

Figure 4.22: Drawing of the experimental setup for PhC transmission measurements. The violet lines depict exemplary ray trajectories with incident angles $\theta_{\mathrm{L},1}$ and $\theta_{\mathrm{L},2}$ illustrating the lateral displacement of the laser beam at high incident angles. (Dimensions in z-direction are not to scale for illustration purposes)

based on the RIs. To estimate $\delta\phi_\mathrm{L}$, i.e. the accuracy of the setup regarding the azimuth angle ϕ_L, the locations of ϕ_L-periodic features in the transmission characteristics of the PhC samples were used. The systematic uncertainty $\gamma^{\mathrm{PhC}}_{\mathrm{Meas}}$ of the measured PD voltage $U_{\mathrm{Meas}}(\theta_\mathrm{L},\phi_\mathrm{L},q)$ was derived from these results by analyzing the variations of $U_{\mathrm{Meas}}(\theta_\mathrm{L},\phi_\mathrm{L},q)$ for changes $\pm\delta\theta_\mathrm{L}$ and $\pm\delta\phi_\mathrm{L}$.

For each sample, the transmission characteristics were acquired for incident angles θ_L from 0° to 60° in 0.5°-steps, ϕ_L from 0° to 90° in 1°-steps, and the two S- and P-polarization states. Due to the different RIs of the hemisphere ($n_{\mathrm{HS}} = 1.82$) and the sample chips ($n_{\mathrm{BF}} = 1.48$), the laser beam was refracted prior to its incidence on the PhC coating. Neglecting any scattering of the light, the laser beam angle θ_L and the incident angle on the PhC θ_{PhC} were correlated through

$$\theta_{\mathrm{PhC}} = \mathrm{asin}\left(\sin(\theta_\mathrm{L})\,\frac{n_{\mathrm{HS}}}{n_{\mathrm{BF}}}\right) \,. \tag{4.29}$$

Due to the finite extent of the samples in the x-y-dimensions, incident angles on the PhC of $\theta_{\mathrm{PhC}} > 76°$ could not be achieved.

4.3.4 Transmission Simulations

The experimental setup was replicated within the optical simulation framework of Zemax to validate simulated transmission characteristics against measured values. The simulations included the geometry of the sample holder, the beam profile from Fig. 4.19a as light source, and the recorded PD angular sensitivity from Fig. 4.19b.

For the PhC transmission simulations, the PhC parameters a, s and h derived from SEM investigations of the samples were used to calculate the corresponding LUTs for the DLL-based implementation. These LUTs contained data for the single wavelength of 405 nm and had the same angular resolution as used in the transmission experiment. The calculations also took into account the presence of the ITO layer in the actual PhC samples. However, this layer was found to have no significant impact on the transmission characteristics. The optical properties of the PDMS film used in the PhC measurements, i.e. the RI n_{PDMS} and the bulk absorption length $l_{\mathrm{Abs,PDMS}}$, were not known in detail. Hence, these parameters were used as variables to adapt the simulated PD voltage $U_{\mathrm{Simu}}(\theta_{\mathrm{L}},\phi_{\mathrm{L}},q)$ to the measured characteristic $U_{\mathrm{Meas}}(\theta_{\mathrm{L}},\phi_{\mathrm{L}},q)$ acquired in the calibration experiment with the plain glass chip as described before.

For each $(\theta_{\mathrm{L}},\phi_{\mathrm{L}},q)$-setting, 10^5 photons were simulated leading to a statistical uncertainty in the simulated PD voltage $U_{\mathrm{Simu}}(\theta_{\mathrm{L}},\phi_{\mathrm{L}},q)$ below 0.1%. The systematic uncertainty $\gamma^{\mathrm{LC}}_{\mathrm{Simu}}$ of the LC goniometer simulations was estimated to be 2% based on the statistical fluctuations in conjunction with the inaccuracies caused by the implemented beam profile and PD sensitivity. For the PhC setup, the systematic simulation uncertainty $\gamma^{\mathrm{PhC}}_{\mathrm{Simu}}$ was derived from data acquired in the calibration experiment using a sample without PhC coating. The relative differences between U_{Meas} and U_{Simu} were averaged over all $(\theta_{\mathrm{L}},\phi_{\mathrm{L}},q)$-triplets to obtain $\gamma^{\mathrm{PhC}}_{\mathrm{Simu}}$.

The simulated PD voltage U_{Simu} was scaled using the average of U_{Meas} over $0 \leq \theta_{\mathrm{L}} \leq 3$. This interval was used as it allowed to compensate for minor fluctuations in individual measurements caused by scattering from impurities.

4.3.5 Analysis of Measured vs. Simulated Transmission Data

The agreement between measured and simulated PD signals was determined by comparing the paired 1D datasets $[U_{\mathrm{Meas}}(\theta_{\mathrm{L}}), U_{\mathrm{Simu}}(\theta_{\mathrm{L}})]_{\phi_{\mathrm{L}},q}$ at fixed values for ϕ_{L} and q. The comparison of these two curves was conducted using a two-sample Kolmogorov-Smirnov test [166]. In this statistical test, the null hypothesis H_0 states that a pair of continuous functions $[f(x), g(x)]$ stems from the same distribution. To test this hypothesis, the accumulative functions $F(X) = \sum_{x<X} f(x)$ and $G(X) = \sum_{x<X} g(x)$ are calculated and the test statistic D_{N_f,N_g} is derived from

$$D_{N_f,N_g} = \sqrt{\frac{N_f N_g}{N_f + N_f}} \sup_x |F_{N_f}(X) - G_{N_g}(X)| \,, \tag{4.30}$$

wherein N_f and N_g denote the number of samples per function $f(x)$ and $g(x)$, respectively, and "sup" is the supremum. The result of D_{N_f,N_g} is compared to the critical value $D_{\mathrm{Crit}}(\alpha)$ taken from tabulated data for a given significance level α. If $D_{N_f,N_g} > D_{\mathrm{Crit}}$, the null hypothesis is rejected with the conclusion that the two functions do not stem from the same distribution at a significance level α [167].

In this work, each sample was tested with this procedure for all $N_{\phi_{\mathrm{L}}}$ azimuth angles ϕ_{L} and the two polarizations S and P at a significance level of $\alpha = 0.05$, which produced a number of

$2N_{\phi_\mathrm{L}}$ decisions about the agreement between simulation and experiment per sample. These results were summarized in the agreement metric η defined as the fraction of N_{H_0}, i.e. the number of paired datasets $[U_\mathrm{Meas}(\theta_\mathrm{L}), U_\mathrm{Simu}(\theta_\mathrm{L})]_{\phi_\mathrm{L},q}$ for which H_0 was not rejected, over the total amount of tested datasets $2N_{\phi_\mathrm{L}}$:

$$\eta = \frac{N_{H_0}}{2N_{\phi_\mathrm{L}}} \; . \tag{4.31}$$

The analysis was conducted using the Kolmogorov-Smirnov implementation of Matlab. The results of η are given in %. In the case of the LC measurements, the filtered measurement data was used for this analysis.

4.4 LSO-based Light Yield and Timing Measurements

4.4.1 Concentrator Experiments

After the validation of the transmission characteristics using measured and simulated results for the goniometer setup, a first step towards the experimental verification of the effects of LCs on the light yield and timing for LSO-based detectors was conducted. However, within the scope of this work it was not feasible to equip an actual SiPM with a micromachined LC, since bare sensor chips without encapsulation were not available from the vendors. Therefore, the measurements were conducted using a conventional PMT in conjunction with a glass chip mimicking the surface of the SiPM as illustrated in Fig. 4.23. In order to compare this metal grid sample with the LC samples in a stable and reproducible manner, the coated glass chip was integrated into the same encapsulated stack as the fabricated LCs as depicted in Fig. 4.23c,f.

These samples were placed on the entrance window of a PMT (XP20D0, Photonis Technologies, Mérignac, France) and an LSO crystal was positioned on top as illustrated in Fig. 4.24a. All components were coupled using optical grease (Q2-3067, $n_\mathrm{Grease} = 1.47$ at $\lambda = 589$ nm, Dow Corning, Midland, MI, USA). The remaining area of the circular PMT window was masked with black tape to detect only photons that propagated through the samples and to allow for a reproducible placement of the samples. The experiments were conducted with two different LSO crystals, the first having a size of ($4\times4\times20$ mm^3) with etched surface finish, the second having a size of ($4\times4\times7$ mm^3) and polished surfaces. Both crystals were wrapped with three layers of diffusely reflecting Teflon tape. The scintillators were irradiated with 511 keV gamma photons from a ^{68}Ge source which was placed centrally over the crystal at a distance of 15 mm. To measure coincident gamma events, a reference setup was used which consisted of a PMT (R9779, Hamamatsu Photonics) equipped with an LSO crystal bonded directly to its entrance window. The crystal had a size of ($6\times6\times6$ mm^3) mm and was also wrapped with three layers of Teflon tape. This system was positioned on the opposite side of the gamma source at distance of 15 mm as depicted in Fig. 4.24b. The entire instrumentation was housed inside a light-tight enclosure. The PMTs were connected to high voltage power supplies (TC 952, Tennelec, Oak Ridge, TN, USA) and were operated at -1250 V (XP20D0) and -1350 V (R9779). The PMT output signals were fed into a high-speed digitizer (Acquiris DC282, Agilent Technologies, Santa Clara, CA, USA) connected to a computer.

Every measurement involved the data acquisition of $2 \cdot 10^5$ coincidence events which were post-processed with Matlab. Assuming perfect linearity of the PMT, the amount of detected scintillation photons N_{Det} can be considered to be proportional to the integral of the PMT voltage U_{PMT} over the entire pulse,

$$N_{\mathrm{Det}} = C \int_0^{\tau} U_{\mathrm{PMT}}(t)\ \mathrm{d}t\ , \tag{4.32}$$

with C being a constant depending on the PMT gain and the signal the amplification. The integration limit τ was set to 300 ns. The correlation between energy and detected photons was calibrated through locating the abscissa $N_{\mathrm{Det,PP}}$ corresponding to the 511 keV photopeak in the histogram of all N_{Det}-values. Afterwards, the energy $E_{\gamma}(i)$ of the i-th registered event could be derived from the corresponding amount of detected photons $N_{\mathrm{Det}}(i)$ through

$$E_{\gamma}(i) = \frac{N_{\mathrm{Det}}(i)}{N_{\mathrm{Det,PP}}} \cdot 511\mathrm{keV}\ . \tag{4.33}$$

For the evaluation of the CRT, the signal of the last dynode stage of each PMT was used. After selecting only events with 430 keV $< E_{\gamma} <$ 650 keV, walk correction was applied through

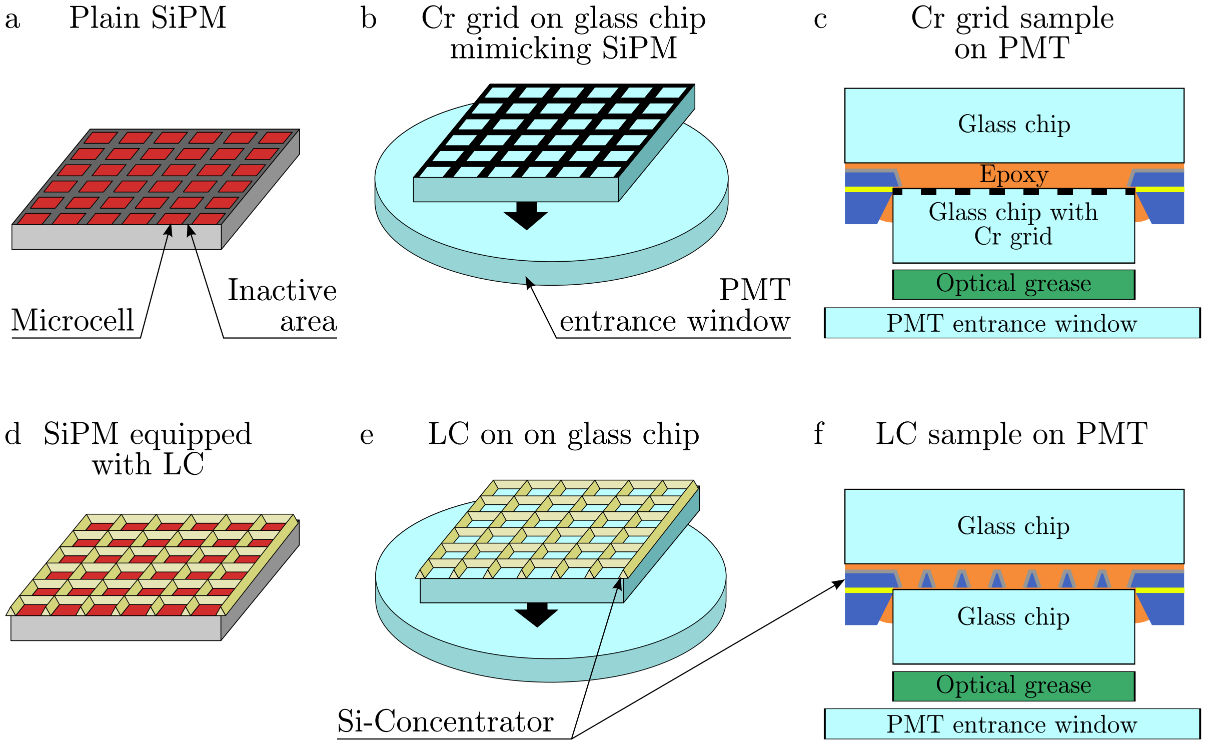

Figure 4.23: Illustration of replacing SiPMs with PMTs to evaluate the impact of LCs. Instead of using an actual plain SiPM (a), a glass-chip coated with a Cr grid is coupled to the entrance window of a PMT to mimic the geometric fill factor of the SiPM (b). The experimental realization of this uses the Cr grid sample consisting of two glass chips bonded via epoxy (c) described in Sec. 4.2.1.4. Similarly, the experiments involving an SiPM equipped with an LC (d) are replaced through the LC placed on a PMT (e) using the samples shown in (f).

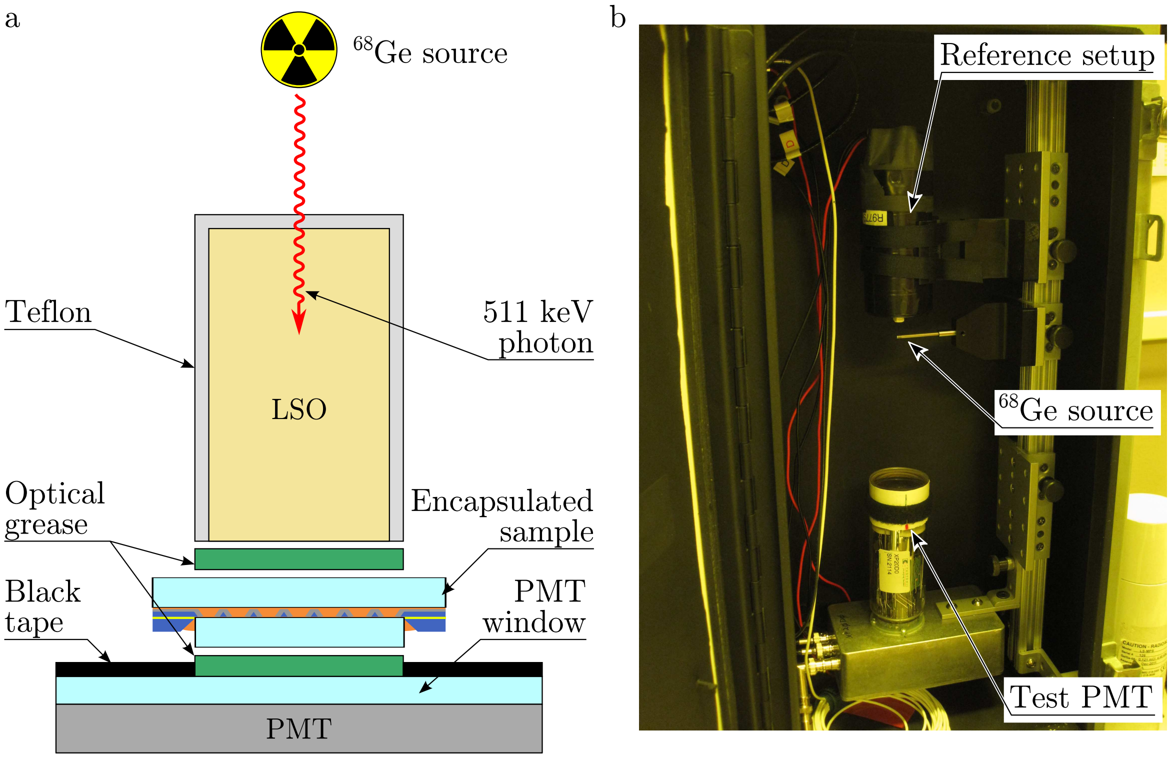

Figure 4.24: a) Drawing of setup involving an LSO crystal wrapped in Teflon, an LC sample encapsulated between two glass chips, and a PMT. The components are optically coupled using grease. b) Photograph of the coincident measurement setup consisting of a reference system at the top, a ^{68}Ge gamma source in the center, and the test setup from (a) on the bottom. Note that no sample or LSO crystal is mounted on the test tube in this photograph and the distance between the source and bottom PMT is larger than during the actual experiments. The color impression of the photograph is due to the yellow light used in the laboratory.

multiplication of the signal with 511 kev / E_γ. Next, a time stamp was generated through the application of an LED, which used a threshold voltage of 10 mV for the reference PMT R9779. For the test PMT, i.e. the XP20D0, the LED threshold was varied from 2 mV to 30 mV to obtain timing curves CRT(U_{LED}) and determine the minimum possible CRT. The CRT of the entire systems results from the contributions of the two PMT setups according to

$$\mathrm{CRT} = \sqrt{\delta t_{\mathrm{Test}}^2 + \delta t_{\mathrm{Ref}}^2}\,, \tag{4.34}$$

wherein δt_{Test} is the timing jitter of the test setup consisting of XP20D0 tube with LC or Cr grid sample. The second contribution δt_{Ref} of the reference system was determined as 140 ps in previous experiments. This allowed calculating δt_{Test} from the measured CRT to study the impact of the LC and Cr grid samples on the timing. To capture the pulse shape of the XP20D0 PMT for different samples and LSO crystals, the anode signal of the tube was recorded with the digitizer for another $80 \cdot 10^3$ coincidence events.

Each measurement consisted of i) positioning the sample and LSO crystal on the PMT; ii) acquisition of the data for timing and pulse shape; iii) detaching of sample and LSO crystal from the setup; iv) removal of the optical grease and cleaning of all interfaces to prepare for the next measurement. This procedure was repeated five times for each sample/LSO combination. The resulting pulse shapes and timing curves were averaged and the standard deviation of the five datasets was used as the error of the measurement.

The difference in light yield obtained for the LC and the Cr grid sample $N_{\mathrm{Det}}^{\mathrm{LC}}/N_{\mathrm{Det}}^{\mathrm{Cr}}$ was compared to its simulated value. To this end, the test setup was reproduced within the optical simulation framework including models of the LC and Cr grid samples based on microscopy images. Computing the CRT based on these optical simulations was not feasible, as the simulation tool simulating the timing resolution was not applicable for this PMT-based detector configuration.

4.4.2 Incompatibility with Photonic Crystal Samples

Using this experimental setup for measuring the effect of PhCs was not possible since it was beyond the scope of this work to fabricate PhC films on actual scintillator surfaces. Also, the PhC gratings realized on glass chips could not be integrated into the measurement setup explained above, as there was no suitable coupling agent available that had an RI in the range of n_{LSO}. Therefore, the studies of PhCs were limited to the validation of the transmission characteristics and the MC simulations.

Chapter 5

Results

This chapter first presents the results of the reference PET detector simulations. Next, the works regarding LCs are summarized, including their optical properties derived from MC simulations, the fabricated samples with their measured transmission characteristics, a MC study regarding the impact of LCs on the light yield and timing of the reference detector, as well as the LSO-based measurements. After that, this chapter presents the results obtained with PhCs. These efforts comprise the implementation of PhCs into the optical MC simulations, a discussion of their optical properties, the characterization of EBL-fabricated samples regarding their transmission characteristics, and the evaluation of a PhC-enhanced PET detector. Further, the concepts of LC and PhCs are combined and their impact on the PET detector performance is studied. Finally, the results of direct nano imprinting of PhC samples are presented, their transmission properties are evaluated, and their implementation in the PET detector module are discussed.

5.1 Simulation Results for Reference Detector

The optical MC simulations of the reference PET detector module yield a total number of $3.42 \cdot 10^6$ (polished configuration) and $3.45 \cdot 10^6$ (etched configuration) scintillation photons that impinge on the LSO exit faces at least once. Of these photons, which are incident with the angular distributions depicted in Fig. 5.1, $1.66 \cdot 10^6$ and $1.80 \cdot 10^6$ are extracted at the first incidence for the polished and the etched configuration, respectively. This leads to first incidence extraction efficiencies of $\chi_{\mathrm{Pol}}^{\mathrm{Ref}}(1) = 0.485$ and $\chi_{\mathrm{Etch}}^{\mathrm{Ref}}(1) = 0.522$. The total amount of photons registered by the SiPMs is $5.80 \cdot 10^5$ (polished configuration) and $6.48 \cdot 10^5$ (etched configuration). Divided by the total amount of $4 \cdot 10^6$ simulated photons, relative light yields of $\Gamma_{\mathrm{Pol}}^{\mathrm{Ref}} = 0.227$ and $\Gamma_{\mathrm{Etch}}^{\mathrm{Ref}} = 0.253$ are obtained. The remaining photons are ignored by the SiPMs due to their limited PDE, escape from the module or are lost through absorption in one of the detector components as summarized in Table 5.1. The timing simulations yield values of $\mathrm{CRT}_{\mathrm{Pol}}^{\mathrm{Ref}} = 237$ ps and $\mathrm{CRT}_{\mathrm{Etch}}^{\mathrm{Ref}} = 229$ ps.

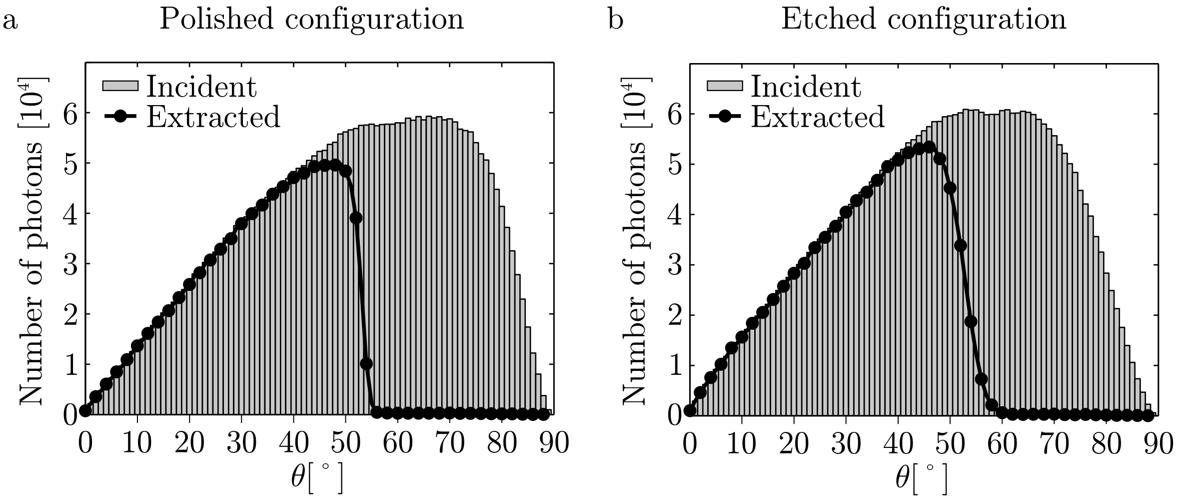

Figure 5.1: Angular distribution $D(1, \theta)$ of photons at their first incidence on the LSO exit faces of the polished (a) and the etched configuration (b), derived from the optical simulations. The bars indicate the amount of photons incident per 1°-bin, the lines represent the extracted photons. The extraction efficiencies $\chi^{\mathrm{Ref}}(1)$ result from dividing the integral of the extracted photons by the integral of the incident photons.

Table 5.1: Survey of simulation results for the polished and etched reference detector module indicating the fractions of the relative light yield versus the different loss mechanisms and the CRT.

Configuration	Polished	Etched
Relative light yield Γ^{Ref}	0.227	0.253
Ignored by SiPM	0.193	0.216
LSO Bulk absorption	0.285	0.229
Wrapping Losses	0.026	0.022
Inactive SiPM areas	0.130	0.144
Spacing between SiPMs	0.057	0.064
Escaping from module	0.082	0.072
$\mathrm{CRT}^{\mathrm{Ref}}$ [ps]	237	229

5.2 Concentrator for Improved Light Collection

5.2.1 Optical Properties of Light Concentrator

The LC geometry for the application on the SiPMs considered in this work was constrained by the microcell size and pitch. Hence, the lateral dimensions were set to $A_{\mathrm{In}} = 50\ \mu$m and $A_{\mathrm{Rec}} = 40\ \mu$m, which defined the maximum acceptance angle $\theta_{\mathrm{Acc}} = \arcsin(A_{\mathrm{Rec}}/A_{\mathrm{In}}) = 53°$. The third LC parameter H_{C} was independent of the SiPM geometry and could be used to manipulate the concentrator acceptance within the transition region around θ_{Acc}. However, larger H_{C}-values also lead to an increased number of photon interactions with the reflectors as illustrated in Fig. 5.2. Since all conventional reflective coatings exhibit absorption, the light collection degrades with increasing concentrator heights.

To study this behavior, the angle-resolved collection efficiency was calculated with optical simulations of LCs with different heights. In these computations, light impinged from within the epoxy encapsulation onto an SiPM which was equipped with an Al-coated LC with variable height H_{C}. The complex-valued RI of Al was measured with ellipsometry (see Fig. 5.3a) and led to an angular reflection characteristic as depicted in Fig. 5.3b. The results of the collection efficiency simulations are shown in Fig. 5.3c. For a plain SiPM, only 64% or less is absorbed in the SiPM due to the limited f_{Geo}. A height $H_{\mathrm{C}} = 3\ \mu$m corresponds to a taper angle of $\zeta_{\mathrm{C}} = 59°$. Hence, photons that impinge on the inactive areas perpendicularly ($\theta = 0°$) are not redirected onto the active microcell and no increase in light collection is visible. Only LCs with $\zeta_{\mathrm{C}} < 45°$, which equals $H_{\mathrm{C}} > 5\ \mu$m, exhibit this effect with continuously increasing benefit until reaching collection efficiencies up to 98% at $\theta = 0°$. At the same time, the cutoff around θ_{Acc} becomes more and more abrupt with larger heights. As can be seen from Fig. 5.3c, the positive effect of LCs in the region of $\theta < \theta_{\mathrm{Acc}}$ starts decreasing again for concentrator heights larger than 40 μm. This is caused by the increasing absorption in the reflective coating as depicted in Fig. 5.3d.

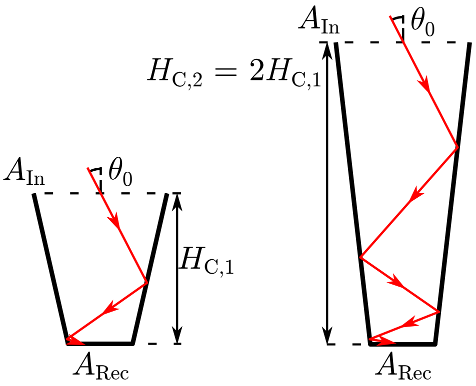

Figure 5.2: LCs with larger heights lead to an increased number of photon interactions with the reflectors. This example depicts a ray incident with θ_0 in the center of two different LCs. The concentrator on the right has twice the height of the configuration on the left side, leading to four reflector interactions instead of two.

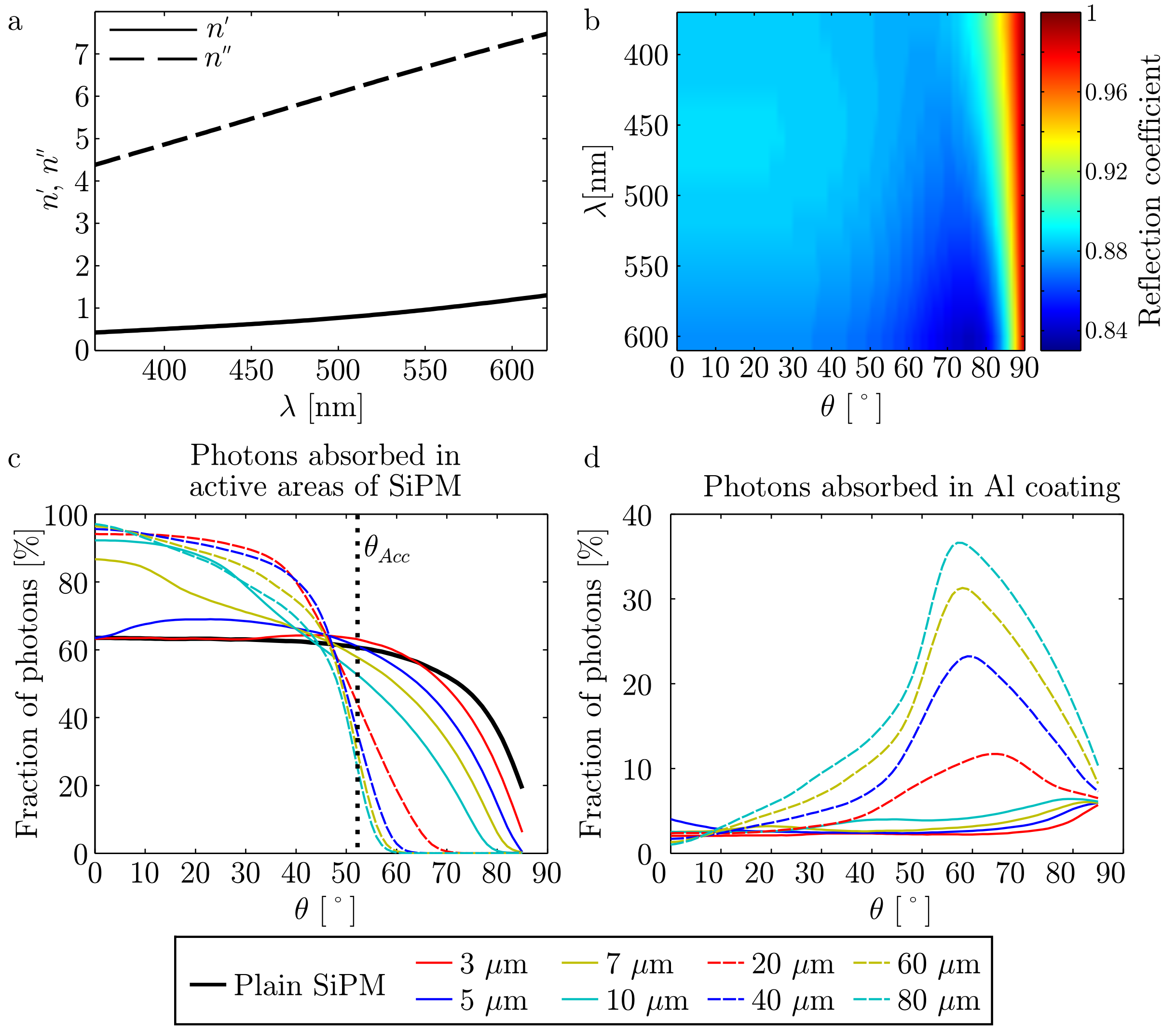

Figure 5.3: a) Real (n') and imaginary part (n'') of complex RI of the Al coating used for the LCs measured with ellipsometry. b) Reflection coefficient vs. wavelength and incident angle θ of the Al coating derived from RI data in (a) for randomly polarized light impinging from a medium with $n = 1.59$. Collection efficiency of LC (c) and absorption in Al coating (d) vs. incident angle θ (averaged over ϕ) for different heights H_{C} derived from optical simulations. Note that a PDE = 1 was assumed in these simulations.

5.2.2 Light Concentrator Samples

5.2.2.1 Evaluation of Etching Techniques

Prior to the fabrication of the samples used for the optical experiments, the two different etching techniques (see Sec. 4.2.1.3) were tested with conventional single-layer Si wafers using only steps b-f and k of the process flow summarized in Fig. 4.10. The first tests were conducted with the DRIE technique which allowed the etching of concentrator geometries with variables heights as depicted in Fig. 5.4. Through adjustment of the various process parameters (gas concentrations, bias voltage, etching time etc.), structures with H_C from 30 μm to 80 μm and rather smooth sidewalls could be achieved (DRIE experiments were conducted by M. Schier, Corporate Technology, Siemens AG, München). The contour of the resulting sidewalls was slightly convex instead of the straight walls of tapered concentrators and concave walls of CPCs. Whether this aspect had a negative influence on the light collection characteristic was not further investigated, since the results of the simulations in Sec. 5.2.4 led to focusing on the second etching technique with KOH. The concentrator geometries fabricated with DRIE were also used to test the ridge sharpening procedure introduced in Fig. 4.11. Through two repetitions of the procedure with an individual thickness of 2 μm of the SiO_2, the ridge could be reduced from initially 2 μm to a few hundred nm as illustrated in Fig. 5.5.

Due to the intrinsic ζ_C-value of 35.3° of KOH-etched cavities, this method provides a means to fabricate LCs with very low heights in the range from 5 to 8 μm, depending on the remaining ridge. Since there occurs no significant under-etching in this process [156], the 3 μm resolution of the used lithography defined the initial ridge width of the resulting concentrator geometry as depicted in Fig. 5.6a. The sharpening procedure was necessary to achieve narrower ridges as illustrated in Fig. 5.6b,c. As the thermal oxidation of Si is based on the diffusion of oxygen molecules, it leads to smoothing and rounding of the corners and edges in comparison to the initially sharp and well defined structures (compare Fig. 5.6a with 5.6b-f). However, the SEM images in Fig. 5.6d-f demonstrate that this fabrication method provided very uniform concentrator geometries with highly smooth surfaces.

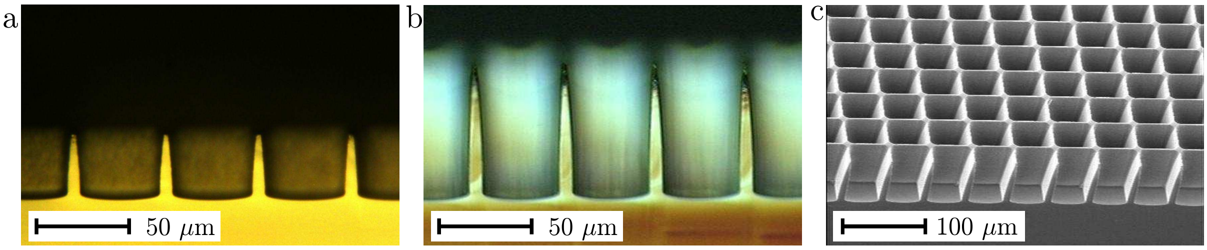

Figure 5.4: Microscope images of the cross section of a concentrator geometry with $H_\mathrm{C} = 35$ μm (a) and $H_\mathrm{C} = 75$ μm (b) fabricated using DRIE. The images were acquired with (a) a VHX 500 microscope (Keyence, Osaka, Japan) and (b) an RM 2000 microscope (Sentech Instruments, Berlin, Germany) leading to different appearances. The SEM image in (c) illustrates the uniformity of the concentrator cavities.

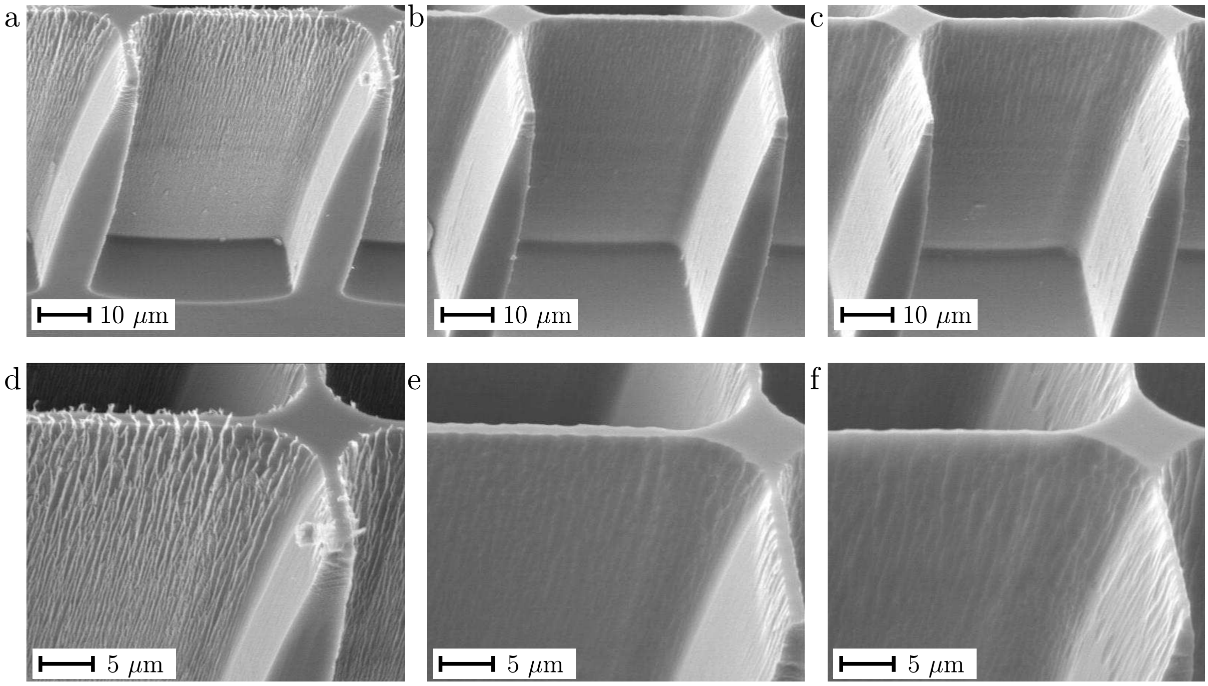

Figure 5.5: SEM images illustrating the ridge sharpening process. The initial ridge width of 2 μm (a) was reduced in two iterations (b,c) to a width of a few hundred nm. The improvement can be clearly seen in the detailed views (d-f) of the images in (a-c). The fiber-like structures visible in (a,d) are remains of the passivation polymer involved in the DRIE process.

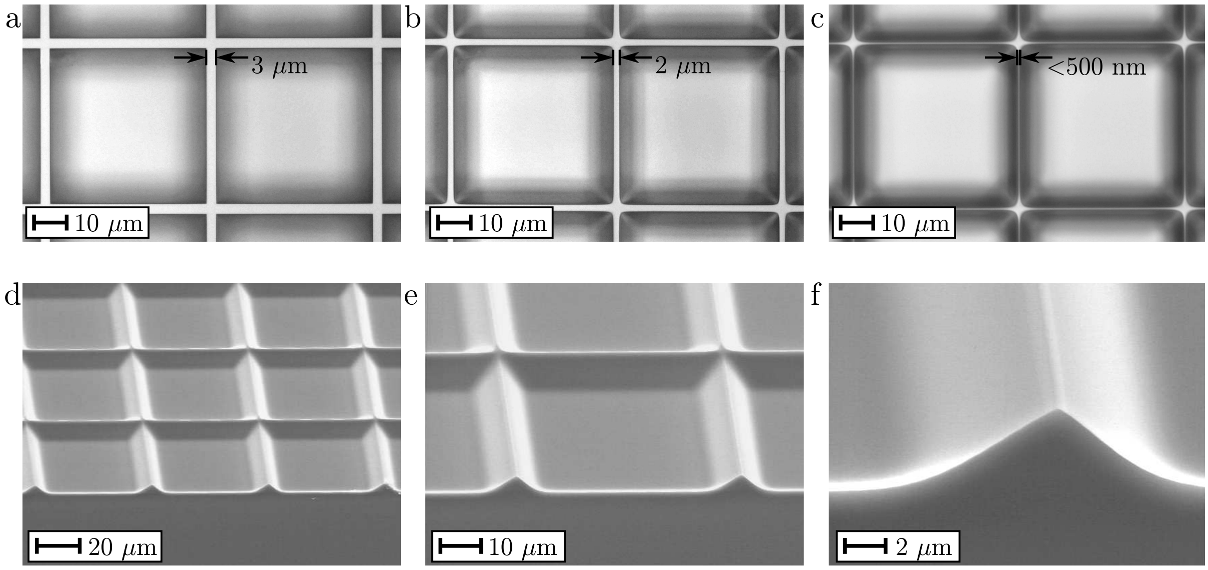

Figure 5.6: Results of the KOH etching test for the LC fabrication. The microscope images of the concentrators seen from above (a-c) demonstrate the ridge sharpening down to a few hundred nm. The SEM images in (d-f) depict the uniform concentrator geometries and smooth surfaces achieved with this technique.

5.2.2.2 Fabrication of Concentrator Samples

The LC samples for the optical experiments were fabricated using the KOH etching technique. Since the taper angle of the concentrator walls is fixed at 54.7°, the device layer thickness of the SOI substrates must be chosen according to the concentrator parameters $A_{\mathrm{In}} = 50\ \mu\mathrm{m}$ and $A_{\mathrm{Rec}} = 40\ \mu\mathrm{m}$. Two kinds of SOI substrates were available for the sample production, one having a device layer thickness of 8 μm, the other having a thickness of 5 μm. As illustrated in Fig. 5.7, this resulted in a concentrator geometry with $A_{\mathrm{Rec}} \approx 35.7\ \mu\mathrm{m}$ for the 8 μm and $A_{\mathrm{Rec}} \approx 40\ \mu\mathrm{m}$ for the 5 μm device layer wafers.

Processing the 8 μm device layer substrates including two iterations of the sharpening procedure yielded samples identified through LC_1 with a cell pitch of 50.0±0.1 μm, a ridge width of $(2.1 \pm 0.1)\ \mu\mathrm{m}$ and $A_{\mathrm{Rec}}^{LC_1} = (39.9 \pm 0.2)\ \mu\mathrm{m}$ (see Fig. 5.8a-c). The corners and edges of the LC_1 samples had slightly rounded contours as illustrated in Fig. 5.8b,c. In the case of the 5 μm device layer substrates, the fabricated samples (LC_2) had a cell pitch of 50.0±0.1 μm, a ridge width of $(2.8 \pm 0.1)\ \mu\mathrm{m}$ and $A_{\mathrm{Rec}}^{LC_2} = (40.9 \pm 0.2)\ \mu\mathrm{m}$ (see Fig. 5.8d-f). A reduction of the ridge width was not possible, as this would have changed the concentrator base width which in turn would have increased $A_{\mathrm{Rec}}^{LC_1}$, which was already slightly larger than the specified value of 40 μm. With these dimensions, the fabricated samples represented concentrators with $f_{\mathrm{Geo}}^{\mathrm{LC1}} = 64\%$ and $f_{\mathrm{Geo}}^{\mathrm{LC2}} = 67\%$. Due to the ridges with widths of 2.1 μm and 2.8 μm, the input sides of the concentrators also had geometric fill factors below 100%. These were 92% (LC_1) and 89% (LC_2).

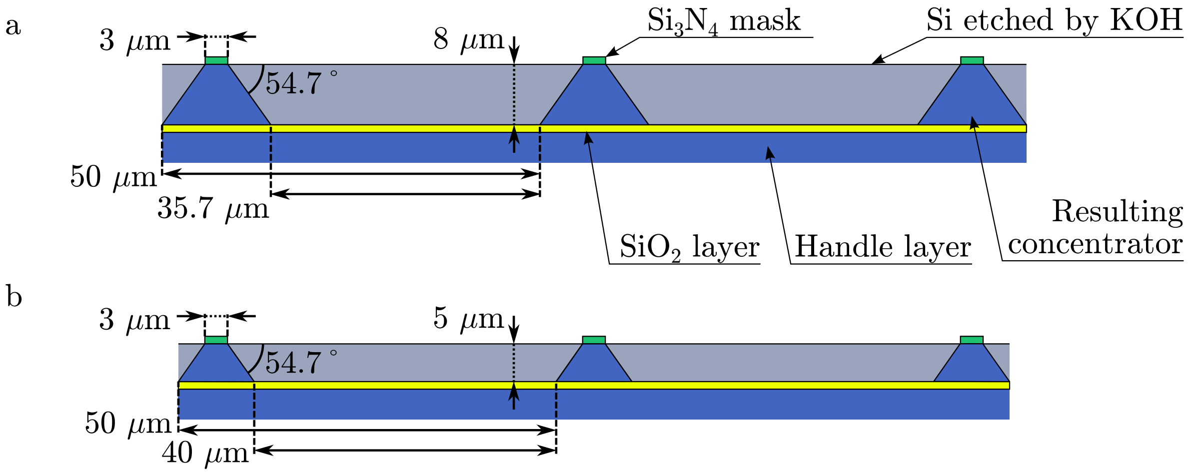

Figure 5.7: Drawing of concentrator geometry resulting from KOH etching with device layer thickness values of 5 μm (a) and 8 μm (b).

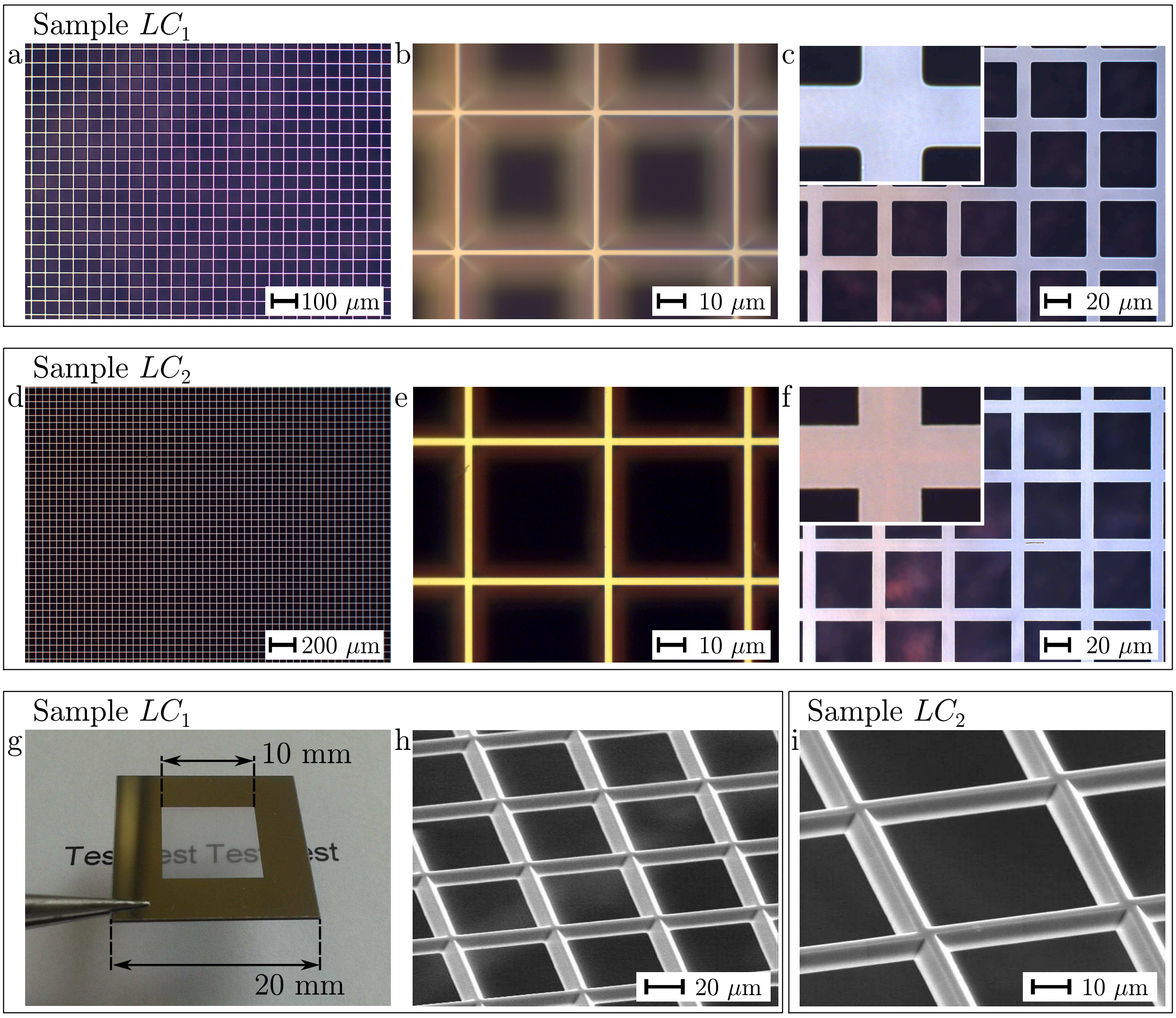

Figure 5.8: Images of the LC samples LC_1 and LC_2. The microscope images of the concentrator input side of LC_1 illustrate the uniform concentrator geometry over large scales (a) as well as the narrow ridges (b). The view in (c) shows the concentrator receiver side of LC_1 with slightly rounded corners due to the oxidization process (see inset). Very uniform structures were also achieved for LC_2 (d) but with slightly larger ridges (e). Since no oxidization process was conducted, LC_2 samples exhibited almost perfect 90°-corners on the input side (e) and the receiver side (f, see inset). Note that the scales of the insets in (c,f) have been omitted for clarity. The photograph of LC_1 in (g) shows the overall sample size and illustrates the transparency of the concentrator grid. The chosen geometry parameters resulted in concentrator grids with very delicate structures as exemplified in the SEM images of LC_1 (h) and LC_2 (i).

5.2.2.3 Encapsulation of Samples

Fabrication of the Cr grid on a glass substrate yielded a rather uniform geometry. The structured cells had a pitch of 50.0±0.1 μm and openings with a length of (40.0±0.1) μm. The isotropic etching process lead to rounded corners as shown in Fig. 5.9a. The reflection and absorption of the Cr layer was calculated from the complex RI data taken from Ref. [151]. The results of these computations are displayed in Fig. 5.9b and show that the layer is approximately 60% absorbing and 40% reflecting over a large range of incident angles and wavelengths.

Besides the chips with the Cr grid, only LC_1 samples were encapsulated with glass and epoxy due to the agreement in the geometry parameters. The resulting samples are shown in Fig. 5.9c,d. The excessive epoxy at the back side was removed using a scalpel to obtain a planar interface which allowed appropriate optical coupling to the PMT entrance window.

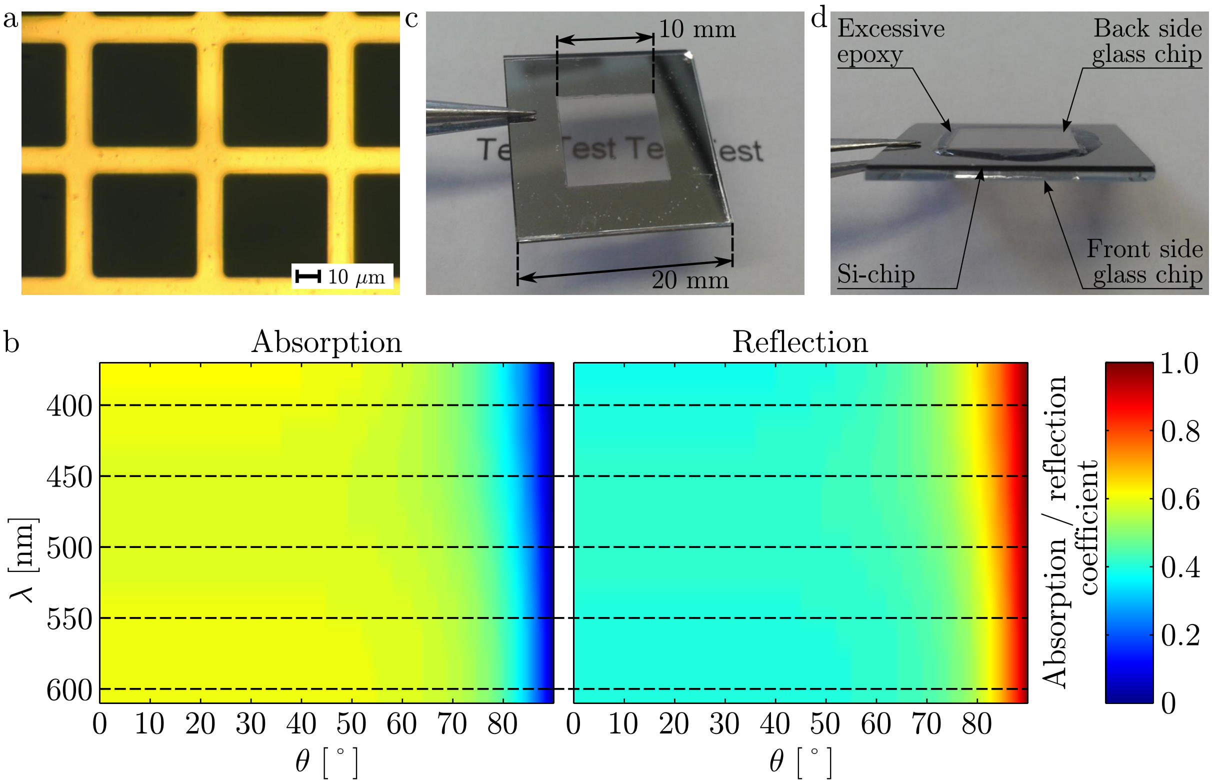

Figure 5.9: a) Microscope images of the Cr grid showing the rounded corners. b) Absorption and reflection coefficient of Cr layer as a function of incident angle and wavelength for randomly polarized light. The data has been calculated based on RI data from Ref. [151]. c) Photograph of the resulting sample for the LSO-based experiments illustrating the transparency despite of the integrated Cr grid. The side view in (d) shows the different components. In the experimental setup, the front side is facing the LSO crystal and the back side is coupled to the PMT window.

5.2.3 Validation of Transmission Characteristics

The transmission characteristics of the LC samples were modulated with oscillations of different frequencies, caused by the coherence of the laser light in combination with the optical resonator formed by sample and PD. Application of the moving average filter to the oscillating data provided smooth characteristics as illustrated in Fig. 5.10. The simulated transmission characteristics were found to be in good agreement with the filtered measurement data for both samples as shown in Fig. 5.11 for selected ϕ_{L} values and in Fig. 5.12 for the entire solid angle investigated. The slope of the characteristic could be reproduced with considerable accuracy. Modest discrepancies could be observed for shallow incident angles. These probably stem from inaccuracies in the sensitivity of the PD model and minor differences between simulations and measurements in the sample position. The quantitative analysis of the agreement between U_{Filtered} and U_{Simu} obtained through the Kolmogorov-Smirnov test yielded values for the agreement metric η of 76% (LC_1) and 73% (LC_2).

Comparing the PD voltage of the two configurations C_{Conc} and C_{Plain} at low incident angles confirms the positive influence of the concentrator geometry on the light collection. At $\theta_{\mathrm{L}} = 0°$, the amount of detected photons of C_{Conc} is by a factor of 1.31 (LC_1) and 1.22 (LC_2) larger than the values obtained for C_{Plain} (see blue dashed line in Fig. 5.11d). These factors are lower than the ratios of input and receiver side fill factors which amount to $92\%/64\% = 1.44$ (LC_1) and $89\%/67\% = 1.33$ (LC_2). The reason for this is that the incident angle of photons on the PD is changed upon being redirected by the LC sidewall. In conjunction with the angle-dependent PD sensitivity, this manipulates the amount of registered photons. This influence on the photon trajectories also leads to increased light collection at shallow incident angles for the plain configuration. Since this effect only occurs due to the experimental setup using the LC placed upside down, it can be neglected for considerations of a real SiPM and merely serves for the validation of simulated versus measured data.

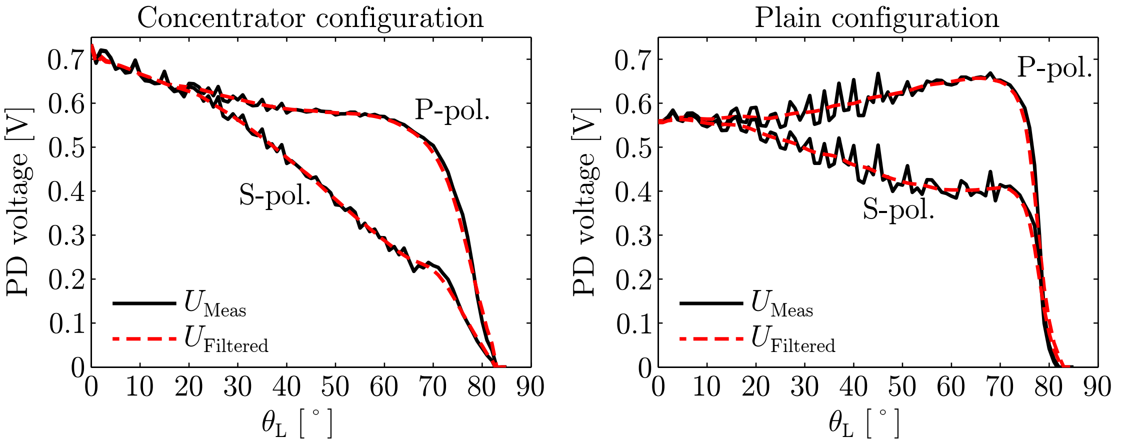

Figure 5.10: Exemplary comparison of measurement results derived from the goniometer experiment and data processed with the moving average filter for sample LC_1 at $\phi_{\mathrm{L}} = 20°$. See Fig. 4.21 for the definition of concentrator and plain configuration. The interferometric oscillations are most pronounced for the plain configuration between 20° and 50°.

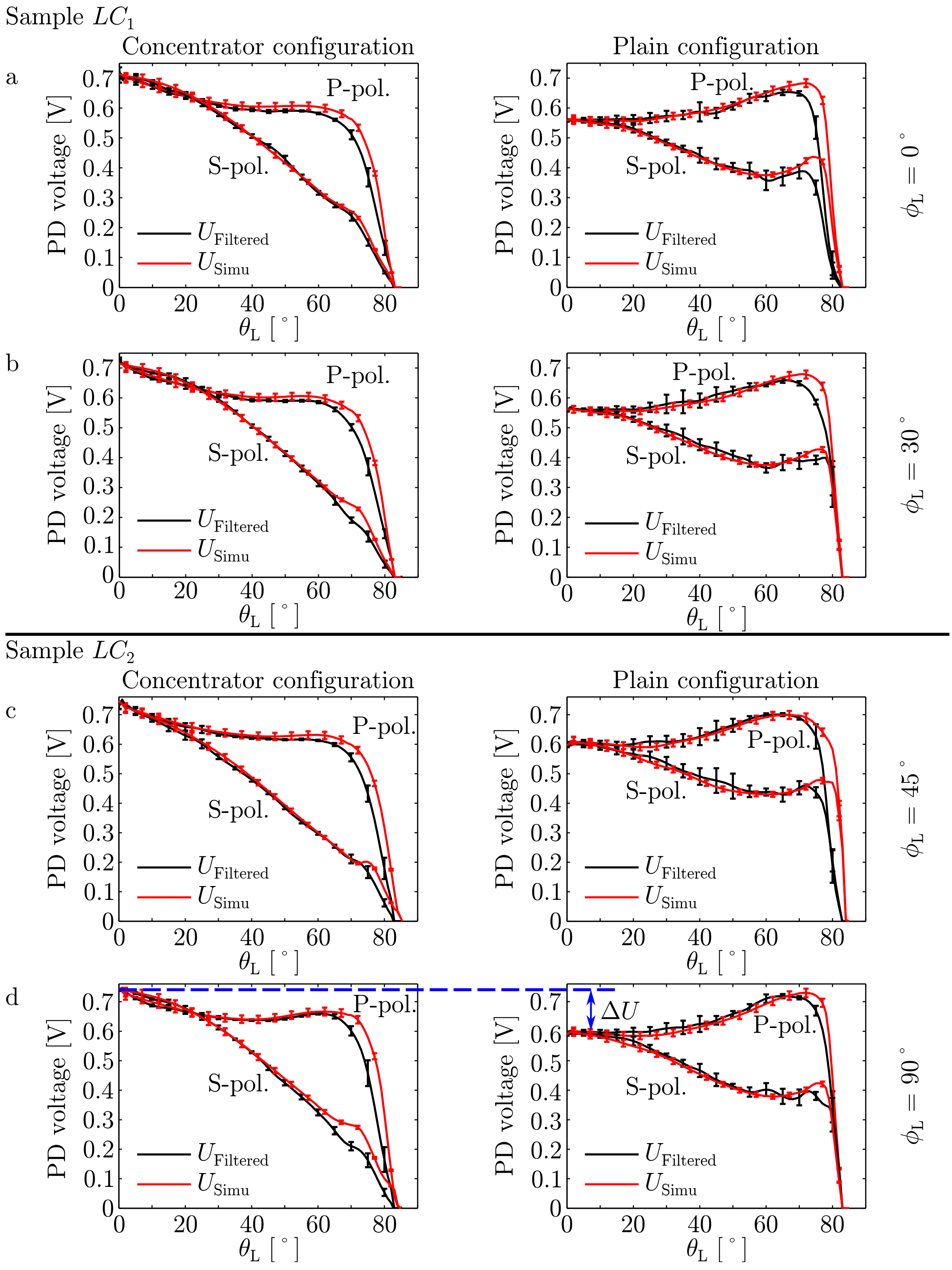

Figure 5.11: Comparison of simulated and filtered measurement data for the transmission characteristic of sample LC_1 and LC_2 at selected ϕ_{L}-values (see individual plots). The blue dashed line in (d) illustrates the improvement ΔU in light collection of the concentrator configuration versus the plain configuration.

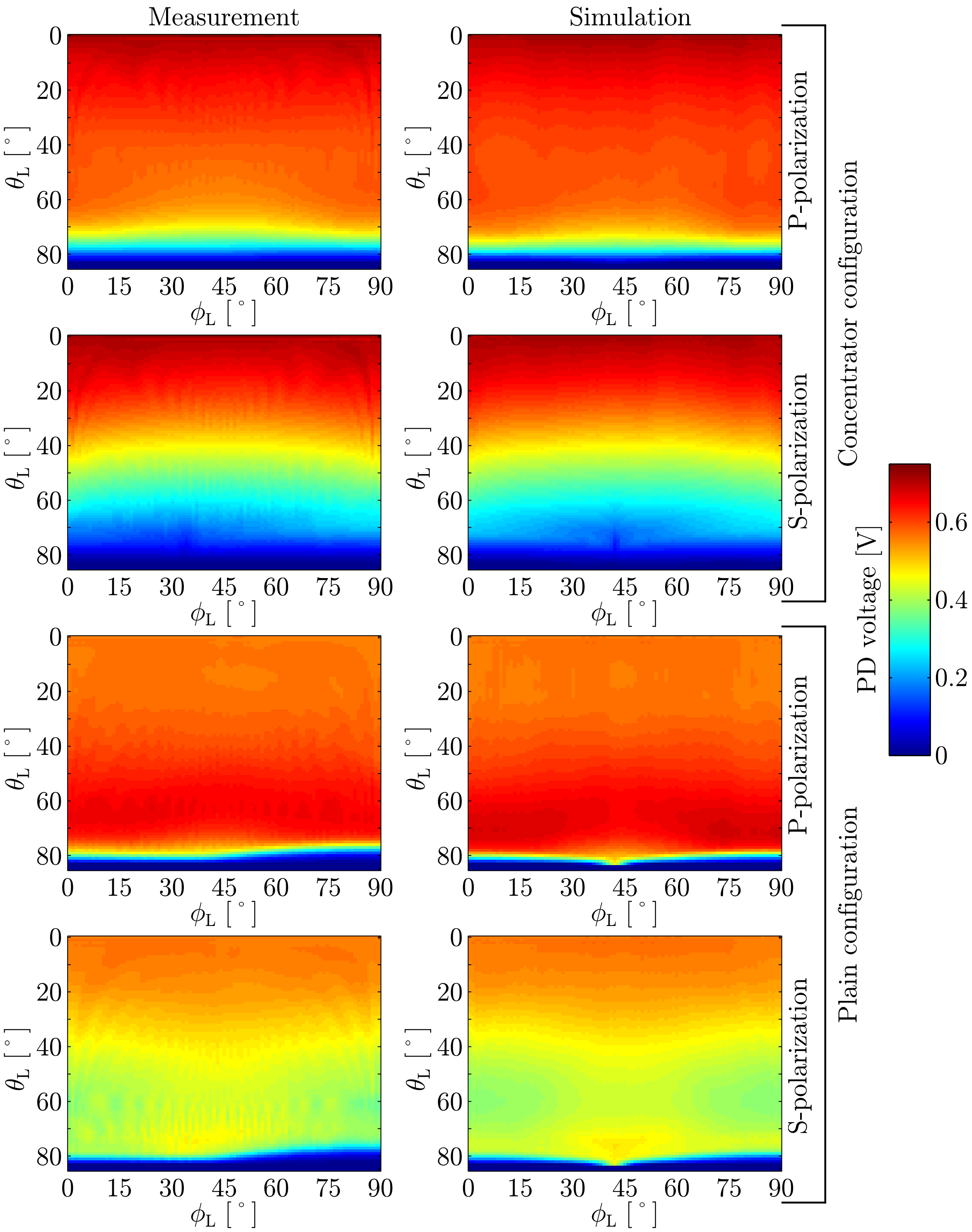

Figure 5.12: Survey of the complete simulated and filtered measurement data for sample LC_1 illustrating the agreement between computed and experimental transmission characteristics. The discrepancies between the data sets visible for $\theta_{\mathrm{L}} > 80°$ lead to different impressions regarding the symmetry of the characteristics. These are caused by inaccuracies of the PD sensitivity model in conjunction with minor sample positioning errors.

5.2.4 Impact of Light Concentrator on PET Detector Performance

The validation of the LC optical properties in the previous section facilitates their implementation into the reference PET detector model to study the impact on the light yield and timing resolution. As shown in Sec. 5.2.1, the angular collection efficiencies of LCs are strongly influenced by their height. However, the optimal concentrator configuration yielding the best light yield and CRT values cannot be found by merely combining the collection efficiencies with the angular distributions from the reference PET detector simulations. Since photons rejected by the concentrator might be incident on the SiPM at later recurrences, the LC geometry must be optimized within the framework of the optical simulations taking into account all possible photon trajectories. For this reason, a sweep of the concentrator height H_C was conducted. For each value of H_C, the polished and etched PET detector modules were equipped with the corresponding concentrator geometry and the optical simulations were carried out.

The results of these H_C sweeps are shown in Fig. 5.13. Equally for the polished and etched configuration, an LC with a height of 4 μm was found to provide the best (i.e. lowest) CRT with values of $\mathrm{CRT}^{\mathrm{LC}}_{\mathrm{Pol}} = 226$ ps and $\mathrm{CRT}^{\mathrm{LC}}_{\mathrm{Etch}} = 218$ ps, constituting an improvement by 5% versus the reference configuration without concentrator. At this H_C value, the relative light yields are $\Gamma^{\mathrm{LC}}_{\mathrm{Pol}} = 0.260$ and $\Gamma^{\mathrm{LC}}_{\mathrm{Etch}} = 0.290$, which represent improvements by 15%.

The 4 μm-LC leads to a modest increase in the angular light collection compared to the reference setup without LC as illustrated in Fig. 5.14a for the etched detector configuration. In contrast to this, LCs with larger heights such as $H_\mathrm{C} = 20$ μm exhibit increased light collection for $\theta < 45°$ and reduced collection for larger incident angles. The integrals of these characteristics divided by the total amount of incident photons yield overall collection efficiencies of 62% (reference), 65% (4 μm-LC), and 62% (20 μm-LC). Although the immediate gain in light collection at first incidence caused by the 4 μm-LC amounts to only 3%, its

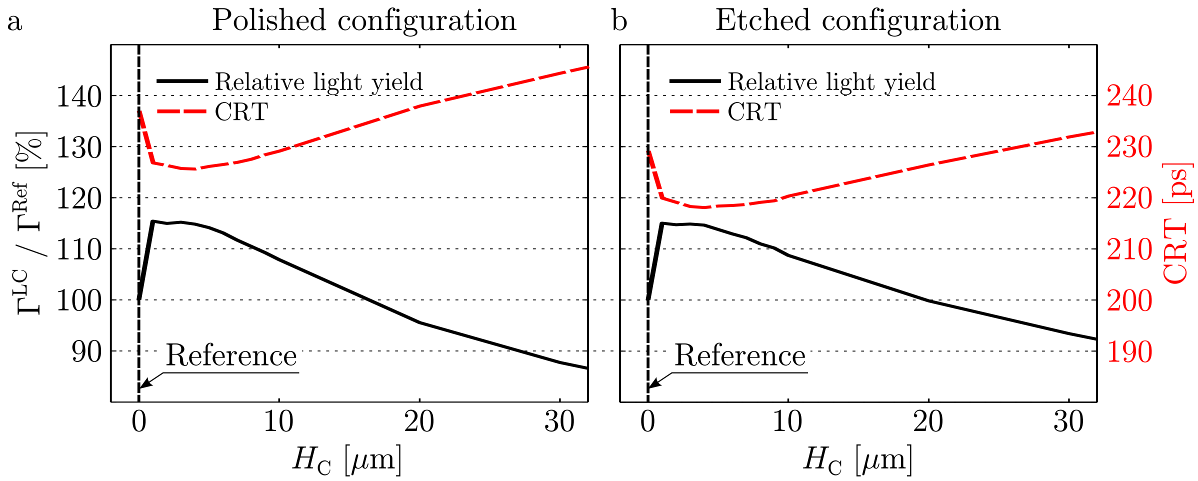

Figure 5.13: Light yield Γ^{LC} relative to reference Γ^{Ref} and CRT as a function of H_C simulated for the polished (a) and etched (b) detector configuration. A concentrator height of 0 corresponds to the reference without concentrator and is highlighted through the vertical dashed lines. Note that the vertical axes on the very left and right apply to both plots. Error bars are not shown, since the statistical inaccuracy was below 0.1%.

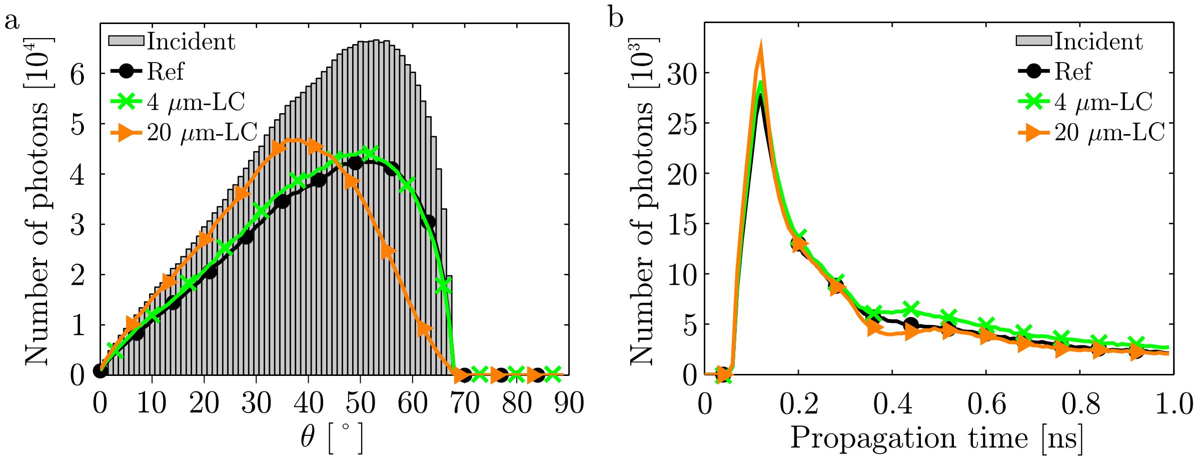

Figure 5.14: a) Comparison of angular collection efficiencies for the reference (Ref), an LC with $H_{\mathrm{C}} = 4$ μm, and an LC with $H_{\mathrm{C}} = 20$ μm for the etched detector configuration. The bars indicate the angular distribution of photons at their first incidence on the SiPM using 1°-bins. The curves depict the photons that are absorbed within the active area of the SiPM. The distribution of incident angles ends at 68° due to the refraction of light at the interface optical glue/epoxy. b) Propagation time distribution of detected photons of the three configurations in (a) using 10 ps bins.

accumulation over photons returning several times on the SiPM surface causes the predicted improvement in light yield by 15%. In the case of the 20 μm-LC, the losses of a higher concentrator caused by increased absorption and rejection of incident photons spoil the benefit of collecting more photons with low incident angles.

The angular characteristics of different LCs also influence the propagation time distribution of detected photons as shown in Fig. 5.14b which in turn affects the CRT. Since photons with low incident angles mostly correspond to direct trajectories and hence short propagation times, the timing distribution of the 20 μm-LC exhibits a higher leading peak than the reference. For the etched detector configuration, this leads to a modest improvement of 3 ps in CRT versus the reference despite the almost identical light yields (see Fig. 5.13b). In contrast to this, the collection efficiencies and propagation time distributions of the reference and the 4 μm-LC are very similar. Nevertheless, the timing simulations revealed an improved CRT for the 4 μm-LC by 11 ps, which is lower than the 16 ps predicted for a 15% gain in light yield by the correlation from Eq. 2.13. A discussion of this discrepancy is given in Sec. 6.4.

The optimal LC configuration differs from the geometry realized in the LC samples: first, the taper angle at $H_{\mathrm{C}} = 4$ μm is 51.3° instead of the 35.3° of the KOH-etched cavities. Secondly, the samples LC_1 had a remaining ridge of 2.1 μm width compared to the perfectly sharp simulated concentrator. The impact of these differences was studied through implementing the geometry of LC_1 into the optical simulations of the detector module. For the polished configuration, this resulted in a light yield of 0.255 and a CRT of 228 ps. For the etched configuration, the light yield was 0.285 and the CRT was 219 ps. These values differ only slightly from the results obtained for the optimal solution with $H_{\mathrm{C}} = 4$ μm and represent improvements of 12% to 13% in light output and 4% in CRT versus the reference.

5.2.4.1 Impact of Fabrication-related Concentrator Imperfections

The gains in light yield and CRT predicted in the previous section were based on simulations that used some idealizations, for instance a perfect alignment of the LC on the SiPM or reflector walls without surface scattering. In this section, the results of a simulation study are presented, that analyzes the impact of fabrication-related imperfections on the performance of an LC. All these studies considered a concentrator with $H_\mathrm{C} = 4\ \mu\mathrm{m}$.

Horizontal Alignment of Concentrator on SiPM If the LC is fabricated as an independent device apart from the SiPM, the mounting on the sensor surface can only be achieved with limited accuracy depending on the assembly process. Typically, pick and place robots are used in the semiconductor industry for automated positioning combining high precision and fast processing. High end systems can provide an accuracy down to 2 μm (standard deviation). To evaluate the sensitivity of the LC approach on the horizontal alignment, the concentrator was placed off-center by a certain distance (see Fig. 5.15), first along one axis (Δx) and then diagonally along both lateral axes ($\Delta x = \Delta y$). The optical MC simulations indicate, that the gain in light yield through the LC is still larger than 10% for a one-dimensional displacement of up to 2 μm (see Fig. 5.16a). For the more realistic situation of LC-misalignment in both lateral dimensions (see Fig. 5.16b), a 2 μm offset already decreases the benefit in light yield to 7%. The negative effects on the timing resolution are even more pronounced and a misalignment of $\Delta x = \Delta y = 2\ \mu\mathrm{m}$ leads to a CRT equal to the reference.

Vertical Gap between Concentrator and SiPM If the LC device is bonded to the SiPM surface using an additional material as glue, it will have a certain vertical distance Δz to the sensor. In the case of using a transparent glue, the inactive areas of the SiPM become accessible to photons despite of the mounted concentrator. This situation was studied through vertical displacing the LC, assuming it was perfectly aligned in the horizontal plane

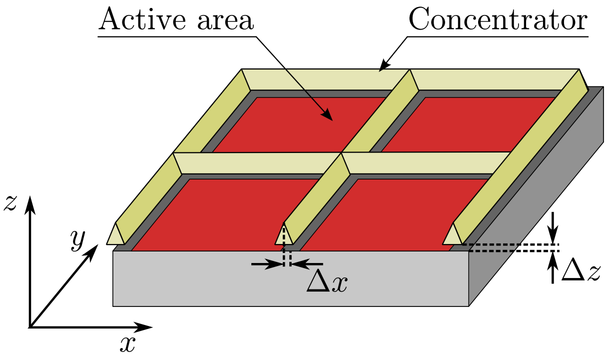

Figure 5.15: Illustration of the fabrication related imperfections of LCs on SiPMs studied. A horizontal misalignment of the LC relative to the SiPM microcells is given through Δx and Δy (not shown). Mounting the LC on the SiPM surface might lead to a vertical gap Δz.

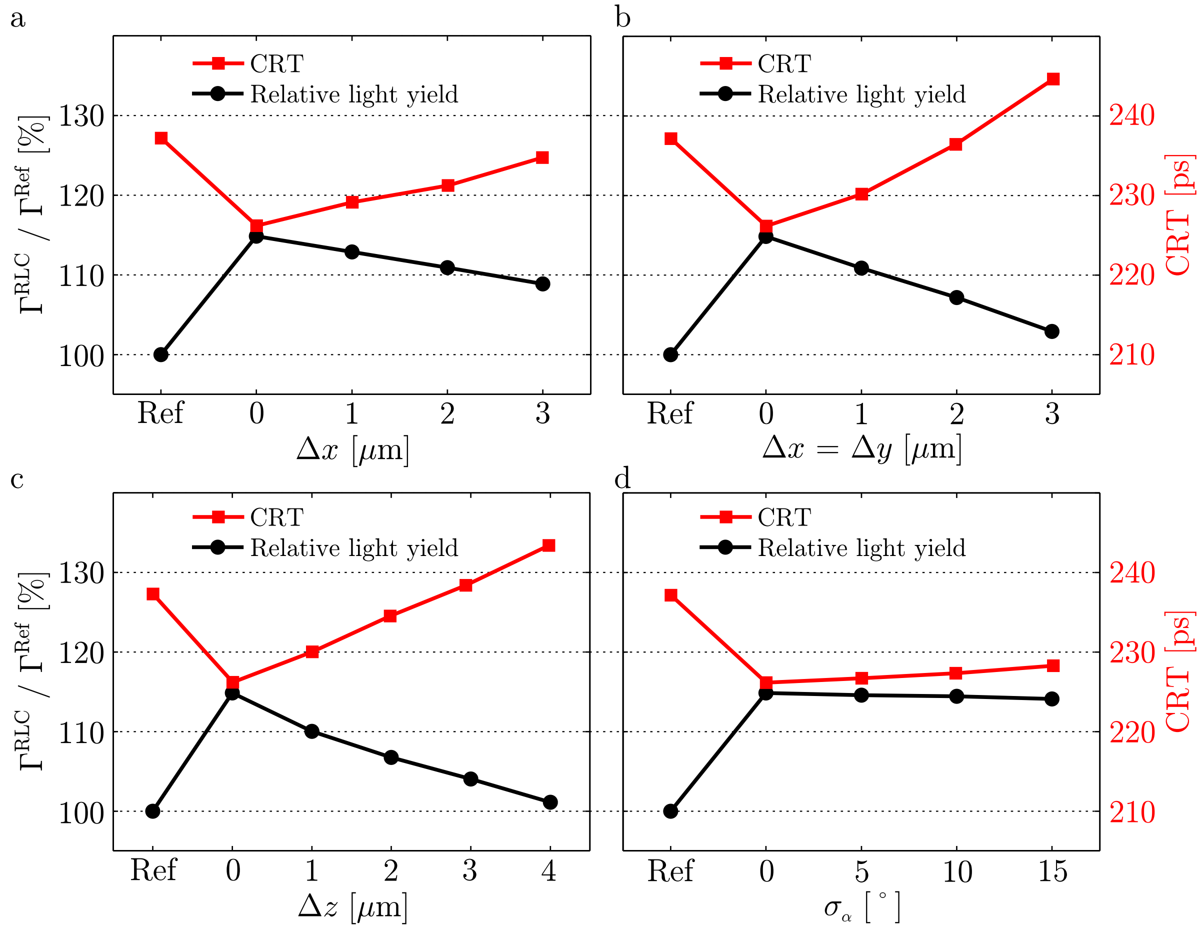

Figure 5.16: Results of the simulation studies evaluating the sensitivity of the LC approach to imperfections such as horizontal misalignment in one (a) or two dimensions (b), a vertical gap between LC and SiPM (c), and reflector walls with rough surfaces (d). The values at the abscissa "Ref" correspond to the results obtained without LC. Error bars are omitted, since the statistical inaccuracy of the simulations was below 0.1%.

and the glue had the same RI as the SiPM epoxy window. The simulation results show, that vertical distances larger than 1 μm cause the improvement in light yield to drop below 10% (see Fig. 5.16c). The CRT was decreasing even faster and a timing resolution inferior to the reference was predicted for an offset of 3 μm.

Surface Scattering of Reflector Walls Depending on the fabrication process used for the LC, the reflecting walls can have a certain roughness that scatters light. The impact of this was studied using the optical simulations with implementations of LCs that had roughness values σ_α from 5° to 15°. Remarkably, the results indicate that for the combination of the investigated detector configuration with a 4 μm-LC, the scattering of photons has only little impact on the light yield and CRT. However, care must be taken for transferring this conclusion to other LC geometries with larger heights and in combination with different scintillator geometries.

5.2.5 LSO-based Light Yield and Timing Measurements

The measurements of light yield and timing using the two LSO/PMT setups were conducted with the encapsulated Cr grid chip and the LC_1 sample, since these had almost identical values of f_{Geo}. The histograms of detected scintillation photons of the two samples are compared in Fig. 5.17 for the (4×4×7) mm^3 and the (4×4×20) mm^3 LSO crystal. The differences in the abscissas of the photopeak between the Cr grid and LC_1 are clearly visible and amount to $N_{\text{Det}}^{\text{LC1}}/N_{\text{Det}}^{\text{Cr}} = (9 \pm 2)\%$ for both scintillator geometries (average ± standard deviation of all acquired data sets). Since the experiments used the same LSO crystal and test PMT, these increases in light output can be attributed to changes in the photon transfer caused by the LC in comparison to the partly absorbing/reflective metal grid mimicking an SiPM. Optical MC simulations of the experimental setup predicted gains in light yield of 8% for both LSO geometries. This agrees with the experimental results within the accuracy of the measurement.

The increase in light collection can also be seen in the pulse shapes of the test PMT depicted in Fig. 5.18a,b. The configurations equipped with the LC_1 sample exhibit larger amplitudes than the Cr grid setups. The increased light yield and PMT pulse amplitudes also lead to an improvement in the temporal resolution as can be seen in the timing curves $\delta t_{\text{Test}}(U_{\text{LED}})$ in Fig. 5.18c,d. The best timing resolution δt_{Test} for the LC_1 configuration was (279 ± 3) ps and (231 ± 3) ps for the 7 mm and 20 mm high LSO, respectively. Using the Cr grid sample, the minimal δt_{Test} values were (289 ± 4) and (239 ± 3). All values represent the average ± standard deviation of the acquired data sets. These results indicate an improvement in timing resolution of 3% (7 mm LSO) and 4% (20 mm LSO), which correlates well to the observed gain in light yield. Although these differences are only modest, they represent significant changes with respect to measurement accuracy and reproducibility.

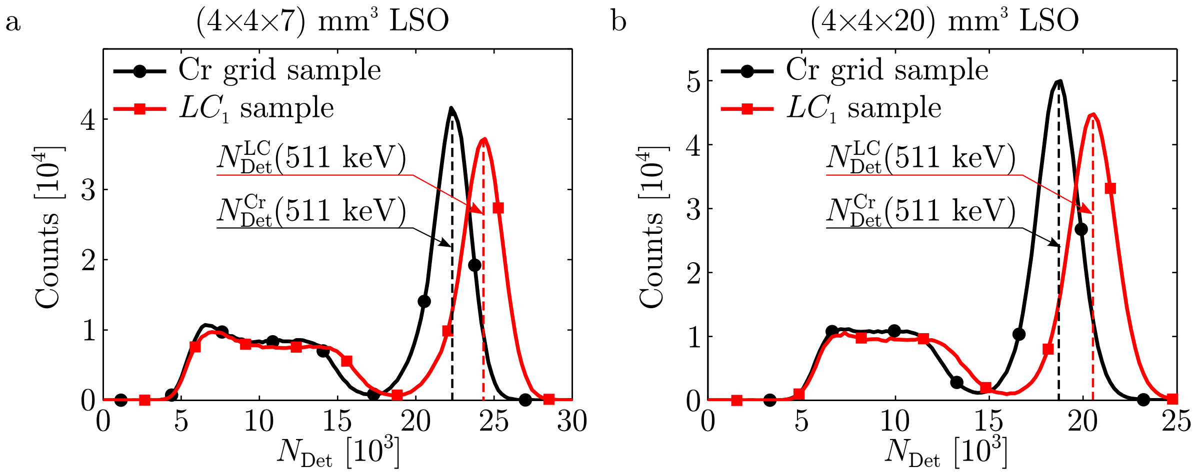

Figure 5.17: Histogram of the amount of detected photons N_{Det} comparing the results of the LC_1 and the Cr grid sample for the (4×4×7) mm^3 LSO (a) and the (4×4×20) mm^3 LSO (b). The abscissas corresponding to the centers of the 511 keV photopeaks are highlighted with dashed lines and illustrate the gain in light output through the concentrator. The plateau in the range from $5 \cdot 10^3$ to approximately $15 \cdot 10^3$ corresponds to the Compton continuum described in Sec. 2.2.3.

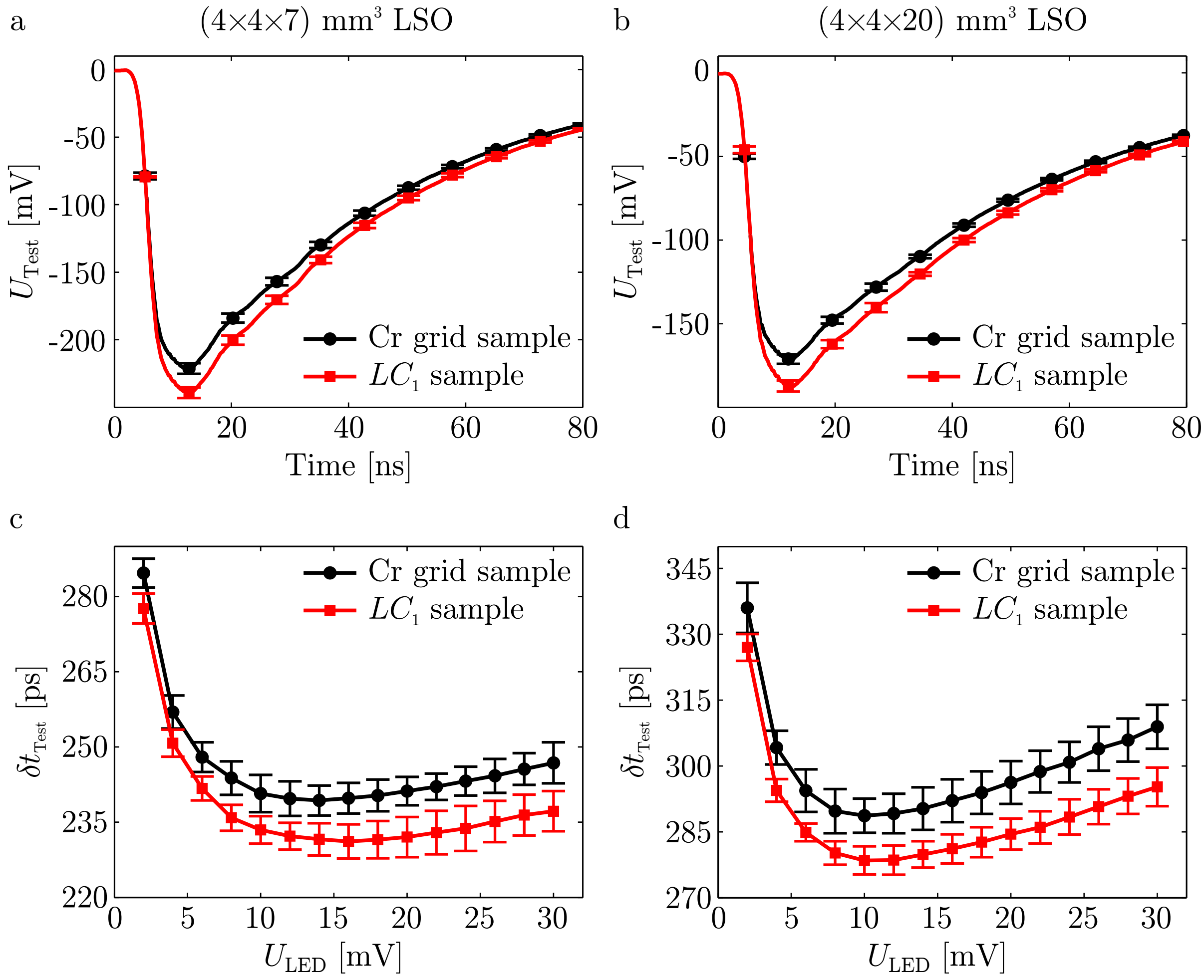

Figure 5.18: Pulse shape of the PMT output comparing the LC_1 and the Cr grid sample for the (4×4×7) mm^3 LSO (a) and the (4×4×20) mm^3 LSO (b). The larger amplitudes in the LC_1 curves are a consequence of the increased light output through the concentrator. This also leads to improved timing resolution δt_{Test} as shown in the timing curves (c,d). The error bars represent ± one standard deviation of the repeated measurements.

5.3 Photonic Crystals for Improved Light Extraction

5.3.1 Implementation of Photonic Crystal Simulations

For each PhC configuration to be implemented into the optical MC simulations, the corresponding LUTs were calculated with GD-Calc. The maximum number of (θ, ϕ)-pairs was 16 200 per wavelength (θ from $0°$ to $180°$ with $0.5°$ increment; ϕ from $0°$ to $45°$ with $1°$ increment). This required a mean computation time of 6 s per (θ,ϕ)-pair using a workstation equipped with a quad core processor (Intel Xeon W3565, 3.2 GHz). The implementation of the PhC DLL into the optical simulations causes an increase in the ray tracing computation time by up to 50% per invocation. The impact on the total simulation time for more complex models strongly depends on the geometry, the number of photon-PhC interactions, and the lengths of the individual photon trajectories. In this work, the simulation time for PET detector modules was reduced by up to 30% for configurations using PhCs due to attenuated light trapping which led to shorter photon paths.

5.3.2 Optical Properties of Photonic Crystals

With the average computation time of 6 s for a single (θ, ϕ)-pair, the calculation of the transmission characteristic $T_{\mathrm{PhC}}(\theta, \phi)$ of an orthogonal PhC took approximately 6 hours 45 minutes using one degree resolution for θ and ϕ. To limit the computation time of the initial parameter sweeps, a rather coarse angular resolution using $\Delta\theta = 5°$ and $\Delta\phi = 5°$ was used. Hence, the resulting curves shown in Fig. 5.19 are not very smooth and the TIR-cutoff appears less abrupt.

The sweeps indicate that the PhC lattice pitch a has the most significant impact on the transmission behavior of PhCs. This is due to the fact that a directly influences the number of propagating diffraction orders according to Eq. 3.33. As demonstrated in Ref. [25], PhCs only cause a non-zero transmission for $\theta > \theta_{\mathrm{TIR}}$ in the so called photonic regime, which applies to the region of $a \gtrsim 0.3 \cdot \lambda$. The reason for this is, that structures which are significantly smaller than the wavelength of the incident light cannot be resolved by the EM wave and do not cause diffraction. However, in the photonic regime, the diffraction also leads to a decrease in transmission for light incident with $\theta < \theta_{\mathrm{TIR}}$, as exemplified in Fig. 5.19a.

As can be seen in Fig. 5.19b, the cavity size s also has a strong influence on the transmission behavior of PhCs whereas the third geometry parameter h has only modest impact (see Fig. 5.19c). The RIs of the PhC bulk and the cavities are also important for the transmission of PhCs as shown in Figs. 5.19d,e. Especially, the transmission for $\theta > \theta_{\mathrm{TIR}}$ is strongly correlated to n_{Bulk} (see Fig. 5.19d). The symmetry of the PhC grating has no significant impact and similar transmission characteristics can be achieved with hexagonal and orthogonal PhCs.

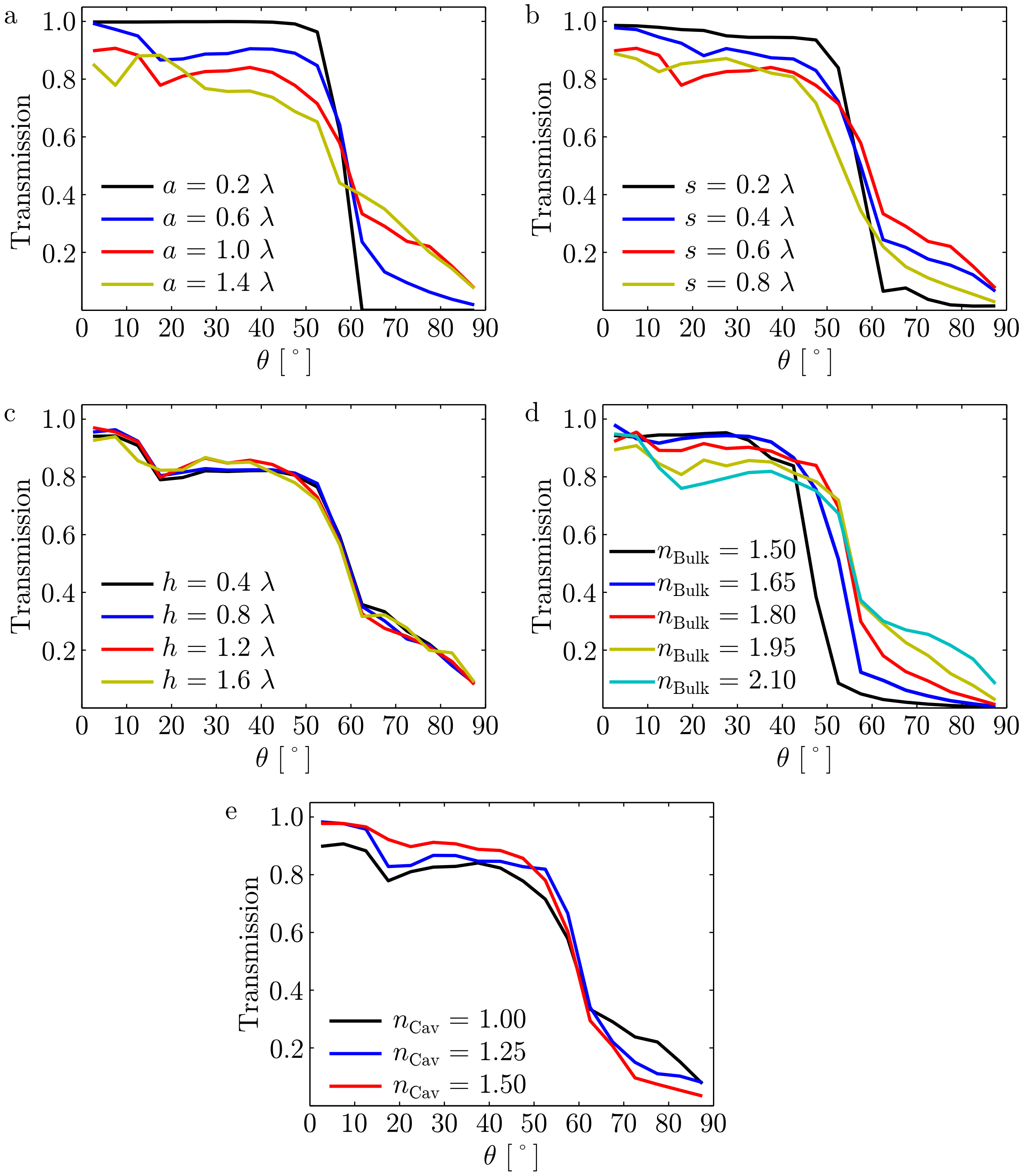

Figure 5.19: Exemplary simulation results of the initial parameter sweeps illustrating the significance of various PhC characteristics such as pitch a (a), cavity size s (b), height h (c), bulk RI n_{Bulk} (d), and cavity RI n_{Cav} (e). The transmission characteristics were derived at a wavelength $\lambda = 420$ nm for an interface between $n_1 = 1.82$ and $n_2 = 1.5$ equipped with a hexagonal PhC. The basic PhC parameters were $a = \lambda$, $h = a$, $r = 0.6 \cdot a$, $n_{\mathrm{Bulk}} = 2$, and n_{Cav}=1. Each subfigure depicts the variation of one characteristic with all other properties being constant.

5.3.3 Photonic Crystal Samples fabricated with EBL

Five different PhC samples were fabricated using the EBL method: two with a hexagonal and three with an orthogonal grating symmetry. The parameters a and s were chosen based on the initial parameter sweeps with the goal to obtain diverse transmission characteristics with pronounced diffractive effects. A summary of the specified geometry parameters and their values confirmed with SEM is surveyed in Table 5.2. The measured values for the pitch a differ from the specifications by $\leq 3\%$. The cavity size s deviates from the specified values by up to 17% (O_1) which is far less accurate than the actual precision of EBL. This inaccuracy was caused by the imperfect adjustment of the EBL focus plane due to the transparency of the substrates. For the same reason, the cavities shown in the SEM images in Figs. 5.20 and 5.21 have a rather round geometry although a quadratic electron beam was used. Variations of the PhC thickness h were negligible.

Table 5.2: Summary of PhC sample characteristics: specified (subscript "Spec") and measured (subscript "Meas") geometry parameters a and s and agreement metric η.

Sample name	PhC symmetry	a_{Spec} [nm]	a_{Meas} [nm]	s_{Spec} [nm]	s_{Meas} [nm]	η [%]
H_1	Hex.	798	793±4	463	506±20	71
H_2	Hex.	630	633±4	277	277±10	98
O_1	Orth.	672	670±6	325	379±10	73
O_2	Orth.	588	584±7	282	325±12	71
O_3	Orth.	504	504±3	290	299±9	77

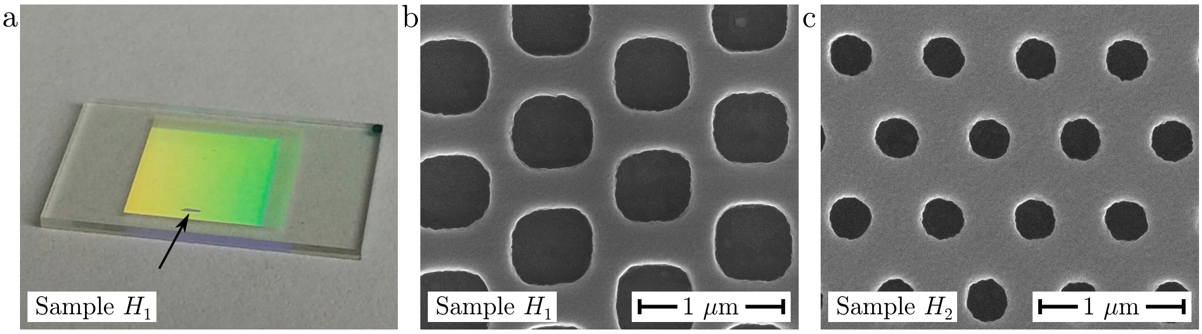

Figure 5.20: a) Photograph of the sample chip H_1. The area coated with the PhC is clearly visible due to the dispersive diffraction of the incident light. The arrow highlights a damaged area of the coating inflicted during the dicing process. The SEM images in (b,c) show the hexagonal samples used for the optical experiments. The different geometries of the cavities (rounded rectangles to cylindrical) caused by misalignment of the EBL focus are clearly visible.

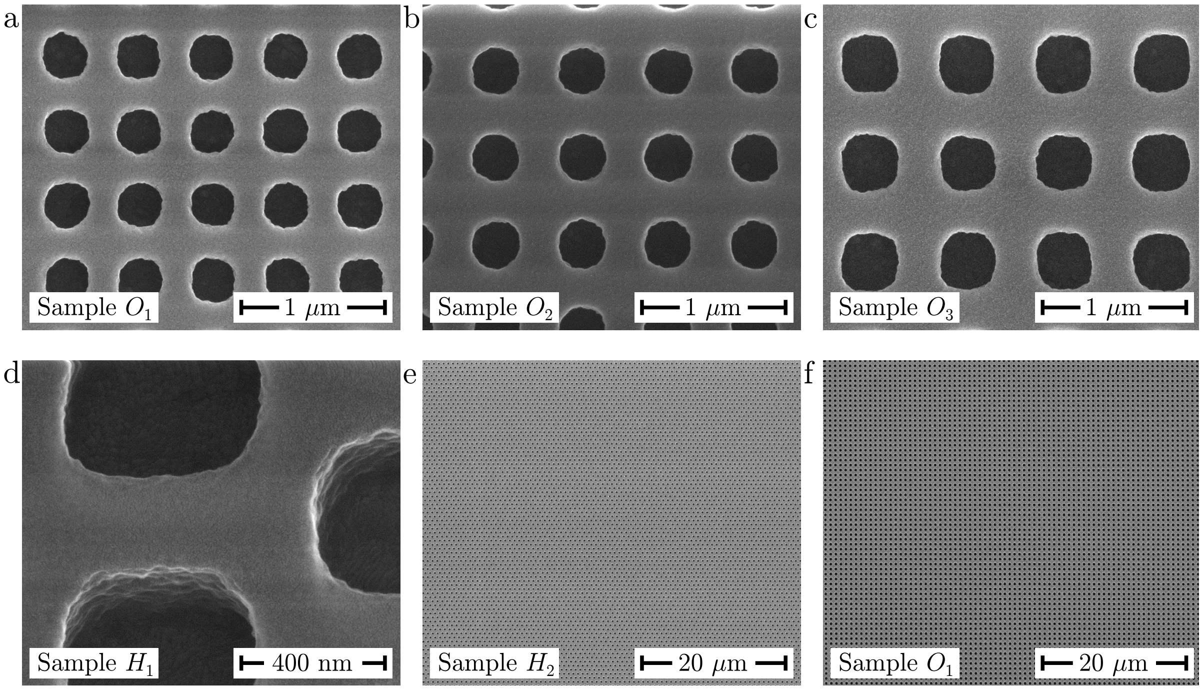

Figure 5.21: SEM images of the orthogonal PhC samples used for the optical experiments (a-c). The close-up view of H_1 with a perspective tilted by 20° in (d) depicts details of the cavities written into the resist. The observed roughness of the cavities in the range of a few nanometers was not found to affect the optical characteristics. The SEM images of H_2 and O_1 in (e) and (f) using lower magnifications than (a-c) illustrate the uniformity of the PhC patterns.

5.3.4 Validation of Transmission Characteristics

First, the calibration experiment using a sample without PhC coating was conducted. For this setup, the best matching between measured and simulated PD signals was obtained by adjusting the optical properties of the PDMS layer to $n_{\mathrm{PDMS}} = 1.45$ and $l_{\mathrm{Abs,PDMS}} = 10$ mm, which led to the curves depicted in Fig. 5.22. The effect of TIR is clearly visible through the cutoff in the PD voltage at 33°, which corresponds to the critical angle for the extraction of light from the glass hemisphere into air. Comparing measured and simulated datasets from the calibration experiment indicated a mean difference of 7% ± 1% leading to $\gamma^{\mathrm{PhC}}_{\mathrm{Simu}} = 8\%$. The observed differences showed a minor dependence on ϕ_{L} and the polarization. The largest discrepancies were observed for θ_{L}-values close to the TIR-related cutoff of the curves. In these regions, the division by very low PD voltages can lead to very large relative differences.

Next, the transmission measurements of the PhC samples were conducted. The data acquired with the angular increment $\Delta\phi_{\mathrm{L}} = 1°$ exhibited no misalignment in the periodic features of the PhC transmission characteristics. Hence, the azimuthal inaccuracy of the setup was estimated as $\delta\phi_{\mathrm{L}} = 1°$. Based on the agreement shown in Fig. 5.22 regarding the TIR-cutoff measured at an increment of $\Delta\theta_{\mathrm{L}} = 0.5°$, the elevation angle inaccuracy was estimated to be $\delta\theta_{\mathrm{L}} = 0.5°$. Analyzing the variation of U_{Meas} for changes $\pm\delta\theta_{\mathrm{L}}$ and $\pm\delta\phi_{\mathrm{L}}$ led to a measurement uncertainty $\gamma^{\mathrm{PhC}}_{\mathrm{Meas}}$ of 7%.

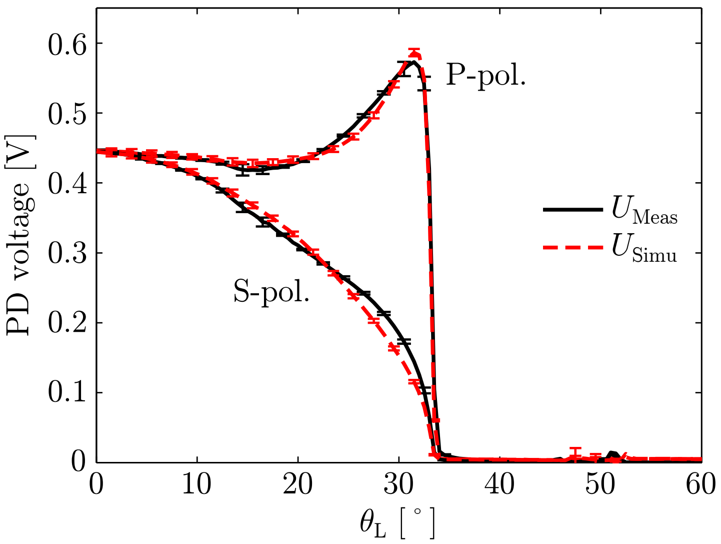

Figure 5.22: PD voltage vs. θ_L averaged over ϕ_L for the calibration experiment using a sample without PhC coating. The TIR-cutoff at 33° is clearly visible. The errorbars represent the standard deviation of the data sets acquired for different ϕ_L-values. The average relative difference was used to estimate $\gamma_{\text{Simu}}^{\text{PhC}}$.

The simulations were found to be in good agreement with the measured transmission characteristics as illustrated in Fig. 5.23. Distinct features such as peaks and dips can be reproduced by the simulations. Even certain spikes in the PD curves around $\theta_L \approx 50°$, which are caused by light scattered from the sample holder and other mechanical fixations, could be observed for both measured and simulated data. This can be seen as an indicator for the accurate replication of the experimental setup within the optical simulations. The agreement of measured and theoretical sample characteristics can also be appreciated in Fig. 5.24, which displays the transmission coefficients of the entire range of (θ_L,ϕ_L,q)-values that have been studied. These plots also show the 90°- and 60°-periodicity of the characteristics of orthogonal and hexagonal PhCs, respectively. The quantitative agreement analysis using the Kolmogorov-Smirnov test led to values for the agreement metric η of 71% or better as detailed in Table 5.2.

Besides the validation of the simulation technique, the results also prove that PhCs exhibit a transmission behavior different from plain interfaces (see Fig. 5.23d). On the one hand, the PD voltage for $\theta_L = 0°$ is up to 25% lower versus the plain surface of the calibration sample. On the other hand, there is no TIR-related cutoff at $\theta_L = 33°$. Instead the transmission coefficient gradually decreases to zero up to an elevation angle of 52°, which corresponds to an incident angle on the PhC of $\theta_{\text{PhC}} = 76°$.

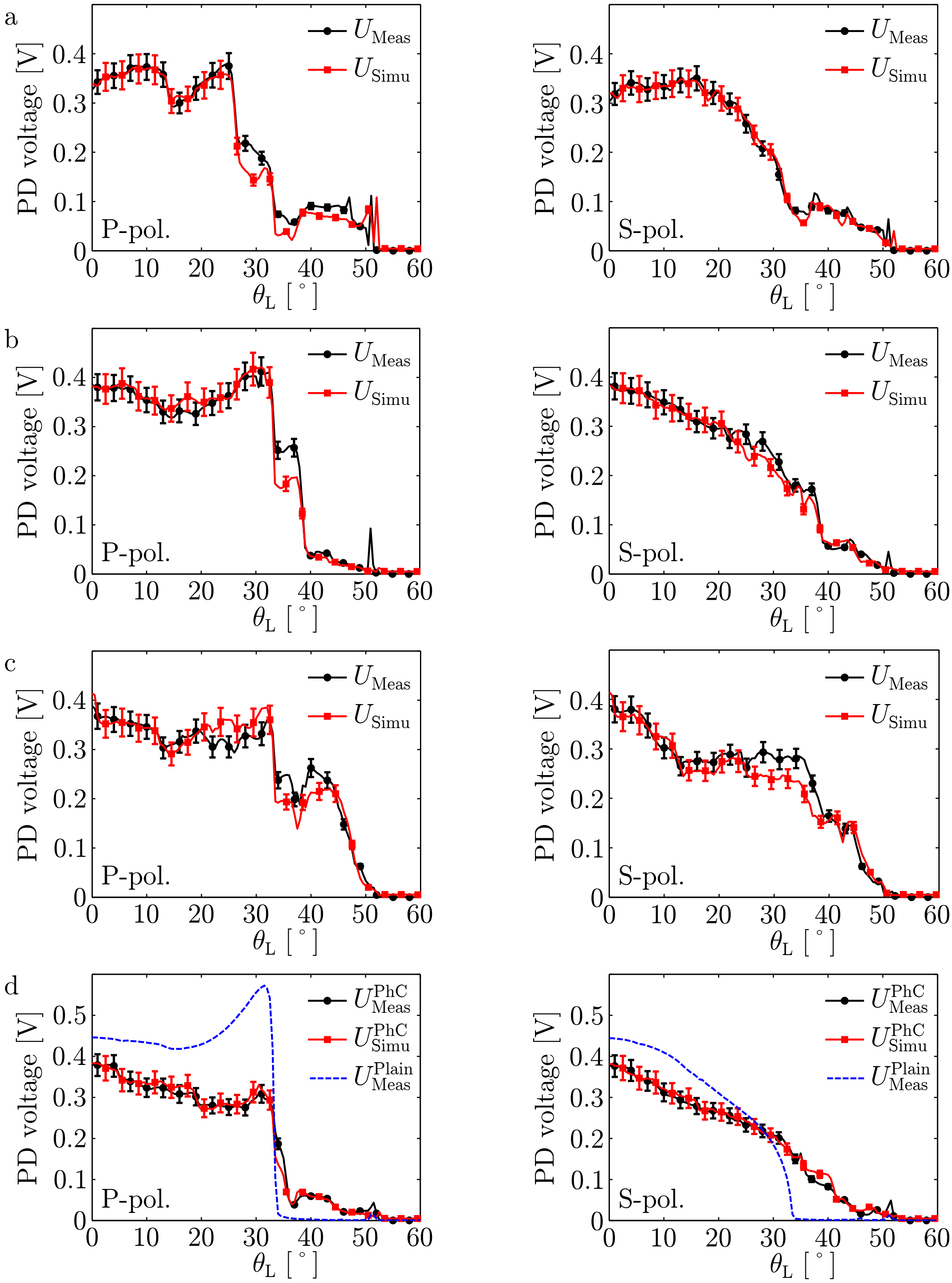

Figure 5.23: Comparison of measured and simulated transmission characteristics of PhC samples at selected ϕ_{L}-values: H_1 at $\phi_{\mathrm{L}} = 0°$ (a), H_2 at $\phi_{\mathrm{L}} = 30°$ (b), O_1 at $\phi_{\mathrm{L}} = 45°$ (c), and O_3 at $\phi_{\mathrm{L}} = 25°$ (d). The curves illustrate the agreement between experiment and simulation. In (d), the transmission characteristic of a plain sample without PhC has been added illustrating the differences in the transmission curves between samples with and without PhC coating.

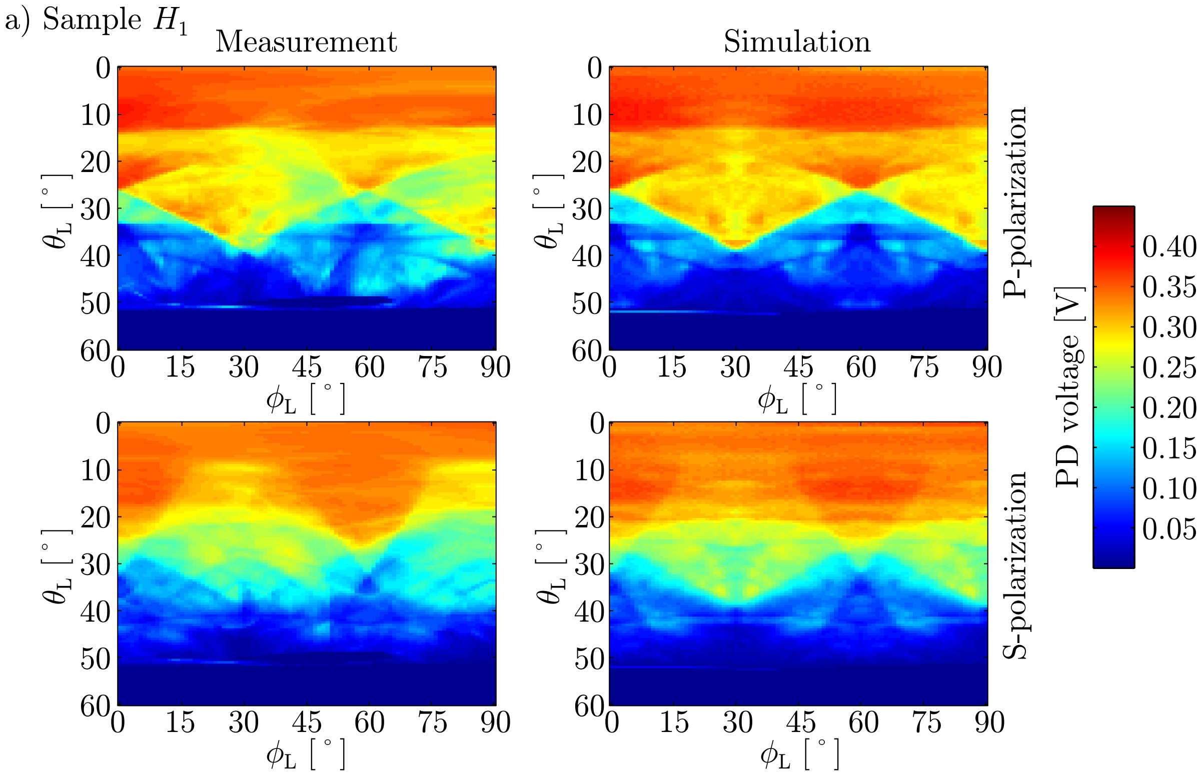
a) Sample H_1

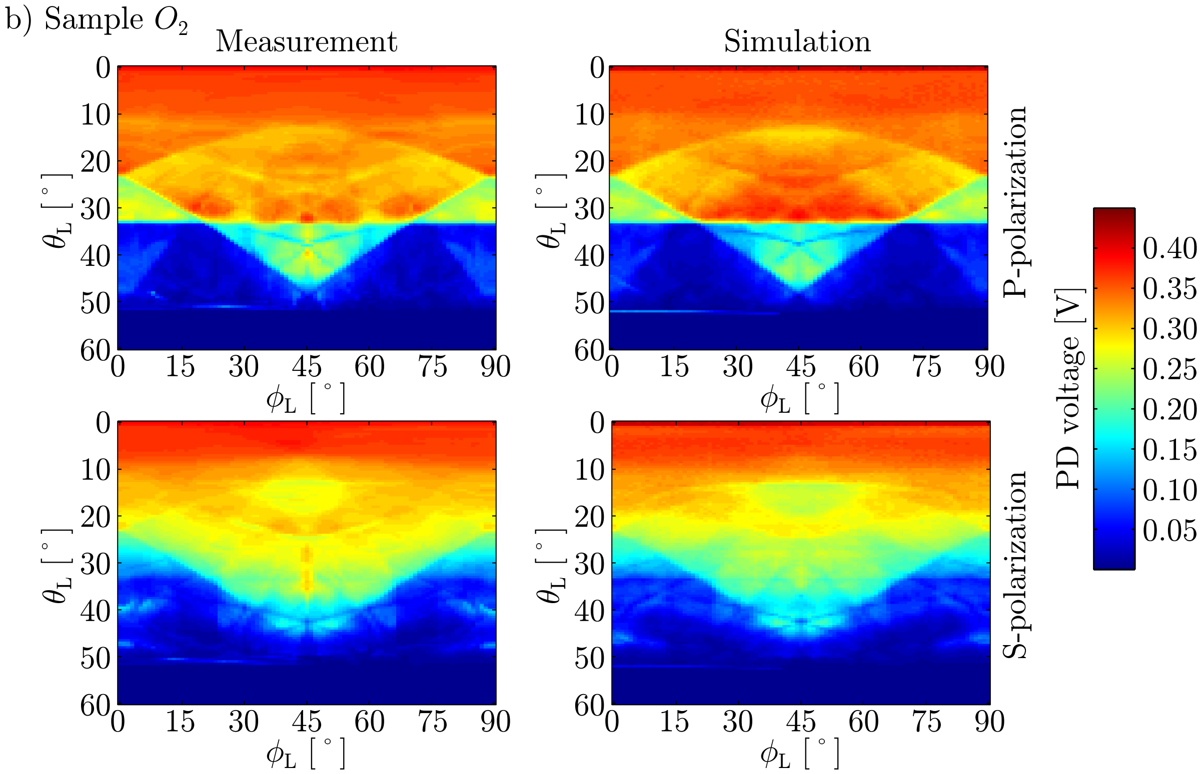
b) Sample O_2

Figure 5.24: PD voltage versus incident angles θ_L and ϕ_L for samples H_1 (a) and O_2 (b) comparing measured and simulated data. The 60°- (a) and 90°-periodicity (b) of the characteristics is clearly visible.

5.3.5 Impact of Photonic Crystals on PET Detector Performance

The results presented in the previous sections indicate that PhCs provide transmission characteristics that do not suffer from a TIR-cutoff. Also, the validation using the optical experiments proved that the DLL-based approach of integrating PhCs into optical MC simulations is suitable for detailing light propagation in PhC enhanced PET detector modules. In this section, these results are put to use through the optimization of the PhC parameters for maximum light extraction and their implementation into the reference PET detector model.

5.3.5.1 Optimization of Photonic Crystals

Since the initial parameter sweeps indicate that a large value of n_{Bulk} and a low value of n_{Cav} leads to higher transmission coefficients for $\theta > \theta_{\text{TIR}}$, the PhCs considered for the PET detector module consisted of the high-index polymer A54 (Brewer Science, Rolla, MO, USA) with air cavities ($n_{\text{Air}} = 1$). The RI of the polymer n_{A54} was measured with ellipsometry and exhibited a real component larger than 2 and a very low imaginary part over the entire LSO emission spectrum (see Fig. 5.25). Sweeps of the parameters a, s and h were conducted for a hexagonal and an orthogonal PhC to calculate the transmission characteristics. These sweeps used a rather coarse angular resolution of $\Delta\theta = \Delta\phi = 5°$ to limit the computation times. The results were used to calculate the extraction efficiencies at first incidence $\chi_{\text{PhC}}(1)$ (see Eq. 4.25) utilizing the angular distribution $D(1, \theta)$ derived from the reference detector simulations (see Fig. 5.1). The relative gain in light extraction caused by PhCs was computed as $\chi_{\text{PhC}}(1)/\chi_{\text{Ref}}(1)$, with the latter being the light extraction of the reference configuration without PhCs. These calculations also took the wavelength-dependent behavior of PhCs into account. The resulting distributions of the relative gain in extraction efficiency are shown in Fig. 5.26 for hexagonal and orthogonal PhCs at the h-values that yield the largest improvements.

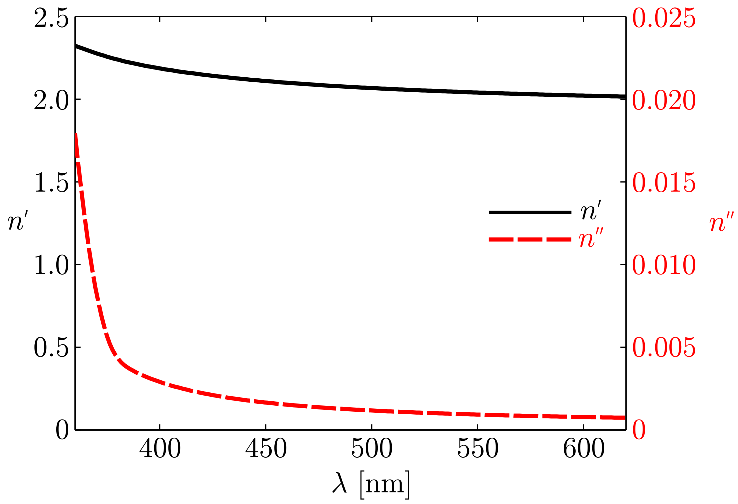

Figure 5.25: Complex RI of polymer considered for the bulk material of the PhCs for use in the PET detector module. The data has been derived from ellipsometry measurements.

a) Polished configuration

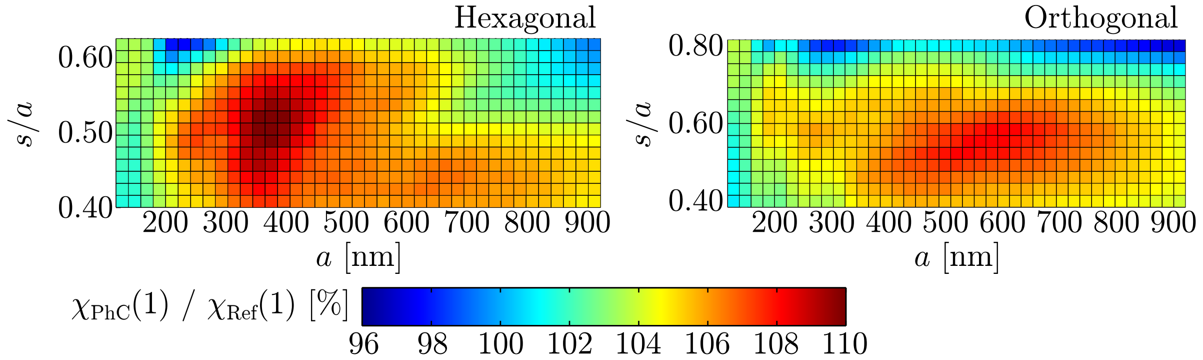

b) Etched configuration

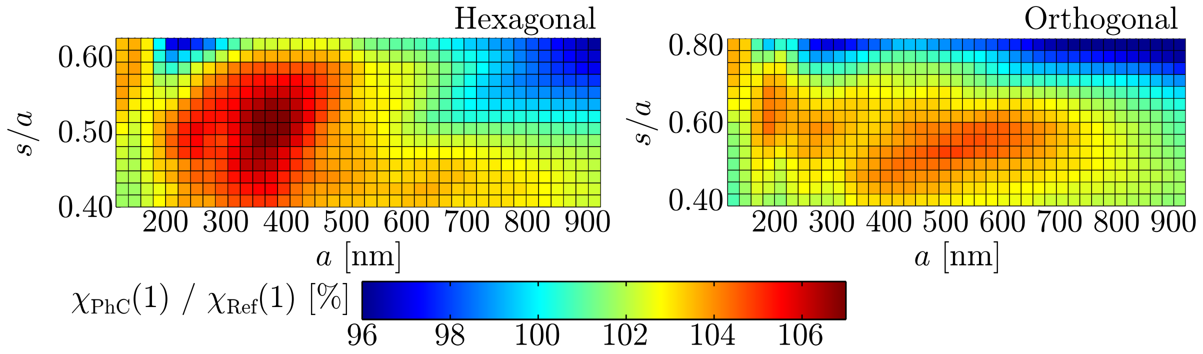

Figure 5.26: Results of the parameter sweeps used for the optimization of the PhCs. The distributions show the gain in light extraction $\chi_{\mathrm{PhC}}(1)/\chi_{\mathrm{Ref}}(1)$ versus a and s (relative to a) for the polished configuration (a) and etched detector configuration (b). The plots display results for the h-values yielding the largest extraction gains, i.e. $h = 325$ nm for the hexagonal and $h = 300$ nm for the orthogonal PhCs. Note the different color scales in (a) and (b).

For the polished detector configuration, the parameter sweeps indicate the highest extraction efficiencies for a hexagonal PhC with $a = 368$ nm, $s = 199$ nm, and $h = 325$ nm ($\mathrm{PhC}^{\mathrm{Hex}}_{\mathrm{Pol}}$) and an orthogonal PhC with $a = 533$ nm, $s = 277$ nm, and $h = 300$ nm ($\mathrm{PhC}^{\mathrm{Ortho}}_{\mathrm{Pol}}$). For the etched configuration, the results for the hexagonal PhC do not differ from the polished values ($\mathrm{PhC}^{\mathrm{Hex}}_{\mathrm{Pol}} = \mathrm{PhC}^{\mathrm{Hex}}_{\mathrm{Etch}}$). The best orthogonal parameters are $a = 512$ nm, $s = 266$ nm, and $h = 300$ nm ($\mathrm{PhC}^{\mathrm{Ortho}}_{\mathrm{Etch}}$). After the determination of the optimized parameter sets, the corresponding PhC transmission properties were recalculated using a resolution of $\Delta\theta = 1°$ for improved accuracy. The optimized PhC gratings exhibit quite distinct spectral transmission characteristics as illustrated in Fig. 5.27. The transmission of the hexagonal PhC varies substantially over the LSO spectrum, whereas the orthogonal gratings have rather uniform characteristics. As demonstrated through the goniometer experiment, the PhC DLL provides polarization-dependent transmission coefficients. For the randomly polarized scintillation photons, the transmission characteristics correspond to the average of S- and P-polarization. The optimized PhC grating lead to the overall extraction curves depicted in Fig. 5.28, which highlight the effect of PhCs avoiding the TIR-cutoff. The integrals of these curves yield extraction efficiencies $\chi_{\mathrm{PhC}}(1)$ up to 0.532 (polished) and 0.556 (etched) which represent improvements up to 10% and 6% versus the reference as detailed in Table 5.3.

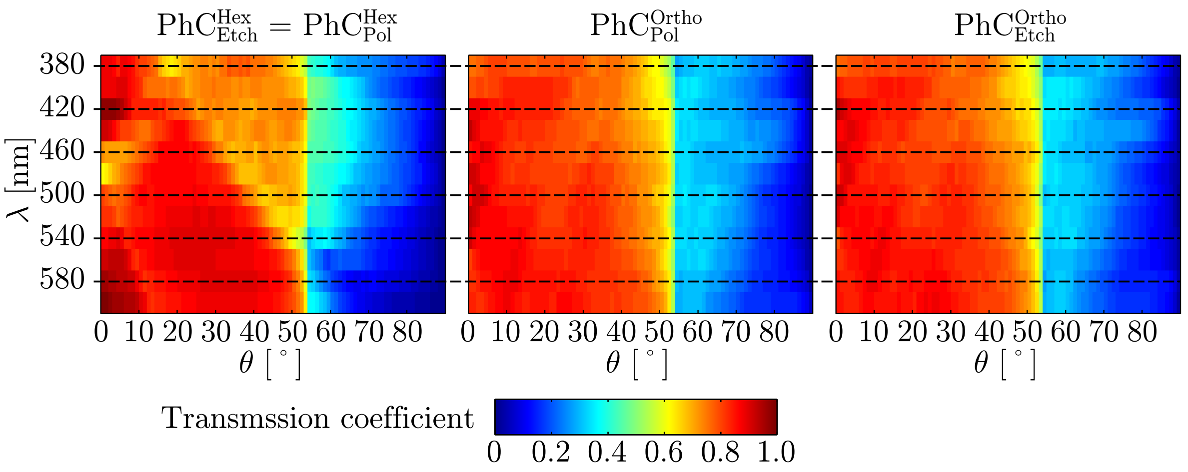

Figure 5.27: Wavelength-dependent transmission characteristics of the LSO/glue interface equipped with the optimized PhC configurations for randomly polarized light. The data shows the PhC properties recalculated with $\Delta\theta = 1°$, averaged over ϕ. Note that the vertical axis on the left applies to all three plots.

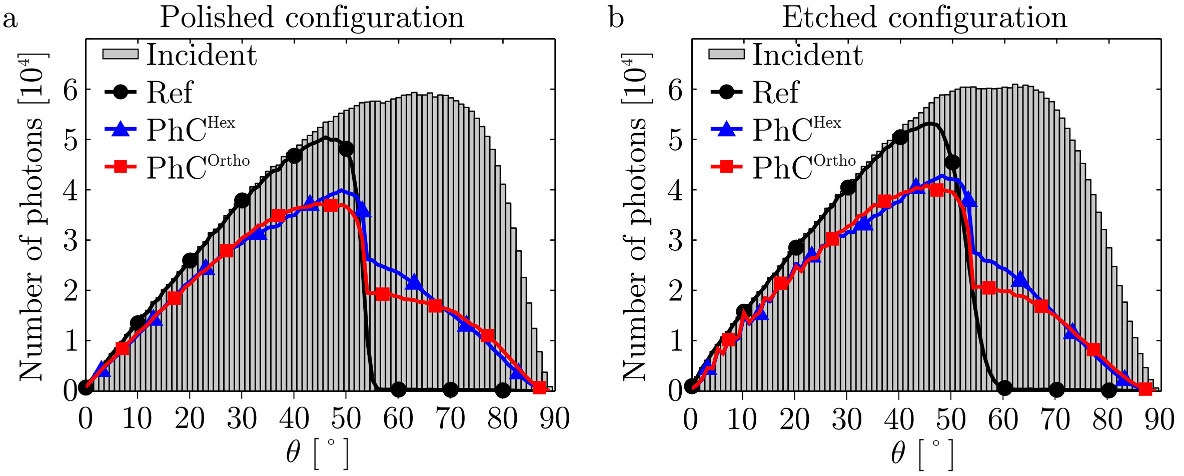

Figure 5.28: Incident angle distribution at first incidence on LSO exit face $D(1, \theta)$ (gray bars) and extracted photons (lines) comparing the reference setup and the PhCs derived from the parameter sweeps for the polished (a) and etched (b) detector configuration. The non-zero transmission of PhCs for $\theta > \theta_{\mathrm{TIR}}$ is clearly visible. The integrals of the extraction curves yield the extraction efficiencies detailed in Tab. 5.3. The data shows the PhC properties recalculated with $\Delta\theta = 1°$.

5.3.5.2 Performance of PET Detector Equipped with Photonic Crystal

The polished and etched detector configurations were modified to obtain new setups using the corresponding optimized gratings $\mathrm{PhC}^{\mathrm{Hex}}$ and $\mathrm{PhC}^{\mathrm{Ortho}}$. The optical simulations indicate a light yield of $\Gamma^{\text{Phc-Hex}}_{\text{Pol}} = 0.265$ and $\Gamma^{\text{Phc-Ortho}}_{\text{Pol}} = 0.263$ for the polished configurations, corresponding to improvements by 17% and 16% versus the reference. For the etched configuration, the computed light yields are $\Gamma^{\text{Phc-Hex}}_{\text{Etch}} = 0.273$ and $\Gamma^{\text{Phc-Ortho}}_{\text{Etch}} = 0.270$, constituting improvements by 8% and 7% compared to the reference.

In all cases, the increases in light yield are larger than the improvements regarding the extraction efficiencies at first incidence due to the positive effect of the PhCs accumulated over several recurrences of photons on the LSO exit face. This is because the detector setup leads to little scattering of the scintillation light, especially in the case of the polished configuration. For the reference setup, those photons which have been reflected at their first incidence on the LSO exit face and return a second or third time tend to have similar incident angle as before (see Fig. 5.29a), leading to a low extraction efficiency. In contrast to this, PhCs transmit a broad spectrum of incident angles and photons which are not transmitted are scattered upon their reflection. Hence, the setups using PhCs exhibit broad spectra of incident angles and higher extraction efficiencies for several recurrences of the photons (see Fig. 5.29b,c) which cause the accumulating positive effect. In general, the same arguments apply to the etched detector configuration. However, the increased scattering of light by the scintillator surfaces leads to a redistribution of reflected photons causing broad distributions of incident angles similar to the PhC setup (see Figs. 5.29d,e). As a consequence, the improvements in extraction efficiency provided by the PhC setups are significantly lower compared to the polished configuration (compare Figs. 5.29c and f) and the accumulative positive effect of PhCs is less pronounced.

The propagation time distribution of detected photons is shown in Fig. 5.30a. As shown before, PhCs lead to a reduced transmission for photons with low incident angles. Since the fastest photons mostly correspond to direct incidence on the LSO exit face with a low angle, the propagation time distribution of the reference setup exhibits a higher peak of the leading pulse compared to the PhC setups. However, approximately 290 ps (polished configuration) after the first detected photons, the accumulated light yield of PhC-equipped detectors starts to exceed the reference setup (see Fig. 5.30b). For the etched configuration, it takes approximately 340 ps for the PhC setups to excel the light yield of the reference.

The timing simulations of the polished configuration yield CRT values of 224 ps ($\mathrm{PhC}^{\mathrm{Hex}}$) and 228 ps ($\mathrm{PhC}^{\mathrm{Ortho}}$), which represent 5% and 4% improvements versus the reference CRT of 237 ps. For the etched configuration, the CRTs were calculated to be 221 ps ($\mathrm{PhC}^{\mathrm{Hex}}$) and 223 ps ($\mathrm{PhC}^{\mathrm{Ortho}}$), constituting an improvement of 3% compared to the reference CRT of 229 ps. Although these values indicate only modest changes in the CRT, they are significantly larger than the statistical inaccuracy of the optical and timing simulations. A summary of these results is given in Table 5.3. Similar to the CRT results of the LC study, these values disagree with the predictions based on the correlation between light yield and timing from Eq. 2.13. Using this equation with the gains in light yield mentioned above, improvements in the CRT up to 7% (polished) and 4% (etched) are expected. The discrepancy between simulated and predicted CRT values can be attributed to the temporal distribution of detected photons and is discussed in detail in Sec. 6.4.

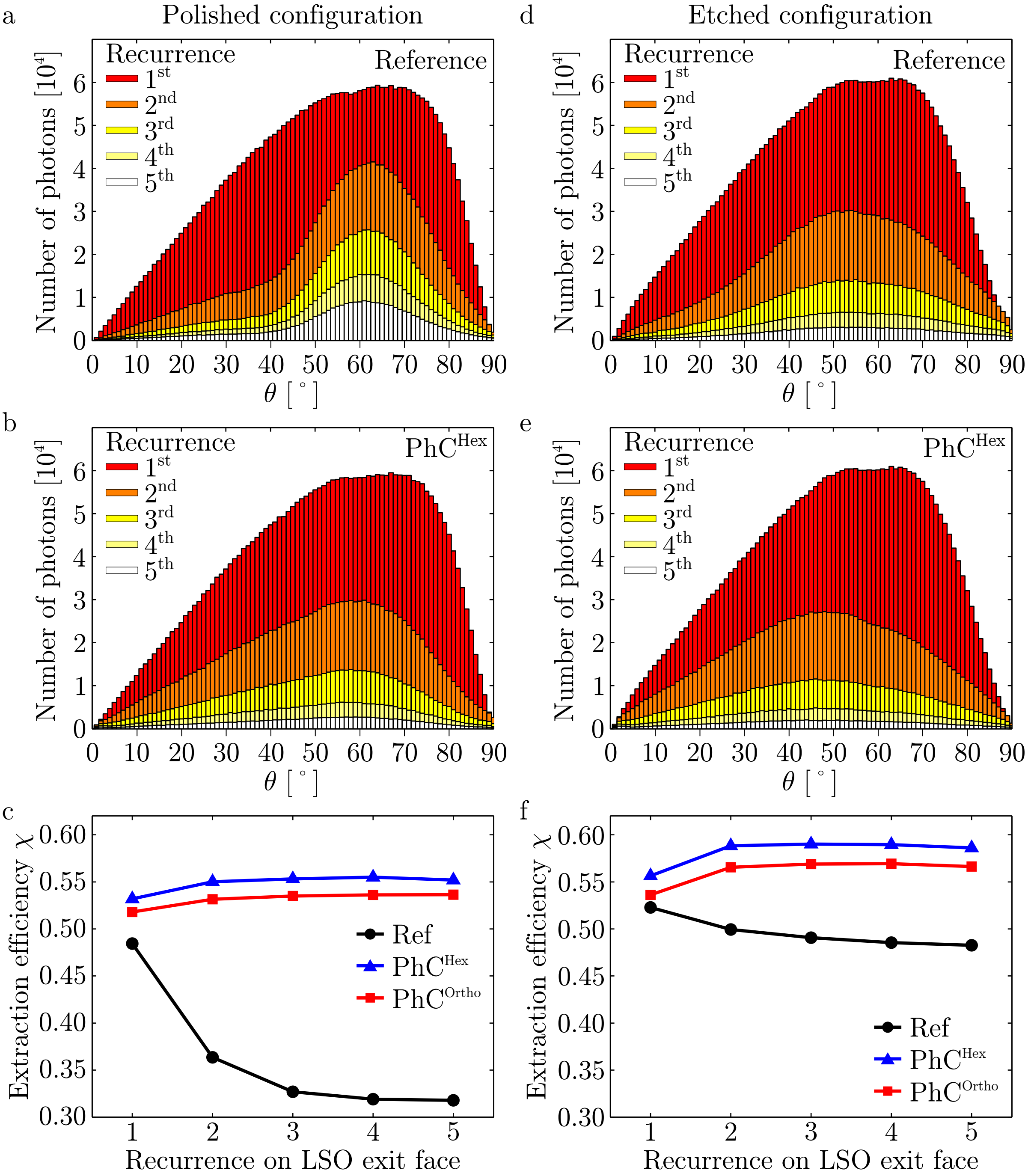

Figure 5.29: The incident angle distributions $D(1{-}5, \theta)$ for the first 5 recurrences of photons on the LSO exit face in the case of the polished configuration (a,b) lead to substantially higher extraction efficiencies for the PhC setups (c) causing the accumulative positive effect on the total light yield. The scattering of light in the etched configuration leads to slightly different angle distributions (d,e). Hence, the extraction efficiencies are more similar for reference and PhC setup (f). (Note that the angle distributions for the orthogonal PhC setups are not shown as they are very similar to the data of the hexagonal PhCs.)

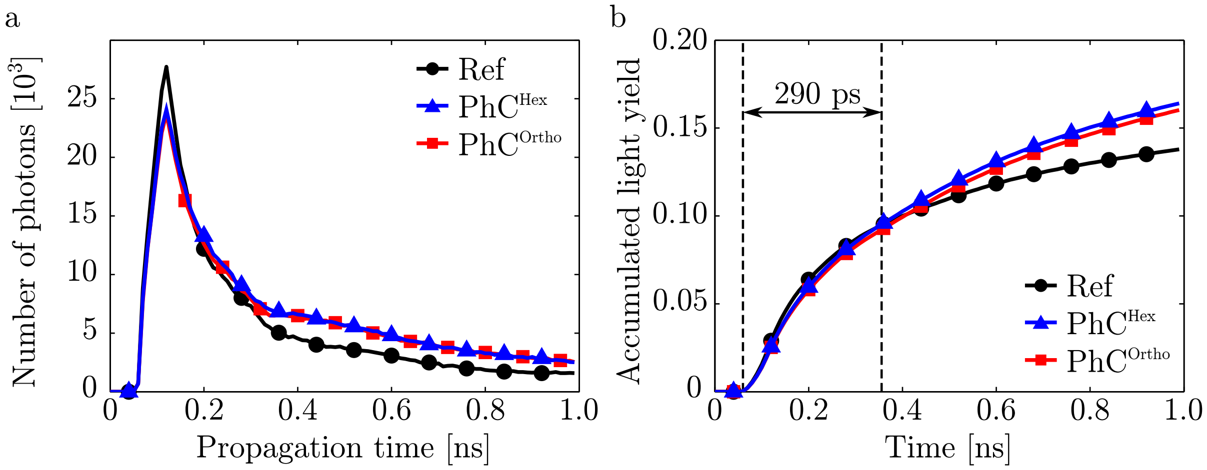

Figure 5.30: a) Propagation time distributions of photons registered by the SiPM for the polished configuration comparing the reference and the two PhC setups using 10 ps bins. Due to the different transmission characteristics, the leading peaks of the PhC timing pulses are slightly lower than the reference curve. b) The accumulated light yield versus time for PhC setups starts exceeding the reference light yield approximately 290 ps after the detection of the first photons. This figure shows only data for the polished configuration. The corresponding results for the etched configuration differ only slightly.

Table 5.3: Summary of geometry parameters, extraction efficiency, light yield and CRT of optimized PhC configurations in comparison to the reference.

	Polished configuration			Etched configuration		
	Ref	PhC^{Hex}	$\text{PhC}^{\text{Ortho}}$	Ref	PhC^{Hex}	$\text{PhC}^{\text{Ortho}}$
a [nm]	-	368	533	-	368	512
s [nm]	-	199	277	-	199	266
h [nm]	-	325	300	-	325	300
$\chi(1)$	0.485	0.532	0.518	0.522	0.556	0.536
$\chi(1)/\chi_{\text{Ref}}(1)$ [%]	100	110	107	100	106	103
Γ	0.227	0.265	0.263	0.253	0.273	0.270
$\Gamma/\Gamma^{\text{Ref}}$ [%]	100	117	116	100	108	107
CRT [ps]	237	224	228	229	221	223
CRT / CRT^{Ref} [%]	100	95	96	100	97	97

5.4 Combining Photonic Crystals with Concentrators

For the study of combining the two approaches presented in the previous sections, the LC and PhC configurations providing the largest improvements in CRT were used. Hence, the reference detector model was equipped with an LC of $H_C = 4$ μm and the hexagonal PhCs.

The LC has only modest influence on the angular distribution of photons impinging a second, third or fourth time on the LSO exit face causing a slight increase in extraction efficiency as depicted in Fig. 5.31. Also, the improved light collection through the LC helps to recover some of the losses in direct photons caused by the PhC transmission characteristic. The angular distribution of photons impinging on the LC in the presence of the PhC coating differs strongly from the reference due to the scattering of light into certain diffraction orders (compare Figs. 5.32a,b and 5.14). Yet, the collection efficiency of the setup using PhCs is increased through the use of an LC from 62% to 64%. Although this represents only a moderate gain, it accumulates over several recurrences of photons on the SiPM. The improvement in light collection, however, is not sufficient to achieve a propagation time distribution with a peak as high as the LC-only setup. Nevertheless, it leads to an amplitude very close to the reference as shown in Fig. 5.32c. This effect adds to the accumulative positive effect of PhCs which is visible in the plot of light yield versus time approximately 290 ps after the first photons (see Fig. 5.32d).

All these effects lead to an overall light yield for the combined setup of 0.302 (polished) and 0.312 (etched), constituting improvements of 33% and 23%, respectively. Also, the timing simulations predict that the CRT of the detector profits significantly from using PhCs in conjunction with an LC. The resulting CRT values of 215 ps (polished) and 212 ps (etched) represent improvements of 9% and 7% versus the reference.

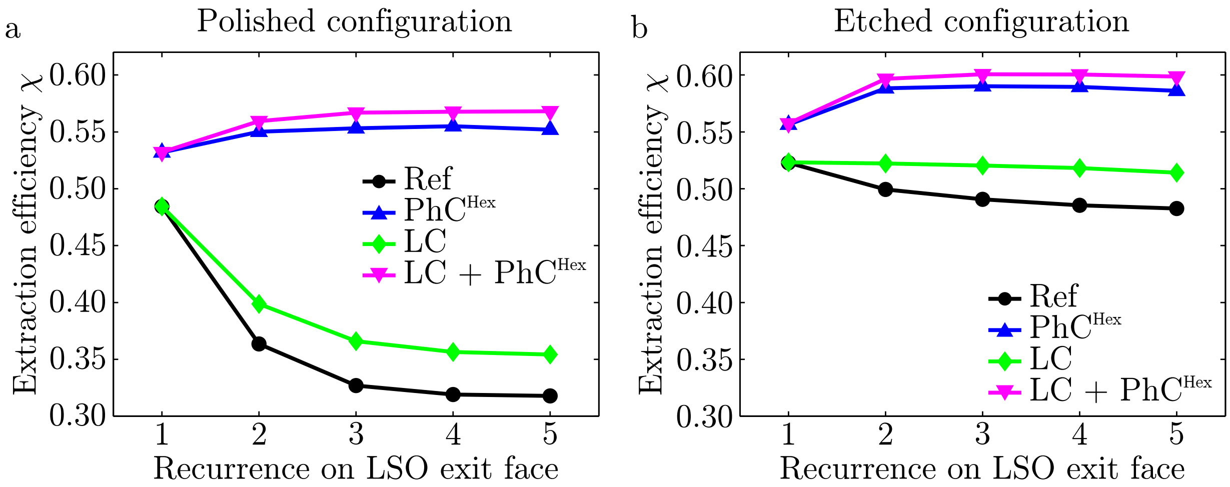

Figure 5.31: Extraction efficiencies at the interface LSO/glue comparing the different detector setups for the polished (a) and etched (b) configuration.

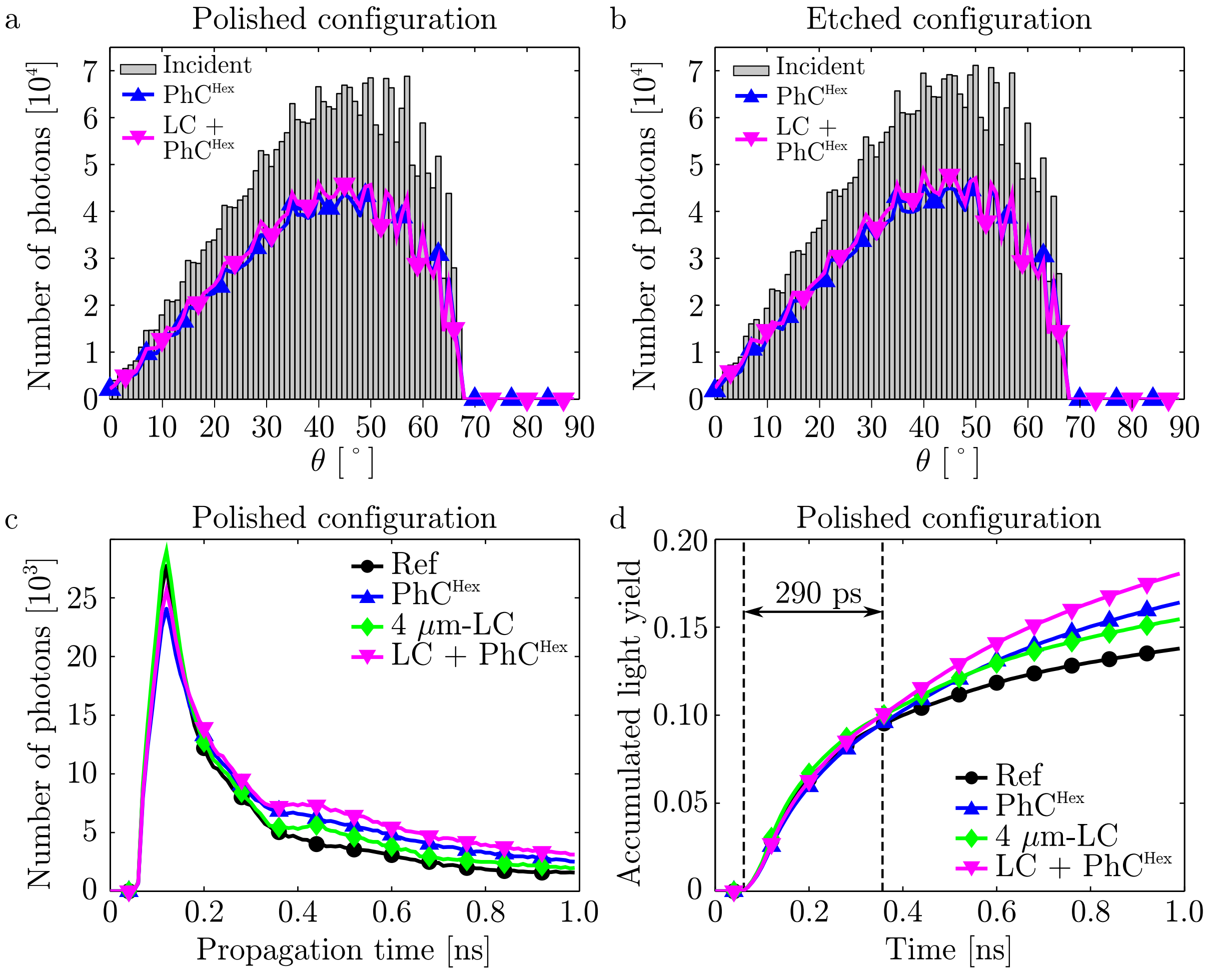

Figure 5.32: Angular distribution of photons at their first incidence on the SiPMs (gray bars) and collected photons (lines) comparing the setup equipped only with the hexagonal PhC and the setup combining PhC^{Hex} and LC for the polished (a) and etched configuration (b). The presence of the LC leads to a modest increase by 2% in the collection of light. The sharp spikes in the angular distribution are caused by the scattering of light into certain diffraction orders by the PhC. c) Propagation time distribution of registered photons of the different setups for the polished configuration. The accumulated light yield versus time in (d) illustrates how the positive effects of LC and PhC add up and their combination starts exceeding the light yield of all other setups approximately 290 ps after the first photons. The timing data of the etched configuration differs only in details and is not shown for brevity.

5.5 Nano Imprinted Photonic Crystals

5.5.1 Nano Imprinted Samples

The Si master required for the direct nano imprinting was fabricated using laser interference lithography. This method produces line gratings if two interfering beams are used. Through subsequent exposure of the resist with rotated interference patterns, biperiodic orthogonal and hexagonal arrays can be achieved. For hexagonal structures, this approach leads to elliptic cavities [168], which have transmission characteristics with more pronounced dependence on the incident azimuthal angle ϕ. Therefore, the fabrication of a mold for the PhC imprinting was limited to an orthogonal grating. Based on the parameter sweeps presented in Sec. 5.3.5, the PhC parameters for the imprinting were chosen to be $a = 567$ nm, $s = 328$ nm, and $h = 300$ nm. These values differ slightly from the optimized settings used for the optical MC study, because they were derived from preliminary sweep results that did not have the same parametric resolution as shown in Fig. 5.26. This procedure was necessary to provide sufficient time for the Si master fabrication.

Examination of the Si master with SEM revealed a cavity diameter of $s = (304 \pm 3)$ nm within a radius of 35 mm around the wafer center. Towards the substrate borders, the size increased up to 356 nm. This deviation and the discrepancy of the measurement with regard to the specified value of 328 nm was caused by the laser interference lithography. The cavity depth was also estimated with SEM yielding $h = 286$ nm (analysis and data provided by Amo GmbH).

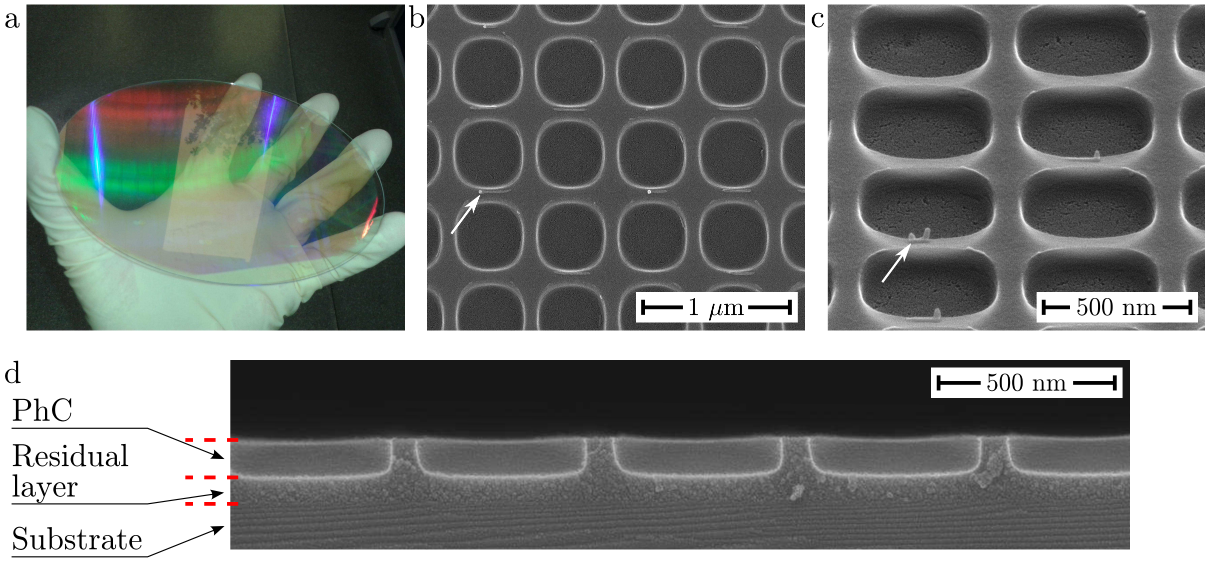

Figure 5.33: Samples fabricated with direct nano imprinting. The photograph in (a) shows the 150 mm diameter glass substrate entirely covered with PhC structures as can be seen through the dispersive reflection. The SEM images show the grating in perpendicular perspective (b) and tilted by 60° (c). The cross section view (d) was used to evaluate the thickness of the PhC and the residual layer. The white arrows in (b,c) indicate minor irregularities that stem from the fabrication process.

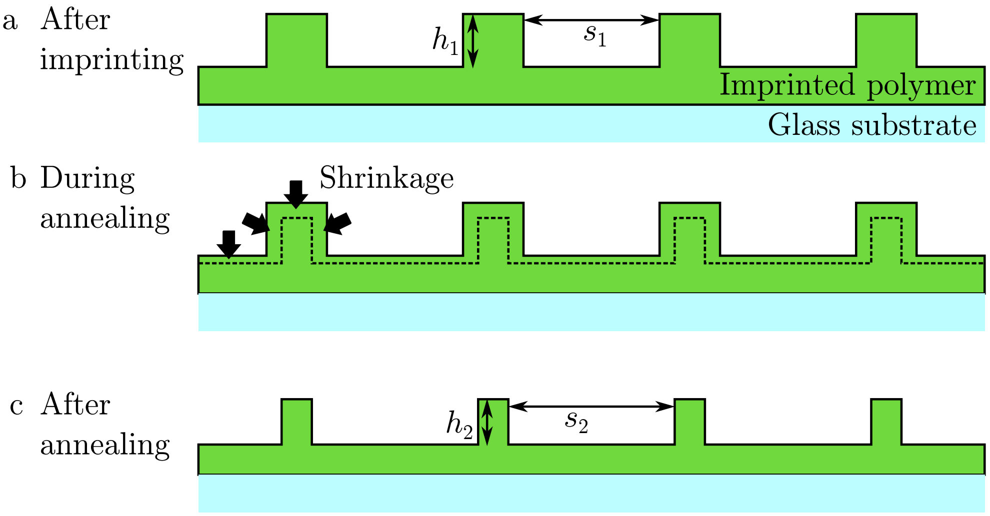

Figure 5.34: Illustration of shrinkage of the A54 polymer. The original dimensions s_1 and h_1 of the PDMS mold (a) are changed during the annealing step (b) yielding the final PhC geometry (c) with new dimensions $s_2 > s_1$ and $h_2 < h_1$.

After casting the PDMS mold from the Si master, direct nano imprinting of the A54 polymer was conducted which resulted in the PhC structures depicted in Fig. 5.33. The geometry of the cavities was evaluated using SEM yielding a pitch of $a = (555 \pm 2)$ nm, a diameter of $s = (459 \pm 4)$ nm, a height of $h = (110 \pm 5)$ nm, and a residual layer thickness of (71 ± 3) nm. The observed pitch differs by 12 nm from the specified value, which stems from small inaccuracies in the laser interference lithography. Significantly larger deviations from the target values and the dimensions of the Si master were observed for the cavity diameter s and height h. The diameter of the PhC cavities in the A54 polymer is 51% larger and their height is approximately 61% lower than measured for the Si master. This discrepancy is most probably caused by the shrinkage of the polymer during UV and thermal curing as illustrated in Fig. 5.34.

5.5.2 Transmission Measurements of Imprinted Samples

The transmission characteristics of the PhC samples fabricated with direct nano imprinting were measured using the goniometer setup. Based on the geometry parameters derived from the SEM investigations, corresponding LUTs were calculated and ray tracing simulations of the goniometer experiment were carried out. As illustrated in Fig. 5.35a for selected ϕ_L-values and in Fig. 5.35b for the entire $(\theta_\mathrm{L},\phi_\mathrm{L},q)$-range, excellent agreement between measured and simulated transmission characteristics was observed. This was confirmed by the Kolmogorov-Smirnov test, which indicated an agreement metric of $\eta = 92\%$. Again, these results demonstrate that the fabricated PhCs provide a significant increase of transmission beyond the TIR-cutoff at $\theta_\mathrm{L} = 33°$. Also, the imprinted structures cause a substantial reduction in the transmission for low θ_L-values by up to 30% compared to an interface without PhCs. This is visualized in Fig. 5.35a by the dashed curve representing the characteristic of a reference sample coated with a plain A54 film.

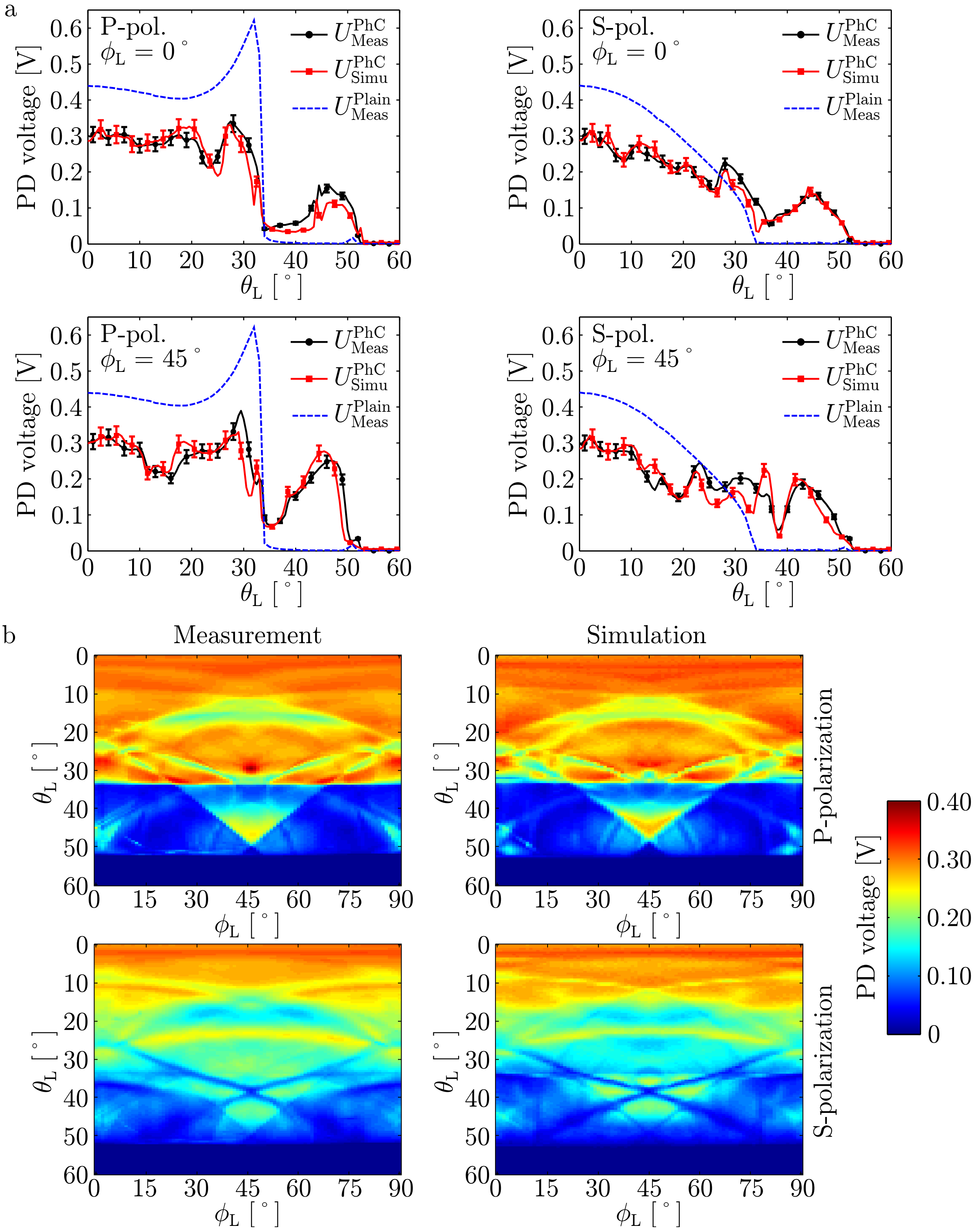

Figure 5.35: Comparison of measured and simulated transmission characteristics of PhC samples fabricated with direct nano imprinting. The curves at selected ϕ_L-values in (a) illustrate the agreement of both curves and exemplify the difference to a plain sample without PhCs. The survey of the data for all (θ_L,ϕ_L,q)-values in (b) further demonstrate the excellent agreement between measurements and simulations.

5.5.3 PET Detector Simulations of Imprinted Photonic Crystals

Since the actual geometry parameters observed in the nano imprinted samples ($\mathrm{PhC}^{\mathrm{NI}}$) deviate from the specified values derived from the parameter sweeps ($\mathrm{PhC}^{\mathrm{Sweep}}$), the two configurations have different transmission characteristics as shown in Fig. 5.36. To study the impact of PhCs as manufactured on the performance of a PET detector module, the corresponding $\mathrm{PhC}^{\mathrm{NI}}$ LUT was calculated and integrated into the detector model of the MC simulation framework via the PhC DLL approach. These computations yield an extraction efficiency at first incidence $\chi^{\mathrm{NI}}(1)$ of 0.461 for the polished and 0.481 for the etched detector configuration. These values represent degradations of 5% (polished) and 8% (etched) compared to the reference setup without PhC. Nevertheless, the MC simulations indicate improved light yield values of $\Gamma^{\mathrm{NI}}_{\mathrm{Pol}} = 0.252$ and $\Gamma^{\mathrm{NI}}_{\mathrm{Etch}} = 0.261$, which constitute gains of 10% (polished) and 3% (etched). The improvements predicted by the computations despite of decreased $\chi^{\mathrm{NI}}(1)$-values are caused by the accumulative effect of PhCs as visualized in Fig. 5.37 through the extraction efficiency of the $\mathrm{PhC}^{\mathrm{NI}}$ setups. However, the light yield of the $\mathrm{PhC}^{\mathrm{NI}}$ setups lies below the reference light yield for the first 530 ps (polished) and 750 ps (etched) as exemplified in Fig. 5.38. This influences the timing resolution negatively which is confirmed by the timing simulations indicating CRT values of 238 ps for $\mathrm{PhC}^{\mathrm{NI}}_{\mathrm{Pol}}$ and 232 ps for $\mathrm{PhC}^{\mathrm{NI}}_{\mathrm{Etch}}$. These are by 1 ps (polished) and 3 ps (etched) longer than the results of the reference setup.

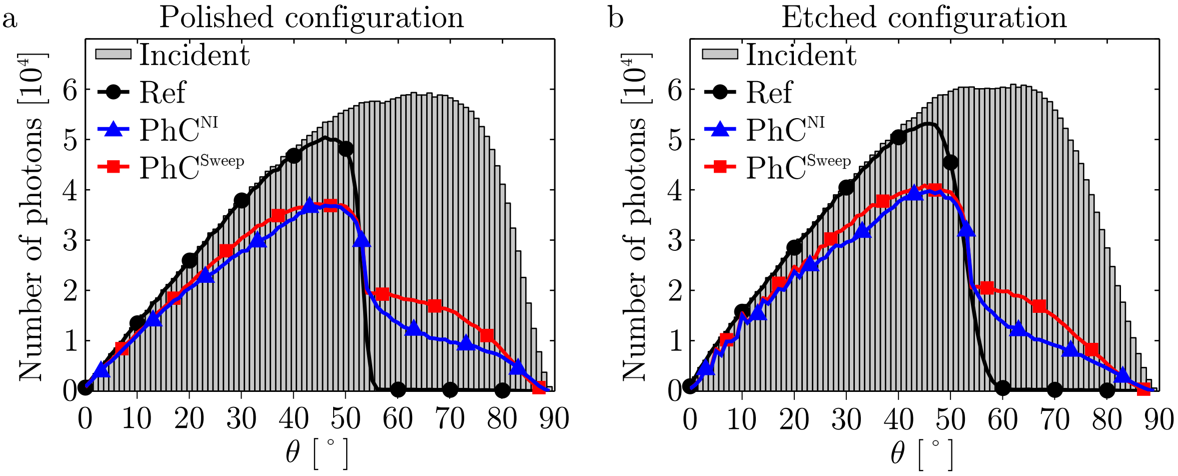

Figure 5.36: Incident angle distribution of photons on the LSO exit face at first recurrence derived from the MC simulations (gray bars) with the extracted photons (colored lines) comparing the reference setup, $\mathrm{PhC}^{\mathrm{NI}}$, and $\mathrm{PhC}^{\mathrm{Sweep}}$ for the polished (a) and etched (b) configuration.

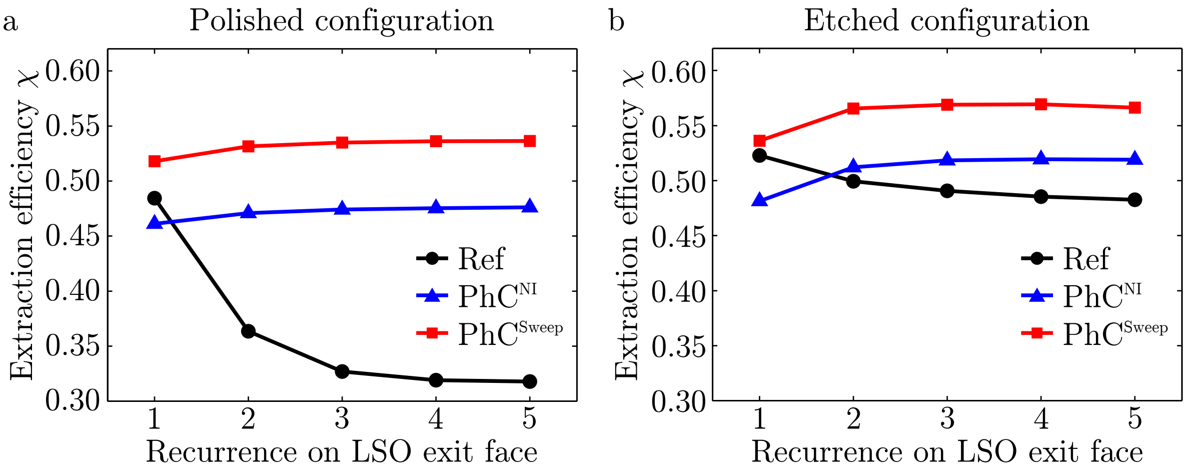

Figure 5.37: Extraction efficiencies over several recurrences of photons on the LSO exit face comparing the reference setup, PhC$^{\mathrm{NI}}$, and PhC$^{\mathrm{Sweep}}$ for the polished (a) and etched (b) configuration.

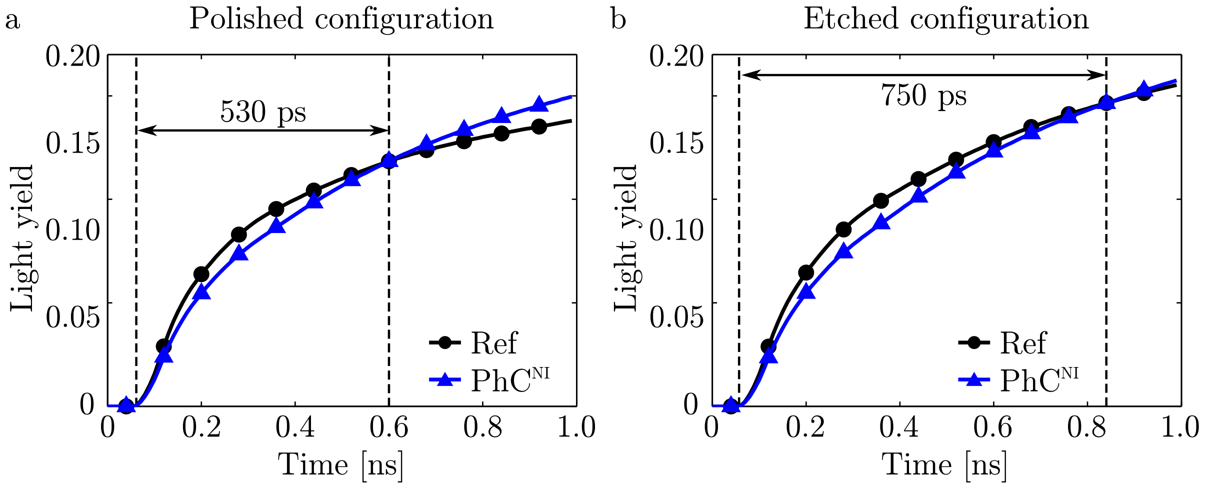

Figure 5.38: Accumulated light yield versus time comparing the reference setup with PhC$^{\mathrm{NI}}$ for the polished (a) and etched (b) configuration. The PhC setup has a lower light yield than the reference for the first 530/750 ps, which leads to a deterioration of the CRT.

Chapter 6

Discussion and Conclusions

6.1 Reference Detector Setup

Notwithstanding the limitations in the photon transfer (see Sec. 2.5.2.1), the optical MC simulations of the reference PET detector setup indicate, that a large fraction of 86% of all scintillation photons reach the LSO exit faces. This result is partly due to low absorption of the LSO bulk and can also be attributed to the arrangement of the 8×8 pixels in the detector. The air gaps between adjacent crystals lead to a lossless reflection of photons with shallow incident angles and permit a rather effective funneling of light towards the exit face. Also, the 8×8 array appears similar to an LSO crystal of size (32×32×20) mm^3 with more pronounced scattering (due to the slightly rough interfaces) to photons that propagate horizontally. This aspect ratio compared to an individual crystal of (4×4×20) mm^3 leads to larger solid angle in which photons can reach the exit face without being absorbed by the reflective wrapping or escaping from the module as illustrated in Fig. 6.1.

Several approaches have been proposed to funnel light more efficiently towards the exit face, such as plasmonic waveguides [144] or metamaterials [169]. However, the results of the optical simulations in this work suggest that the photon transfer from the scintillation location to the extraction faces represents no major limitation for the performance of this PET detector configuration. Consequently, the potential benefit of the intricate concepts mentioned above can be estimated to be rather modest in relation to the efforts required for their implementation, at least for the detector configuration considered here.

In contrast to the photon transfer towards the exit face, the light trapping in LSO due to TIR was confirmed to be a severe limitation of the detector performance by the optical simulations. With regard to this effect, the etched detector configuration was found to have a slightly different angular distribution of incident photons as well as a more continuous transmission characteristic compared to the polished configuration. This led to a larger extraction efficiency resulting in better light yield and CRT results for the etched scintillators. Nevertheless, these results underline the need for improved light extraction and motivated the studies regarding the PhC gratings.

Also, the simulation results indicate that a substantial fraction of scintillation photons is lost due to absorption in the inactive SiPM areas. Although the actual values derived from

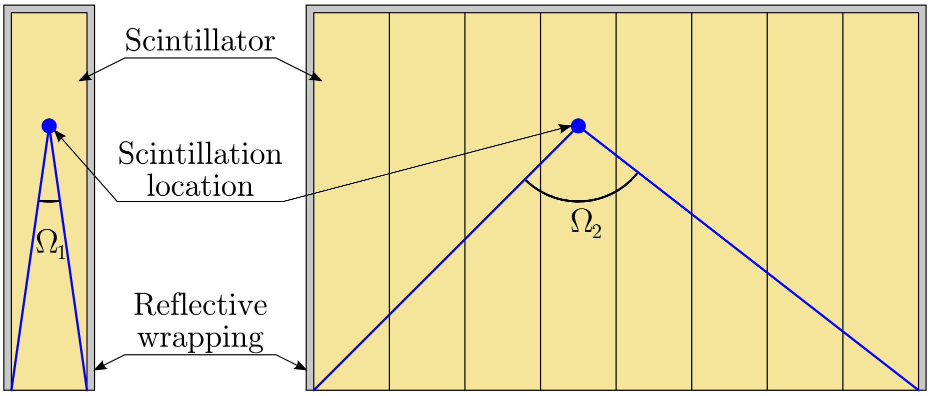

Figure 6.1: Comparison of solid angles Ω_1 and Ω_2 in which photons can reach the scintillator exit faces without interacting with the reflective wrapping: an individual scintillator crystal of (4×4×20) mm^3 (left) and 8 adjacent pixels of (4×4×20) mm^3 (right). Note that scattering is neglected in this illustration.

the computations are based on certain assumptions regarding the optical properties of the SiPM surface, it can be concluded with high certainty that the limited geometric fill factor of current SiPMs represents a considerable limitation of the sensor performance. Therefore, equipping SiPM microcells with LCs bears the potential to avoid some of these losses and improve the collection of fast photons which is of special interest for TOF applications.

6.2 Concentrator for Improved Light Collection

The simulation study characterizing the light collection versus concentrator height shows that rather distinct characteristics can be achieved. This allows adapting the geometry to the given angular distribution of photons incident on the SiPM. The results also indicate that the absorption within the reflective coating plays an important role and increases continuously with higher concentrators.

The results from the DRIE- and KOH-based tests show that LC geometries can be fabricated with different heights and sidewall geometries. It has been shown that very narrow ridges below 1 μm can be achieved through the sharpening process. Especially, the etching method using KOH allowed the fabrication of LC samples with very smooth surfaces. Among further advantages of KOH etching are the broad availability of the procedure as it is a very common method for Si micromachining and the reproducible etching results which are clearly defined by the intrinsic crystal structure of the Si substrates. The latter also represents a major limitation of this approach, as it constrains the concentrator taper angle to $\zeta_C = 35.3°$.

The LC samples fabricated with KOH etching exhibited very uniform structures and geometry parameters very close to the specified values, especially in the case of the LC_1 samples. However, with the SOI substrates available, the remaining concentrator ridge could not be reduced further than (2.1±0.1) μm with the oxidation-based sharpening procedure. This could be further optimized to achieve even lower ridge widths by using SOI substrates with adapted device layer thickness.

The angle-resolved transmission characteristics of the LC samples measured with the goniometer setup exhibited several oscillations caused by the coherence of the used laser diode and the experimental configuration. Application of the moving average filter provided sufficient suppression of these oscillations which allowed the direct comparison with the characteristics obtained through optical simulations with incoherent light. This analysis indicated that the optical characteristics could be reproduced with good agreement within the MC simulations for the LC geometry of the fabricated samples. This was further documented by the agreement metric derived from the Kolmogorov-Smirnov test. The measurements also confirmed that the concentrator geometry increases the collection of photons with low incident angles significantly.

The MC simulation study implementing an LC with variable height into the reference PET detector setup indicates that considerable improvements in light yield and timing can be achieved. It was also found that the surface roughness of the LSO crystals play no significant role for these results, at least regarding the polished and etched configurations considered in this work. Initially, tapered LCs were chosen as they offer the capability of collecting all photons incident with low angles which increases the detection of light at the beginning of the scintillation pulse. In contrast to this, the best performance is predicted for a concentrator with $H_\mathrm{C} = 4\ \mu$m, which exhibits only modest improvement in the collection of direct photons with low incident angles. Although higher concentrators collect more light for incident angles lower than 45°, they reject more photons beyond this threshold and suffer from increased absorption in the reflective coating. While the first is an intrinsic characteristic of LCs, the latter could be reduced by using a coating with higher reflectivity.

The potential of using better reflector materials was evaluated through repeating the optical simulations with an ideal coating exhibiting a reflectivity of 100%. As shown in Fig. 6.2, the ideal reflector changes the distribution of collected photons only slightly. This is further documented through the integrals of these curves, i.e. the overall collection efficiency at first incidence on the SiPM, which amount to 66% for the ideal coating for both polished and etched LSO crystals. This represents only a minor improvement compared to the 65% efficiency obtained for the concentrator with lossy Al-coating. These small differences accumulate over several recurrences of photons on the SiPM and result in an increased light yield of 21% for the ideal reflector versus the reference without concentrator. Given the fact that lossy Al-coatings provide 15% gain in light yield, improved reflective materials offer only moderate potential for improvement. Consequently, the rejection of photons with $\theta > \theta_\mathrm{Acc}$ can be considered to be the more severe limitation of the LC performance. However, this conclusion cannot be generalized to all detector and LC configurations. This is because the angular distribution of photons incident on the SiPM represents an important aspect for these considerations and strongly depends on several detector characteristics such as scintillator geometry, surface roughness, RIs of optical glue and epoxy, etc.

Although the manufactured samples allowed the successful validation of the simulated properties, the utilized production workflow using subtractive processes represents a strategy that is not compatible with SiPM mass production in terms of complexity and costs. This is further supported by the sensitivity analysis of the LC performance regarding fabrication-related imperfections, which indicate the high level of accuracy required for the assembly. Therefore, it is necessary to integrate the production and mounting of the LC into the SiPM fabrication workflow and to replace the subtractive LC-structuring approach with additive

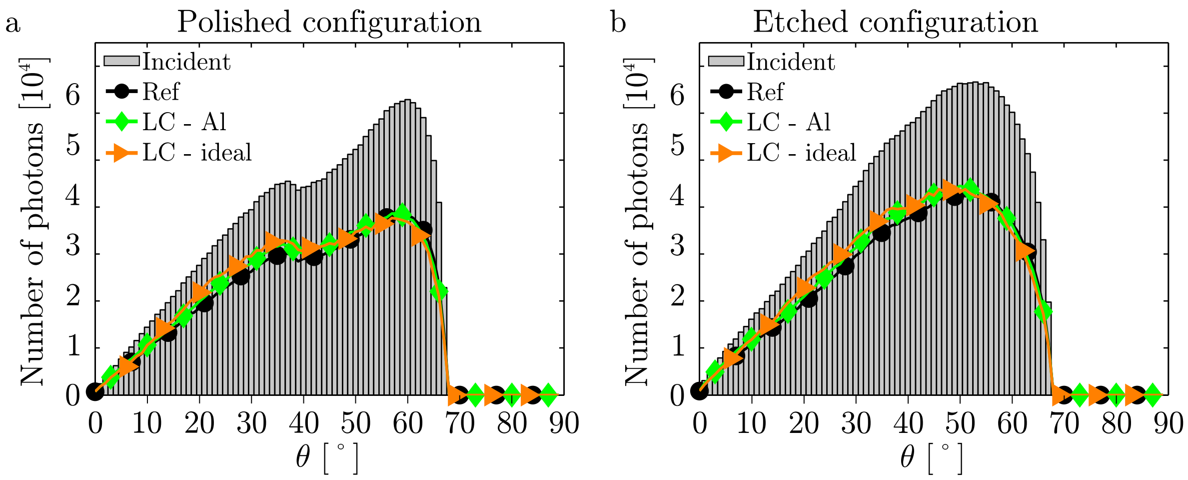

Figure 6.2: Angular distribution of photons at their first incidence on the SiPM (gray bars) and collected photons for the polished (a) and etched (b) detector configuration. The curves illustrate that for both settings, the ideal LC having 100% reflectivity does not change the collection efficiency significantly.

techniques. Possible strategies for this include spin coating and structuring of polymers, epitaxy or electro/electroless plating [117]. Obviously, the development of suitable fabrication processes and integration into the SiPM production can only be done in direct collaboration with the sensor manufacturers. This transfer, however, is beyond the scope of this work.

Concentrators with a height of 4 μm have a geometry that is similar to the samples fabricated with KOH etching. Therefore, the encapsulated LC samples utilized for the LSO-based light yield and timing measurements represent adequate replacements of the optimal solutions derived from the simulations of the PET detector module. Also, the optical properties of the Cr grid used to mimic the plain SiPM surface agree reasonably well with characteristics assumed for the inactive sensor areas. The experiments indicated that the LC provided a gain in light yield versus the Cr grid by 9%. The concentrator manipulated the photon transfer in such a way that the amplitude of the PMT pulse's leading peak was increased which also led to improved timing resolution. The experimental results were further supported by the results from optical simulations of the LSO setup.

Admittedly, the experiment of replacing an actual SiPM with a metal grid that is placed on top of a PMT entrance window cannot verify the predicted benefit of LCs for SiPMs. Yet, they are a strong indicator that the sensor performance can be improved through the use of an adequate light concentrating device and hence represent an important first step towards further studies with real SiPMs. These studies would also allow gathering more detailed information about the optical properties of the sensor surface, which would help to improve the computational model which until now was based on several assumptions. As mentioned before, the collaboration with the SiPM manufacturers is indispensable for these next steps.

6.3 Photonic Crystals for Improved Light Extraction

The implementation of PhCs into the optical MC simulations using the DLL-based approach had no adverse impact on the stability or performance of the computations. However, the initial calculation of the LUTs requires significant computational resources which scale with the angular and spectral resolution. These calculations took up to 57 hours for an individual PhC LUT comprising 12 wavelengths and angular ranges for θ from 0° to 180° with 1° increment and ϕ from 0° to 45° with 5° increment.

The initial simulation study of the PhC optical properties show that their characteristics are influenced by several parameters. It was shown that PhCs not only provide notable transmission beyond the TIR threshold, but also increased reflection for low incident angles. The results also underlined the importance of a high-index PhC bulk, which constrains the range of materials that can potentially be used for practical implementations with high-index scintillators.

Using EBL for writing the PhC structures proved to be a flexible means to produce different grating geometries with uniform patterns over areas of (8×8) mm^2 on a single substrate. In combination with utilizing the EBL resist itself as bulk material for the PhCs, this led to a rather simple fabrication workflow without the need for etching processes. The geometric features of some of the presented samples did not meet the specified values, mainly regarding the cavity diameters. However, this represents no major issue as it can be corrected through adequate definition of the EBL focus plane and dose adjustments of the electron beam prior to writing the actual structures. The novel method of direct nano imprinting was found to represent an attractive alternative to EBL. A detailed discussion of this fabrication technology is given in Sec. 6.5.

The angle-resolved transmission measurements with the goniometer setup allowed the successful validation of the sample transmission characteristics and of the implementation of the PhC simulations into the optical MC tool. The quantitative agreement between measured and simulated data apparent from the presented PD voltage curves was confirmed by the statistical analysis. These results also demonstrate that PhCs can provide substantial transmission beyond the TIR threshold, albeit at the cost of increased reflection at lower incident angles.

After this confirmation of the computational framework, the grating geometry was optimized in parameter sweeps to find configurations for improved light extraction from the LSO crystals. Arguably, the use of an optimization algorithm to find the optimal PhC geometry could have provided even better settings. However, the parameter sweeps were chosen instead, as they allowed the application of the same data to different angular distributions of photons allowing for more flexibility in adapting the PhC to the detector configuration. Due to the large amount of computational resources required by the PhC calculations, it was decided early on in the course of this project to focus on sweeps instead of optimization algorithms.

The MC simulations of the PhC-enhanced detector configurations indicated improvements in light yield and CRT that depend on the surface roughness of the LSO crystals. The benefits were found to be more pronounced for the polished configuration due to a larger increase in the extraction efficiency and a strong accumulation of this positive effect over several recurrences of photons at the LSO exit faces. For the etched configuration, the initial gain in extraction efficiency is only moderate and the accumulative effect is weaker. Although the predicted improvements for light yield and CRT are rather modest, especially for the etched configuration, they represent significant changes with regard to the accuracy of the optical and timing simulations. Nevertheless, these results suggest that further optimization of the PhCs is necessary to match the performance gains of rough scintillators such as the etched configuration with the benefits obtained for the polished configuration. This optimization could take into account refined geometries that are more complex than simple cylindrical cavities or different PhC bulk materials. Also, the discrepancy between gains in light yield and CRT (see discussion in Sec. 6.4) implies, that a more sophisticated optimization procedure for the PhC geometry should be developed that also considers the propagation time of detected photons. In summary, the relatively low gains in CRT in relation to the high costs of the EBL technology used for the PhC fabrication emphasize the need for an alternative production method. This approach must combine nanometer resolution with economic efficiency to pave the way for the potential implementation of PhCs in future detector systems. A potential candidate for this is direct nano imprinting as detailed in Sec. 6.5.

Although the presented MC study confirms the potential of PhCs to enhance the light output and CRT of LSO-based PET detectors, the reported values are more modest than the results given in Refs. [24, 28]. However, care must be taken for comparing these findings with the results presented in this work, since they were derived for a different scintillator geometry based on a single crystal and used air instead of glue for the coupling to the photosensor.

A critical point in the determination of the PhC geometry and the study of its impact on the light yield and timing resolution is the angular distribution of incident photons used for the optimization. In this work, an angular distribution of photons at their first incidence was used that had been derived from simulations of the reference detector module as described in previous sections. Transferring these results to different detector configurations must be done with caution, since all parameters such as scintillator geometry, surface scattering, reflector material etc., have an influence on the angular distribution of photons on the scintillator exit face. However, this distribution cannot be measured as it occurs only within the scintillator. Therefore, experiments with PhC-equipped scintillators only provide information about the the accumulated effect of PhCs over all recurrences of photons inside the crystal. Nevertheless, in combination with angle-resolved transmission measurements such as presented in this work, these results can serve to gain deeper insight into the complex mechanisms of scintillation photon propagation.

6.4 Combining Photonic Crystals with Concentrators

It has been shown that LCs and PhCs have rather contrary angular characteristics: LCs increase the collection of photons with low, i.e. direct, incident angles whereas PhCs lead to the extraction of light from the scintillator with large, i.e. shallow, incident angles. Nevertheless, the optical simulations of the detector setup combining PhCs and LCs indicate that the two approaches do not interfere negatively with each other. Instead, the positive effects of both concepts add up and this synergy was observed equally for the polished and etched detector configuration. Admittedly, the benefit due to the individual contributions of LCs and PhCs appears moderate compared to the required efforts of their realization, especially in the case of the etched configuration. However, the performance predicted for the PET detector module equipped with both LC and PhCs represent remarkable improvements in light yield and CRT compared to the reference.

Besides, comparing the results obtained for the different detector setups provides information about the influence of the photon propagation time distribution on the CRT of the system. Initially, the goal of the LC concept was to enhance the detection of fast photons in order to improve the timing resolution. Although the propagation time distribution of the LC setup exhibited a larger peak than the reference distribution, the gain in CRT was lower than the predicted value derived from Eq. 2.13 for the improvements in light yield. Interestingly, the same discrepancy was observed for the PhC setups, although their impact on the propagation time distribution is contrary to the effects caused by LCs. This can be explained through the study of the accumulated light yield versus time $\Gamma^x(t)$ of a certain configuration x, relative to the course of the reference light yield $\Gamma^{\mathrm{Ref}}(t)$. This is depicted in Fig. 6.3 for the three configurations: i) 4μm-LC only; ii) PhC$^{\mathrm{Hex}}$ only; iii) 4μm-LC and PhC$^{\mathrm{Hex}}$ combined.

The gains in light yield predicted with Eq. 2.13 for the CRT results from the MC simulations (horizontal dashed lines in Fig. 6.3) coincide with the contour of $\Gamma^x(t)/\Gamma^{\mathrm{Ref}}(t)$ at a certain time t_1 after the detection of the first photons at t_0. This can be interpreted in a way that mainly photons registered in the interval $[t_0, t_1]$ are relevant for the CRT of the system and gains in light yield beyond t_1 do not add any benefit for the timing. This interval was found to be 600 ps for the polished and 680 ps for the etched configuration. From this, it can be concluded that further improvement of the CRT could be achieved if the amount of photons was increased specifically in this timing-relevant interval.

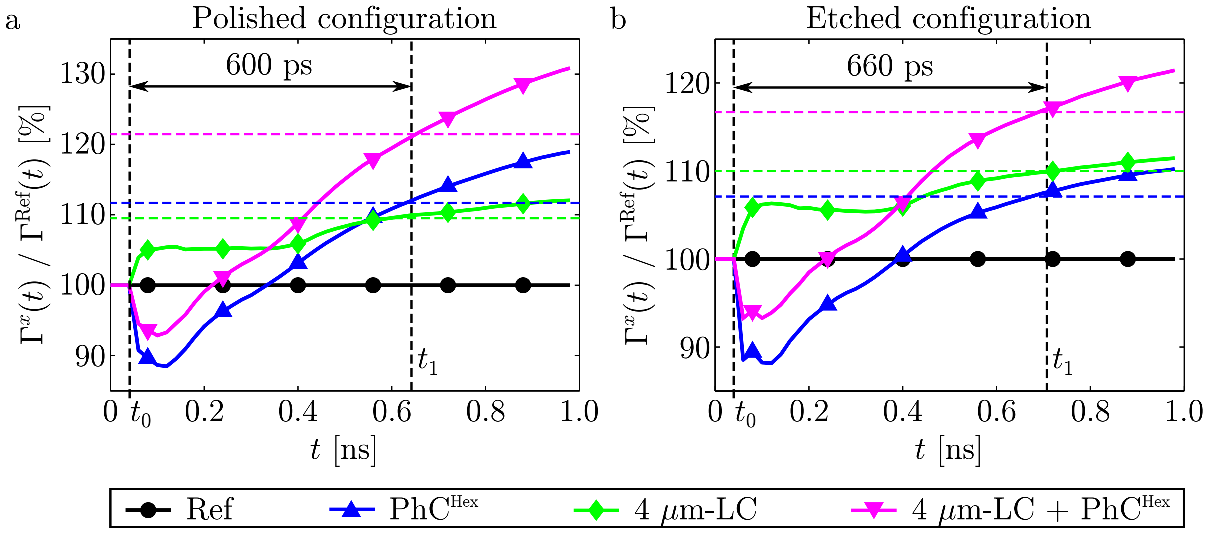

Figure 6.3: Comparison of the light yield of the different detector setups relative to the reference $\Gamma^x(t)/\Gamma^{\mathrm{Ref}}(t)$ versus time for polished (a) and etched configuration (b). The horizontal dashed lines represent the gains in light yield predicted with Eq. 2.13 for the CRT results from the MC simulations. Their colors correspond to the different setups.

6.5 Nano Imprinted Photonic Crystals

Although the introduced PhC fabrication method of direct nano imprinting offers less flexibility than EBL, its simple workflow and high throughput represent highly appealing characteristics for the implementation in commercial systems. A further advantage is that an imprinting system with a surface conformal mold such as the one used in this work can be adapted rather easily for the processing of scintillator crystals with variable geometries and surface roughness. In contrast to this, EBL usually puts rather strict requirements on substrates regarding format and planarity.

The geometry of the PhC samples fabricated with direct nano imprinting did not agree well with the specified values. One reason for this was the laser interference lithography method used for the Si master production, which lead to inaccurate cavity diameters and a rather non-uniform diameter distribution towards the outer regions of the substrate. Further, the transfer of the PhC geometry from the PDMS mold into the polymer layer led to strong modifications of the cavity size and depth caused by the polymer shrinkage during the annealing step. Nevertheless, these aspects represent no general drawback of the imprinting method, as both can be compensated through proper process parameters. For instance, a more precise lithography such as EBL could be used to obtain highly accurate cavity diameters in all regions of the substrate. Taking into account the shrinking behavior of the polymer in the definition of the grating parameters would achieve PhC layers with adequate geometries. However, it is was beyond the scope of this work to readjust these settings and manufacture a second batch of imprinted samples.

The transmission characteristics of the nano imprinted samples further document the typical properties of PhCs with increased transmission beyond the TIR-threshold and reduced transmission for more direct incident angles. The properties could be reproduced with high accuracy using the optical simulation framework. The mismatch of the specified PhC geometry and the grating as manufactured leads to significant differences in the transmission properties. The optical MC simulations of a PET detector module equipped PhCs as imprinted indicate only minor benefits for the light yield of the system. Due to the adverse propagation time distributions of these configurations, the timing simulations indicate no improvement by the imprinted PhCs and the CRT was calculated to be inferior to the reference setup.

Despite these rather negative simulation results, this work showed that the method of fabricating PhCs with direct nano imprinting offers great potential for future PET detector generations. The workflow was shown to be rather simple and the efforts required to refine the process parameters that cause inaccurate geometries are modest. Based on the simulation results with optimized PhC configurations, nano imprinted PhCs with adequate geometries can be expected to contribute significant improvements in future PET detector modules while providing a highly cost-effective and widely compatible manufacturing technology.

6.6 Conclusions

This work presents a detailed discussion of the optical processes in an LSO-based PET detector. The trapping of light inside the high-index scintillator and the limited geometric fill factor of current SiPMs were found to constitute severe limitations of the detector performance. The proposed approaches of LCs and PhCs to improve the light yield and CRT were studied in detail using optical simulations. For this, a novel method of implementing PhCs into an optical MC tool was developed. The calculated transmission characteristics were successfully validated through goniometer experiments using samples produced with various semiconductor fabrication processes. The MC studies of implementing LCs and PhCs into an LSO-based PET detector indicated that both approaches bear the potential to improve the light yield and CRT of the system as summarized in Table 6.1. Combining the two concepts did not exhibit adverse effects and their benefits added up providing significant performance gains. The positive influence of LCs on the light yield and timing was confirmed in first scintillator-based experiments. Finally, the feasibility of producing PhCs through nano imprinting was demonstrated pioneering a promising fabrication alternative that is compatible with potential implementations in future PET detectors.

Table 6.1: Summary of predicted gains in light yield Γ and CRT derived from the optical MC simulations for the proposed approaches of LCs and PhCs.

	Polished configuration				Etched configuration			
	Ref.	LC	PhC	LC + PhC	Ref.	LC	PhC	LC + PhC
Γ	0.227	0.260	0.265	0.302	0.253	0.290	0.273	0.312
$\Gamma/\Gamma^{\text{Ref}}$ [%]	100	115	117	133	100	115	108	123
CRT [ps]	237	226	224	215	229	218	221	212
CRT/CRT$^{\text{Ref}}$ [%]	100	95	95	91	100	95	97	93

Chapter 7

Summary and Outlook

Despite the growing importance of PET in the clinical fields of oncology, cardiology, and neurology, improvements in characteristics such as sensitivity, accuracy, and spatial resolution are required to further the diagnostic quality. This progress can also contribute to improved patient care in other fields, e.g musculoskeletal disorders [170]. To this end, it is necessary that the evolution of PET detector systems continues putting further weight behind problems yet unsolved. The progress in PET technology and methodology during the last decades was marked by the introduction of improved radiopharmaceuticals, scintillator materials, and photosensors. In the light of these advances, the optimization of the optical processes in PET detectors became more relevant if not essential, since improved photon statistics can enhance the energy and timing resolution which results in gains in SNR and overall image quality [22, 25, 32, 33, 62]. Simultaneously, recent developments in micro and nano technologies allow the manipulation of light in unique ways and provide new tools to optimize the propagation of scintillation light. Therefore, the goal of this work was to investigate and improve the scintillation light transfer in state of the art PET detectors making use of micro and nano optical devices. To this end, tailored simulation techniques were developed and validated through optical experiments in conjunction with samples fabricated with techniques from the semiconductor industry.

One focus of these efforts was the improvement of light collection by silicon photomultipliers through light concentrators. While previous studies only considered the macroscopic fill factor of sensor arrays on the chip level [110], this work concentrated on the microscopic fill factor on the Geiger cell level. Optical Monte Carlo simulations of this concept indicated that significant gains can be achieved when using a concentrator with suitable geometry and highly reflective coating. These findings were supported by experimental results that were derived from a setup with LSO scintillators and a photomultiplier tube equipped with a metal grid that mimicked the micro cell structure of a silicon photomultiplier. A sensitivity analysis regarding concentrator geometry versus performance revealed that this approach requires very precise manufacturing and assembly technologies. This work presented concentrator samples produced with semiconductor fabrication processes that met these requirements to a large part. Nevertheless, the results were limited to a proof of principle stage, in which the technology transfer to actual silicon photomultipliers as well as the experimental verification of the concentrator benefit in PET detector implementations remained untapped.

Consequently, the next step must be the initiation of a close collaboration with the manufacturers of silicon photomultipliers in order to evaluate the feasibility of the light concentrator approach under real working conditions. Notwithstanding the progress in silicon photomultiplier technology during the last years [52, 171], certain intrinsic characteristics such as cross talk and dark current remain limiting factors for the improvement of sensor performance through higher geometric fill factors [18, 19]. Therefore, the proposed concept of increasing the photon collection with a light concentrator on the microcell level represents an appealing alternative for further gains in device sensitivity.

A second focus of this work was the increase of light extraction from high-index scintillators using two-dimensional slabs of photonic crystals. Although previous studies reported significant gains in light yield and timing resolution for this approach, the applied simulation tools did not take into account all diffractive properties of photonic crystals [23, 25]. This work presented a novel combined simulation method that considers all wavelength-, angular-, and polarization-dependent properties of photonic crystals that influence not only the reflection and transmission behavior of material interfaces, but also the scattering of photons. The experiments used to validate this technique revealed that the simulations could reproduce the observed optical characteristics with high accuracy. Further optical Monte Carlo simulations of a PET detector module showed that photonic crystals can have a positive impact on the light yield and timing resolution. The results revealed that the estimated benefit depended on the surface properties of the scintillator crystals and more moderate impact was observed for rather rough scintillator configurations compared to highly polished crystals with more pronounced performance gains. It was also predicted by the simulations that combining the concepts of photonic crystals with light concentrators did not exhibit adverse interactions but rather a synergistic summation of the individual positive effects. Admittedly, the parameter sweeps used in this work for the optimization of the photonic crystal coatings represent only a small fraction of possible configurations. In a next step, this analysis should be extended to aspects such as photonic crystals with non-uniform geometries in the third dimension and variable refractive indices of the bulk material. With the help of these investigations, configurations could be obtained that excel the performance of the coatings discussed in this work and provide even larger gains in light yield and timing matching the results presented previously for individual scintillator crystals [23, 24].

The balance between performance gains and fabrication efforts of photonic crystals require novel manufacturing techniques to make these coatings a viable perspective for future PET detector generations. This work evaluated direct nano imprinting of photonic crystals and highly promising results were obtained. Compared to the strategies presented elsewhere for structuring scintillator surfaces [23, 24, 72, 122], the approach based on direct imprinting offers reduced complexity while providing nanometer resolution. Several process parameters were not optimized yet, which led to inaccurate grating geometries. Nevertheless, the feasibility of this technique was demonstrated and the resulting photonic crystals could be characterized well with the combined simulation framework. It is a recognized limitation of this work that the transfer of the fabrication process from glass substrates to scintillator crystals was not achieved. For this, mechanical modifications of the imprinting system's substrate holder would have been necessary in order to accommodate scintillator crystals. With these modifications in conjunction with the necessary adjustments of the process parameters influencing grating geometry, direct nano imprinting offers a unique means for the accurate and cost-effective fabrication of photonic crystals on scintillators of various formats.

To summarize, this work demonstrated the potential of light concentrators and photonic crystals for improving the light yield and timing resolution of state of the art PET detectors. This ultimately leads to an increase in signal to noise ratio and overall image quality, which can help to provide better diagnostic quality and patient care.

Bibliography

[1] D. L. Bailey et al. *Positron emission tomography: basic sciences.* Springer, 2005.

[2] G. J. Kelloff et al. "Progress and promise of FDG-PET imaging for cancer patient management and oncologic drug development". In: *Clin. Canc. Res.* 11.8 (Apr. 2005), pp. 2785–2808. DOI: `10.1158/1078-0432.CCR-04-2626`.

[3] R. Bar-Shalom et al. "Clinical performance of PET/CT in evaluation of cancer: additional value for diagnostic imaging and patient management". In: *J. Nucl. Med.* 44.8 (Aug. 2003), pp. 1200–1209.

[4] K. Facey et al. *Overview of the clinical effectiveness of positron emission tomography imaging in selected cancers.* Gray Pub., 2007.

[5] U. Nestle et al. "Comparison of different methods for delineation of 18F-FDG PET–positive tissue for target volume definition in radiotherapy of patients with non–small cell lung cancer". In: *J. Nucl. Med.* 46.8 (Aug. 2005), pp. 1342–1348.

[6] M. A. Seltzer et al. "The impact of PET on the management of lung cancer: the referring physician's perspective". In: *J. Nucl. Med.* 43.6 (June 2002), pp. 752–756.

[7] L. Kostakoglu and S. J. Goldsmith. "PET in the Assessment of Therapy Response in Patients with Carcinoma of the Head and Neck and of the Esophagus". In: *J. Nucl. Med.* 45.1 (Jan. 2004), pp. 56–68.

[8] C. Klein et al. "Assessment of myocardial viability with contrast-enhanced magnetic resonance imaging comparison with positron emission tomography". In: *Circulation* 105.2 (2002), pp. 162–167. DOI: `10.1161/hc0202.102123`.

[9] J Schwitter et al. "Assessment of myocardial perfusion in coronary artery disease by magnetic resonance: a comparison with positron emission tomography and coronary angiography". In: *Circulation* 103.18 (2001), pp. 2230–2235. DOI: `10.1161/01.CIR.103.18.2230`.

[10] M. Schwaiger, S. Ziegler, and S. G. Nekolla. "PET/CT: challenge for nuclear cardiology". In: *J. Nucl. Med.* 46.10 (Oct. 2005), pp. 1664–1678.

[11] R. E. Coleman. "Positron emission tomography diagnosis of Alzheimer's disease". In: *PET Clinics* 2.1 (Jan. 2007), pp. 25–34. DOI: `10.1016/j.cpet.2007.09.003`.

[12] S. Gilman et al. "Differentiation of Alzheimer's disease from dementia with Lewy bodies utilizing positron emission tomography with 18F fluorodeoxyglucose and neuropsychological testing". In: *Exp. Neurol.* 191 (Feb. 2005), S95–S103. DOI: `10.1016/j.expneurol.2004.06.017`.

[13] C. Melcher and J. Schweitzer. "Cerium-doped lutetium oxyorthosilicate: a fast, efficient new scintillator". In: *IEEE Trans. Nucl. Sci.* 39.4 (Aug. 1992), pp. 502–505. DOI: `10.1109/23.159655`.

[14] K Wienhard et al. "The ECAT HRRT: performance and first clinical application of the new high resolution research tomograph". In: *IEEE Trans. Nucl. Sci.* 49.1 (Feb. 2002), pp. 104–110. DOI: `10.1109/TNS.2002.998689`.

[15] W. W. Moses. "Time of flight in PET revisited". In: *IEEE Trans. Nucl. Sci.* 50.5 (Oct. 2003), pp. 1325–1330. DOI: `10.1109/TNS.2003.817319`.

[16] R. Grazioso et al. "APD performance in light sharing PET applications". In: *IEEE Nuclear Science Symposium Conference Record (NSS/MIC).* Vol. 3. Oct. 2003, pp. 1899–1903. DOI: `10.1109/NSSMIC.2003.1352250`.

[17] K Yamamoto et al. "Development of multi-pixel photon counter (MPPC)". In: *IEEE Nuclear Science Symposium and Medical Imaging Conference Record (NSS/MIC).* Vol. 2. 2006, pp. 1094–1097. DOI: `10.1109/NSSMIC.2006.356038`.

[18] D. Henseler et al. "SiPM performance in PET applications: An experimental and theoretical analysis". In: *IEEE Nuclear Science Symposium Conference Record (NSS/MIC).* Oct. 2009, pp. 1941–1948. DOI: `10.1109/NSSMIC.2009.5402157`.

[19] C. Kim et al. "Time-of-flight PET-MR detector development with silicon photomultiplier". In: *IEEE Nuclear Science Symposium and Medical Imaging Conference Record (NSS/MIC).* Oct. 2012, pp. 3533–3536. DOI: `10.1109/NSSMIC.2012.6551808`.

[20] W. W. Moses and M. Ullisch. "Factors influencing timing resolution in a commercial LSO PET camera". In: *IEEE Trans. Nucl. Sci.* 53.1 (Feb. 2006), pp. 78–85. DOI: `10.1109/TNS.2005.862980`.

[21] M. Kronberger, E. Auffray, and P. Lecoq. "Probing the concepts of photonic crystals on scintillating materials". In: *IEEE Trans. Nucl. Sci.* 55.3 (June 2008), pp. 1102–1106. DOI: `10.1109/TNS.2008.922827`.

[22] F. Bauer et al. "Measurements and Ray-Tracing Simulations of Light Spread in LSO Crystals". In: *IEEE Trans. Nucl. Sci.* 56.5 (Oct. 2009), pp. 2566–2573. DOI: `10.1109/TNS.2009.2030411`.

[23] A. Knapitsch et al. "Effects of Photonic Crystals on the Light Output of Heavy Inorganic Scintillators". In: *IEEE Trans. Nucl. Sci.* 60.3 (June 2013), pp. 2322–2329. DOI: `10.1109/TNS.2013.2262574`.

[24] P Lecoq, E Auffray, and A Knapitsch. "How Photonic Crystals Can Improve the Timing Resolution of Scintillators". In: *IEEE Trans. Nucl. Sci.* 60.3 (June 2013), p. 1653. DOI: `10.1109/TNS.2013.2260768`.

[25] M. Kronberger, E. Auffray, and P. Lecoq. "Improving light extraction from heavy inorganic scintillators by photonic crystals". In: *IEEE Trans. Nucl. Sci.* 57.5 (Oct. 2010), pp. 2475–2482. DOI: `10.1109/TNS.2010.2063438`.

[26] S. Fan et al. "High extraction efficiency of spontaneous emission from slabs of photonic crystals". In: *Phys. Rev. Lett.* 78.17 (Apr. 1997), pp. 3294–3297. DOI: `10.1103/PhysRevLett.78.3294`.

[27] J. D. Joannopoulos et al. *Photonic crystals: molding the flow of light.* Princetion, NJ: Princeton university press, 2011.

[28] A. Knapitsch et al. "Results of photonic crystal enhanced light extraction on heavy inorganic scintillators". In: *IEEE Trans. Nucl. Sci.* 59.5 (Oct. 2012), pp. 2334–2339. DOI: `10.1109/TNS.2012.2184556`.

[29] Hamamatsu Photonics. *Multi Pixel Photon Counters.* Jan. 2014. URL: `http://www.hamamatsu.com/jp/en/product/category/3100/4004/index.html`.

[30] S. Seifert et al. “A comprehensive model to predict the timing resolution of SiPM-based scintillation detectors: theory and experimental validation”. In: *IEEE Trans. Nucl. Sci.* 59.1 (Feb. 2012), pp. 190–204. DOI: `10.1109/TNS.2011.2179314`.

[31] A. N. Otte et al. “Status of Silicon Photomultiplier Development as optical Sensors for MAGIC/EUSO-like Detectors”. In: *Proceedings of the 29th International Cosmic Ray Conference, Pune, India*. 2005, p. 39.

[32] H. Rothfuss et al. “Monte Carlo simulation study of LSO crystals”. In: *IEEE Trans. Nucl. Sci.* 51.3 (June 2004), pp. 770–774. DOI: `10.1109/TNS.2004.829753`.

[33] E. Lorincz et al. “Light output analyzes of scintillator crystal pins and array for PET detector modules”. In: *IEEE Nuclear Science Symposium Conference Record (NSS/MIC)*. Oct. 2008, pp. 4868–4871. DOI: `10.1109/NSSMIC.2008.4774331`.

[34] M. Janecek and W. W. Moses. “Simulating scintillator light collection using measured optical reflectance”. In: *IEEE Trans. Nucl. Sci.* 57.3 (June 2010), pp. 964–970. DOI: `10.1109/TNS.2010.2042731`.

[35] A. Granov, L. Tiutin, and T. Schwarz. *Positron emission tomography*. Springer, 2012.

[36] J. M. Ollinger and J. A. Fessler. “Positron-emission tomography”. In: *IEEE Signal Process. Mag.* 14.1 (1997), pp. 43–55. DOI: `10.1109/79.560323`.

[37] S. R. Cherry, M. Dahlbom, and M. E. Phelps. *PET: Physics, Instrumentation, and Scanners*. Springer, 2006.

[38] H.-P. W. Schlemmer et al. “Simultaneous MR/PET Imaging of the Human Brain: Feasibility Study”. In: *Radiology* 248.3 (Sept. 2008), p. 1028. DOI: `10.1148/radiol.2483071927`.

[39] L. G. Strauss and P. S. Conti. “The applications of PET in clinical oncology.” In: *J. Nucl. Med.* 32.4 (Apr. 1991), pp. 623–48.

[40] G. Stöcklin and V. Pike. *Radiopharmaceuticals for Positron Emission Tomography-Methodological Aspects*. Vol. 24. Springer, 1993.

[41] R. Weissleder et al. *Molecular Imaging, Principles and Practice*. PMPH-USA, 2010.

[42] T. Beyer et al. “A combined PET/CT scanner for clinical oncology”. In: *J. Nucl. Med.* 41.8 (Aug. 2000), pp. 1369–1379.

[43] P. Kinahan et al. “Attenuation correction for a combined 3D PET/CT scanner”. In: *Med. Phys.* 25 (1998), p. 2046. DOI: `10.1118/1.598392`.

[44] P. E. Kinahan, B. H. Hasegawa, and T. Beyer. “X-ray-based attenuation correction for positron emission tomography/computed tomography scanners”. In: *Semin. in Nucl. Med.* Vol. 33. 3. Elsevier. July 2003, pp. 166–179. DOI: `10.1053/snuc.2003.127307`.

[45] E. M. Haacke et al. *Magnetic resonance imaging: physical principles and sequence design*. Wiley-Liss New York, 1999.

[46] M. Hofmann et al. “Towards quantitative PET/MRI: a review of MR-based attenuation correction techniques”. In: *Eur. J. Nucl. Med. Mol. Imaging* 36.1 (Mar. 2009), pp. 93–104. DOI: `10.1007/s00259-008-1007-7`.

[47] D. W. Townsend and S. R. Cherry. “Combining anatomy and function: the path to true image fusion”. In: *Eur. Radiol.* 11.10 (Oct. 2001), pp. 1968–1974. DOI: `10.1007/s003300101007`.

[48] D. W. Townsend, T. Beyer, and T. M. Blodgett. “PET/CT scanners: a hardware approach to image fusion”. In: *Semin. Nucl. Med.* Vol. 33. 3. Elsevier. July 2003, pp. 193–204. DOI: `10.1053/snuc.2003.127314`.

[49] D. Lardinois et al. “Staging of non–small-cell lung cancer with integrated positron-emission tomography and computed tomography”. In: *N. Engl. J. Med.* 348.25 (Dec. 2003), pp. 2500–2507. DOI: `10.1016/0003-4975(95)00752-0`.

[50] B. J. Pichler et al. “Performance test of an LSO-APD detector in a 7-T MRI scanner for simultaneous PET/MRI”. In: *J. Nucl. Med.* 47.4 (Apr. 2006), pp. 639–647.

[51] G. Delso et al. “Performance measurements of the Siemens mMR integrated whole-body PET/MR scanner”. In: *J. Nucl. Med.* 52.12 (Dec. 2011), pp. 1914–1922. DOI: `10.2967/jnumed.111.092726`.

[52] G. Llosá et al. “Novel silicon photomultipliers for PET applications”. In: *IEEE Trans. Nucl. Sci.* 55.3 (June 2008), pp. 877–881. DOI: `10.1109/TNS.2008.922812`.

[53] E. Roncali and S. R. Cherry. “Application of silicon photomultipliers to positron emission tomography”. In: *Ann. Biomed. Eng.* 39.4 (Apr. 2011), pp. 1358–1377. DOI: `10.1007/s10439-011-0266-9`.

[54] S. Strother, M. Casey, and E. Hoffman. “Measuring PET scanner sensitivity: relating countrates to image signal-to-noise ratios using noise equivalents counts”. In: *IEEE Trans. Nucl. Sci.* 37.2 (Apr. 1990), pp. 783–788. DOI: `10.1109/23.106715`.

[55] M. Conti. “State of the art and challenges of time-of-flight PET”. In: *Phys. Med.* 25.1 (Mar. 2009), p. 1. DOI: `10.1016/j.ejmp.2008.10.001`.

[56] J. B. Birks. *The theory and practice of scintillation counting.* Oxford, U.K.: Pergamon, 1964.

[57] P Dorenbos, J. T. M. de Haas, and C. Van Eijk. “Non-proportionality in the scintillation response and the energy resolution obtainable with scintillation crystals”. In: *IEEE Trans. Nucl. Sci.* 42.6 (Dec. 1995), pp. 2190–2202. DOI: `10.1109/23.489415`.

[58] R. Post and L. Schiff. “Statistical limitations on the resolving time of a scintillation counter”. In: *Phys. Rev.* 80.6 (Dec. 1950), p. 1113. DOI: `10.1103/PhysRev.80.1113`.

[59] Y. Shao. “A new timing model for calculating the intrinsic timing resolution of a scintillator detector”. In: *Phys. Med. Biol.* 52.4 (Feb. 2007), p. 1103. DOI: `10.1088/0031-9155/52/4/016`.

[60] E Auffray et al. “A comprehensive & systematic study of coincidence time resolution and light yield using scintillators of different size, wrapping and doping”. In: *IEEE Nuclear Science Symposium and Medical Imaging Conference Record (NSS/MIC).* Oct. 2011, pp. 64–71. DOI: `10.1109/NSSMIC.2011.6154402`.

[61] P Lecoq et al. “Progress on photonic crystals”. In: *IEEE Nuclear Science Symposium Conference Record (NSS/MIC).* Nov. 2010, pp. 1970–1975. DOI: `10.1109/NSSMIC.2010.5874119`.

[62] N Ghal-Eh. “Light transport contribution to the timing characteristics of scintillation detectors”. In: *Radiat. Phys. Chem.* 80.3 (Mar. 2011), pp. 365–368. DOI: `10.1016/j.radphyschem.2010.11.005`.

[63] M. Conti. “Improving time resolution in time-of-flight PET”. In: *Nucl. Instr. Meth. Phys. Res., Sect. A* 648 (Aug. 2011), S194–S198. DOI: `10.1016/j.nima.2010.11.171`.

[64] D. M. Binkley. “Optimization of scintillation-detector timing systems using Monte Carlo analysis”. In: *IEEE Trans. Nucl. Sci.* 41.1 (Feb. 1994), pp. 386–393. DOI: `10.1109/23.281528`.

[65] W.-S. Choong. “The timing resolution of scintillation-detector systems: Monte Carlo analysis”. In: *Phys. Med. Biol.* 54.21 (Oct. 2009), p. 6495. DOI: `10.1088/0031-9155/54/21/004`.

[66] N. Brekke et al. “A Monte Carlo based simulation of an high speed ADC-based TOF-PET read-out system”. In: *IEEE Nuclear Science Symposium Conference Record (NSS/MIC)*. Oct. 2010, pp. 3022–3024. DOI: `10.1109/NSSMIC.2010.5874353`.

[67] J. Breuer et al. “Detailed Monte-Carlo simulation of SiPM-based scintillation detectors for PET”. In: *International Workshop on New Photon-detectors (PhotoDet), Orsay, France*. June 2012.

[68] G. F. Knoll. *Radiation detection and measurement*. Wiley. com, 2010.

[69] M. Weber. “Scintillation: mechanisms and new crystals”. In: *Nucl. Instr. Meth. Phys. Res., Sect. A* 527.1 (July 2004), pp. 9–14. DOI: `10.1016/j.nima.2004.03.009`.

[70] P. A. Rodnyi. *Physical processes in inorganic scintillators*. Vol. 14. CRC PressI Llc, 1997.

[71] N. W. Ashcroft and M. D. N. *Solid State Physics*. Saunders College Publishing, 2013.

[72] M. Kronberger, P. Lecoq, and C. W. Fabjan. “Optimization of the light extraction from heavy inorganic scintillators”. PhD thesis. Technical University Wien, 2008.

[73] S. Manohara et al. “On the effective atomic number and electron density: a comprehensive set of formulas for all types of materials and energies above 1keV”. In: *Nucl. Instr. Meth. Phys. Res., Sect. B* 266.18 (Sept. 2008), pp. 3906–3912. DOI: `10.1016/j.nimb.2008.06.034`.

[74] J Glodo et al. “Effects of Ce concentration on scintillation properties of $\mathrm{LaBr_3}$: Ce”. In: *IEEE Trans. Nucl. Sci.* 52.5 (Oct. 2005), pp. 1805–1808. DOI: `10.1109/TNS.2005.856906`.

[75] C. L. Melcher. “Scintillation crystals for PET.” In: *J. Nucl. Med.* 41.6 (2000), p. 1051.

[76] M. M. Ter-Pogossian et al. “Super PETT I: a positron emission tomograph utilizing photon time-of-flight information”. In: *IEEE Trans. Med. Imaging* 1.3 (Nov. 1982), pp. 179–187. DOI: `10.1109/TMI.1982.4307570`.

[77] R Gariod et al. “The LETI positron tomograph architecture and time of flight improvements”. In: *Proceedings of The Workshop on Time of Flight Tomography*. 1982, pp. 25–29.

[78] T. Lewellen et al. “Performance measurements of the SP3000/UW time-of-flight positron emission tomograph”. In: *IEEE Trans. Nucl. Sci.* 35.1 (Feb. 1988), pp. 665–669. DOI: `10.1109/23.12808`.

[79] B Mazoyer et al. “Physical characteristics of TTV03, a new high spatial resolution time-of-flight positron tomograph”. In: *IEEE Trans. Nucl. Sci.* 37.2 (Apr. 1990), pp. 778–782. DOI: `10.1109/23.106714`.

[80] S. Cherry et al. “MicroPET: a high resolution PET scanner for imaging small animals”. In: *IEEE Trans. Nucl. Sci.* 44.3 (June 1997), pp. 1161–1166. DOI: `10.1109/23.596981`.

[81] J. Huber et al. “A LSO scintillator array for a PET detector module with depth of interaction measurement”. In: *IEEE Nuclear Science Symposium Conference Record (NSS/MIC)*. Vol. 2. 2000, pp. 14–46. DOI: `10.1109/NSSMIC.2000.950023`.

[82] N. K. Doshi et al. “Design and evaluation of an LSO PET detector for breast cancer imaging”. In: *Med. Phys.* 27 (2000), p. 1535. DOI: `10.1118/1.599019`.

[83] C. M. Pepin et al. “Properties of LYSO and recent LSO scintillators for phoswich PET detectors”. In: *IEEE Trans. Nucl. Sci.* 51.3 (June 2004), pp. 789–795. DOI: `10.1109/TNS.2004.829781`.

[84] R. Nutt. “Is LSO the future of PET?” In: *Eur. J. Nucl. Med. Mol. Imaging* 29.11 (Nov. 2002), pp. 1523–1524. ISSN: 1619-7070. DOI: `10.1007/s00259-002-0987-y`.

[85] J. S. Karp. “Is LSO the future of PET?” In: *Eur. J. Nucl. Med. Mol. Imaging* 29.11 (Nov. 2002), pp. 1525–1528. ISSN: 1619-7070. DOI: `10.1007/s00259-002-0987-y`.

[86] M Schmand et al. “Performance results of a new DOI detector block for a high resolution PET-LSO research tomograph HRRT”. In: *IEEE Trans. Nucl. Sci.* 45.6 (Dec. 1998), pp. 3000–3006. DOI: `10.1109/23.737656`.

[87] H. Herzog et al. “NEMA NU2-2001 guided performance evaluation of four Siemens ECAT PET scanners”. In: *IEEE Trans. Nucl. Sci.* 51.5 (Oct. 2004), pp. 2662–2669. DOI: `10.1109/TNS.2004.835778`.

[88] T Beyer et al. “PET/CT-Tomographie mit neuem PET-Detektormaterial für ultraschnelle Bildgebung in der klinischen Onkologie”. In: *Electromedica* 2 (2002), p. 169.

[89] M. Brambilla et al. “Performance characteristics obtained for a new 3-dimensional lutetium oxyorthosilicate–based whole-body PET/CT scanner with the National Electrical Manufacturers Association NU 2-2001 Standard”. In: *J. Nucl. Med.* 46.12 (2005), pp. 2083–2091.

[90] G. Muehllehner and J. S. Karp. “Positron emission tomography”. In: *Phys. Med. Biol.* 51.13 (June 2006), R117. DOI: `10.1088/0031-9155/51/13/R08`.

[91] T. K. Lewellen. “Time-of-flight PET”. In: *Semin. Nucl. Med.* Vol. 28. 3. July 1998, pp. 268–275. DOI: `10.1016/S0001-2998(98)80031-7`.

[92] Hamamatsu Photonics. *Photomultiplier Tubes: Basics and Applications*. Hamamatsu Photonics, 2007. URL: `https://www.hamamatsu.com/resources/pdf/etd/PMT_handbook_v3aE.pdf`.

[93] Y Shao et al. “Development of a PET detector system compatible with MRI/NMR systems”. In: *IEEE Trans. Nucl. Sci.* 44.3 (July 1997), pp. 1167–1171. DOI: `10.1109/23.596982`.

[94] S. H. Maramraju et al. “Small animal simultaneous PET/MRI: initial experiences in a 9.4 T microMRI”. In: *Phys. Med. Biol.* 56.8 (Mar. 2011), p. 2459. DOI: `10.1088/0031-9155/56/8/009`.

[95] M Kapusta et al. “Avalanche photodiodes in scintillation detection for high resolution PET”. In: *IEEE Nuclear Science Symposium Conference Record*. Vol. 1. 1998, pp. 733–737. DOI: `10.1109/NSSMIC.1998.775240`.

[96] Hamamatsu Photonics. *Opto-Semiconductor Handbook*. Hamamatsu Photonics, 2013. URL: `https://www.hamamatsu.com/resources/pdf/ssd/e02_handbook_si_photodiode.pdf`.

[97] V Golovin and V. Saveliev. “Novel type of avalanche photodetector with Geiger mode operation”. In: *Nucl. Instr. Meth. Phys. Res., Sect. A* 518.1 (Feb. 2004), pp. 560–564. DOI: `10.1016/j.nima.2003.11.085`.

[98] M. Mazzillo et al. “Silicon photomultiplier technology at STMicroelectronics”. In: *IEEE Trans. Nucl. Sci.* 56.4 (Aug. 2009), pp. 2434–2442. DOI: `10.1109/TNS.2009.2024418`.

[99] D Renker. “Geiger-mode avalanche photodiodes, history, properties and problems”. In: *Nucl. Instr. Meth. Phys. Res., Sect. A* 567.1 (Nov. 2006), pp. 48–56. DOI: `10.1016/j.nima.2006.05.060`.

[100] C. Piemonte. “A new silicon photomultiplier structure for blue light detection”. In: *Nucl. Instr. Meth. Phys. Res., Sect. A* 568.1 (Nov. 2006), pp. 224–232. DOI: `10.1016/j.nima.2006.07.018`.

[101] P Buzhan et al. “Silicon photomultiplier and its possible applications”. In: *Nucl. Instr. Meth. Phys. Res., Sect. A* 504.1 (May 2003), pp. 48–52. DOI: `10.1016/S0168-9002(03)00749-6`.

[102] S. Logunov and S. Kuchinsky. “Experimental and theoretical study of bulk light scattering in CaF2 monocrystals”. In: *J. Appl. Phys.* 98.5 (Sept. 2005), p. 053501. DOI: `10.1063/1.2034085`.

[103] C. O. Steinbach et al. “Optical scattering length of LYSO scintillator crystals”. In: *IEEE Nuclear Science Symposium Conference Record (NSS/MIC)*. Oct. 2011, pp. 2653–2656. DOI: `10.1109/NSSMIC.2011.6152711`.

[104] W. Demtröder. *Experimentalphysik 2 - Elektrizität und Optik*. Springer, 2002.

[105] J. Huber et al. “Geometry and surface treatment dependence of the light collection from LSO crystals”. In: *Nucl. Instr. Meth. Phys. Res., Sect. A* 437.2 (Nov. 1999), pp. 374–380. DOI: `10.1016/S0168-9002(99)00766-4`.

[106] M. Janecek and W. W. Moses. “Measuring light reflectance of BGO crystal surfaces”. In: *IEEE Trans. Nucl. Sci.* 55.5 (Oct. 2008), pp. 2443–2449. DOI: `10.1109/TNS.2008.2003253`.

[107] P. Beckmann and A. Spizzichino. *The Scattering of Electromagnetic Waves from Rough Surfaces*. Pergamon, New York, 1963.

[108] S. Schröder et al. “Modeling of light scattering in different regimes of surface roughness”. In: *Opt. Express* 19.10 (May 2011), pp. 9820–9835. DOI: `10.1364/OE.19.00982`.

[109] A. González Martínez et al. “Innovative PET detector concept based on SiPMs and continuous crystals”. In: *Nucl. Instr. Meth. Phys. Res., Sect. A* 695 (Dec. 2012), pp. 213–217. DOI: `10.1016/j.nima.2011.11.029`.

[110] G. Barbarino et al. “Light Concentrators for Silicon Photomultipliers”. In: *Phys. Procedia* 37 (2012), pp. 709–714. DOI: `10.1016/j.phpro.2012.02.420`.

[111] C. Piemonte et al. “Performance of a novel, small-cell, high-fill-factor SiPM for TOF-PET”. In: *IEEE Nuclear Science Symposium Conference Record (NSS/MIC)*. Oct. 2013, pp. 1–3. DOI: `10.1109/NSSMIC.2013.6829170`.

[112] J. Chaves. *Introduction to nonimaging optics*. Vol. 134. CRC PressI Llc, 2008.

[113] H. Garg. *Solar energy: fundamentals and applications*. Tata McGraw-Hill Education, 2000.

[114] P Benıtez and J. Miñano. “Concentrator optics for the next-generation photovoltaics”. In: *Next Generation Photovoltaics* (2003), p. 285.

[115] A. Rabl. “Comparison of solar concentrators”. In: *Sol. Energy.* 18.2 (1976), pp. 93–111. DOI: `10.1016/0038-092X(76)90043-8`.

[116] R. Winston. “Principles of solar concentrators of a novel design”. In: *Solar Energy* 16.2 (Oct. 1974), pp. 89–95. DOI: `10.1016/0038-092X(74)90004-8`.

[117] R. Ghodssi. *MEMS materials and processes handbook*. Springer Science+ Business Media, 2011.

[118] D Wahl, V. Mikhailik, and H Kraus. “The Monte-Carlo refractive index matching technique for determining the input parameters for simulation of the light collection in scintillating crystals”. In: *Nucl. Instr. Meth. Phys. Res., Sect. A* 570.3 (Jan. 2007), pp. 529–535. DOI: `10.1016/j.nima.2006.10.099`.

[119] W. H. Southwell. “Gradient-index antireflection coatings”. In: *Opt. Lett.* 8.11 (1983), pp. 584–586. DOI: `10.1364/OL.8.000584`.

[120] J.-Q. Xi et al. “Optical thin-film materials with low refractive index for broadband elimination of Fresnel reflection”. In: *Nature Photon.* 1.3 (Mar. 2007), pp. 176–179. DOI: `10.1038/nphoton.2007.26`.

[121] S Möller and S. Forrest. “Improved light out-coupling in organic light emitting diodes employing ordered microlens arrays”. In: *J. Appl. Phys.* 91.5 (2002), pp. 3324–3327. DOI: `10.1063/1.1435422`.

[122] J. Cates, J. Hayward, and X Zhang. “Increased Light Extraction From Inorganic Scintillators With Laser-Etched Microstructures”. In: *IEEE Trans. Nucl. Sci.* 60.2 (Apr. 2013), pp. 1027–1032. DOI: `10.1109/TNS.2013.2249090`.

[123] I. Schnitzer et al. “30% external quantum efficiency from surface textured, thin-film light-emitting diodes”. In: *Appl. Phys. Lett.* 63.16 (1993), pp. 2174–2176. DOI: `10.1063/1.110575`.

[124] J.-Y. Cho et al. “Improvement of photon extraction efficiency of GaN-based LED using micro and nano complex polymer structures”. In: *Nanoscale Res. Lett.* 6.1 (Oct. 2011), pp. 1–6. DOI: `10.1186/1556-276X-6-578`.

[125] P Pignalosa et al. “Giant light extraction enhancement of medical imaging scintillation materials using biologically inspired integrated nanostructures”. In: *Opt. Lett.* 37.14 (July 2012), pp. 2808–2810. DOI: `10.1364/OL.37.002808`.

[126] T. Yamasaki, K. Sumioka, and T. Tsutsui. “Organic light-emitting device with an ordered monolayer of silica microspheres as a scattering medium”. In: *Appl. Phys. Lett.* 76.10 (2000), pp. 1243–1245. DOI: `10.1063/1.125997`.

[127] S.-Y. Hsu et al. “Extraction enhancement in organic light emitting devices by using metallic nanowire arrays”. In: *Appl. Phys. Lett.* 92.1 (2008), p. 013303. DOI: `10.1063/1.2828712`.

[128] C. Wiesmann et al. “Photonic crystal LEDs–designing light extraction”. In: *Laser Photon. Rev.* 3.3 (Apr. 2009), pp. 262–286. DOI: `10.1002/lpor.200810053`.

[129] Z. Zhu et al. “Enhanced light extraction efficiency for glass scintillator coupled with two-dimensional photonic crystal structure”. In: *Opt. Mat.* 35.12 (Oct. 2013), pp. 2343–2346. DOI: `10.1016/j.optmat.2013.06.029`.

[130] J. D. Joannopoulos et al. *Photonic Crystals - Molding the Flow of Light.* Princeton University Press, 2008.

[131] J. D. Jackson. *Classical Electrodynamics.* John Wiley & Sons, Inc., 1999.

[132] H. Miyazaki et al. “Photonic material for designing arbitrarily shaped mirrors and microcavities in two dimensions”. In: *J. Appl. Phys.* 95.9 (Apr. 2004), pp. 4555–4558. DOI: `10.1063/1.1691484`.

[133] B. Temelkuran and E. Ozbay. “Experimental demonstration of photonic crystal based waveguides”. In: *Appl. Phys. Lett.* 74.4 (1999), pp. 486–488. DOI: `10.1063/1.123163`.

[134] Y Ohtera et al. “Photonic crystal polarisation splitters”. In: *Electron. Lett.* 35.15 (July 1999), pp. 1271–1272. DOI: `10.1049/el:19990875`.

[135] M Notomi. “Theory of light propagation in strongly modulated photonic crystals: Refractionlike behavior in the vicinity of the photonic band gap”. In: *Phys. Rev. B* 62.16 (Oct. 2000), p. 10696. DOI: `10.1103/PhysRevB.62.10696`.

[136] H. Kosaka et al. “Superprism phenomena in photonic crystals”. In: *Phys. Rev. B* 58.16 (Oct. 1998), R10096. DOI: `10.1103/PhysRevB.58.R10096`.

[137] C. Luo, S. G. Johnson, and J. Joannopoulos. “All-angle negative refraction in a three-dimensionally periodic photonic crystal”. In: *Appl. Phys. Lett.* 81.13 (Sept. 2002), pp. 2352–2354. DOI: `10.1063/1.1508807`.

[138] C. Luo et al. “All-angle negative refraction without negative effective index”. In: *Phys. Rev. B* 65.20 (May 2002), 201104–R. DOI: `10.1103/PhysRevB.65.201104`.

[139] M. Fujita et al. “Simultaneous inhibition and redistribution of spontaneous light emission in photonic crystals”. In: *Science* 308.5726 (May 2005), pp. 1296–1298. DOI: `10.1126/science.1110417`.

[140] M. Boroditsky et al. “Light extraction from optically pumped light-emitting diode by thin-slab photonic crystals”. In: *Appl. Phys. Lett.* 75.8 (1999), pp. 1036–1038. DOI: `10.1063/1.124588`.

[141] A. A. Erchak et al. “Enhanced coupling to vertical radiation using a two-dimensional photonic crystal in a semiconductor light-emitting diode”. In: *Appl. Phys. Lett.* 78.5 (2001), pp. 563–565. DOI: `10.1063/1.1342048`.

[142] A. David, H. Benisty, and C. Weisbuch. “Optimization of light-diffracting photonic-crystals for high extraction efficiency LEDs”. In: *J. Display Technol.* 3.2 (June 2007), pp. 133–148. DOI: `10.1109/JDT.2007.896736`.

[143] E. G. Loewen and E. Popov. *Diffraction gratings and applications.* CRC Press, 1997.

[144] A. R. Knapitsch. “Photonic Crystals: Enhancing the Light Output of Scintillation Based Detectors”. PhD thesis. CERN, 2012.

[145] A Levin and C. Moisan. “A more physical approach to model the surface treatment of scintillation counters and its implementation into DETECT”. In: *IEEE Nuclear Science Symposium Conference Record (NSS/MIC).* Vol. 2. 1996, pp. 702–706. DOI: `10.1109/NSSMIC.1996.591410`.

[146] S Agostinelli et al. “GEANT4 - a simulation toolkit”. In: *Nucl. Instr. Meth. Phys. Res., Sect. A* 506.3 (July 2003), pp. 250–303. DOI: `10.1016/S0168-9002(03)01368-8`.

[147] M. Moharam and T. Gaylord. “Rigorous coupled-wave analysis of planar-grating diffraction”. In: *J. Opt. Soc. Amer.* 71.7 (1981), pp. 811–818. DOI: `10.1364/JOSA.71.000811`.

[148] K. C. Johnson. *Grating Diffraction Calculator (GD-Calc) - Coupled-Wave Theory for Biperiodic Diffraction Gratings.* 2008. URL: `http://software.kjinnovation.com/GD-Calc.pdf`.

[149] H. Zaidi and A. Del Guerra. “An outlook on future design of hybrid PET/MRI systems”. In: *Med. Phys.* 38.10 (Sept. 2011), p. 5667. DOI: `10.1118/1.3633909`.

[150] R. Mao, L. Zhang, and R.-Y. Zhu. “Optical and scintillation properties of inorganic scintillators in high energy physics”. In: *IEEE Nuclear Science Symposium Conference Record (NSS/MIC).* Vol. 3. 2007, pp. 2285–2291. DOI: `10.1109/NSSMIC.2007.4436602`.

[151] Filmetrics Inc., San Diego, CA, USA. *Refractive index database.* Jan. 2014. URL: `http://www.filmetrics.com/refractive-index-database/`.

[152] R. Slates et al. “Chemical polishing of LSO crystals to increase light output”. In: *IEEE Nuclear Science Symposium Conference Record (NSS/MIC).* Vol. 2. 1999, pp. 939–942. DOI: `10.1109/NSSMIC.1999.845817`.

[153] G. E. Jellison Jr et al. “Spectroscopic refractive indices of monoclinic single crystal and ceramic lutetium oxyorthosilicate from 200 to 850 nm”. In: *J. Appl. Phys.* 112.6 (Sept. 2012), p. 063524. DOI: `10.1063/1.4752421`.

[154] T.-R. Hsu. *MEMS & Microsystems: Design, Manufacture, and Nanoscale Engineering.* John Wiley & Sons, 2008.

[155] H. Fujiwara. *Spectroscopic ellipsometry: principles and applications.* John Wiley & Sons, 2007.

[156] A. Horn. "Modellierung und Simulation orientierungsabhängiger Ätzprozesse in Silizium". PhD thesis. Technical University Munich, 2006.

[157] Schott, Mainz, Germany. *Glass catalogue.* July 2014. URL: `www.schott.com`.

[158] S. Y. Chou, P. R. Krauss, and P. J. Renstrom. "Nanoimprint lithography". In: *J. Vac. Sci. Technol. B* 14.6 (1996), pp. 4129–4133. DOI: `10.1116/1.588605`.

[159] H. K. Cho et al. "Light extraction enhancement from nano-imprinted photonic crystal GaN-based blue light-emitting diodes". In: *Opt. Express* 14.19 (2006), pp. 8654–8660. DOI: `10.1364/OE.14.008654`.

[160] S. H. Kim et al. "Fabrication of photonic crystal structures on light emitting diodes by nanoimprint lithography". In: *Nanotechnology* 18.5 (Jan. 2007), p. 055306. DOI: `10.1088/0957-4484/18/5/055306`.

[161] K.-S. Han et al. "Enhanced performance of solar cells with anti-reflection layer fabricated by nano-imprint lithography". In: *Sol. Energ. Mat. Sol. C.* 95.1 (Jan. 2011), pp. 288–291. DOI: `10.1016/j.solmat.2010.04.064`.

[162] R. Ji et al. "UV enhanced substrate conformal imprint lithography (UV-SCIL) technique for photonic crystals patterning in LED manufacturing". In: *Microelectron. Eng.* 87.5 (2010), pp. 963–967. DOI: `10.1016/j.mee.2009.11.134`.

[163] H. van Wolferen and L. Abelmann. "Laser Interference Lithography". In: *Lithography: Principles, Processes and Materials.* Ed. by T. C. Hennessy. Hauppauge NY, USA: Nova Publishers, Jan. 2011, pp. 133–148. URL: `http://doc.utwente.nl/78097/`.

[164] K.-J. Byeon et al. "Enhanced light output from vertical light-emitting diodes with an imprinted highly refractive polymer layer". In: *Curr. Appl. Phys.* 11.4 (July 2011), pp. 147–150. DOI: `10.1016/j.cap.2010.12.040`.

[165] Y.-C. Lee, C.-Y. Chen, and Y.-Y. Chou. "Fabrication of high-refractive-index microstructures and their applications to the efficiency improvement of GaN-based LEDs". In: *Opt. Express* 19.106 (Nov. 2011), A1231–A1236. DOI: `10.1364/OE.19.0A1231`.

[166] F. J. Massey Jr. "The Kolmogorov-Smirnov test for goodness of fit". In: *J. Am. Stat. Assoc.* 46.253 (1951), pp. 68–78. DOI: `10.1080/01621459.1951.10500769`.

[167] D. J. Sheskin. *Handbook of parametric and nonparametric statistical procedures.* CRC Press, 2003.

[168] J. Menezes et al. "Band gap of hexagonal 2D photonic crystals with elliptical holes recorded by interference lithography". In: *Opt. Express* 14.11 (2006), pp. 4873–4879. DOI: `10.1364/OE.14.004873`.

[169] T. Frach and A. Thon. *Method to optimize the light extraction from scintillator crystals in a solid-state detector.* US Patent 8,481,948. July 2013.

[170] D. A. Torigian et al. "PET/MR imaging: technical aspects and potential clinical applications". In: *Radiology* 267.1 (Apr. 2013), pp. 26–44. DOI: `10.1148/radiol.13121038`.

[171] C. Degenhardt et al. "The digital silicon photomultiplier—a novel sensor for the detection of scintillation light". In: *IEEE Nuclear Science Symposium Conference Record (NSS/MIC).* 2009, pp. 2383–2386. DOI: `10.1109/NSSMIC.2009.5402190`.

List of Figures

List of Tables

List of Publications

Peer-reviewed Journals

C. Thalhammer, J. Breuer, T. Fuehrer, A. Popescu, H. Hedler, T. Walther, and T. Niendorf. "Combining Photonic Crystal and Optical Monte Carlo Simulations: Implementation, Validation and Application in a Positron Emission Tomography Detector". In: *IEEE Trans. Nucl. Sci.* 61.6 (Dec. 2014), pp. 3618-3626, DOI: `10.1109/TNS.2014.2365879`.

C. Thalhammer, W. Renz, L. Winter, F. Hezel, J. Rieger, H. Pfeiffer, A. Graessl, F. Seifert, W. Hoffmann, F. von Knobelsdorff-Brenkenhoff, V. Tkachenko, J. Schulz-Menger, P. Kellman, and T. Niendorf. "Two-dimensional sixteen channel transmit/receive coil array for cardiac MRI at 7.0 T: design, evaluation, and application". In: *J. Magn. Reson. Imaging* 36.4 (Oct. 2012) pp. 847-57. DOI: `10.1002/jmri.23724`.

S. Klix, A. Els, K. Paul, A. Graessl, C. Oezerdem, O. Weinberger, L. Winter, C. Thalhammer, T. Huelnhagen, J. Rieger, H. Mehling, J. Schulz-Menger, and T. Niendorf. "On the subjective Acceptance during Cardiovascular Magnetic Resonance Imaging at 7.0 Tesla". In: *PLoS ONE* 10.1:e0117095 (Jan. 2015). DOI: `10.1371/journal.pone.0117095`

A. Graessl, L. Winter, C. Thalhammer, W. Renz, P. Kellman, C. Martin, F. von Knobelsdorff-Brenkenhoff, V. Tkachenko, J. Schulz-Menger, and T. Niendorf. "Design, evaluation and application of an eight channel transmit/receive coil array for cardiac MRI at 7.0 T". In: *Eur. J. Radiol.* 82.5. (May 2013) pp. 752-759. DOI: `10.1016/j.ejrad.2011.08.002`

T. Niendorf, A. Graessl, C. Thalhammer, M. Dieringer, O. Kraus, D. Santoro, K. Fuchs, F. Hezel, S. Waiczies, B. Ittermann, and L. Winter. "Progress and promises of human cardiac magnetic resonance at ultrahigh fields: a physics perspective". In: *J. Magn. Reson.* 229 (Apr. 2013) pp. 208-222. DOI: `10.1016/j.jmr.2012.11.015`

F. von Knobelsdorff-Brenkenhoff, V. Tkachenko, L. Winter, J. Rieger, C. Thalhammer, F. Hezel, A. Graessl, M. Dieringer, T. Niendorf, and J. Schulz-Menger. "Assessment of the right ventricle with cardiovascular magnetic resonance at 7 Tesla". In: *J. Cardiov. Magn. Reson.* 15.23 (Mar. 2013). DOI: `10.1186/1532-429X-15-23`

F. Hezel, C. Thalhammer, S. Waiczies, J. Schulz-Menger, and T. Niendorf. "High spatial resolution and temporally resolved T2* mapping of normal human myocardium at 7.0 Tesla: an ultrahigh field magnetic resonance feasibility study". In: *PLoS One* 7.12:e52324 (Dec. 2012). DOI: `10.1371/journal.pone.0052324`

L. Winter, P. Kellman, W. Renz, A. Graessl, F. Hezel, C. Thalhammer, F. von Knobelsdorff-Brenkenhoff, V. Tkachenko, J. Schulz-Menger, and T. Niendorf. “Comparison of three multichannel transmit/receive radiofrequency coil configurations for anatomic and functional cardiac MRI at 7.0 T: implications for clinical imaging”. In: *Eur. Radiol.* 22.10 (Oct. 2012) pp. 2211-2220. DOI: `10.1007/s00330-012-2487-1`

Conferences

C. Thalhammer, J. Breuer, A. Popescu, H. Hedler, and T. Niendorf. “Implementation of Photonic Crystal Simulations into a Monte Carlo Code to Investigate Light Extraction from Scintillators”. In: *Conference on Lasers and Electro-Optics Europe and International Quantum Electronics Conference* (May 2013). DOI: `10.1109/CLEOE-IQEC.2013.6801469`.

C. Thalhammer, A. Popescu, H. Hedler, and T. Niendorf. “Photonic Crystals for Improved Light Extraction from Scintillators: Impact of Scintillator Parameters”. In: *Verhandlungen der deutschen physikalischen Gesellschaft* (Mar. 2013).

C. Thalhammer and H. Hedler. “Improving the Photon Yield of Indirect X-Ray Detectors”. In: *2nd Siemens Healthcare Detector Conference* (Mar. 2013). Unpublished.

C. Thalhammer, W. Renz, H. Pfeiffer, J. Rieger, L. Winter, F. Hezel, F. Seifert, W. Hoffmann, R. Seemann, and T. Niendorf. “Design, Evaluation and Application of a two-dimensional TX/RX Surface Coil Array For Cardiac MRI at 7 T”. In: *Proceedings of the International Society of Magnetic Resonance in Medicine (ISMRM)* 19 (May 2011) p. 326. URL: `http://cds.ismrm.org/protected/11MProceedings/files/326.pdf`

München, 15. März 2015

Christof Thalhammer

Acknowledgment

This project has been supported by so many people in so many ways. In particular, I would like to thank my supervisor Prof. Dr. T. Niendorf, who was an excellent mentor and contributed significantly to my scientific and personal development during the last 5 years. I highly appreciate his efforts in the collaboration with Siemens Corporate Technology and his guidance in my transition from the student's phase to a professional career. Also, I would like to thank Prof. Dr. O. Benson for supporting my dissertation and helping with university matters.

I would like to thank my supervisor from Siemens-side Dr. H. Hedler. He was a tremendous adviser who always contributed inspiring new ideas, offered new perspectives, put trust in my work from the very beginning, and guided me through the world of research at Siemens Corporate Technology. Further, my fellow PhD student and friend M. Wick contributed significantly to this work. He had endless patience in helping me with the procedures in the clean room facilities and our conversations and coffee breaks helped me get through the hard times of the project. Also, I want to thank all of my colleagues at Siemens Corporate Technology, who supported my project in various ways.

I highly appreciate the help of Dr. J. Breuer from Siemens Healthcare. This thesis would not have been possible without his insight into PET systems and their simulations. I would also like to direct special thanks to Dr. T. Führer and Prof. Dr. T. Walther at the Technical University Darmstadt. Their support and expertise in optical experiments were fundamental for my work and I always enjoyed my visits in Darmstadt. Further, I want to thank the Siemens Molecular Imaging R&D department in Knoxville and Dr. R. Ji from Suess Microtec for facilitating last minute experiments that allowed me to finalize this project.

I owe very special thanks to my entire family. Your love and care made me the person I am today. Finally, I want to thank Maren, who always believed in me and made me hang on, even in hard and frustrating times. You are my everything!

Eigenständigkeitserklärung

Hiermit erkläre ich, die Dissertation selbstständig und nur unter Verwendung der angegebenen Hilfen und Hilfsmittel angefertigt zu haben. Ich habe mich nicht anderwärts um einen Doktorgrad in dem Promotionsfach beworben und besitze keinen entsprechenden Doktorgrad. Die Promotionsordnung der Mathematisch-Naturwissenschaftlichen Fakultät I, veröffentlicht im Amtlichen Mitteilungsblatt der Humboldt-Universität zu Berlin Nr. 21/2009 am 06. Juli 2009, habe ich zur Kenntnis genommen.

München, 15. März 2015

Christof Thalhammer